SEMICONDUCTOR NANOPARTICLES AS PLATFORM FOR BIO-APPLICATIONS AND ENERGY RELATED SYSTEMS.

Alba María Matas Adams

Dipòsit Legal: T 55-2016

UNIVERSITAT ROVIRA I VIRGILI
SEMICONDUCTOR NANOPARTICLES AS PLATFORM FOR BIO-APPLICATIONS AND ENERGY RELATED SYSTEMS.
Alba María Matas Adams
Dipòsit Legal: T 55-2016

Semiconductor Nanoparticles as Platform for Bio-Applications and Energy Related Systems

Alba María Matas Adams

Doctoral Thesis

Tarragona 2015

UNIVERSITAT ROVIRA I VIRGILI

UNIVERSITAT ROVIRA I VIRGILI
SEMICONDUCTOR NANOPARTICLES AS PLATFORM FOR BIO-APPLICATIONS AND ENERGY RELATED SYSTEMS.
Alba María Matas Adams
Dipòsit Legal: T 55-2016

UNIVERSITAT ROVIRA I VIRGILI
SEMICONDUCTOR NANOPARTICLES AS PLATFORM FOR BIO-APPLICATIONS AND ENERGY RELATED SYSTEMS.
Alba María Matas Adams
Dipòsit Legal: T 55-2016

UNIVERSITAT ROVIRA I VIRGILI
SEMICONDUCTOR NANOPARTICLES AS PLATFORM FOR BIO-APPLICATIONS AND ENERGY RELATED SYSTEMS.
Alba María Matas Adams
Dipòsit Legal: T 55-2016

UNIVERSITAT ROVIRA I VIRGILI
SEMICONDUCTOR NANOPARTICLES AS PLATFORM FOR BIO-APPLICATIONS AND ENERGY RELATED SYSTEMS.
Alba María Matas Adams
Dipòsit Legal: T 55-2016

Emilio Palomares Gil, Group Leader at the Institute of Chemical Research of Catalonia (ICIQ), Tarragona and Research Professor at the Catalan Institute for Research and Advanced Studies (ICREA), Barcelona.

CERTIFIES:

That the present research study, entitled "Semiconductor Nanoparticles as Platform for Bio-Applications and Energy Related Systems" presented by Alba María Matas Adams for the award of the degree of Doctor, has been carried out under my supervision in ICIQ.

Tarragona October 2015

Prof. Dr. Emilio Palomares Gil

UNIVERSITAT ROVIRA I VIRGILI

ICIQ
Institut Català d'Investigació Química

UNIVERSITAT ROVIRA I VIRGILI
SEMICONDUCTOR NANOPARTICLES AS PLATFORM FOR BIO-APPLICATIONS AND ENERGY RELATED SYSTEMS.
Alba María Matas Adams
Dipòsit Legal: T 55-2016

UNIVERSITAT ROVIRA I VIRGILI
SEMICONDUCTOR NANOPARTICLES AS PLATFORM FOR BIO-APPLICATIONS AND ENERGY RELATED SYSTEMS.
Alba María Matas Adams
Dipòsit Legal: T 55-2016

A mis padres y a Jose.

UNIVERSITAT ROVIRA I VIRGILI
SEMICONDUCTOR NANOPARTICLES AS PLATFORM FOR BIO-APPLICATIONS AND ENERGY RELATED SYSTEMS.
Alba María Matas Adams
Dipòsit Legal: T 55-2016

UNIVERSITAT ROVIRA I VIRGILI
SEMICONDUCTOR NANOPARTICLES AS PLATFORM FOR BIO-APPLICATIONS AND ENERGY RELATED SYSTEMS.
Alba María Matas Adams
Dipòsit Legal: T 55-2016

Acknowledgments

UNIVERSITAT ROVIRA I VIRGILI
SEMICONDUCTOR NANOPARTICLES AS PLATFORM FOR BIO-APPLICATIONS AND ENERGY RELATED SYSTEMS.
Alba María Matas Adams
Dipòsit Legal: T 55-2016

Acknowledgments

I would like to use the first pages of my thesis just to give thanks, thanks to all the people without whom this little piece of work would not have been possible.

Everybody starts saying thanks to their PhD supervisor, but in my case it comes from my heart as without the opportunity he gave me I could not have done this. Without knowing me at all he gave me the opportunity to start to work as well as supporting me, hearing me rant about how things do not work, and also personally helping us with everything he could over these years so I just want to say, thank you Emilio! Without your craziness this could not have worked.

Mihaela, thank you for giving me the chance to bring out the biologist inside me, and allowed me to play with cells those 4 months in your group, I will never forget it!

Also, I want to thank the different people that have been with me these years in this adventure in Tarragona.

First of all the people from the lab, where I started working with Iván and Georgiana who were my first contact with the investigation madness.

They showed me in first hand how this world worked and how research was done, Iván also showed me a different side of Tarragona (thank you for letting us know about Istambul, many nice dinners took place there, jejeje), and with a special thanks to Georgiana, without your help this thesis could not have been completed, you heard my complaints and when the experiments did not work out you were there to help me, to come up with ideas and to listen to me, as well as to meet outside the lab and talk about our things and problems, because of this I have to say a big thank you.

While I did not work directly with Josep, he also listened to me and answer all my many and crazy questions regarding quantum dots, titania and everything my mind could imagine and question.

Also I want to thank the people that where there from the beginning: Vijay, John, James, Aurelien, Nuria, Lydia, Toni, Werther and Laia (those Bojos per la Quimica times were very important to me, it made me realize I would not mind teaching, something that I always though that was not made for me), and the last part of the group that arrived just this year: Ilario, Sofia (thank you for continuing with the onions project!!! Jejeje, you finally did it!), Jesús (good luck with everything!) and Cristina (even though we only coincided in the lab for a few months with all of the

talks we had I think I know you a little bit to be able to say to you, be strong! You will make it!).

Also, my two girls (I know Jose will not be jealous if I say it, jejeje), Eva and Bea, thank you for all of your help, the paperwork, the bureaucracy complaints and the gossiping (this was the best part). You were always there for me and to help me when I needed. Thank you for all of you advice regarding the thesis rehearsal and psychosis.

Likewise, the people from the support area with a special thanks to Fernando Bozoglian, you were the first person from outside our group I came in contact with and helped me with my technological issues, when the equipment were against me and did what they wanted and with the QDs problems I encountered with along this years.
Rita Marimon from the URV in the Servei, I do not think that without your help I would have been able to get so nice TEM images as I did, as well as with the confocal (thanks for those marathon seasons with Nerea, hearing her saying crazy things… those are moments I will never forget…).

To my Malaga friends in Tarragona: Dani, Martín, and in the last year Rocio, thank you for all the times you heard us complain, for the long talks we had and for the places we went together as well as all of the experiences over these years. Rocio, thank you for coping with us when we talked about chemistry and ICIQ and you were as bored as no one has been before, you also contribute with your chemistry free point of view.
And my friends that I left in Malaga, Mary (thank you for those Skype moments at 12 at night talking about nothing but being there for me when I needed someone to talk), Irene (remembering that past times were not always better), Raquel sis (for being there since we were just newborns) and Raquel (you were the first person I talked with at uni and were there always).

Last, but not least, I want to thank my family. My parents, for giving me the education as well as the love and support that led me to this point. For coping with me my whole life, for supporting me with my decision to come here as an adventure and the start of my new life.

Acknowledgments

To my sister, for those moments when I forget what I do, when I´m just your sister and I can say silly things and act the crazy I am.

To my family in Salinas (grandparents, aunts, uncles and cousins) as well as the one in England (thank you aunty Carol for the Sunday calls, I am going to miss them!!!).

Also, to my new family, Julia, Pedro and Javi (ok, also Jose Grande, jejeje), even though I am not part of your family, you make me feel like if I was, thank you for letting me in.

And finally to you, Jose, without you this adventure would not have been possible. Who would have said when we meet 9 years ago that we were going to be here? You have been my everything this four years, thank you for being with me, when I cried, complained, was tired and being the crazy me, as well as for the good moments, the laughs, the places we have been to, the staying in bed until late and helping me with everything (experiments, house and even cooking, jejeje), I can only say I love you, thank you and next adventure stop: London!!!

UNIVERSITAT ROVIRA I VIRGILI
SEMICONDUCTOR NANOPARTICLES AS PLATFORM FOR BIO-APPLICATIONS AND ENERGY RELATED SYSTEMS.
Alba María Matas Adams
Dipòsit Legal: T 55-2016

UNIVERSITAT ROVIRA I VIRGILI
SEMICONDUCTOR NANOPARTICLES AS PLATFORM FOR BIO-APPLICATIONS AND ENERGY RELATED SYSTEMS.
Alba María Matas Adams
Dipòsit Legal: T 55-2016

A mis padres, Ali y Jose.

UNIVERSITAT ROVIRA I VIRGILI
SEMICONDUCTOR NANOPARTICLES AS PLATFORM FOR BIO-APPLICATIONS AND ENERGY RELATED SYSTEMS.
Alba María Matas Adams
Dipòsit Legal: T 55-2016

UNIVERSITAT ROVIRA I VIRGILI
SEMICONDUCTOR NANOPARTICLES AS PLATFORM FOR BIO-APPLICATIONS AND ENERGY RELATED SYSTEMS.
Alba María Matas Adams
Dipòsit Legal: T 55-2016

Semiconductor Nanoparticles as Platform for Bio-Applications and Energy Related Systems

1.Quantum Dots

2.Up Conversion Nanoparticles

3.Other Materials

UNIVERSITAT ROVIRA I VIRGILI
SEMICONDUCTOR NANOPARTICLES AS PLATFORM FOR BIO-APPLICATIONS AND ENERGY RELATED SYSTEMS.
Alba María Matas Adams
Dipòsit Legal: T 55-2016

1.Quantum Dots Introduction

UNIVERSITAT ROVIRA I VIRGILI
SEMICONDUCTOR NANOPARTICLES AS PLATFORM FOR BIO-APPLICATIONS AND ENERGY RELATED SYSTEMS.
Alba María Matas Adams
Dipòsit Legal: T 55-2016

1. Quantum Dots

1.1 Introduction

Quantum dots (QD) are nanometer scale semiconductor crystals composed of group II to VI or III to V elements that are definided as particles with physical dimensions smaller than the exciton Bohr radius.[1]

They were firstly synthesized by Murray, Norris and Bawendi in 1993[2], and described as semiconductor nanocrystallites, with physical properties dominated by the spatial confinement of the excitons, that is, exciting the sample, an electron from the semiconductor is promoted from the valence band to the conduction band, generating a hole, leading to the formation of an exciton. This way, the electronic characteristics are related to the size and shape of the individual crystal, as decreasing its size the gap between the HOMO and the LUMO level will increase. [3–5]

Due to quantum confinement effects present in the Quantum Dots, since the radius is smaller than the Bohr exciton radius, they present an intermediate state between a macroscopic crystal (presenting a valence and conduction band) and a semiconductor (where the valence and conduction band are discrete). Therefore, they present the states in their bands very close between them, as it can be seen in Figure 1.

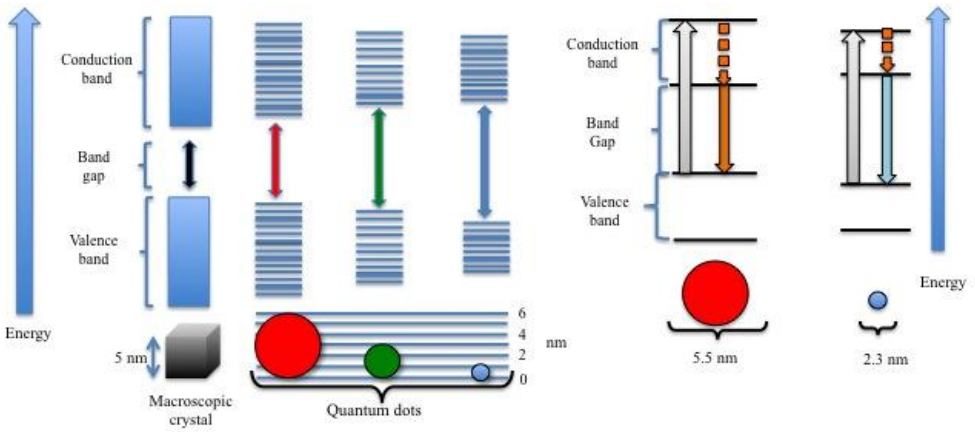

Figure 1. *Difference of the band gaps with size.*

This band gap separation will depend on the size of the QD, the smaller the QD, the closer the states that form the bands will be, in consequence, the bands will also be smaller producing a bigger band gap than for the bigger QDs. In summary, by

controlling the synthesis, the band-gap can be modified selectively, leading to the synthesis of nanoparticles with highly tunable electronic and optical properties.

Taking this into account, the larger the band gap (small nanocrystals), the more energy they will emit, which means a emission in the blue part of the spectrum. While for smaller band gaps (big nanocrystals) the emission will be in the red part of the spectrum as it can be seen in Figure 2. This means that the energy emitted is inversely proportional to the size of the quantum dot.

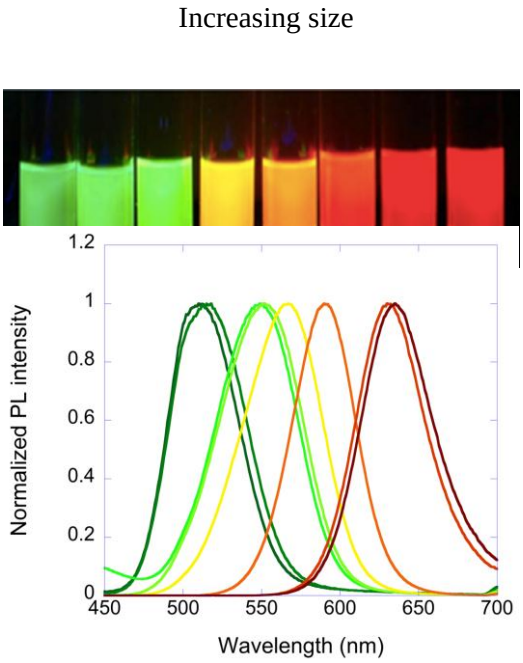

Figure 2. *Fluorescence spectra of different CdTe QDs (prepared at ICIQ) excited at 405 nm at room temperature.*

As well as the size, the shape can also be controlled in the synthesis, forming dots, nanorods, nanowires or tetrapods, as shown in Figure 3, where different surfactants were used to control the reactivity of the surface, but in this thesis we will focus on the synthesis of cadmium based quantum dots, as the quantum world is too vast to address everything.

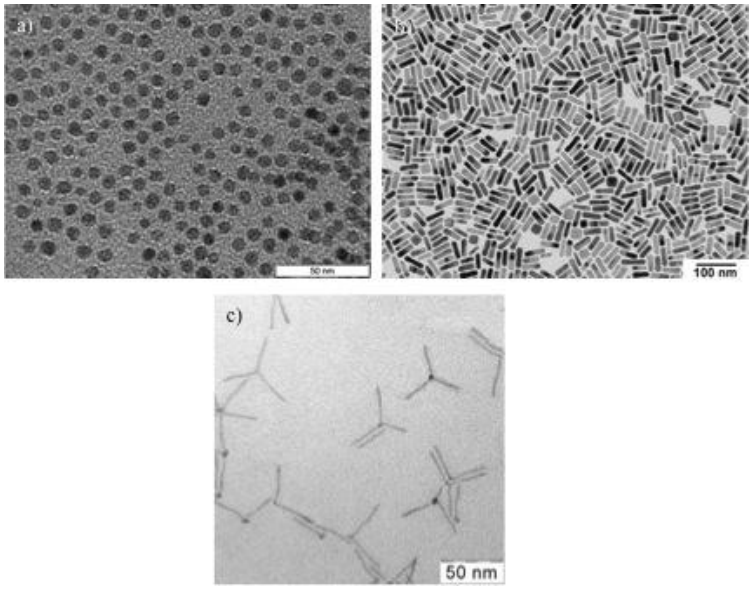

Figure 3. *TEM image of a) dots, b) rods, c) tetrapods.*

QDs present unique advantages when compared to typical organic dyes, as they exhibit broader absorption and narrower emission spectrum (Figure 4), relatively long life times and major resistance to photobleaching.[6,7]

Also, a notable difference and a factor of considerable use is that with the same excitation source, different QDs can be excited and emit in different wavelengths that do not overlap, while for each dye a specific wavelength of excitation is needed, thus QDs allow performing multiplexing experiments without the need of very expensive equipment.

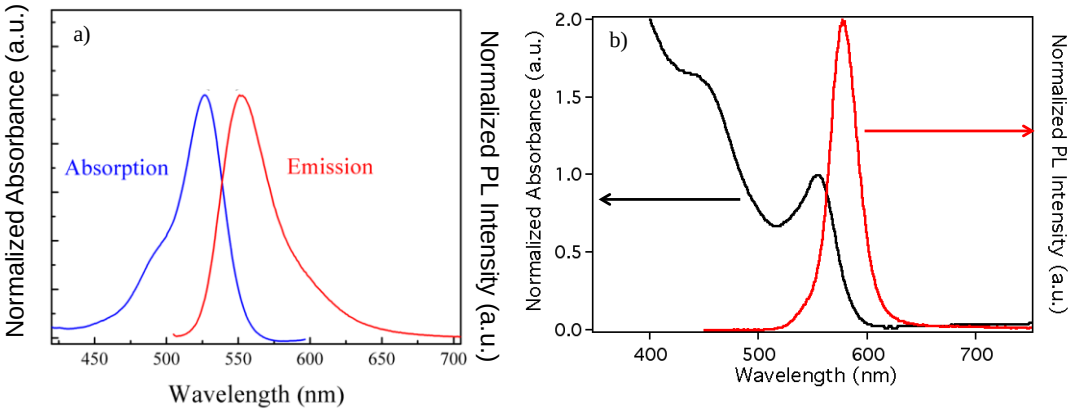

Figure 4. *Absorption and emission of a) Rhodamine 6G, b) CdSe QDs*

1.2 QDs Synthesis

QDs are generally synthesized by reacting inorganic precursors in the presence of organic ligands, which eventually form a molecular coating around the QD core and stabilize the nanoparticles against aggregation.

As it will be explained, chemical modification of this coating allows the regulation of the physicochemical properties of the QDs and also the passivation of the nanocrystal surface with a protective layer of another inorganic material, yielding to core/shell QDs.[2,8,9]

Although QDs present better properties than organic dyes as improved photostability, in some cases there is a decrease in the fluorescence when the nanocrystals are injected into tissues or whole animals.[10,11] This effect can be due to the slow degradation of the ligands on the surface and of the coating, leading to surface defects, and because of this, quenching of the fluorescence.

This is why for biological applications, the ligands on the surface of the quantum dots have to be controlled and even in some cases is necessary to resort to shell coatings, to provide minimal non-specific binding, but at the same time to maintain the stability and avoid any possible oxidation, and most important of all, to maintain the strong fluorescence.[12]

There has been several routes used to synthesized the QDs[13] that can be classified in two types of approaches: top-down processing or bottom-up depending on the starting materials.

In the top-down approach, a bulk semiconductor is thinned using techniques as molecular beam epitaxy, lithography or reactive-ion etching. The size and shapes are quite controlled in the synthesis, but the incorporation of impurities into the QDs may be a disadvantage.[13] It also requires quite expensive techniques that not every lab possesses, as in our case, that is the reason behind why this approach has not been used in this thesis.

For the bottom-up approach, the colloidal QDs are prepared by self-assembling using solutions followed by chemical reduction, and can also be divided into two methods:

a) Wet-chemical methods

b) Vapor-phase methods

In this thesis, all the synthesis are included in the wet-chemical methods, which can be described as precipitation methods with control of parameters for a single solution or mixture of solutions, and involves the nucleation of the nanoparticles and the controlled growth.

The nucleation can be homogeneous (when the atoms or molecules combine and reach the critical size without the assistance of a pre-existing solid interface), heterogeneous (when there is a pre-existing solid interface) or secondary nucleation.[14]

These methods are: microemulsion, sol-gel, microwaves, hot-solution decomposition and electrochemistry.

For the vapor-phase methods, the layers are grown in an atom-by-atom process, so the formation of the QDs takes place on a substrate without patternings.[15,16] Here, sputtering can be noticed, liquid metal ion sources or aggregation of gaseous monomers as vapor-phase methods.

In the following pages, the synthesis of QDs will be explained in greater detail.

a) CdSe

One of the first techniques developed for the synthesis of cadmium based QDs was the hydrothermal synthesis, where the growth of the quantum dot depends on the kinetics as well as the thermodynamic barriers present in the reaction.

For this growth, a high initial temperature is needed for the nucleation of the nanoparticle, as well as controlling the precursor addition to the reaction.

This technique relies on the conductivity of heat from the reaction vessel to the solvent and to the reactive species.

As previously reported, Murray et al. presented the synthesis of CdSe quantum dots using a hot injection method[2], where dimethylcadmium was mixed with tri-n-octylphosphine (TOP) to form a solution that was mixed with another solution formed by TOPSe and TOP and heated at 230-260ºC.

Depending on the size desired (wavelength of interest) the heating time was different.

It is also possible that the CdSe act as a protecting shell for different QDs as CdS (synthesis also developed in Bawendi´s group) as seen in the work by Battaglia et al.[17],

and in this case, not only the photoluminescence quantum yield (PLQY) could be improved from around 20% to 40% as the shell protects from oxidation and trap formations, but also the emission wavelength could be tuned from 520 to 650 nm by only changing the thickness of the shell due to the type of core/shell structure formed.

Core/shell heterostructures can be divided into two depending on the position of the conduction and valence band of both the core (QD) and the shell, as represented in Scheme 1.[18,19]

In type-I, the conduction band of the shell is higher than the conduction band of the core, while the valence band of the shell is lower in energy than the core´s one, so the electrons and holes are confined in the core. Some examples are the structures as CdSe/CdS and CdSe/ZnS.

In type-II, both the valence band and the conduction band of the shell present higher energy than the core (or lower, depending on the case), so one carrier is confined in the core while the other is in the shell. In this case, as examples, we may notice CdTe/CdSe or CdSe/ZnTe, that allow access to longer wavelengths compared with the wavelengths of emission of the cores. And also this emission can be tuned not only modifying the size of the core but also the size of the shell, in the case of CdTe/CdSe the emission can be tuned from 700 nm over to 1000nm. Additionally, they present longer radiative lifetimes due to the slow electron-hole recombination of the excitons, as the holes are confined away from the surface. The main issue observed in these structures is the low PLQY, in most cases lower than 10%. If an extra layer of ZnTe is grown over the CdTe/CdSe QDs, the PLQY can be raised up to 20% but is still lower than in the case of the core alone.

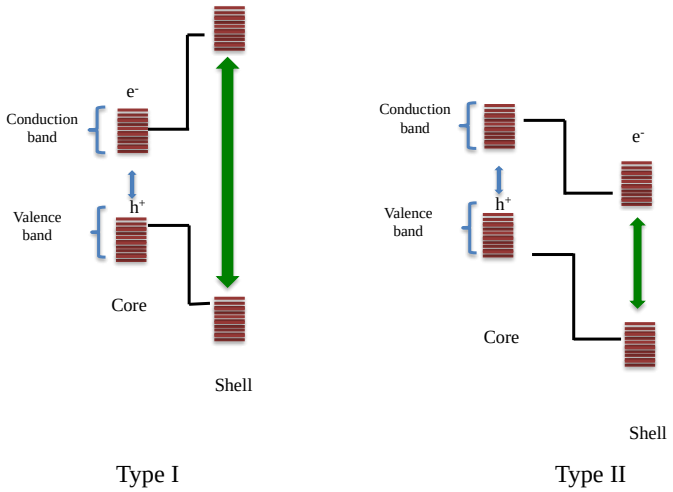

Scheme 1. Diagram of type-I and type-II core/shell heterostructures

The drawback of the hot injection technique is that thermal gradients are formed through the solution, producing non uniform reaction conditions.

If this is taken to large scale reactions, the thermal gradients are also magnified, producing even worse nucleation processes and therefore, a broader size distribution.[20]

This gradient problem can be solved using microwave techniques and also can make the reaction scalable, as well as allow their use in reactions with high activation energies and slow reaction rates.

The reaction can be carried out in any microwave, but the reaction temperature, microwave power and mode quality are quite critical to be able to achieve nanocrystals with good structural and optical quality as well as good size dispersion.

Erbec et al.[20] prepared CdSe QDs using microwaves, but from two different cadmium sources:

1) A single cadmium and selenium source precursor ($Li_4[Cd_{10}Se_4(SPh)_{16}]$).

2) Using different sources of cadmium and selenium (cadmium oxide and tetrabutyl phosphine selenide) as well as it used a strong microwave absorber as trioctylphosphine oxide following Qu and Peng´s method.[21]

Schumacher et al. presented a similar investigation where they synthesize CdSe QDs by microwaves, but water soluble.[22] These QDs also presented a shell of ZnS that provided passivation for the CdSe core as well as reducing the toxicity.

Their approach was based on the addition of a water-soluble Zn^{2+} complex, to a

solution containing CdSe initial nanocrystals and MPA. Subsequent microwave heating of these initial solutions for less than 2 h can result in high-quality CdSe/ZnS based QDs possessing good PLQY and biocompatibility.

b) CdTe

The main issue present in the case of CdSe QDs is that most of the synthesis produce QDs not water soluble due to the hydrophobic chains of the ligands, so they cannot be directly used for bioapplications.

To avoid this hydrophobicity, two main strategies can be followed.
One of them is to transfer the hydrophobic nanocrystals to an aqueous phase by a coverage step using hydrophilic polymers (that is mostly the case with CdSe QDs), or in the other hand, to exchange the hydrophobic ligands present in the nanocrystals by others that are hydrophilic, this is the case for the synthesis of CdTe QDs.
Both approaches require an extra complicated manipulation step in the synthesis, and besides this, it reduces the PLQY after the changes, due to the water strong polarity.[23,25]

A solution was to synthesize the nanocrystal directly in water, as seen in some cases for CdSe, with the advantages of avoiding the extra modification steps, as well as avoiding the use of organic and toxic solvents, and being cheaper.
Most of the synthetic methods use conventional convective heating due to the high temperatures needed for the nucleation and growth of the quantum dots, presenting the same problem of temperature gradients as for CdSe. In order to overcome this problem, microwave techniques were also employed.

The microwave assisted synthesis presents two main advantages regarding the formation of CdTe quantum dots: 1) the temperature can be rapidly increased due to the microwave energy, incrementing the kinetics. 2) the heating is more homogeneous as the effects from the temperature gradients are reduced.
One of the problems that arise from this synthesis, is the broad size distribution obtained (full-width of half-maximum ranging from 35 to 60 nm), which can difficult their use in biological applications. However, by controlling the microwave irradiation time, the size could be controlled.

He et al.[26] prepared different sized nanocrystals CdTe quantum dots using a NaHTe precursor in the presence of thioglycolic acid (TGA) or mercapto propionic acid (MPA) by controlling the microwave irradiation.
These two agents (TGA and MPA) are responsible for the high PLQY obtained (up to 90%) with this technique, as their role is to occupy surface sites instead of Te, preventing the oxidation of the Tellurium atoms, after UV light irradiation for some time.

Similarly to the synthesis of CdSe, there are also microwave assisted synthesis of core/shell CdTe quantum dots. In the case that the ZnS shell is grown directly on the surface of the QD, this leads to a low PLQY as well as a broad size distribution, due to their large lattice mismatch[27], but if an in between layer of CdS is grown between CdTe and ZnS, as its band gap energy and lattice constant is between them, it reduces the non-radiative surface defects as well as it improves the PLQY.

While the microwave assisted synthesis of CdTe quantum dots is a way of obtaining QDs with a controlled synthesis and good PLQY, it requires special equipment not present in all the laboratories, so an alternative is the use of the hydrothermal techniques.
The first application of this method was in the work presented by Murray et al.[2], the same method used in the synthesis of CdSe, but the source of tellurium was $(TMS)_2Te$.
It presented the disadvantages of requiring high temperatures and long reaction times[28], as well as finally obtaining nanocrystals with bad PLQY, but it was proven that playing around with the concentration of the precursor and time, the latter defect could be improved.[29]
Low concentration of precursor leads to smaller crystals (lower wavelengths of emission) and better PLQY, but if the reaction time was increased the PLQY decreased. The reason behind this effect is the excess of cadmium monomers that exist at the initial stage of the nanocrystal growth.

Also, the FWHM of the emission peak depends on the reaction temperature, as higher the temperature is, narrower the emission peak, as it increases the diffusion rate of the atoms of the nanocrystals surface.

With this method, good and stable (chemically and photochemically) CdTe QDs are achieved that could be used without any further treatment in biological applications.

As in the case of CdSe, if CdTe is a core in a core shell heterostructure, that is capped with CdSe, the emission wavelength could be tuned, modifying the shell thickness, from 700 to 1000 nm [19] what could not be achieved only modifying the size of the core.

c) $Zn_xCd_{1-x}S$ /$Zn_xCd_{1-x}Se$

As previously mentioned, the main effort while investigating quantum dots, was focused on the preparation of different color emitting QDs or core/shell nanoparticles by changing the size of the nanocrystal, but this can cause problems in some applications, especially when the size of the nanocrystal is too small, as in the case of blue emitting QDs, because of the instability of small cadmium based quantum dots.
Nonetheless, there have been some reports on synthesing blue ZnSe or ZnTe QDs due to the wide band gap but the main problem with these QDs is the cost of the precursors, as well as the toxicity.

To avoid the instability and toxicity, mixed ternary nanocrystals were synthesized, for example $Zn_xCd_{1-x}Se$ by Zhong and coworkers[30] with luminescent properties comparable to CdSe.
Using this work as a model, the same group presented the synthesis of other ternary mixed nanocrystals with a wide band gap, as is the case of $Zn_xCd_{1-x}S$ that presented even better optical properties[31], in particular, the narrowest FWHM, comparable to the CdSe ones as shown in Figure 5.

In this case, it is not necessary to change the size of the QD to change the fluorescence only by controlling the molar ratio between Zn^{2+} and Cd^{2+} different emission wavelengths could be achieved.[32]
But modifying the reaction time has the opposite effect than in CdSe QDs, instead of growing and tuning the emission to the red, the emission with time changes to the blue, as it will be explained further in this thesis.

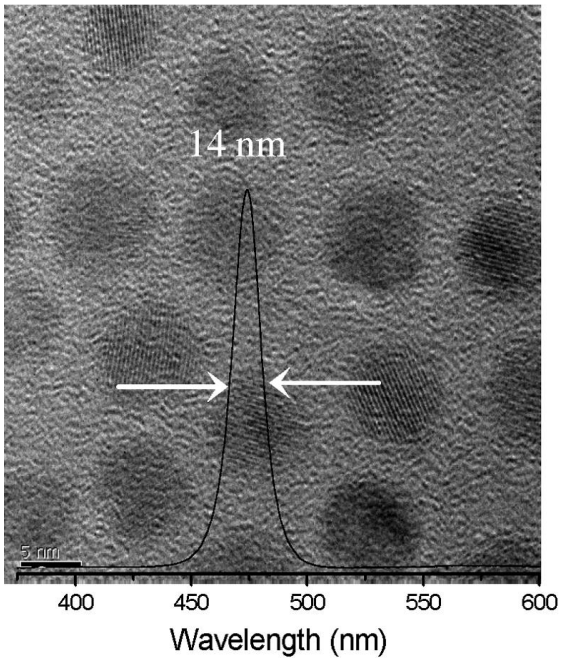

Figure 5. *Emission and TEM image of monodisperse wurtzite $Zn_xCd_{1-x}S$. Image used with the permission of the authors.*[31]

For the synthesis of $Zn_xCd_{1-x}S$, a mixture of CdO, ZnO, oleic acid, and octadecene was used and heated for the subsequent growth and annealing of the resulting nanocrystals.

The synthesized nanocrystals presented narrow size distribution, as well as a wurtzite hexagonal structure, PLQY ranging from 25 to 50%, and the narrowest FWHM presented for QDs.

In the synthesis, a CdSe nanocrystal is formed as the seed, and then Zn and Se precursors are incorporated at high temperature to grow the final structure, the problem was that most of the CdSe QDs synthesized presented a quite large size, and even if the size was small, the heat needed after the addition of Zn and Se allowed the CdSe seeds to continue their growth, making it rather difficult to obtain final small wavelengths of emission.

To avoid this, the same group developed an embryonic nuclei-induced alloying process for the preparation of these $Zn_xCd_{1-x}Se$ QDs with blue emission.[33]

Their method consisted on consecutive nucleation and growth stages to form the nanocrystal, where CdO and stearic acid were mixed and heated. When the solution turned clear, the mixture was cooled down to room temperature so TOPO and HDA could be added.

The resulting mixture was heated under vacuum and a mixture of Se in TOP was injected. Up to this step, the CdSe nuclei were formed.

To continue with the synthesis, a solution of $ZnEt_2$ in TOP was quickly injected for the growth of the final nanocrystals.

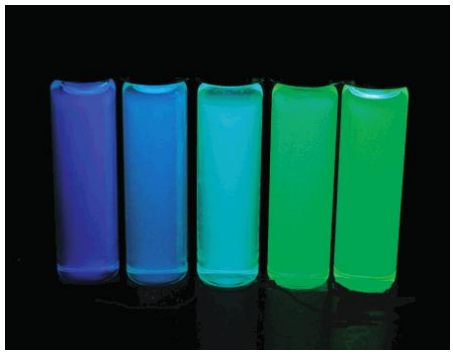

Figure 6. *Composition-tunable emission colors of the obtained $Zn_xCd_{1-x}Se$ nanocrystals in the blue-to-green spectral region excited with a UV lamp. Image used with the permission of the authors.*[33]

If the preparation of $Zn_xCd_{1-x}Se$ was tried in situ mixing the Zn and Cd precursor together with Se in TOPO/HDA at high temperature, ZnSe and CdSe nucleate separately due to the lattice mismatch between them.

The same effect is observed if Zn and Cd precursors are added sequentially, so it is necessary that the nucleation of CdSe takes place first, and then the crystal growth of the desired composition, as depicted in Figure 7.

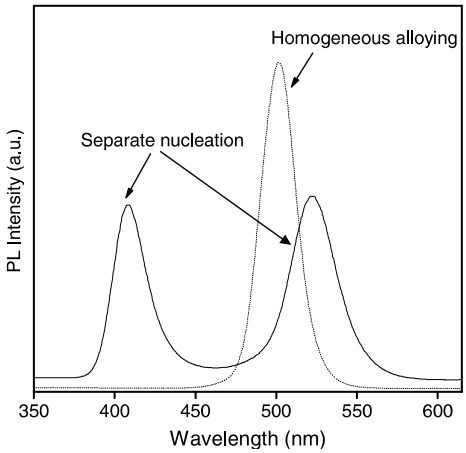

Figure 7. *PL spectra of the nanocrystals after 30 min of heating comparing the separate nucleation and the homogeneous alloying. Image used with the permission of the authors.*[33]

This is related with the growing and emission phenomena discussed at the beginning of this section. The longer the reaction time, the more to the blue the emission is tuned, due to the formation of ZnSe instead of $Zn_xCd_{1-x}Se$.
Also, a problem with increasing the reaction times is that the PLQY decrease drastically, from 30% at 5s, to 1% after 90 min of reaction.

In 2008, Michael Y. Chiang´s group[34] synthesized cysteine-capped $Zn_xCd_{1-x}Se$ without the need to previously form the CdSe nuclei, so the Zn, Cd and Se precursor could be injected at the same time at low temperatures in the presence of cysteine as a surface stabilizing agent. Although these QDs were water soluble, the PLQY was moderate (around 15%). However, it was noticed that if the QDs were irradiated for a period of time, the PLQY could improve, in this case, after 20 hours, it went from a 13 to a 26%.

Instead of using unmodified cysteine as a capping agent, Cao et al.[35] used N-acetyl-L-cysteine (NAC) that is inexpensive, stable and environmentally friendly, improving the PLQY without the use of radiation.
Another advantage was that varying the NAC concentration, the emission wavelength could be partially tuned, without increasing the concentration of Cd^{2+}, due to the competition between Se^{2-} and NAC to link to the cations present in the growing nanocrystals, the higher the concentration of NAC, the smaller the nanocrystals.

Last but not least, in 2012, Zhong´s group presented the synthesis of $Zn_xCd_{1-x}S$ nanocrystals with tunable emission over the entire visible spectrum using copper as a dopant as seen in Figure 8.[36] Modifying the ratio between Zn and Cu, the emission could be tuned.

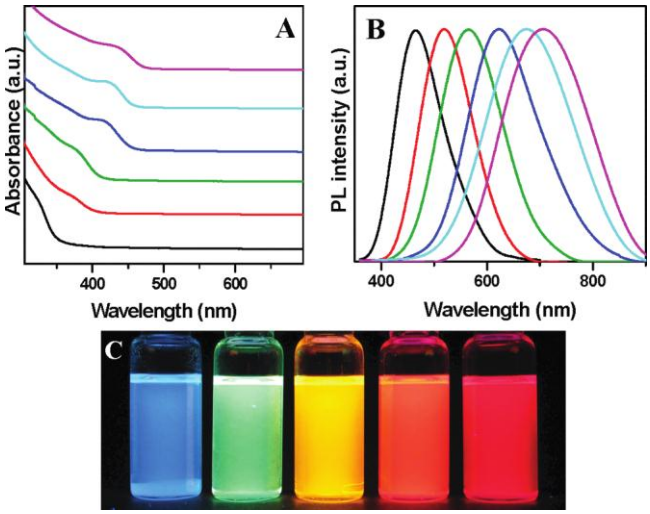

Figure 8. *Normalized a) UV-vis absorption and b) emission of Cu: $Zn_xCd_{1-x}S/ZnS$ QDs under different Cd/Zn precursor ratio. c) Emission of the samples under a UV lamp. Image used with the permission of the authors.*[36]

They reported a facile one-pot non-injection synthesis with all of the reagents loaded at room temperature. The high PLQY exhibited by these QDs (up to 65%) was preserved even after ligand exchange.

For the synthesis, Zn, Cd, Cu as well as the S precursor (formed by dissolving sulfur in ODE at 120ºC) were mixed with DDT and ODE and heated to allow the growth of the nanocrystals, in addition of allowing the introduction of a small amount of copper dopant inside the host.

This structure only had a PLQY of around 6%, but if there is an extra injection of Zn precursor, this will lead to the formation of a core/shell structure with ZnS and the PLQY was enhanced to more than 50%.

The presence of heavy metals in these type of QDs is an important and controversial issue that in some cases has a big influence in the use of the QDs as biological probes but it has been demonstrated that the coating plays an important role in the cytotoxicity, as the polymeric or inorganic coating can decrease the liberation of the heavy metals into the organism.

1.3 Toxicity

The QDs used in this thesis are composed of a well known toxic element as cadmium, and in the case of their direct use on cell culture the performed cytotoxicity studies

showed low viability of the cells after a certain period of time as well as affecting the cell growth.[37–39]

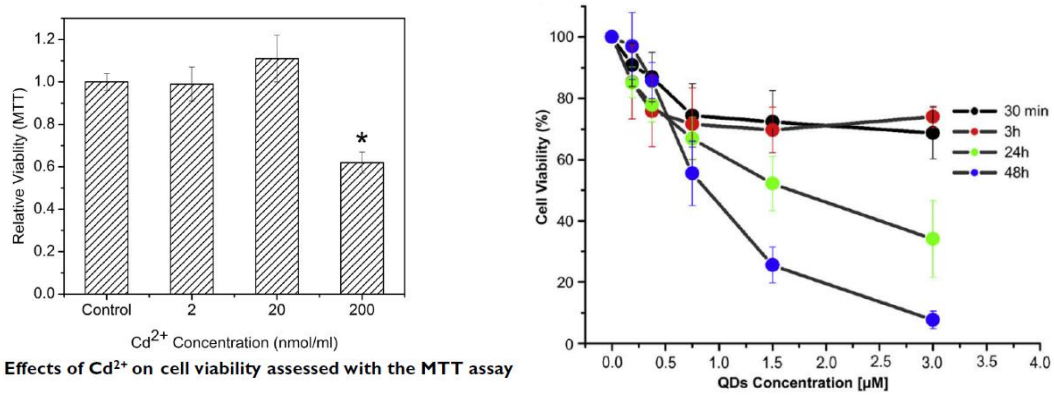

Figure 9. *Cell viability vs. [QD]. Image used with the permission of the authors.*[37,39]

The mechanisms behind this toxicity are not very well known, but different theories have been postulated, like the leakage of Cd^{2+} from the QDs core following its absorption by the cells decreasing the cell viability (Figure 9) or the interaction with different intracellular components. The degree of damage however depends on the cell line.

Cd^{2+} ion is able to interfere in the DNA repair, as well as substitute physiological zinc and generate reactive oxygen species (ROS).

Different groups have studied the possible effects of the heavy metals in different cell lines exposing them to group II-IV QDs as CdTe, CdSe, and capped QDs. Most of the cell lines used for the experiments was liver- and lung-derived, as these organs are the most affected after incubation with toxic elements where most of the external agents accumulate.

Specifically, the liver is the primary site of cadmium ions accumulation, and it is known that low levels of these ions (100-400 μM) are able to reduce the viability of liver cells in vitro.

Derfus et al. oxidized mercaptoacetic acid (MAA) stabilized CdSe QDs with ultraviolet irradiation. They observed a release of free cadmium ions into the solution, which produced the death of primary liver cells[40], as the cadmium is able to bind to the sulfhydryl groups of mitochondrial proteins, as well as produce the thiol group inactivation that leads to oxidative stress and mitochondrial dysfunction.

If the concentrations of cadmium ions liberated are really low, it is not a problem, as there is a metallothionein protein that is able to detoxify the cadmium sequestering it into an inert complex, but the levels present of this protein are quite low.
This group noticed that the TOPO-QDs just synthesized were not toxic, but if before functionalizing them with MAA they were left in the open air for 30 min and then functionalized, the cell viability decreased dramatically due to the oxidative effect of O_2 over the CdSe.

In order to confirm this observation / hypothesis, the authors enhanced the oxidative effect using high-energy optical illumination to catalyze the oxidation process over the MAA-CdSe QDs, and they saw that the longer the exposure time, the higher the decrease in viability even for the lowest concentration of QDs (Figure 10).

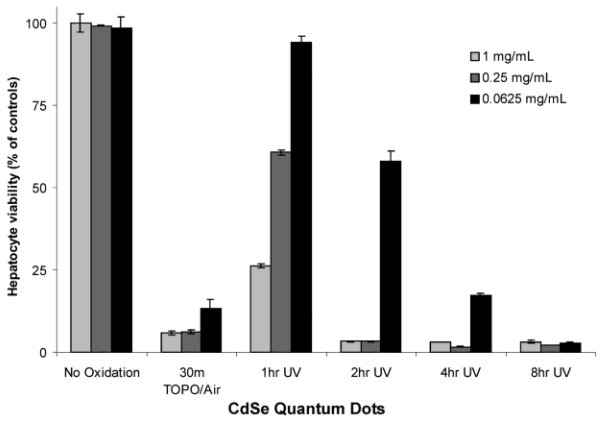

Figure 10. *Toxicity of CdSe quantum dots in liver culture model. Image used with the permission of the authors.*[40]

After the exposure, the absorption spectra was measured observing a blue shift in the excitonic peak, due to the decrease of size of the nanoparticle with the liberation of the cadmium ions, as the oxygen oxidizes the chalcogenide atoms (in this case Se forming SeO_2) and desorbs from the surface, leaving behind reduced cadmium atoms that will also be released. But when the surface is not oxidized, then the Cd atoms that are in the surface of the QDs are bounded to the Se atoms as well as to the ligand decreasing the toxicity, as the capping agent is the one that is affected by the oxygen or the UV light.
Furthermore, this irradiation also produces free radicals in aqueous solution as proven by Itty Ipe et al.[41]

Both groups also tested the toxicity of the same QDs, but with the presence of a surface coating as ZnS, that is added to increase the PLQY. Although it increased the stability of the QD, it decreased the surface oxidation and avoided the formation of free radicals.

But acid reagents as hypochlorous acid (HOCl, found in the interior of some cells as phagocytic cells), are able to degrade even polymer encapsulated QDs as they are able to diffuse across the polymer coating layer.[42]

This effect decreased the PLQY of the QD as it produced soluble Cd, Zn, S and Se species, as the HOCl is also able to bind to the chalcogenides, in the same way as oxygen acts, liberating these species. The same holds for hydrogen peroxide, but with slower kinetic rates.

A way to avoid the "etching" effect of HOCl, or H_2O_2, is to use a polymer coating. Like the amino groups, the polymers play a functional role and are able to react with the HOCl. Similarly, reducing agents as mercaptoethanol are able to scavenge the acid molecules, protecting the QDs.

Moreover, Martin J. D. Clift group analyzed the uptake and intracellular fate of different coated quantum dots in vitro. The QDs were localized within the endosomes, as in Figure 11, and lysosomes, independently of the cell line used (kidney cells as in the case of Hanaki et al.[43] or mammary epithelial tumor cells in Parak et al.[44] investigation). Exposing them to acidic or oxidative environments deeply affects their toxicity, also independently of the surface coating.[45]

Lovric et al. noticed that the smaller the QDs, more easily it was for them to penetrate into the nucleus, while larger QDs stay in the cytoplasm[46], in some cases, as when they present larger size due to protective capping layers, they are able to go inside the cells by endocytosis, so the QDs will be surrounded by a endosome[47,48] , allowing them to penetrate the membrane of the cell.

Once inside, two possible mechanisms can take place.

A possibility is the degradation of the vesicle and consequently release of the nanoparticles inside the cell liberating the heavy metals.

One way to avoid this problem is to infiltrate or enclose the quantum dots with inert materials like polymers or silica[49], which do not modify the QDs properties, but prevent the leakage since the harsh environments present in the cells will affect the

coating layer and not the QDs. Keeping this in mind, the materials shown in this thesis, with potential use in vivo (as the QDs coated with gold or the QDs to detect cystic fibrosis), are protected by silica or different polymers.

The other possibility is the extracellular elimination of the vesicle and recycling, when it recognizes the QDs as strange so it can be eliminated by the body. Depending on the elimination rate, other organs can catch the QDs, and store them, producing toxic effects in the long run.

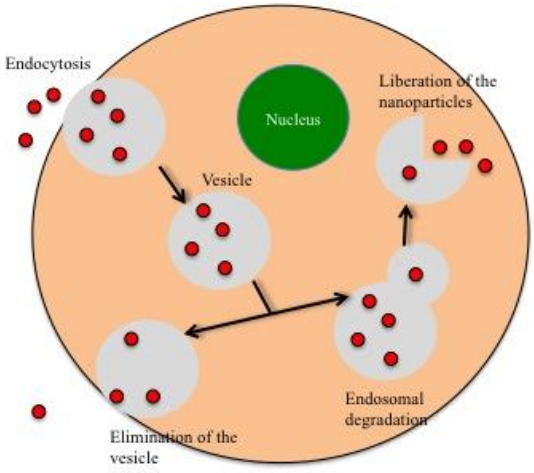

Figure 11. *Endocytosis, liberation or elimination of nanoparticles. Legend: nanoparticles (red), endosomes (grey), nucleus (green), cell (orange).*

Differently to the metal ions toxicity, QDs are able to reach organelles that are inaccessible to the metal ions, so when they are uptake by the cells the QDs are packed into small intracellular vesicles and transported to the perinuclear region, while the metal ions are predominantly located in the cytoplasm.

The toxicity of any material can be easily measured in vitro using metabolic activity or membrane permeability assays, but in vivo this is more difficult and not so straightforward.

Experiments injecting QDs into animals, such as rats, showed that the organs of the reticuloendothelial systems (body defense system) took up nonspecifically and retain most of the QDs injected.

Ballou et al.[50] observed that, depending on the surface coating; the place of accumulation (liver, skin and bone marrow) and time differed. Only PEG-coated QDs remained visible in circulation 1 hour after the injection, and after necropsy (even

after 5 months) the fluorescence from the QDs was visible in the lymph nodes and bone marrow. But as previously mentioned, due to the polymer coating, they were located inside vesicles of phagocytic cells and no sign of breakdown of the QDs was observed, indicating they can be used in biology.

In the case of ZnS-capped QDs, the degradation of the QDs was observed by Fitzpatrick et al.[51] in mice after 2 year, however Hauck et al.[52] performed a similar experiment and even though they also observed degradation, no organ damage or inflammation where found.

The discrepancy in toxicity comparing QDs in vitro and in vivo experiments comes from the nature of the experiments. For the in vivo experiments the nanoparticles are in constant flux over the cells so only a fraction of the injected nanoparticles will interact with the cells, while for the in vitro experiments the cells are in constant contact with the nanoparticles so the effect is drastically enhanced in vitro.

Quoting Paracelsus "The Dose Makes the Poison", the concentration of the QDs is the limiting factor that will make them toxic or not, but is the intracellular, not the extracellular concentration that correlates with the cytotoxicity.[53]

1.4 Applications

Besides all the main advantages previously mentioned, as broad absorption and narrow emission spectra, low photobleaching, high PLQY and a controllable toxicity, the possibility of a quite easy post-synthesis modification of the surface (Figure 12) has allowed the QDs to be used for multiplexing as well as another broad range of applications, ranging from computing, Photovoltaic Devices[54–56] , Light Emitting Devices (LEDs)[57,58], also Photodetector Devices[59] and lastly, but not least, in biology[60–62].

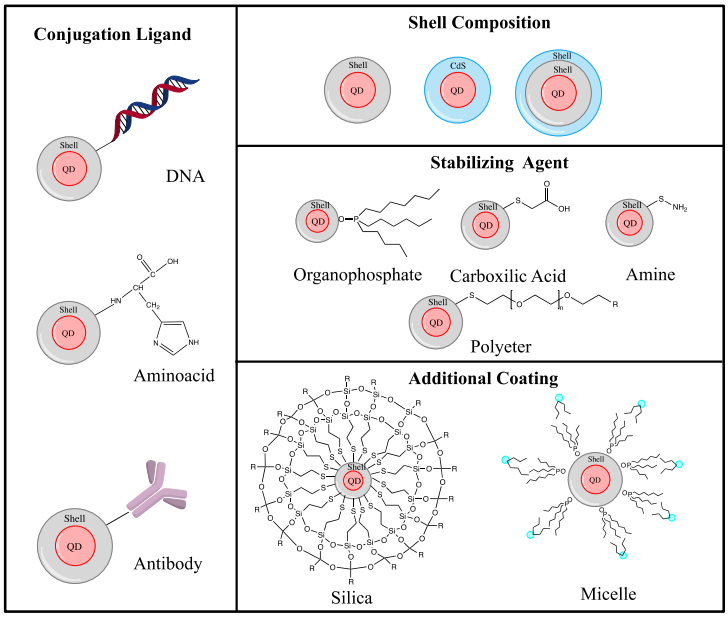

Figure 12. *Possible post-synthesis modifications of the QDs.*

In the past few years, they have been used as a potent agent for biomedical labeling or imaging [63] due to the previously mentioned advantages.

They have been used to label xenopus embryos by microinjection[64], also to label mortalin, a p-glycoprotein, an important molecule in tumor cells so it could be localized [65,66], as well as for the detection of pathogen and toxins as Salmonella Typhi [67]or Hepatitis B and C [68] , and to track single particles as seen also in one of the chapters of this thesis [69,70],they have been even used for *in vivo* animal imaging of tumors [10], as well as organs [71] and to track metastatic tumor cells extravasation by intracellular labeling[72].

They can also be used as pH sensors[73,74]. Previous work developed by our group using dual QDs silica nano-onions allows the quantitative detection of pH changes making use of a reference internal QD and an external QD layer sensitive to the pH variations in the environment[75].

Photodynamic therapy (PDT) is a technique developed in the 1900s that uses non-toxic compounds that absorb light, and then become toxic for malignant or diseased cells.

It needs a Photosensitizer (PS) agent, that is the compound that absorbs the light) that will transfer energy to the oxygen, causing cytotoxicity reactions in the cells that are exposed to the photosensitizer, so it is quite a direct method.

The first photosensitizer used was an hematophorphyrind derivative[76], as a second generation one example was the gold nanoparticles coated with a Zn-phtalocyannine complex[77] and QDs could be conjugated to photosensitizers or used as such[78] ,as they can emit in the near-IR region as opposed to the other photosensitizer agents as well as they are, or can be made, water soluble, these properties allowed also the use of Up Conversion Nanoparticles as photosensitizers agents, as it will be explained later on in the up conversion nanoparticles section.

In most of the cases QDs are used in PDT as donors[79,80], which means that they are excited by the light that is shined, and instead of relaxing and emitting light or heat (radiative or non radiative recombination as seen in Scheme 2a.), the energy is transferred to the acceptor molecule or photosensitizer agent by FRET (Förster Resonance Energy Transfer), and this agent will be the responsible for the generation of the ROS. For a successful FRET process, the energy levels of the QD and the acceptor have to be carefully chosen to allow the energy transfer, as depicted by the mechanism in Scheme 2b. In this thesis, the FRET approach was employed for the ratiometric detection of biomolecules involved in cystic fibrosis.

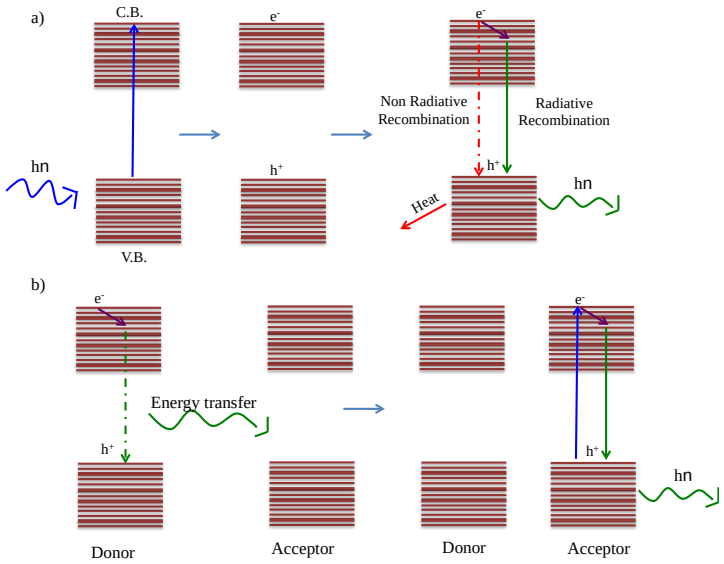

Scheme 2. *a) Radiative or non radiative recombination processes, b) FRET mechanism*

Mamedova et al. conjugated two differently coloured CdTe QDs to an antibody and to an antigen, forming a latter immunocomplex between the antigen and the antibody.[81] For the conjugation, sulfo-NHS and EDC reaction was followed[82], forming on the one

hand, green CdTe-IgG (anti-BSA) and on the other hand red CdTe-BSA. When the immunocomplex is formed (green CdTe-IgG/BSA-red CdTe), the fluorescence from the green CdTe was quenched and there was an enhancement in the case of the red fluorescence due to the FRET phenomena.

In 1996, the same group analysed the electronic energy transfer between proximal CdSe QDs, in a closed packed solid design using a mixture of two different CdSe sizes.[83] They observed the quenching of the luminescence in the case of the small CdSe and the enhancement for the larger ones, as the electrons transfer from the small to the big quantum dots.

This discovery was used by Willard et al.[84] using CdSe/ZnS (core/shell QDs) to observe the specific binding of different proteins (in this case, biotinylated bovine serum albumin to tetramethylrhodamine labeled streptavidin), where the QDs, attached to one of the proteins, are the donors, while the other protein is attached to an organic acceptor dye (TMR). When the proteins binds, and the distance is between the right value, once the QD is excited (with the appropriate wavelength where the excitation of the dye is minimum), the electron will transfer to the dye, so the fluorescence of the dye was enhance, and the ligand-receptor binding could be detected as shown in Figure 13. A similar approach was used in the development of the cystic fibrosis sensor shown in Chapter 3.

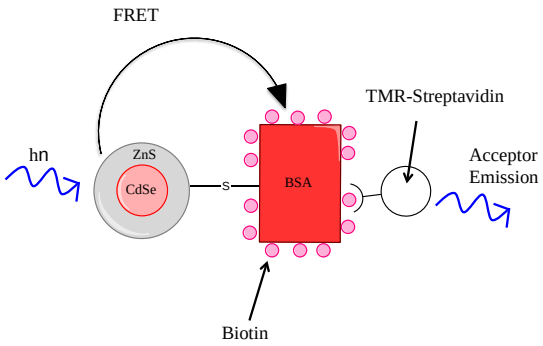

Figure 13. *Schematic of FRET binding assay by Willard et al.*[84]

References:

1. Chan, W. C. W. *et al.* Luminescent quantum dots for multiplexed biological detection and imaging. *Curr. Opin. Biotechnol.* **13,** 40–46 (2002).

2. Murray, C. B., Norris, D. J. & Bawendi, M. G. Synthesis and characterization of nearly monodisperse CdE (E = sulfur, selenium, tellurium) semiconductor nanocrystallites. *J. Am. Chem. Soc.* **115,** 8706–8715 (1993).

3. Alivisatos, A. P. Semiconductor Clusters, Nanocrystals, and Quantum Dots. *Science* **271,** 933–937 (1996).

4. Yoffe, A. D. Semiconductor quantum dots and related systems: Electronic, optical, luminescence and related properties of low dimensional systems. *Adv. Phys.* **50,** 1–208 (2001).

5. Reimann, S. M. & Manninen, M. Electronic structure of quantum dots. *Rev. Mod. Phys.* **74,** 1283–1342 (2002).

6. Resch-Genger, U., Grabolle, M., Cavaliere-Jaricot, S., Nitschke, R. & Nann, T. Quantum dots versus organic dyes as fluorescent labels. *Nat. Methods* **5,** 763–75 (2008).

7. Russ Algar, W., Massey, M. & Krull, U. J. The application of quantum dots, gold nanoparticles and molecular switches to optical nucleic-acid diagnostics. *TrAC Trends Anal. Chem.* **28,** 292–306 (2009).

8. Green, M. The nature of quantum dot capping ligands. *J. Mater. Chem.* **20,** 5797–5809 (2010).

9. Reiss, P., Protière, M. & Li, L. Core/Shell semiconductor nanocrystals. *Small* **5,** 154–68 (2009).

10. Gao, X., Cui, Y., Levenson, R. M., Chung, L. W. K. & Nie, S. In vivo cancer targeting and imaging with semiconductor quantum dots. *Nat. Biotechnol.* **22,** 969–976 (2004).

11. Dyadyusha, L. *et al.* Quenching of CdSe quantum dot emission, a new approach for biosensing. *Chem. Commun.* 3201–3203 (2005). doi:10.1039/b500664c

12. Jamieson, T. *et al.* Biological applications of quantum dots. *Biomaterials* **28,** 4717–32 (2007).

13. Bera, D., Qian, L., Tseng, T.-K. & Holloway, P. H. Quantum Dots and Their Multimodal Applications: A Review. *Materials (Basel).* **3,** 2260–2345 (2010).

14. Burda, C., Chen, X., Narayanan, R. & El-Sayed, M. A. Chemistry and Properties of Nanocrystals of Different Shapes. *Chem. Rev.* **105,** 1025–1102 (2005).

15. Xin, S. H. *et al.* Formation of self-assembling CdSe quantum dots on ZnSe by molecular beam epitaxy. *Appl. Phys. Lett.* **69,** 3884 (1996).

16. Swihart, M. T. Vapor-phase synthesis of nanoparticles. *Curr. Opin. Colloid Interface Sci.* **8,** 127–133 (2003).

17. Battaglia, D., Li, J. J., Wang, Y. & Peng, X. Colloidal two-dimensional systems: CdSe quantum shells and wells. *Angew. Chem. Int. Ed. Engl.* **42,** 5035–9 (2003).

18. Dorfs, D., Hickey, S. & Eychmüller, A. in *Nanotechnologies for the Life Sciences* (ed. Kumar, C. S. S. R.) (Wiley-VCH Verlag GmbH & Co. KGaA, 2011). doi:10.1002/9783527610419.ntls0199

19. Kim, S., Fisher, B., Eisler, H.-J. & Bawendi, M. Type-II Quantum Dots: CdTe/CdSe(Core/Shell) and CdSe/ZnTe(Core/Shell) Heterostructures. *J. Am. Chem. Soc.* **125,** 11466–11467 (2003).

20. Gerbec, J. A., Magana, D., Washington, A. & Strouse, G. F. Microwave-enhanced reaction rates for nanoparticle synthesis. *J. Am. Chem. Soc.* **127,** 15791–800 (2005).

21. Qu, L. & Peng, X. Control of Photoluminescence Properties of CdSe Nanocrystals in Growth. *J. Am. Chem. Soc.* **124,** 2049–2055 (2002).

22. Schumacher, W., Nagy, A., Waldman, W. J. & Dutta, P. K. Direct Synthesis of Aqueous CdSe/ZnS-Based Quantum Dots Using Microwave Irradiation. *J. Phys. Chem. C* **113,** 12132–12139 (2009).

23. Wuister, S. F., Swart, I., van Driel, F., Hickey, S. G. & de Mello Donegá, C. Highly Luminescent Water-Soluble CdTe Quantum Dots. *Nano Lett.* **3,** 503–507 (2003).

24. Bao, H., Gong, Y., Li, Z. & Gao, M. Enhancement Effect of Illumination on the Photoluminescence of Water-Soluble CdTe Nanocrystals: Toward Highly Fluorescent CdTe/CdS Core−Shell Structure. *Chem. Mater.* **16,** 3853–3859 (2004).

25. Wang, Y. *et al.* Mechanism of Strong Luminescence Photoactivation of Citrate-Stabilized Water-Soluble Nanoparticles with CdSe Cores. *J. Phys. Chem. B* **108,** 15461–15469 (2004).

26. He, Y. *et al.* Microwave-Assisted Synthesis of Water-Dispersed CdTe Nanocrystals with High Luminescent Efficiency and Narrow Size Distribution. *Chem. Mater.* **19,** 359–365 (2007).

27. He, Y. *et al.* Microwave Synthesis of Water-Dispersed CdTe/CdS/ZnS Core-Shell-Shell Quantum Dots with Excellent Photostability and Biocompatibility. *Adv. Mater.* **20,** 3416–3421 (2008).

28. Gao, M. *et al.* Strongly Photoluminescent CdTe Nanocrystals by Proper Surface Modification. *J. Phys. Chem. B* **102,** 8360–8363 (1998).

29. Zhang, H. *et al.* Hydrothermal Synthesis for High-Quality CdTe Nanocrystals. *Adv. Mater.* **15,** 1712–1715 (2003).

30. Zhong, X., Han, M., Dong, Z., White, T. J. & Knoll, W. Composition-tunable Zn(x)Cd(1-x)Se nanocrystals with high luminescence and stability. *J. Am. Chem. Soc.* **125,** 8589–94 (2003).

31. Zhong, X., Feng, Y., Knoll, W. & Han, M. Alloyed Zn(x)Cd(1-x)S nanocrystals with highly narrow luminescence spectral width. *J. Am. Chem. Soc.* **125,** 13559–63 (2003).

32. Pu, Y.-C. & Hsu, Y.-J. Multicolored Cd1−xZnxSe quantum dots with type-I core/shell structure: single-step synthesis and their use as light emitting diodes. *Nanoscale* **6,** 3881–3888 (2014).

33. Zhong, X., Zhang, Z., Liu, S., Han, M. & Knoll, W. Embryonic Nuclei-Induced Alloying Process for the Reproducible Synthesis of Blue-Emitting Zn x Cd 1- x Se Nanocrystals with Long-Time Thermal Stability in Size Distribution and Emission Wavelength. *J. Phys. Chem. B* **108,** 15552–15559 (2004).

34. Liu, F.-C., Cheng, T.-L., Shen, C.-C., Tseng, W.-L. & Chiang, M. Y. Synthesis of Cysteine-Capped Zn(x)Cd(1)(-)(x)Se alloyed quantum dots emitting in the blue-green spectral range. *Langmuir* **24,** 2162–7 (2008).

35. Cao, J., Xue, B., Li, H., Deng, D. & Gu, Y. Facile synthesis of high-quality water-soluble N-acetyl-L-cysteine-capped Zn(1-x)Cd(x)Se/ZnS core/shell quantum dots emitting in the violet-green spectral range. *J. Colloid Interface Sci.* **348,** 369–76 (2010).

36. Zhang, W., Zhou, X. & Zhong, X. One-pot noninjection synthesis of Cu-doped Zn(x)Cd(1-x)S nanocrystals with emission color tunable over entire visible spectrum. *Inorg. Chem.* **51,** 3579–87 (2012).

37. Wang, L., Nagesha, D. K., Selvarasah, S., Dokmeci, M. R. & Carrier, R. L. Toxicity of CdSe Nanoparticles in Caco-2 Cell Cultures. *J. Nanobiotechnology* **6,** 11–26 (2008).

38. Su, Y. *et al.* The cytotoxicity of CdTe quantum dots and the relative contributions from released cadmium ions and nanoparticle properties. *Biomaterials* **31,** 4829–34 (2010).

39. Su, Y. *et al.* The cytotoxicity of cadmium based, aqueous phase - synthesized, quantum dots and its modulation by surface coating. *Biomaterials* **30,** 19–25 (2009).

40. Derfus, A. M., Chan, W. C. W. & Bhatia, S. N. Probing the Cytotoxicity of Semiconductor Quantum Dots. *Nano Lett.* **4,** 11–18 (2004).

41. Ipe, B. I., Lehnig, M. & Niemeyer, C. M. On the generation of free radical species from quantum dots. *Small* **1,** 706–9 (2005).

42. Mancini, M. C., Kairdolf, B. A., Smith, A. M. & Nie, S. Oxidative quenching and degradation of polymer-encapsulated quantum dots: new insights into the long-term fate and toxicity of nanocrystals in vivo. *J. Am. Chem. Soc.* **130,** 10836–7 (2008).

43. Hanaki, K. *et al.* Semiconductor quantum dot/albumin complex is a long-life and highly photostable endosome marker. *Biochem. Biophys. Res. Commun.* **302,** 496–501 (2003).

44. Parak, W. J. *et al.* Cell Motility and Metastatic Potential Studies Based on Quantum Dot Imaging of Phagokinetic Tracks. *Adv. Mater.* **14,** 882–885 (2002).

45. Clift, M. J. D., Brandenberger, C., Rothen-Rutishauser, B., Brown, D. M. & Stone, V. The uptake and intracellular fate of a series of different surface coated quantum dots in vitro. *Toxicology* **286,** 58–68 (2011).

46. Lovrić, J. *et al.* Differences in subcellular distribution and toxicity of green and red emitting CdTe quantum dots. *J. Mol. Med.* **83,** 377–85 (2005).

47. Fischer, H. C., Hauck, T. S., Gómez-Aristizábal, A. & Chan, W. C. W. Exploring primary liver macrophages for studying quantum dot interactions with biological systems. *Adv. Mater.* **22,** 2520–4 (2010).

48. Jaiswal, J. K., Mattoussi, H., Mauro, J. M. & Simon, S. M. Long-term multiple color imaging of live cells using quantum dot bioconjugates. *Nat. Biotechnol.* **21,** 47–51 (2003).

49. Ma, Q., Serrano, I. C. & Palomares, E. Multiplexed color encoded silica nanospheres prepared by stepwise encapsulating quantum dot/SiO2 multilayers. *Chem. Commun.* **47,** 7071–7073 (2011).

50. Ballou, B., Lagerholm, B. C., Ernst, L. A., Bruchez, M. P. & Waggoner, A. S. Noninvasive imaging of quantum dots in mice. *Bioconjug. Chem.* **15,** 79–86 (2004).

51. Fitzpatrick, J. A. J. *et al.* Long-term persistence and spectral blue shifting of quantum dots in vivo. *Nano Lett.* **9,** 2736–41 (2009).

52. Hauck, T. S., Anderson, R. E., Fischer, H. C., Newbigging, S. & Chan, W. C. W. In vivo quantum-dot toxicity assessment. *Small* **6,** 138–44 (2010).

53. Chang, E., Thekkek, N., Yu, W. W., Colvin, V. L. & Drezek, R. Evaluation of quantum dot cytotoxicity based on intracellular uptake. *Small* **2,** 1412–7 (2006).

54. Huynh, W. U., Dittmer, J. J. & Alivisatos, A. P. Hybrid nanorod-polymer solar cells. *Science* **295,** 2425–7 (2002).

55. Gur, I. Air-Stable All-Inorganic Nanocrystal Solar Cells Processed from Solution. *Science (80-.).* **310,** 462–465 (2005).

56. Sargent, E. H. Infrared photovoltaics made by solution processing. *Nat. Photonics* **3,** 325–331 (2009).

57. Colvin, V. L., Schlamp, M. C. & Alivisatos, A. P. Light-emitting diodes made from cadmium selenide nanocrystals and a semiconducting polymer. *Nature* **370,** 354–357 (1994).

58. Dabbousi, B. O., Bawendi, M. G., Onitsuka, O. & Rubner, M. F. Electroluminescence from CdSe quantum-dot/polymer composites. *Appl. Phys. Lett.* **66,** 1316 (1995).

59. Konstantatos, G. & Sargent, E. H. Solution-Processed Quantum Dot Photodetectors. *Proc. IEEE* **97,** 1666–1683 (2009).

60. Chan, W. C. Quantum Dot Bioconjugates for Ultrasensitive Nonisotopic Detection. *Science (80-.).* **281,** 2016–2018 (1998).

61. Michalet, X. *et al.* Quantum dots for live cells, in vivo imaging, and diagnostics. *Science* **307,** 538–44 (2005).

62. Medintz, I. L., Uyeda, H. T., Goldman, E. R. & Mattoussi, H. Quantum dot bioconjugates for imaging, labelling and sensing. *Nat. Mater.* **4,** 435–46 (2005).

63. Bruchez Jr., M. Semiconductor Nanocrystals as Fluorescent Biological Labels. *Science (80-.).* **281,** 2013–2016 (1998).

64. Dubertret, B. *et al.* In vivo imaging of quantum dots encapsulated in phospholipid micelles. *Science* **298,** 1759–62 (2002).

65. Kaul, Z. *et al.* Mortalin imaging in normal and cancer cells with quantum dot immuno-conjugates. *Cell Res.* **13,** 503–7 (2003).

66. Sukhanova, A. *et al.* Biocompatible fluorescent nanocrystals for immunolabeling of membrane proteins and cells. *Anal. Biochem.* **324,** 60–67 (2004).

67. Yang, L. & Li, Y. Simultaneous detection of Escherichia coli O157:H7 and Salmonella Typhimurium using quantum dots as fluorescence labels. *Analyst* **131,** 394–401 (2006).

68. Gerion, D. *et al.* Room-Temperature Single-Nucleotide Polymorphism and Multiallele DNA Detection Using Fluorescent Nanocrystals and Microarrays. *Anal. Chem.* **75,** 4766–4772 (2003).

69. Dahan, M. *et al.* Diffusion dynamics of glycine receptors revealed by single-quantum dot tracking. *Science* **302,** 442–445 (2003).

70. Winter, P. W. *et al.* Rotation of Single Cell-Surface Fc Receptors Examined by Quantum Dot Probes. *Biophys. J.* **102,** 653–654 (2012).

71. Parungo, C. P. *et al.* Intraoperative identification of esophageal sentinel lymph nodes with near-infrared fluorescence imaging. *J. Thorac. Cardiovasc. Surg.* **129,** 844–50 (2005).

72. Voura, E. B., Jaiswal, J. K., Mattoussi, H. & Simon, S. M. Tracking metastatic tumor cell extravasation with quantum dot nanocrystals and fluorescence emission-scanning microscopy. *Nat. Med.* **10,** 993–998 (2004).

73. Tomasulo, M., Yildiz, I. & Raymo, F. M. pH-sensitive quantum dots. *J. Phys. Chem. B* **110,** 3853–5 (2006).

74. Yun, Z., Zhengtao, D., Jiachang, Y., Fangqiong, T. & Qun, W. Using cadmium telluride quantum dots as a proton flux sensor and applying to detect H9 avian influenza virus. *Anal. Biochem.* **364,** 122–7 (2007).

75. Serrano, I. C., Ma, Q. & Palomares, E. QD-'Onion'-Multicode silica nanospheres with remarkable stability as pH sensors. *J. Mater. Chem.* **21,** 17673–17679 (2011).

76. Dougherty, T. J. Photodynamic therapy (PDT) of malignant tumors. *Crit. Rev. Oncol. Hematol.* **2,** 83–116 (1984).

77. Hone, D. C. *et al.* Generation of Cytotoxic Singlet Oxygen via Phthalocyanine-Stabilized Gold Nanoparticles: A Potential Delivery Vehicle for Photodynamic Therapy. *Langmuir* **18,** 2985–2987 (2002).

78. Samia, a C., Chen, X. & Burda, C. Semiconductor quantum dots for photodynamic therapy. *J. Am. Chem. Soc.* **125,** 15736–15737 (2003).

79. Ma, J., Chen, J.-Y., Idowu, M. & Nyokong, T. Generation of singlet oxygen via the composites of water-soluble thiol-capped CdTe quantum dots-sulfonated aluminum phthalocyanines. *J. Phys. Chem. B* **112,** 4465–9 (2008).

80. Qi, Z.-D. *et al.* Biocompatible CdSe quantum dot-based photosensitizer under two-photon excitation for photodynamic therapy. *J. Mater. Chem.* **21,** 2455 (2011).

81. Wang, S., Mamedova, N., Kotov, N. A., Chen, W. & Studer, J. Antigen/Antibody Immunocomplex from CdTe Nanoparticle Bioconjugates. *Nano Lett.* **2,** 817–822 (2002).

82. Staros, J. V. N-hydroxysulfosuccinimide active esters: bis(N-hydroxysulfosuccinimide) esters of two dicarboxylic acids are hydrophilic, membrane-impermeant, protein cross-linkers. *Biochemistry* **21,** 3950–3955 (1982).

83. Kagan, C., Murray, C., Nirmal, M. & Bawendi, M. Electronic Energy Transfer in CdSe Quantum Dot Solids. *Phys. Rev. Lett.* **76,** 1517–1520 (1996).

84. Willard, D. M., Carillo, L. L., Jung, J. & Van Orden, A. CdSe−ZnS Quantum Dots as Resonance Energy Transfer Donors in a Model Protein−Protein Binding Assay. *Nano Lett.* **1,** 469–474 (2001).

UNIVERSITAT ROVIRA I VIRGILI
SEMICONDUCTOR NANOPARTICLES AS PLATFORM FOR BIO-APPLICATIONS AND ENERGY RELATED SYSTEMS.
Alba María Matas Adams
Dipòsit Legal: T 55-2016

Chapter 1

The effect of the silica thickness on the enhanced emission in single particle Quantum Dots coated with gold nanoparticles

UNIVERSITAT ROVIRA I VIRGILI
SEMICONDUCTOR NANOPARTICLES AS PLATFORM FOR BIO-APPLICATIONS AND ENERGY RELATED SYSTEMS.
Alba María Matas Adams
Dipòsit Legal: T 55-2016

1.Introduction

Due to the similar size of nanocolloidal materials with those of the biological structures, the design, fabrication and application of nanoparticles into chemical biology is generating a new field known as bionanotechnology.[1] One of the main aims of this new field relies in the identification or imaging of relevant areas in biological samples with nanometer resolution.[2] To do that, materials designed for imaging may include a series of characteristics including a high signal output upon excitation with the appropriate source, small size to increase the spatial resolution, and biocompatibility.[3] During the recent years several materials have been studied as candidates for bioimaging.[4,5] Between them it is worthy to mention quantum dots as fluorescent tags.[6]

Semiconductor quantum dots (QDs) have been applied for detection and imaging in several areas, ranging from microarray technology to fluorescence in situ hybridization and for vivo imaging.[7–9] Compared with organic dyes they present an upgrade in properties such as size-tunable absorption and emission, extremely broad and intense absorption enabling a unique flexibility in excitation, high fluorescence quantum yields even in the NIR wavelengths[10], but on the negative side, intrinsic chemical nature make them degradable under biological conditions giving rise to the leaching of extremely toxic species. Both, the degradation and toxicity can be adequately controlled by appropriate coating of the particles usually with biocompatible inorganic oxides or by protecting them with polymers.[11–13]

Although light emission by quantum dots is excellent, the increase of their native fluorescence implies both the decrease of power at the sample and/or the reduction of the readout time, parameters that are of key importance to avoid sample degradation especially when imaging biological samples.

Strategies to increase the photoluminiscenece mainly rely in the appropriate coupling of the quantum dot with near electromagnetic field provided by a plasmonic particle. Although this effect, known as metal-enhancement fluorescence (MEF) or surface-enhanced fluorescence (SEF),[14] is well known and has been demonstrated over the time for quantum dots on a variety of optical substrates (including films and particles),[15] most of the efforts for producing highly brilliant QDs take advantage of

the well establish protocols for the coating of metallic NPs with dielectric materials, retaining the QDs on the outer shell.[16–18] This approach, although efficient in terms of photoluminescence yield, is subject to the same drawbacks as the as prepared QDs, degradation and toxicity. On the other hand the isolation of the plasmonic nanoparticles inhibits its coupling to produce intense electromagnetic fields (i.e. hot spots), thus reducing the degree of enhancement obtained.[19] Another important aspect when producing QDs with enhanced emission is the spacer thickness. For the case of surface-enhanced Raman scattering (SERS), the near electromagnetic field provided by the plasmonic nanoparticle decays exponentially with the distance to the surface. On the other hand and contrary to SERS, which is a first layer effect, MEF requires of a minimum interdistance, to avoid quenching of the emission by the metallic surface. Although the coupling between QDs and the NPs is known to be efficient at interdistances around 10 nm,[16] small changes in this distance result in considerable gaining (or loss) of the emission intensity.

Here we present a method consisting in the controlled coating of quantum dots with silica and the retention of metal nanoparticles on the outer silica shells yielding highly brilliant although biocompatible hybrid particles. This approach allows for the fine-tuning of the spacer shell size that is exploited for the study of the optimal separation of the QD-NP interdistance to maximize the fluorescent enhancement both in an ensemble solution of particles and at the single particle level.

2. Experimental

2.1 Synthesis of CdSe. TOPO (3.0 g), ODPA (0.280 g) and CdO (0.060 g) were mixed in a 50 mL flask, heated to ca. 150°C and exposed to vacuum for ca. 1 h. Under nitrogen, the solution was heated to 320°C to fully dissolve the CdO until it turned optically clear and colourless.

Then, 1.5 g of TOP was injected in the flask and the temperature was set to 380°C. Meanwhile, 0.058 g of Se was dissolved in 0.360 g TOP, and when this temperature was reached, it was injected into the flask. Immediately after injection, the heating mantle was removed allowing the flask to cool down to 100ºC. At that temperature, 2 mL of anhydrous toluene was injected and the nanocrystals were precipitated adding an excess of methanol. Repeated redissolution in toluene and precipitation with the addition of methanol and centrifugation was performed to achieve pure CdSe nanocrystals.

2.2 Synthesis of CdSe@silica nanospheres. For this synthesis, a reverse microemulsion method was followed, where, under vigorous stirring, 0.8 mL QDs and 0.64 mL TEOS were introduced into a liquid system containing 15 mL of cyclohexane and 2.6 mL non-ionic surfactant NP7. After 30 min, 0.2 mL ammonia (32%) was injected. The microemulsion was stirred for different periods of time (from 2-24 hours) to allow different growths, and different thickness. Because the hydrolysed TEOS and NP7 molecules replaced the original hydrophobic ligands of CdSe QDs in this reverse microemulsion system, silica grew around the hydrophobic QDs smoothly.

2.3 Gold coating. 10 mg of a dried sample of CdSe@SiO_2 was resuspended in 5 ml of isopropanol. CdSe@SiO_2 were amino functionalized adding 45 mL of a 0.64 mM 3-aminopropyltrimethoxysilane (APS) solution to 2.5 mL (2 mg/mL) of the dispersion of CdSe@SiO2 in isopropanol. The excess of APS was removed by three centrifugation-redispersion cycles with isopropanol (5500 rpm, 30 min) and 2 cycles more with pure water. Finally, the amino-functionalized CdSe@SiO_2 nanoparticles were dispersed in water to a final concentration of 2 mg/ml.

Gold nanoparticles were prepared by standard THPC reduction [20] and adsorbed by a drop-wise addition of 2.5 ml (2 mg/mL) of CdSe@SiO_2 previously functionalized to 20 ml of a solution of gold nanoparticles (3-10 nm; 10^{-3} M in gold), under magnetic stirring for 15 h. The excess of gold nanoparticles was removed by several centrifugation-redispersion cycles with pure water. Finally, the CdSe@SiO2@Au nanoparticles were dispersed in isopropanol.

3. Results and Discussion

Hybrid CdSe-QD@SiO_2@AuNPs nanoparticles were synthesized via a multistep procedure, which involved the preparation of hydrophobic CdSe QDs, the controlled silica-shell deposition on their surfaces (to allow hydrophilic interactions), modification of the silica surfaces with -NH_2 groups (for further functionalization), and finally the self-assembly of the preformed gold nanoparticles onto the silica shell (Figure 1a).

CdSe QDs were prepared via standard high-temperature reaction in TOPO/ODPA mixture. This protocol gives rise to homogeneous spheroidal particles of approximately 4 nm in diameter with absorption and emission bands centre at 645 and

652 nm, respectively (Figure 1b). The coating of the prepared QDs with a silica shell of controlled thickness was achieved through a microemulsion method using tergitol and tetraethyl orthosilicate as surfactant and silica precursor, respectively.[21,22] With this method the shell thickness can be effectively delimited by controlling the deposition time. Finally preformed gold nanoparticles from 3 to 10 nm were self-assembled on the previous amino-functionalized silica shell. This yields homogeneous AuNPs coatings on the material surface (Figure 1c).

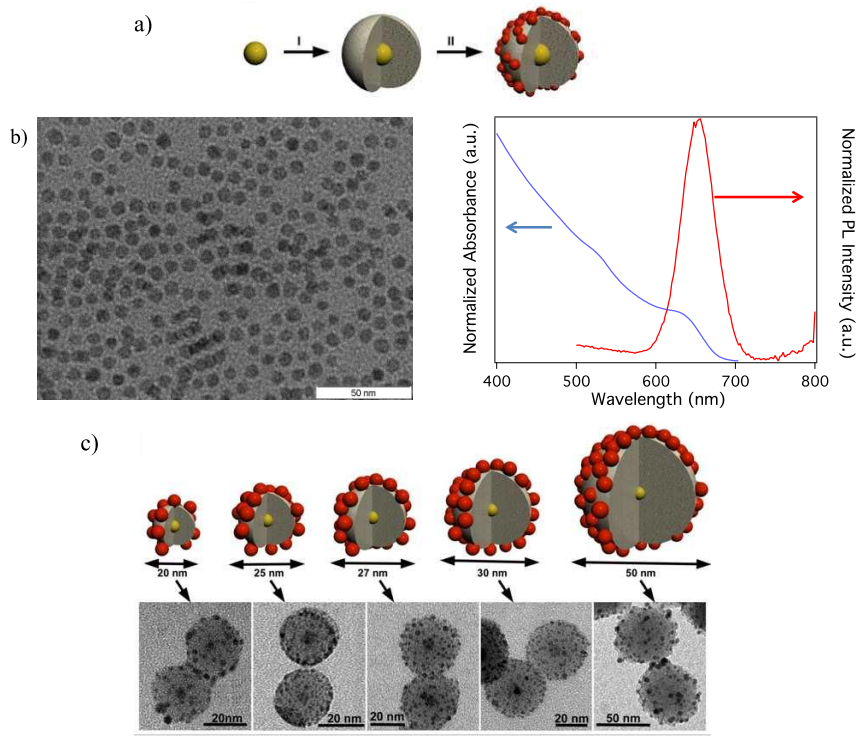

Figure 1. *a) Schematic illustration for the synthesis of CdSe@SiO_2@AuNPs. b) TEM image and absorption and emission spectra of the as-prepared CdSe quantum dots. c) Schemes and TEM images of the QDs coated with different silica shell thickness (8, 10.5, 11.5, 13 and 23 nm)*

Notably, in contrast with the as prepared AuNPs which are characterized by a well-defined Localized Surface Plasmon Resonance (LSPR) band centred at 520 nm, the QDs@SiO2@AuNPs exhibit a broadened band red shifted to 556 nm (Figure 2a) attributed to the plasmon coupling in between the gold particles and the subsequent generation of hot spots.[23] The absorption and spectra for the QDs as prepared and after silica coating are shown in Figures 2a and b. After the silica coating, although the absorption spectra of the coated and uncoated QDs remains similar (Figure 2a), the natural photoluminescence of the QDs decreases around 20 % (Figure 2a). This experimental fact has been reported many times[24] and is ascribed to the removal of

shallow trap states due to the exchange of ligands and the decrease in charged species on the QD surface for samples that do show trap state emission before silanization.[25,26] The emission spectra obtained for the colloidal solutions of QDs@SiO2@AuNPs as a function of their spacer distance (silica shell thickness, Figure 2b) and a comparison of the intensities (Figure 2c) shows a marked increase of the photoluminescence with the increase of shell thickness until a maximum at 11.5 nm (up to 6 fold the natural emission of the QD). From this point onwards the photoactivity abruptly decays to similar levels as in the case of the silica coated quantum dots. The increase in the intensity with the thickness of the shell can be explained in light of the two main effects that affect the emission which are both distance dependent: the emission quenching due to resonant energy transfer from photoexcited QDs to metal colloidal nanoparticle and the enhancement of photoluminescence promoted by the excitation of the localized surface plasmon resonances in the NPs.

Although the effect of this compromise between the variables is already known and appropriate interdistances have been set in a appoint in between the 5 to 20 nm of separation,[16] it is of key importance to note that small changes within the shell thickness affect notably to the material emission. Thus, in our case, the variation of just a single nm (from 10.5 nm to 11.5 nm) doubles the emission signal. Conversely the slight increase in the thickness of the shell yields to a considerable decrease in the emission. In this case the only variable affecting the effect is the exponential decay of the plasmonic electromagnetic field with the distance to the metallic surface.

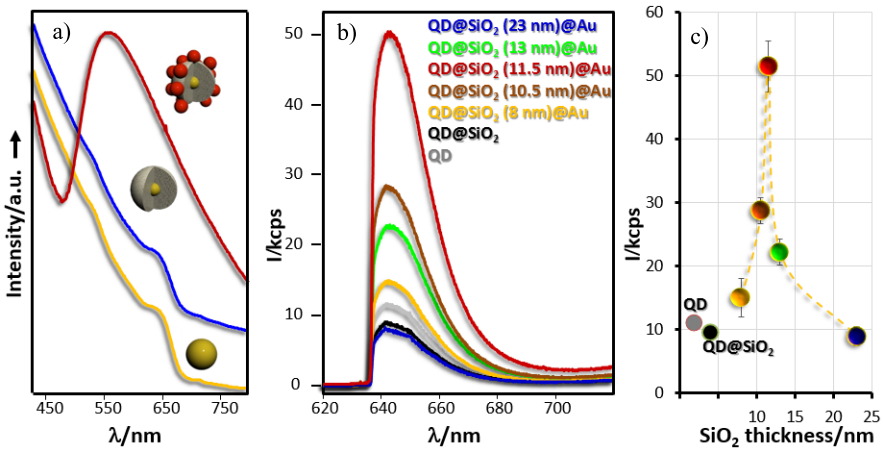

Figure 2. *a) Absorption spectra of the as-prepared CdSe quantum dots (yellow), after silica coating (blue) and after gold attachment (red). Localized surface plasmon resonance for the QDs@SiO$_2$@AuNPs colloids. b) Emission spectra and c) comparison of the emission at the maximum for the as-prepared quantum dots, after silica coating and after the self-assembly of the AuNPs on the silica coated QDs with the different silica thickness.*

To test for the applicability of our hybrid materials as single particles for imaging an experiment was designed for the isolation of single particles on a substrate and marking their position with a focusing ion beam (Figure 3).[27] SEM, optical, and SERS mapping of the different particles show that although MEF signals can be found for all the particles those corresponding to the particle with 11.5 nm of separation are consistently brighter and require smaller acquisition times and/or smaller powers at the sample with the subsequent protection of the sample from photodegradation.

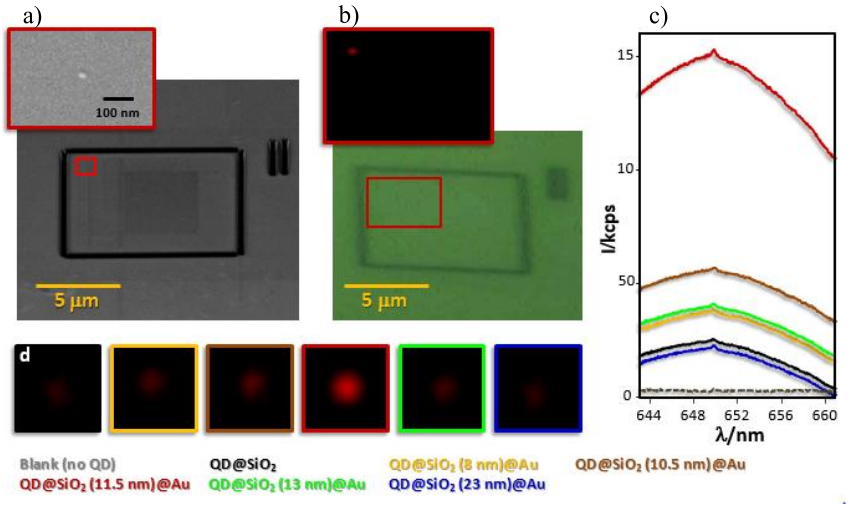

Figure 3. *a) SEM, b) optical and MEF images of single quantum dots from a diluted solution spin-coated on a silicon wafer, c) MEF spectra and d) imaging of the corresponding materials as a function of the silica shell thickness.*

4. Conclusions

In conclusion, we have developed a multistep synthesis of hybrid superstructures that comprise quantum dot cores and dense layers of gold nanoparticles separated by a silica shell. This architecture allows for versatile control of QD−metal interactions through control of the thickness of the dielectric spacer. The shell thickness was optimized at the nanometre scale in order to increase the enhanced photoluminescence. Further characterization of the emission at the single particle regime shows that our brighter particles require smaller acquisition times to yield better imaging results. We anticipate that these materials may pave the road to new (bio) imaging applications where both time and power can be decreased.

References

1. Saha, K., Agasti, S. S., Kim, C., Li, X. & Rotello, V. M. Gold nanoparticles in chemical and biological sensing. *Chem. Rev.* **112,** 2739–79 (2012).

2. Hartmann, R., Carregal-Romero, S., Parak, W. J. & Rivera Gil, P. *Nanobiotechnology-Inorganic Nanoparticles vs Organic Nanoparticles*. *Frontiers of Nanoscience* **4,** (Elsevier, 2012).

3. Abalde-Cela, S. *et al.* Surface-enhanced Raman scattering biomedical applications of plasmonic colloidal particles. *J. R. Soc. Interface* **7,** S435–50 (2010).

4. Riehemann, K. *et al.* Nanomedicine--challenge and perspectives. *Angew. Chem. Int. Ed. Engl.* **48,** 872–97 (2009).

5. Weckhuysen, B. M. Chemical imaging of spatial heterogeneities in catalytic solids at different length and time scales. *Angew. Chem. Int. Ed. Engl.* **48,** 4910–43 (2009).

6. Zhang, F., Ali, Z., Amin, F., Riedinger, A. & Parak, W. J. In vitro and intracellular sensing by using the photoluminescence of quantum dots. *Anal. Bioanal. Chem.* **397,** 935–42 (2010).

7. Huang, J. G., Leshuk, T. & Gu, F. X. Emerging nanomaterials for targeting subcellular organelles. *Nano Today* **6,** 478–492 (2011).

8. Knipe, J. M., Peters, J. T. & Peppas, N. A. Theranostic agents for intracellular gene delivery with spatiotemporal imaging. *Nano Today* **8,** 21–38 (2013).

9. Michalet, X. *et al.* Quantum dots for live cells, in vivo imaging, and diagnostics. *Science* **307,** 538–44 (2005).

10. Resch-Genger, U., Grabolle, M., Cavaliere-Jaricot, S., Nitschke, R. & Nann, T. Quantum dots versus organic dyes as fluorescent labels. *Nat. Methods* **5,** 763–75 (2008).

11. Soenen, S. J. *et al.* Cellular toxicity of inorganic nanoparticles: Common aspects and guidelines for improved nanotoxicity evaluation. *Nano Today* **6,** 446–465 (2011).

12. Zhang, F. *et al.* Polymer-coated nanoparticles: a universal tool for biolabelling experiments. *Small* **7,** 3113–27 (2011).

13. Thanh, N. T. K. & Green, L. A. W. Functionalisation of nanoparticles for biomedical applications. *Nano Today* **5,** 213–230 (2010).

14. Aslan, K. *et al.* Metal-enhanced fluorescence: an emerging tool in biotechnology. *Curr. Opin. Biotechnol.* **16,** 55–62 (2005).

15. Biju, V., Itoh, T., Anas, A., Sujith, A. & Ishikawa, M. Semiconductor quantum dots and metal nanoparticles: syntheses, optical properties, and biological applications. *Anal. Bioanal. Chem.* **391,** 2469–2495 (2008).

16. Kulakovich, O. *et al.* Enhanced Luminescence of CdSe Quantum Dots on Gold Colloids. *Nano Lett.* **2,** 1449–1452 (2002).

17. Liu, N., Prall, B. S. & Klimov, V. I. Hybrid gold/silica/nanocrystal-quantum-dot superstructures: synthesis and analysis of semiconductor-metal interactions. *J. Am. Chem. Soc.* **128,** 15362–3 (2006).

18. Grzelczak, M. *et al.* Photoluminescence Quenching Control in Quantum Dot–Carbon Nanotube Composite Colloids Using a Silica-Shell Spacer. *Adv. Mater.* **18,** 415–420 (2006).

19. Halas, N. J., Lal, S., Chang, W.-S., Link, S. & Nordlander, P. Plasmons in Strongly Coupled Metallic Nanostructures. *Chem. Rev.* **111,** 3913–3961 (2011).

20. Duff, D. G., Baiker, A. & Edwards, P. P. A new hydrosol of gold clusters. 1. Formation and particle size variation. *Langmuir* **9,** 2301–2309 (1993).

21. Ma, Q., Serrano, I. C. & Palomares, E. Multiplexed color encoded silica nanospheres prepared by stepwise encapsulating quantum dot/SiO2 multilayers. *Chem. Commun.* **47,** 7071–7073 (2011).

22. Serrano, I. C., Ma, Q. & Palomares, E. QD-'Onion'-Multicode silica nanospheres with remarkable stability as pH sensors. *J. Mater. Chem.* **21,** 17673–17679 (2011).

23. Tsoutsi, D. *et al.* Quantitative surface-enhanced Raman scattering ultradetection of atomic inorganic ions: the case of chloride. *ACS Nano* **5,** 7539–46 (2011).

24. Zhang, B. *et al.* A novel method to enhance quantum yield of silica-coated quantum dots for biodetection. *Nanotechnology* **19,** 465604 (2008).

25. Wang, Y. *et al.* Mechanism of Strong Luminescence Photoactivation of Citrate-Stabilized Water-Soluble Nanoparticles with CdSe Cores. *J. Phys. Chem. B* **108,** 15461–15469 (2004).

26. Wolcott, A. *et al.* Silica-coated CdTe quantum dots functionalized with thiols for bioconjugation to IgG proteins. *J. Phys. Chem. B* **110,** 5779–89 (2006).

27. Yang, M. *et al.* SERS-active gold lace nanoshells with built-in hotspots. *Nano Lett.* **10,** 4013–9 (2010).

UNIVERSITAT ROVIRA I VIRGILI
SEMICONDUCTOR NANOPARTICLES AS PLATFORM FOR BIO-APPLICATIONS AND ENERGY RELATED SYSTEMS.
Alba María Matas Adams
Dipòsit Legal: T 55-2016

Chapter 2

Layer-by-layer encapsulation of Quantum Dots for flow cytometry applications

UNIVERSITAT ROVIRA I VIRGILI
SEMICONDUCTOR NANOPARTICLES AS PLATFORM FOR BIO-APPLICATIONS AND ENERGY RELATED SYSTEMS.
Alba María Matas Adams
Dipòsit Legal: T 55-2016

1. Introduction

Conventional flow cytometry requires multiple detectors for simultaneous identification of different 'analytes' since this method measures a single fluorescence signal per detector.[1] Moreover, the possible number of feasible color-codes due to different excitation wavelengths and spectrally broad emission bands limits the 'analyte' identification, as explained below, using conventional organic dyes or fluorescent proteins.[2]

Multiplexed methods allow the simultaneous measurement of multiple types of samples using a single detector being the final aim to increase detectable parameters per fluorescence channel.

The development of multicolor flow cytometry has been given new perspectives with the arrival of the quantum dots (QDs) technology that seems tailor made for multicolor flow cytometry, permitting the overcome of obstacles such as, limited fluorochrome availability, limited sensitivity of combining multiple organic fluorochromes or the need of several excitation sources and detectors.[3,4] Whereas each organic dye must be excited with a specific wavelength of light, a single light source can excite the QDs that emit at different wavelengths, so the QDs are used to label and detect multiple targets simultaneously allowing multiplex platforms. Further, their absorbance is so high and the noise to signal ratio is so low that the emission is brighter than in the case of dyes.[5]

Combining QDs luminescence color, intensity and lifetime provides high order of multiplexing (x colors with y lifetimes and z intensities would lead to $x^{(y*z)}$ different codes)[6] for the simultaneous detection of multiple biological functions. In line with this, in instruments with two or more lasers, QDs can be multiplexed with other fluorochromes to successfully measure even more colors.

But the main issue of QDs is that the emission can overlap in some cases using the same source of excitation, and can be detect in the same channel as other QDs or dyes. To avoid this problem, there is a process known as compensation, which subtracts the fluorescence that arrives to the other channels until the signal in each channel represents the true signal that has to be detected.[7,8]

QDs have attracted great interest in multiplexed bioassays, biotechnological applications and bioimaging.[9,10] In contrast to the traditional fluorophores, QDs possess excellent optical properties, such as continuous absorption profiles, robust signal intensity, narrow emission spectra, and improved brightness with outstanding resistance to photobleaching and degradation. Moreover, the development of QDs@nano- or micro-encoded spheres (silica, polymers) as bio-molecular probes can provide new insights that overcome several limitations of individual QDs as biological markers, i.e. better photostability of the embedded QDs in the bead matrix[11,12], larger available surface for chemical reactions, higher binding capacity of the microspheres, less toxicity[13,14], and easier manipulation. For example, our own group has prepared multicode silica nanospheres of 'onion' type with high stability in the biological pH range, i.e. 4–9.[15]

A problem to overcome after the encapsulation of QDs by silica is the scattering effect originated from such material, leading to broad fluorescent peaks, hindering its use for multiplex flow cytometry, as the fluorescent signals will overlap.
One solution was the encapsulation in polymer beads, like polystyrene, as done by Han et al. in 2001[16], where after synthesizing the polystyrene beads, they were swelled and then the different QDs were added inside the porous surface.
A question rose whether there could be energy transfer between the QDs, but it was proven that there was enough spatial separation between the QDs population that they did not suffer from energy transfer processes.
The problem with this approach is that the real incorporation of QDs was not controlled and there was a huge risk of leaching, as the bond between the polymer and the QD is not sufficiently strong.

A different alternative is the layer-by layer (LbL) approach, firstly described by Decher et al. in 1991[17] where the different polymers were grown one by one by the alternative deposition of polyanions and polycations over a substrate (silica, or polystyrene nanoparticles), and the fluorochromes were trapped inside like a sandwich. An interesting advantage is that after the growth of the layers, the core can be dissolved and remove to achieve a hollow capsule.[18]

Herein we present a series of polyelectrolyte multilayer (PEM) quantum dots-encapsulated polystyrene beads prepared by the LbL technique as promising fluorescent tags for multiplex quantitative and qualitative assays of biomolecules.

Based on the experiments of Chattopadhyay et al.[3] we choose blue and red QDs for our experiments (based on the minimal compensation requirements of green and yellow quantum dots and the brightness of red quantum dots, several quantum dots can be successfully multiplexed with other fluorochromes in instruments with two or more lasers).

2. Experimental

Reagents. Trilite™ Blue - Carboxyl CdSeS Core Nanocrystals and Trilite™ Red - Carboxyl CdSeS Core Nanocrystals were purchased form Crystalplex and diluted to 0.25 mg/mL in water.

PS-COOH-KM83 carboxyl functionalized polystyrene particles were purchased from Microparticles GmbH.

Poly (allylamine hydrochloride), Poly (sodium 4-styrenesulfonate) and Poly (acrylic acid, sodium salt) solution (PAH, PSS, PAA respectively) as well as PBS were purchased from Sigma Aldrich and used without any modifications. Sodium chloride was purchased from Panreac.

Solutions. A 0.5 M MilliQ NaCl aqueous solution was prepared as cleaning buffer and used to prepare the 2 mg/mL solutions of the polymers: PAH, PSS and PAA.

Polyelectrolyte multilayer (PEM) quantum dots-encapsulated polystyrene beads

1 mL of polystyrene (PS), containing $3x10^7$ million beads, was centrifuged for 4 min at 14000 rpm. The pellet was then mixed with 1 mL of PAH aqueous solution, sonicated for 60 sec and incubated for 20 min with shaking (400 rpm) at room temperature. After this, it was washed twice with 1 mL of NaCl 0.5 M (4 min at 14000 rpm).

Then, the pellet obtained was mixed with 1 mL of PSS aqueous solution, sonicated for 60 sec and incubated for 20 min with shaking (400 rpm) at room temperature. Finally, it was washed twice with 1 mL of NaCl 0.5 M (4 min at 14000 rpm). These

two steps were repeated once more in the same order (PAH, PSS), followed by adding another layer of PAH as depicted in Scheme 1.

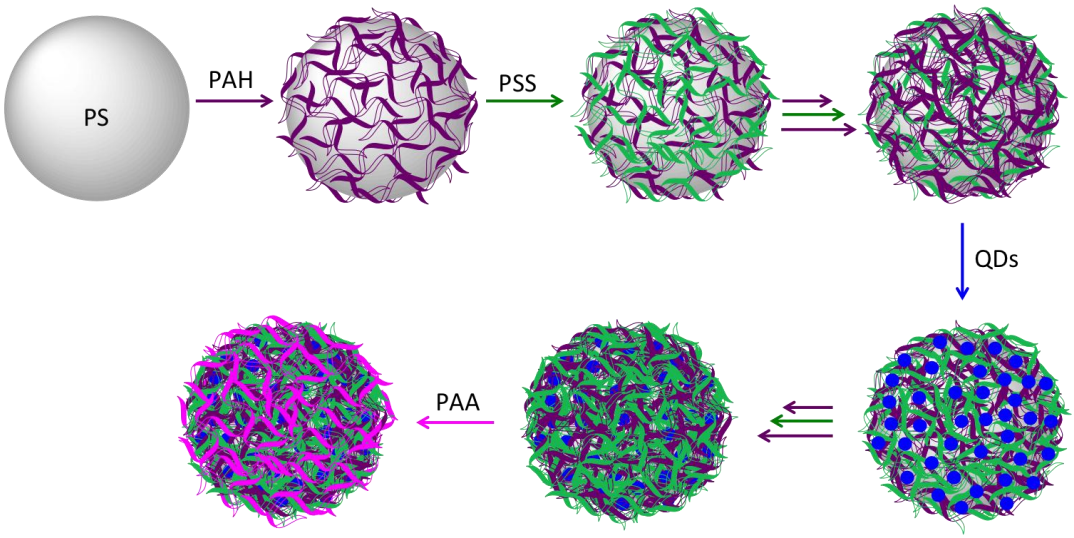

Scheme 1.*PEM consists of alternative layers of polycations (PAH) and polyanions (PSS) finally coated with PAA.*

For the attachment of the quantum dots to the previous PAH-coated PS beads, 1 mL of QDs (with a concentration of 0.25 mg/mL) was added, sonicated for 60 sec and incubated with shaking for 20 min as previously mentioned. The QDs embedding step was repeated five times and then washed with NaCl 0.5 M 3 times. Scheme 1 represents the encapsulation of blue QDs but it is the same for the red QDs and for the mixture of both blue and red QDs.

To complete the process, the following layers were grown over the QDs: PAH, PSS, PAH, PSS and PAH in this order. To end the layer growth, a final layer of PAA was added (for a carboxyl functionalization in the surface of the system), using the same conditions as before. In the end, the pellet was washed three times with NaCl aqueous solution and three times with MilliQ water, respectively, and resuspended in PBS and stored at 4ºC.

In Table 1, the different codes for the different QDs used along this chapter are shown.

QD	λem (nm)	Code
Blue	490	PS-Blue
Red	625	PS-Red
Blue and red	490 and 625	PS-Mix (1:1)

Table1. *QDs used and codes for the LbL assembly.*

Bio-functionalization. A TAMRA-labeled peptide (NH_2-Cys-Lys-Arg-Val-Lys-TAMRA) was used for the surface-functionalization of the QDs@PS. TAMRA (or carboxytetramethylrhodamine) is a rhodamine-derivative with an emission centered at 575-580 nm.

In consequence, two different emission signals should be detected, one coming from the quantum dots encapsulated in the polystyrene beads, and a second one originated from the dye.

For each one of the conjugations, 990 μL of QD-PS in PBS were mixed with 10 μL of the TAMRA labeled peptide (with final concentration of 4 μg/mL) with a slow shake for 20 min and over night in the fridge. The following day, the pellet was washed with PBS twice, resuspended in 1 ml of PBS and stored at dark at 4ºC. The different populations obtained after adding the peptide-TAMRA will be used along this chapter as denominated in Table 2.

QD	λ_{em} (nm)	Code
Blue	490 and 580	PS-Blue-TAMRA
Red	625 and 580	PS-Red-TAMRA
Blue and red	490,625 and 580	PS-Mix (1:1)-TAMRA

Table 2. *Codes after the peptide-TAMRA conjugation to the PS-QDs.*

Scheme 2 represents the final structure after the conjugation of the peptide-TAMRA to a QD-PS bead. The number of TAMRA molecules attached to the surface is not analyzed in the chapter so it is only a representation.

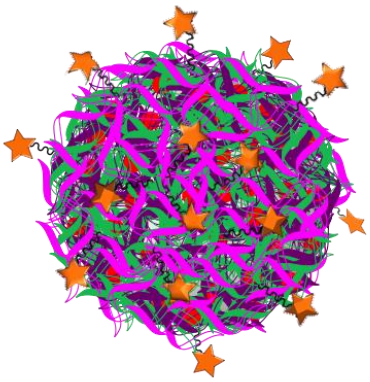

***Scheme 2**. Representation of the Red-PS-Peptide-TAMRA structure. TAMRA is represented by stars.*

Characterization techniques. Photoluminescence (PL) spectra were recorded using a 1 cm path length quartz cell in a Shimadzu UV spectrophotometer 1700 and an Aminco-Bowman Series 2 luminescence spectrometer.

True color fluorescence images were taken using a Nikon TE2000-E CCD microscope.

Flow cytometry measurements were performed with a LSR Fortessa 4L, using a blue and yellow lasers and the AmCyan (blue QDs), QDot 605-A (red QDs) and PE-YG-A (TAMRA) detector filters.

Environmental Scanning Electron Microscopy images were recorded using a FEI Quanta 600 ESEM microscope.

3. Results and discussion

Environmental SEM was used to characterize free PS beads before starting any experiments, to verify the size and dispersion. After more than 100 measurements, an average size of 5.02 μm was established which was in agreement with the commercial data (5.05 μm).

Furthermore the images obtained (Figure 1) showed that while there was a good dispersion in some of the sample, in others some of the beads were forming doublets and bigger associations as particles coated with PAH/PSS show a small tendency to aggregate forming doublets and triplets.[19]

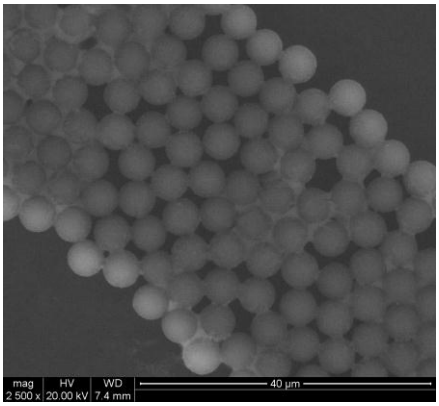

Figure 1. *ESEM image of commercial PS beads.*

Additionally, fluorescence measurements were performed on the QDs revealing a peak centered at 490 nm for the blue QDs (Figure 2a), and for red QDs at 625 nm (Figure 2b). The mixture consisting in blue and red QDs (1:1) showed two peaks corresponding to each QD, though the intensity was not 1:1, due to the different Quantum Yield (QY) of each QD.

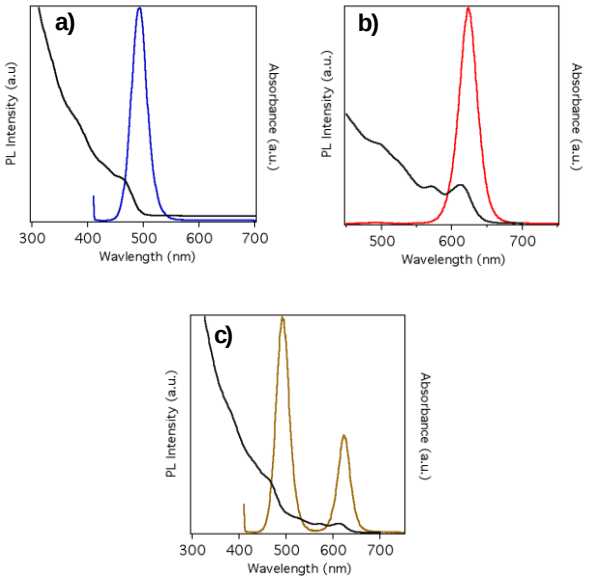

Figure 2*. Fluorescence spectrum of a) Blue QDs (λ_{em}=490nm), b) Red QDs (λ_{em}=625nm), c) Mixture of red and blue 1:1(λ_{em}=490 and 625 nm). Legend: Black (Absorbance), Color (Emission).*

The starting amount of PS beads has to be controlled for the final flow cytometry readings as with less than 8-10 million beads of PS per ml will be difficult to read enough events to achieve good resolution. Considering this, we started with around 30 million beads of PS.

The layer formation process is regulated by the electrostatic bonds that will appear between the different polymers with the PS surface as well as with the QDs. Finally PAA will add carboxyl groups to the final structure[4].

A drawback of this configuration is the nanoparticles tendency to aggregate[19] (Figure 3), giving misleading signals in flow cytometry.

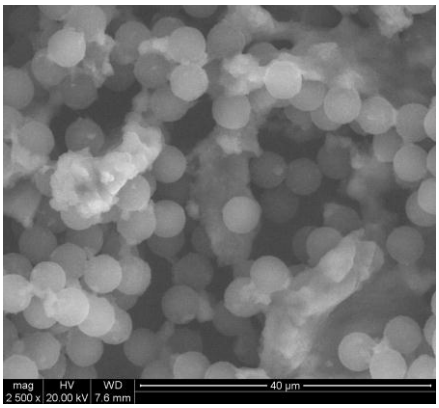

Figure 3. *ESEM image of PS-QDs aggregates.*

The fluorescence after the LbL assembly was also measured. As it can be seen in Figure 4, the signal for PS-blue and PS-red present the same intensity of just the QDs (black and colored line, respectively) and it is displaced only a few nanometers, proving that the internalization was 100% effective.

In the case of PS-mix (Figure 4c), the intensity was affected. This effect could be explained by the impossibility to control how the mixture of QDs attach to the PAH surface as both type of QDs are incubated at the same time. Might be that the bond formation is competitive between both type of QDs and it is not 100% effective. Even though we did not perform such experiment, a solution could be to incubate first with one type of QDs and then with the other.

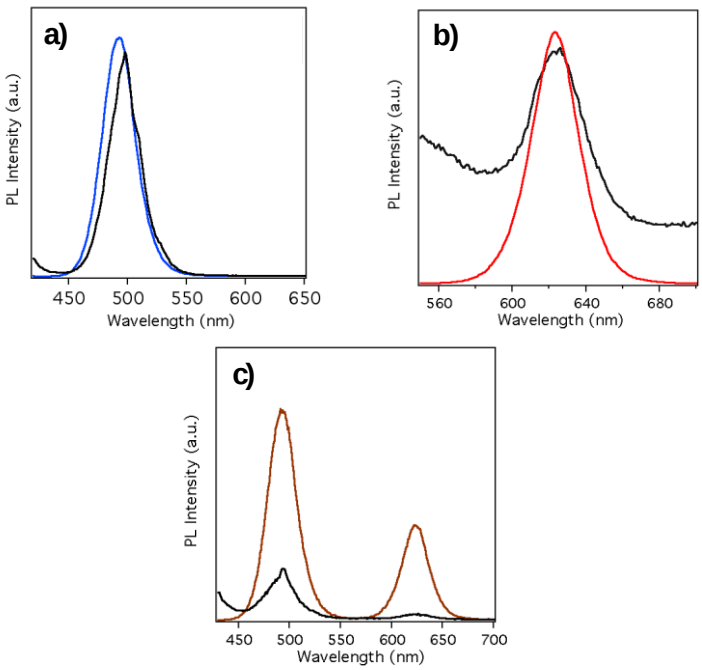

Figure 4. *Fluorescence of a) PS-Blue, b) PS-Red and c) PS-Mix (1:1) Legend: Blue (Blue QDs), Red (Red QDs), Brown (mixture of red and blue QDs), Black (PS-blue, PS-red or PS-mix).*

When comparing the fluorescence from the spectrophotometer with the flow cytometry measurements (Figure 4 vs. Figure 5 and Figure 6), it could be seen that the same results were obtained.

While the unstained beads (Figure 5a) show no fluorescence in the AmCyan channel (blue QDs channel) nor in the Qdot 605 (red QDs channel), the PS-blue beads display signal in the AmCyan channel and the PS-red appears only in the QDot605 channel.

A small signal is visible in the Qdot 605 channel for the PS-blue beads as the compensation was not perfect. This practice is commonly accepted to avoid overcompensation.

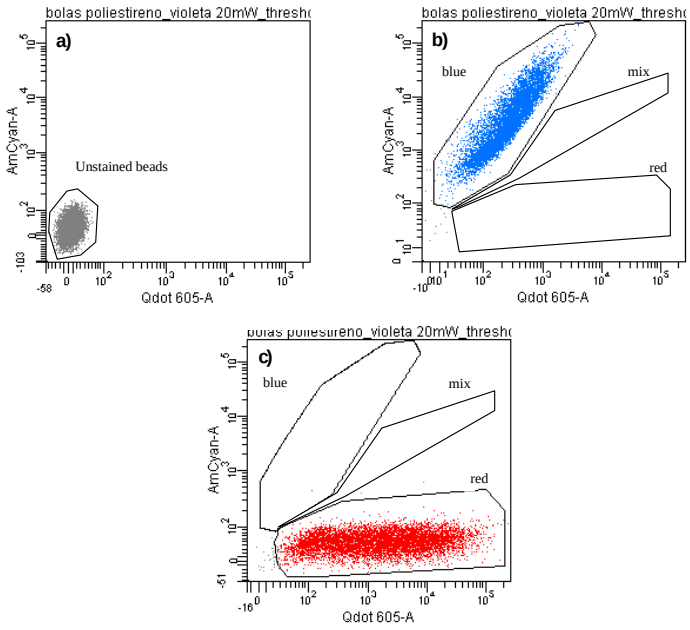

Figure 5. *Flow Cytometer results from a) PS beads, b) PS-blue, c) PS-red.*

Figure 6 shows the case for the PS-mix (Figure 6a) where the fluorescence can be found in the intersection between AmCyan and Qdot605, as there is signal form both type of QDs. The intensity in both cases is quite similar.

Finally, in Figure 6b all of the different samples were mixed and measured, at the same time, with the cytometer corroborating our theory; it is possible to elucidate different populations of PS (stained and not stained) in the same mixture at the same time, using only one source for excitation. It is worth pointing out that only a 405 nm laser was used for all the assays, while most reported systems require two or more for multiplex detection. [20]

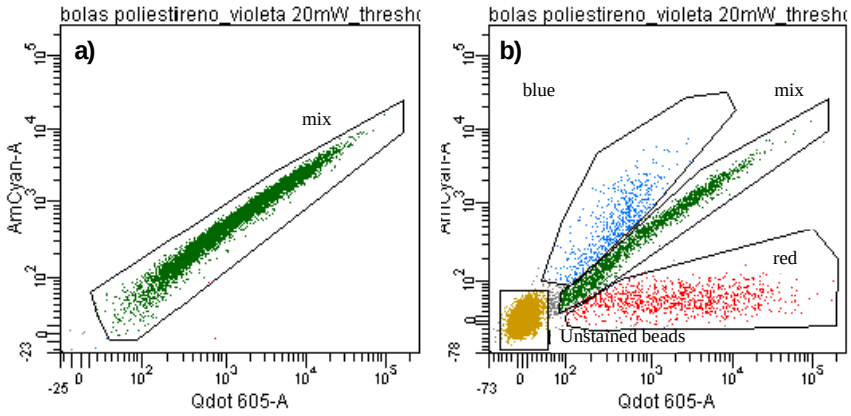

Figure 6. *Flow cytometer results for a) PS-mix and b) after the mixture of every population.*

We also analyzed the pellets by true color fluorescence (Figure 7 and 8) showing the fluorescence of each one of the quantum dots. The blue emission (λ=490 nm) is shown in Figure 7b for the PS-Blue beads and Figure 8b in the case of the PS-mix and the red emission (λ=625 nm) is depicted in Figure 7c and 8c.

In all of the cases the fluorescence seems to come from the surface of the beads, it is only around the beads.

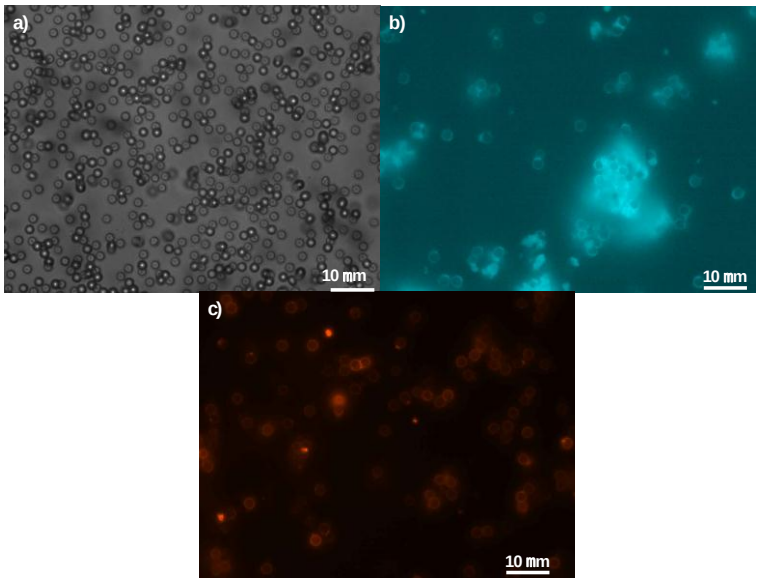

Figure 7. *True color fluorescence microscope images of a) Unstained PS-beads b) PS-Blue and c) PS-red*

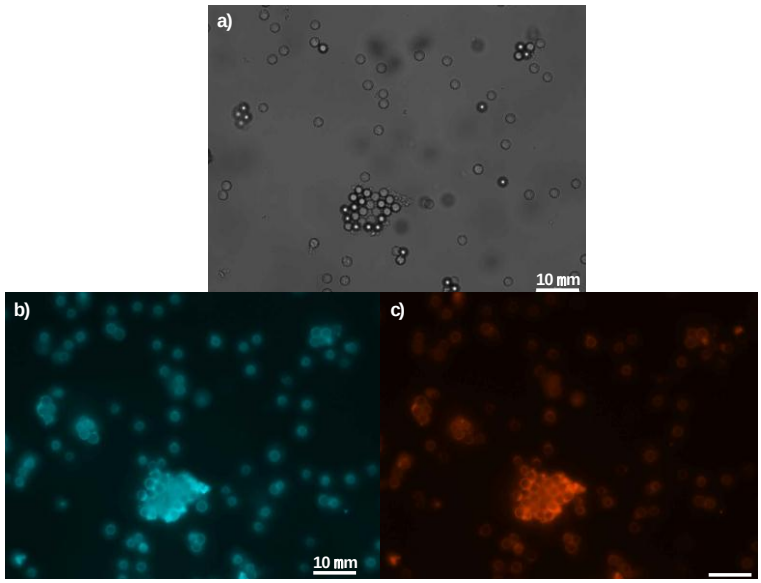

Figure 8. *True color fluorescence microscope images PS- mix showing a) No fluorescence image b) emission at λ=490 nm and c) emission at λ=625 nm*

After demonstrating that the different fluorescent populations could be identified at the same time using flow cytometry with only one source of excitation, the next step of our experiments lead to the conjugation of a TAMRA-labeled peptide (NH_2-Cys-Lys-Arg-Val-Lys-TAMRA) to the different beads to functionalize them and to add an extra fluorescent signal (TAMRA λ_{em}=580 nm).

It has been demonstrated that trypsin can cut the peptide sequence we choose by the Arginine aminoacid, causing the separation of TAMRA from the bead it was attached to. This will lead to a decrease or disappearance of the TAMRA fluorescent signal depending on the concentration of added trypsin. .
In this case an extra yellow laser was needed to measure the samples by flow cytometry (as TAMRA does not absorb at 405 nm) and will be read in the PE-YG channel.

Figure 9 depicts the different flow cytometry signals obtained in each case. For the PS-blue-TAMRA (Figure 9a), the signal can be observed in both the AmCyan channel as well as in the PE-YG channel, so the peptide functionalization was effective. The same was observed for the PS-red-TAMRA (Figure 9b), with good signal of stained beads in the Qdot-605 and PE-YG channel.

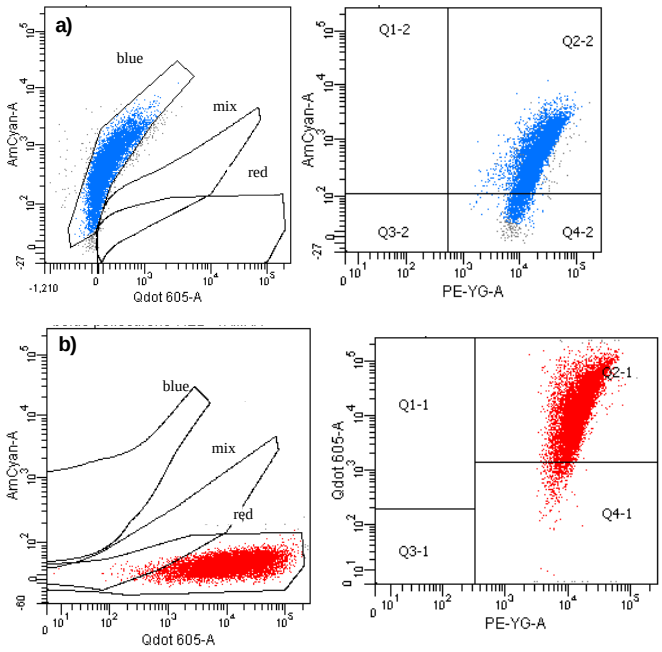

Figure 9. *Flow cytometer results for a) PS-blue-TAMRA and b) PS-red-TAMRA.*

Finally, in the case of the PS-mix-TAMRA (Figure 10) there is a signal in the intersection of the AmCyan and Qdot 605 for both QDs as well in the channel with a positive sign for TAMRA.

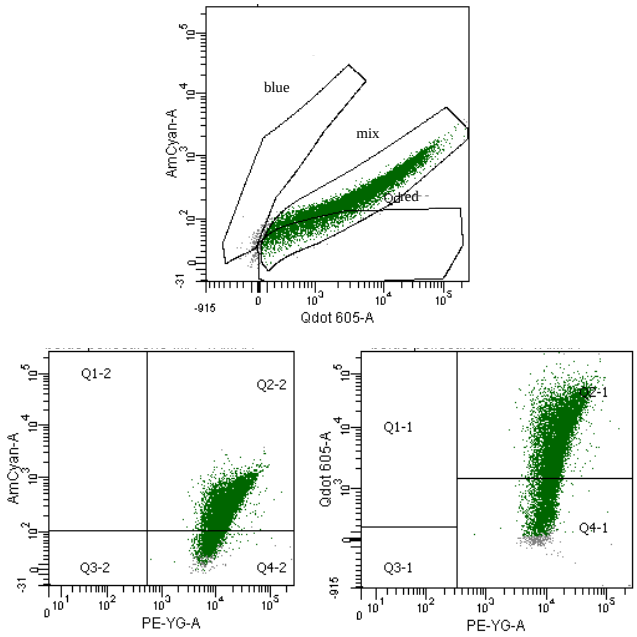

Figure 10. *Flow cytometer results after the conjugation of the peptide-TAMRA with PS-mixture.*

In all cases, the intensity of TAMRA signal is higher than the one coming from the QDs, so with only 4 μg/mL it could be detected, making us realize that we could use less concentration to determine the lower limit of detection and work with less peptide-TAMRA concentration.

These results confirm that the combination QDs-fluorochromes can be detected by flow cytometry and opens new possibilities for the detection and determination of different biological compounds. In this sense, we are currently developing this work and complementing the cystic fibrosis sensor reported previously by our group[21].

The system was formed by a red QD@SiO_2@greenQD-peptide-TAMRA. The Förster Energy Transfer (FRET) effect between the green QD and TAMRA was studied using a red QD as an internal reference. Initially, the green QD will absorb the light and instead of emitting it, the energy will be transferred to TAMRA, producing a reduction in the green QD emission and increase in the TAMRA signal. But if the sample is incubated with trypsin, the peptide will be cleaved and the FRET process will be disrupted, so after washing, depending on the concentration of trypsin, the

emission of the green QD had to increase and the signal from TAMRA decrease or disappear, while the red emission remained unmodified.

The difference is that in this case we will not use FRET and we do not need an internal reference, as the signal from the QDs will not be affected.
We will be able to analyze qualitatively as well as quantitatively the trypsin effect for its use as a detector of cystic fibrosis.
Preliminary studies showed (Figure 11) that we could modify the TAMRA signal depending on the concentration of trypsin, however, more studies are required in order to validate the method.

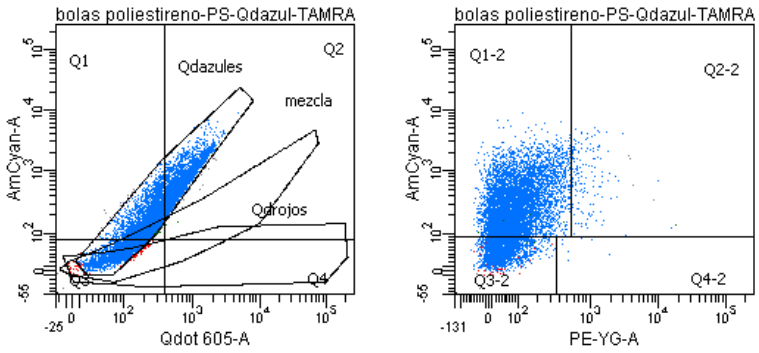

Figure 11. *Flow cytometer results after the incubation of 150.000 µg/L of trypsin with PS-blue*

4. Conclusions

A new, simple and cheap method to encapsulate QDs has been presented, with the possibility of controlling, up to a certain degree, the internalization process, resulting from the electrostatic forces that control the encapsulation like the method of Sheng et al.[22]
Other methods, like the one described by Han et al.[23] have the disadvantage that the degree of incorporation will change every time, because the PS beads were chemically swollen, what is impossible to control.

This structure was used to discriminate between several populations of PS beads marked with QDs with different emission.

If all the populations were mixed in the same container and passed through the flow cytometer, with the use of only one laser (405 nm), all of them could be identified by color and separated.

Another possibility theorized was the use of these beads as a detector for cystic fibrosis, as it is was proven that the beads could also be functionalized with the active peptide previously used, that after being cut with trypsin will produce a modification in the intensity of the TAMRA signal. The variation in signal can be correlated afterwords with the different CF profiles (CF homozygotic, heterozygotic or normal).

Different incubation experiments of the PS-QDs-TAMRA with trypsin have been done, showing one of them, and the results are promising, but it has to be studied to a larger degree before it can be assured that it is a possible detection method for cystic fibrosis.

References

1. Henel, G. & Schmitz, J. Basic Theory and Clinical Applications of Flow Cytometry. *Lab. Med.* **38,** 428–436 (2007).

2. Bele, M., Siiman, O. & Matijević, E. Preparation and flow cytometry of uniform silica-fluorescent dye microspheres. *J. Colloid Interface Sci.* **254,** 274–282 (2002).

3. Chattopadhyay, P. K. *et al.* Quantum dot semiconductor nanocrystals for immunophenotyping by polychromatic flow cytometry. *Nat. Med.* **12,** 972–7 (2006).

4. Li, J., Zhao, X.-W., Zhao, Y.-J. & Gu, Z.-Z. Quantum-dot-coated encoded silica colloidal crystals beads for multiplex coding. *Chem. Commun. (Camb).* 2329–31 (2009). doi:10.1039/b823173g

5. Wu, X. *et al.* Immunofluorescent labeling of cancer marker Her2 and other cellular targets with semiconductor quantum dots. *Nat. Biotechnol.* **21,** 41–6 (2003).

6. Hötzer, B., Medintz, I. L. & Hildebrandt, N. Fluorescence: Fluorescence in Nanobiotechnology: Sophisticated Fluorophores for Novel Applications (Small 15/2012). *Small* **8,** 2290–2290 (2012).

7. Roederer, M. Spectral compensation for flow cytometry: visualization artifacts, limitations, and caveats. *Cytometry* **45,** 194–205 (2001).

8. Chattopadhyay, P. K. *Quantum Dot Technology in Flow Cytometry*. *Methods in Cell Biology* **102,** (Elsevier Inc., 2011).

9. Ho, Y.-P. & Leong, K. W. Quantum dot-based theranostics. *Nanoscale* **2,** 60–8 (2010).

10. Jamieson, T. *et al.* Biological applications of quantum dots. *Biomaterials* **28,** 4717–32 (2007).

11. Mumin, M. A., Xu, W. Z. & Charpentier, P. A. Quantum dots/silica/polymer nanocomposite films with high visible light transmission and UV shielding properties. *Nanotechnology* **26,** 315702 (2015).

12. Yoon, C. *et al.* Highly luminescent and stable white light-emitting diodes created by direct incorporation of Cd-free quantum dots in silicone resins using the thiol group. *J. Mater. Chem. C* **3,** 6908–6915 (2015).

13. Liu, J. *et al.* Toxicity assessment of phospholipid micelle-encapsulated cadmium-based quantum dots using Kunming mice. *RSC Adv.* **3,** 1768 (2013).

14. Su, Y. *et al.* The cytotoxicity of cadmium based, aqueous phase - synthesized, quantum dots and its modulation by surface coating. *Biomaterials* **30,** 19–25 (2009).

15. Serrano, I. C., Ma, Q. & Palomares, E. QD-'Onion'-Multicode silica nanospheres with remarkable stability as pH sensors. *J. Mater. Chem.* **21,** 17673–17679 (2011).

16. Han, M., Gao, X., Su, J. Z. & Nie, S. Quantum-dot-tagged microbeads for multiplexed optical coding of biomolecules. *Nat. Biotechnol.* **19,** 631–5 (2001).

17. Decher, G. & Hong, J. D. Buildup of Ultrathin Multilayer Films by a Self-Assembly Process: II. Consecutive Adsorption of Anionic and Cationic Bipolar Amphiphiles and Polyelectrolytes on Charged Surfaces. *Berichte der Bunsengesellschaft für Phys. Chemie* **95,** 1430–1434 (1991).

18. Donath, E., Sukhorukov, G. B., Caruso, F., Davis, S. A. & Möhwald, H. Novel Hollow Polymer Shells by Colloid-Templated Assembly of Polyelectrolytes. *Angew. Chemie Int. Ed.* **37,** 2201–2205 (1998).

19. Schnäckel, A., Hiller, S., Reibetanz, U. & Donath, E. Fluorescent bead arrays by means of layer-by-layer polyelectrolyte adsorption. *Soft Matter* **3,** 200–206 (2007).

20. Perfetto, S. P., Chattopadhyay, P. K. & Roederer, M. Seventeen-colour flow cytometry: unravelling the immune system. *Nat. Rev. Immunol.* **4,** 648–655 (2004).

21. Castelló Serrano, I., Stoica, G., Matas Adams, A. & Palomares, E. Dual core quantum dots for highly quantitative ratiometric detection of trypsin activity in cystic fibrosis patients. *Nanoscale* **6,** 13623–13629 (2014).

22. Sheng, W. *et al.* In-Situ Encapsulation of Quantum Dots into Polymer Microspheres. *Langmuir* **22,** 3782–3790 (2006).

23. Han, M., Gao, X., Su, J. Z. & Nie, S. Quantum-dot-tagged microbeads for multiplexed optical coding of biomolecules. *Nat. Biotechnol.* **19,** 631–635 (2001).

UNIVERSITAT ROVIRA I VIRGILI
SEMICONDUCTOR NANOPARTICLES AS PLATFORM FOR BIO-APPLICATIONS AND ENERGY RELATED SYSTEMS.
Alba María Matas Adams
Dipòsit Legal: T 55-2016

Chapter 3

Dual core Quantum Dots for highly quantitative ratiometric detection of trypsin activity

UNIVERSITAT ROVIRA I VIRGILI
SEMICONDUCTOR NANOPARTICLES AS PLATFORM FOR BIO-APPLICATIONS AND ENERGY RELATED SYSTEMS.
Alba María Matas Adams
Dipòsit Legal: T 55-2016

1. Introduction

The detection of human recessive diseases has been dominated by the use of organic dyes fluorescent biomarkers, helping researchers to study and analyze gene expression[1], cell cycle [2], and enzymatic activity.[3]

Among several proteolytic enzymes, trypsin has attracted much attention, as it is a target in the study of various important human recessive diseases including, for example, cystic fibrosis (CF).[4]

Recent advances in the field of nanoscience and the evaluation of enzyme proteolytic processes have taken advantage of short peptide substrates,[5,6] that can be specifically cleaved by trypsin[7] allowing a new route to analyze and trace enzymatic activity, and therefore, its concentration in human serum, blood or tissues.

However many of these studies[8,9] resulted just on qualitative data for the presence of the homozygous recessive genotype (the individuals with the disease) and, moreover, cannot differentiate between heterozygotic human carriers (those individuals that carry an allele for the disease but do not express it) and the unaffected persons.

Of particular interest, in these bio-analytical systems, is the use of Förster Resonance Energy Transfer (FRET)[10–12], a process that involves two fluorophores where, initially, one of the fluorophores can transfer energy to the second one. These pair of fluorophores are known as energy donor and energy acceptor pair, respectively.

The efficiency of this energy transfer process is inversely proportional to the sixth power of the distance between donor and acceptor making FRET extremely sensitive to short distances between the two fluorophores[13–15].

Pioneering work by other research groups has focussed on QD-QD[16], QD-dye[17], QD-dye-dye (in a two-step FRET process[18–20] or dual-donor FRET[21,22] systems), rare earth-QD-dye[23], or QD-plasmonic nanoparticles.[24,25] Besides, the use of peptide-conjugated quantum dots proved to be successful for proteolytic enzyme assays.[10,18]

We took this approach one step further by protecting the quantum dots by silica shells[26] and including a fixed standard probe inside the nanosensor, thus upgrading the properties of the system from qualitative sensing to accurate ratiometric determination of enzymatic activity. Due to the properties of quantum dots and the efficiency of the FRET process, our system can be used as an excellent probe for

trypsin assay as an alternative for the traditional approaches of CF diagnosis[27] and other pancreatic-related diseases.

Pancreatic insufficiency (PI) is commonly associated with diseases such as cystic fibrosis (the most common cause) or pancreatitis, in which the patients have a shortage of the digestive enzymes necessary to break down food. Besides, certain gastrointestinal diseases, such as stomach ulcers and Crohn's disease may also induce PI. However, all these diseases have their own clinical and genetic features in addition to the biochemical markers. For example, trypsin concentration is always lower in cystic fibrosis than in Crohn's disease.[28] Fecal chymotrypsin and fecal elastase 1 (FE1) are another biochemical markers used to determine exocrine PI.[29] Both trypsin and chymotrypsin are exclusively of pancreatic origin, and their quantitative measurement can be used to indicate pancreatic function. FE1 is not affected by bacterial degradation (as trypsin or chymotrypsin) or pancreatic enzyme supplementation, thus being useful to determine the pancreatic function in CF. However, low FE1 levels can occur in children with short gut syndrome as well as patients with the Shwachman-Diamond syndrome who otherwise have normal pancreatic function.[30] Therefore, the trypsin test is a promising method to help detect CF in symptomatic newborns or infants, or anyone to determine whether a person is a CF carrier (*i.e.* has a CF gene mutation).

Early diagnosis of cystic fibrosis has the potential to dramatically improve the life quality and survival of millions of people dealing with this chronic illness, of genetic origins, by developing early and personalized treatment, preventing malnutrition and allowing access to counseling.

Many countries have established a default screening for newborns that involves quantifying trypsinogen in the blood of the babies (immunoreactive trypsinogen test, or IRT), which typically makes use of fluorescent-based immunoassays. However, these tests still have the drawbacks of specificity, time-effectiveness and user-friendliness. Additionally, due to a considerable percentage of false positives inherent to this test, babies with abnormal results must have to be either tested again for IRT or, alternatively, undergo genetic testing to determine whether they have at least one mutated copy of the cystic fibrosis gene (human carriers).[31,32]

Infants with a second abnormal newborn IRT screen or carrier genotype need a sweat test to confirm the cystic fibrosis diagnosis. Sweat testing however cannot be performed accurately in the first days after birth, and it may be difficult to obtain an adequate sweat sample during the first two to three weeks after birth, especially for premature babies. If the volume of sweat obtained is inadequate, the test should be repeated. The overall procedure is long (weeks to months) and sometimes considered invasive by the parents.[33]

We present herein a well-designed and cost effective nanosystem, based on FRET, using an internal reference that unequivocally permits the ratiometric determination of trypsin in the range of enzyme concentrations relevant for clinical diagnosis of cystic fibrosis in minutes, with high sensitivity. Our method provides specific information about whether or not the individuals are CF carriers (heterozygotic genotype), as well as about the risk of having a child affected with CF (homozygotic genotype). CF is the most life threatening recessive genetic condition affecting Caucasian children and diagnosis often comes at a point when significant and irreversible damage has already occurred. The challenge is to develop a detection method that will allow for early diagnosis and treatment with sufficient time to adopt lifestyle changes or use agents to prevent or retard disease development.

A short peptide substrate previously marked with TAMRA, a Rhodamine-derived (carboxy-tetramethyl-rhodamine) dye with fluorescence emission at λ = 575 nm, (see Scheme 1) is anchored to the surface of a silica nanosphere containing two types of CdSe quantum dot nanocrystals with different fluorescence emission wavelengths.

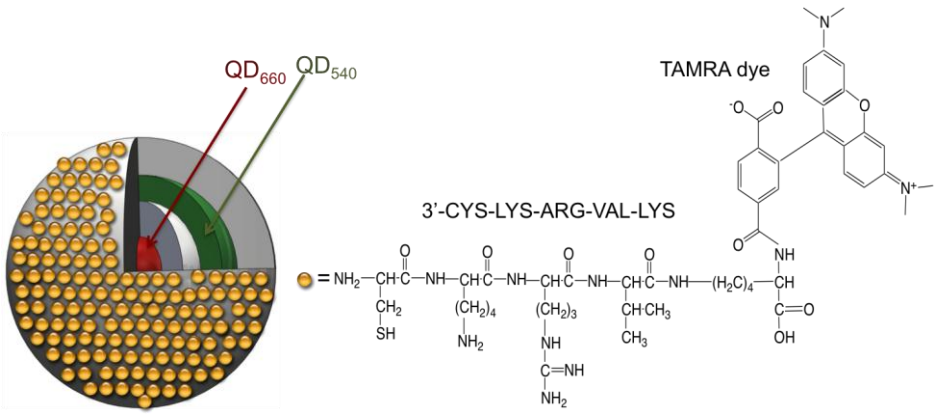

Scheme 1. *Pictorial description of the 2nanoSi system with QD_{660} (red) at the core of the nanosilica sphere, QD_{540} (green) at the silica coating layer and the attached small TAMRA-labeled peptide on the outer surface of the silica coating layer.*

2.Experimental

2.1 Synthesis of QD. The procedure to obtain red CdSe QDs was using TOPO-TOP as capping ligand.

A selenium precursor was prepared by mixing 0.058 gr of selenium powder with 434 mL of trioctyl phosphine (TOP) and stirred under argon. A mixture of 3 gr of trioctyl phosphine oxide (TOPO), 0.060 gr of cadmium oxide (CdO) and 0.280 gr of octadecylphosphonic acid (ODPA) were placed in a round-bottomed flask, stirred and heated to 150ºC under argon and after 2 hours, the temperature was increased to 300ºC. When the mixture turned colorless, 1.5 gr of TOP were injected and then the temperature was raised up to 370ºC.

When the mixture reached 370ºC the selenium precursor was quickly injected. The reaction was run for 5 min and then cooled down to 100ºC. After stopping the reaction, samples were cooled and washed with chloroform and acetone three times and stored in chloroform.

To obtain green CdSe QDs the synthesis was modified. The selenium precursor was prepared mixing 0.118 gr of selenium powder with 1 mL of TOP, while in a different flask 0.128 mg of CdO, 20 mL of octadecene (ODE) and 2 mL of oleic acid were degassed for 10 min. After that period of time, the temperature was raised up to 240ºC under Ar. When the solution was clear, 0.34 mL of the selenium precursor were quickly injected and left 90 sec to allow the growth of the QDs. After stopping the reaction, samples were cooled and washed with chloroform and acetone three times and stored in chloroform.

2.2 Synthesis of QD@silica nanospheres. The experiments were performed using CdSe core quantum dots with emission wavelength at 540 nm (green, d=2.7 nm) and 660 nm (red, d=5.6 nm). Next, single and two colors quantum dots embedded silica nanospheres, *i.e.* QD_{540}@silica and QD_{660}@silica@QD_{540}@silica, respectively, were prepared by the reverse microemulsion method as detailed elsewhere.[34,35] An amine functionalization was done adding 30 µL of APTMS ((3-aminopropyl)-trimethoxysilane) and 80 µL of THPM (3-(trihydroxysilyl)propyl methylphosphonate) to the reaction and leaving to stir for 24 hours at room temperature.

2.3 Peptide-functionalization of QD@silica nanospheres. The positive surface of the QD_{540}@silica nanospheres (given by APTMS) was functionalized with two different TAMRA-labelled peptides:

Pro-active: NH_2-Cys-Lys-Arg-Val-Lys-TAMRA

In-active: NH_2-Cys-Lys-Pro-Val-Lys-TAMRA

The two different sequences TAMRA-labelled peptides were particularly designed for our study by BIOTREND.

Glutaraldehyde was used to bind the amine functional groups of the peptides with the amine groups of the silica nanospheres surface as described in the following methodology. 2 mL of QD_{540}@silica-APTMS in PBS and 0.25 mL of glutaraldehyde (0.25 mg/mL) were mixed and shaked for 4 h at 37 ºC. Then the solution was centrifuged to remove the unreacted glutaraldehyde, washed and finally the pellet was resuspended in PBS. A determined amount of TAMRA-labelled peptides was added and shaked for 20 hours at 4ºC. After this time, the solution was centrifuged to remove the unbound peptides. In the end, the TAMRA-labelled peptide-functionalized QD@silica nanospheres were resuspended in 5 mL and stored in PBS.

2.4 Enzymatic digestion. A determined concentration of trypsin between 25-350 μg/L was added to the labelled peptides-nanospheres and mixed for a period of time: from 30 sec to 120 min, at 37 ºC. After this time, the mixture was heated up to 70ºC and held for 1 h in order to denaturalize the enzyme and stop the reaction. If not measured immediately after the enzymatic digestion, it is recommended to keep the samples in the freezer until the analysis.

3.Results and discussion

In brief, the 2nanoSi system consists of a 77 nm silica nanosphere with a nanocrystal CdSe ($CdSe_{660}$) core with luminescence emission maximum at λ = 660 nm, and a second shell of silica embedding the second type of CdSe nanocrystal with luminescence emission maxima at λ = 540 nm ($CdSe_{540}$). Upon light excitation at λ = 405 nm, both types of CdSe quantum dots undergo fluorescence emission. Moreover, due to the FRET process between the $CdSe_{540}$@2nanoSi, as energy donor, and the TAMRA dye, as energy acceptor, it is possible to register TAMRA fluorescence emission at λ = 575 nm. Control experiments show negligible emission

of TAMRA upon excitation at λ = 405 nm (see Fig. A6 annex). In the presence of trypsin, the proteolytic activity of the enzyme leads to the cleavage of the peptide and the FRET process is disrupted. Thus, by measuring the signal increase at λ = 540 nm, that corresponds to the $CdSe_{540}$@2nanoSi, it is possible to correlate the changes in the emission intensity with the enzyme activity using an internal reference, which fluorescence emission remains constant through the proteolytic process.

The use of a single quantum dot fluorophore in our system (1nanoSi, Fig. A1 and A2 annex) already allowed for the qualitative analysis of the trypsin proteolytic activity. Nonetheless, a key figure of merit of our approach is to be able to quantify the enzymatic activity and, thus, the use of an internal reference in our fluorescence system. In this case, the internal reference is the $CdSe_{660}$@2nanoSi (Fig. A7 annex) with fluorescence emission at λ = 660 nm. Hence, the reference $CdSe_{660}$ material has the advantage of not being influenced by the TAMRA concentration and the excitation intensity as it occurs with commercial immuno-fluorescence intensity based measurements. FRET is observed when "donor" and "acceptor" are sufficiently close one to another and when there is sufficient spectral overlap between the emission spectrum of the donor and absorption spectrum of acceptor. The average distance between TAMRA and $CdSe_{660}$ is more than 40 nm, while the photoluminescence emission spectrum of the label and the photoluminescence absorption spectrum of the first QD population ($CdSe_{660}$) has a spectral overlap below 30% area/area, conditions which effectively precludes FRET between the label (as donor) and the $CdSe_{660}$ (as acceptor).

Thus, the use of two QDs fluorophores with distinguishable emission spectra allows us to establish a measurable ratio, namely, I_{540}/I_{660}. Moreover, the emission intensity at λ = 660 nm remains constant as the QD_{660} at the silica nanospheres does not influence the FRET process. The key feature in our 2nanoSi is that, due to the absorption properties of the nanocrystal quantum dots, both fluorophores can be excited at the same wavelength (λ = 405 nm), but only the nanocrystals in the outer layer emitting at 540 nm undergo FRET with the TAMRA dye. Despite the small overlap between the emission of QD_{660} and the absorption of TAMRA, the distance between them (around 38 nm) does not allow energy transfer to occur. On the other

hand, the distance and the overlap between QD_{540} and TAMRA are sufficient for FRET to occur.

Using TCSPC and steady-state emission spectroscopy, we determined a FRET efficiency of 47% between the QD_{540} and the TAMRA dye. The calculated R_0 (distance at which the efficiency of FRET is 50%) is 4.982 nm, and the distance between $CdSe_{540}$ and TAMRA dye (r) is 5.10 nm calculated from the fluorescence measurements.

Next, the number of TAMRA -labelled peptides attached to the silica nanosphere surface was found to be one via the Förster model.[36] For the complete calculations, see the annex. This result clearly indicates that with only one QD@silica – peptide-dye donor-acceptor pair, our system displays a remarkable FRET efficiency of approx. 50%. Previous studies with one pair QD donor – dye acceptor reported lower efficiency, *i.e.* 22%.[11] These authors required up to five acceptor molecules to increase the efficiency up to 58%.

Fig. 1 illustrates the changes in the fluorescence emission of 2nanoSi in the presence of two different trypsin concentrations, 25 µg/L (Fig. 1a) *versus* 350 µg/L (Fig. 1b**)**. As expected, increasing the enzyme concentration leads to faster recovery of the original emission at 540 nm (Fig. 1b). The complete enzyme concentration study can be found in Fig. A8 annex.

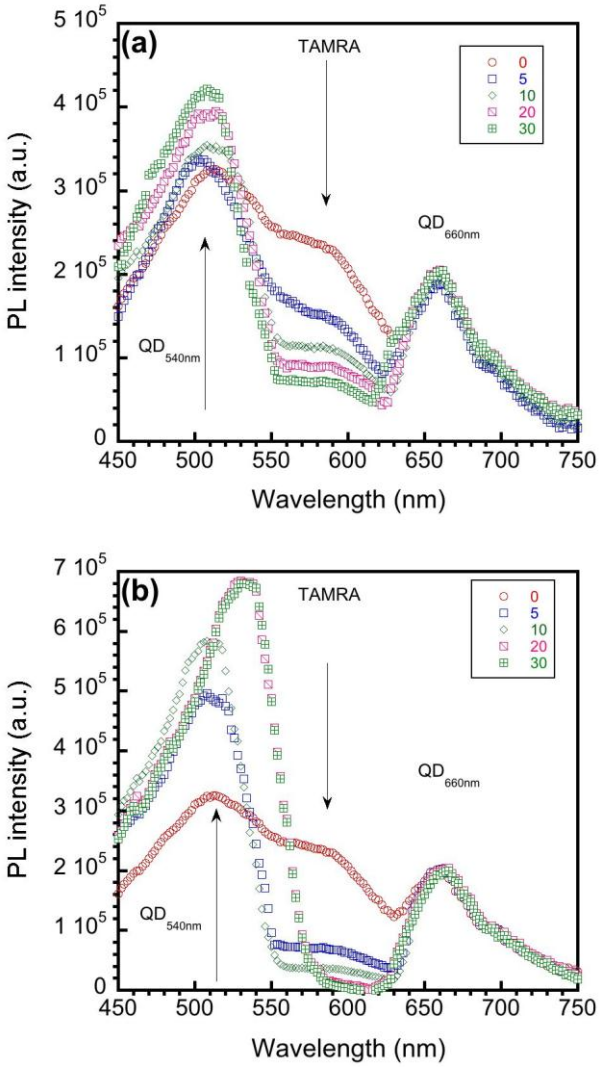

Figure 1. *2nanoSi emission spectra (a) after digestion with 25 μg/L of trypsin, and (b) after digestion with 350 μg/L. The figure legends correspond to the enzymatic digestion time in min (0-30 min).*

Trypsin concentration for the different cystic fibrosis genotypes is undeniably tissue-specific. Consequently, the trypsin concentration in fecal samples displays the following trend: CF-diagnosed 0 - 30 μg/g, while a non-CF medical check is above 80 μg/g.[37] On the other hand, the distribution of serum trypsin concentration in patients with cystic fibrosis,[38] is homozygotic (0-90 μg/L), normal (160-340 μg/L), and heterozygotic (91-349 μg/L), respectively. Coincidentally, the trypsin ranges in stool samples highly match those in blood, *i.e.* non-CF > 80 μg/g stool *versus* heterozygote and healthy > 90 μg/L blood.

Taking into account these values of trypsin, and considering the specificity of the 2nanoSi, we performed the study of the enzymatic digestion using the "*pro-active*" labelled peptide in a wide range of trypsin concentrations (25-350 μg/L) that fall in

the ranges found for CF patients mentioned above. Fig. 2 shows the ratio between the PL emission peaks of both QD_{540} and QD_{660} (I_{540}/I_{660}) during enzymatic digestion for 120 min in different enzyme concentrations. As expected, there is a direct relationship between the enzymatic digestion rate and the enzyme concentration that allowed us to unequivocally differentiate between the different enzyme concentrations used. In other words, the higher the trypsin concentration the shorter the time we need to reach a plateau in our kinetic measurements. Hence, analysing the trypsin activity at early digestion times using our 2nanoSi ratiometric system (for example 10 min) we can differentiate between the different trypsin concentrations as shown in Fig. 3.

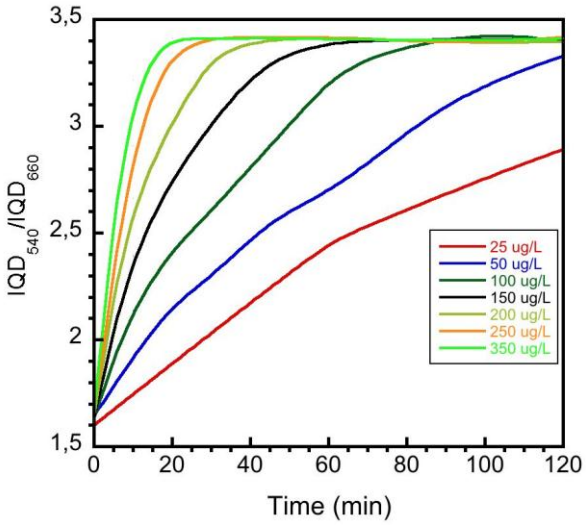

Figure 2. *Kinetics of the enzymatic digestion as a function of trypsin concentration using the ratio between PL emission peaks of both QD_{540} and QD_{660} at the 2nanoSi system.*

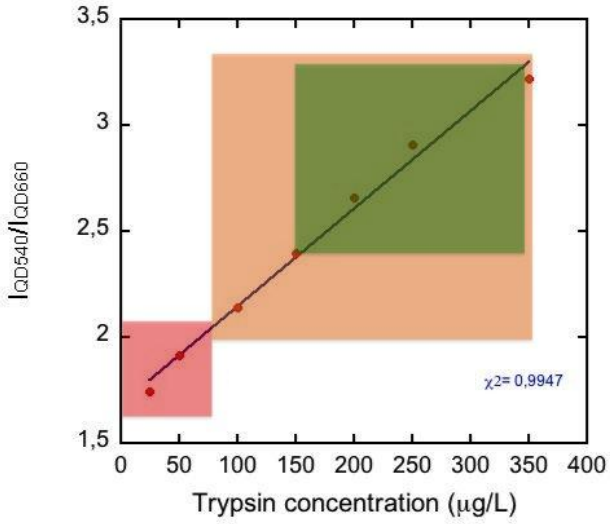

Figure 3. *Calibration curve resulting from fitting the fluorescence I_{540}/I_{660} experimental values from Fig. 2 at the enzyme digestion time of 10 min. Red, orange and green correspond to CF homozygotic, CF heterozygotic and normal, respectively.*

As it can be seen, the calibration curve proved to be highly linear (χ^2=0.99) and allowed us to determine the trypsin concentration at levels that are clinically relevant for the cystic fibrosis prognosis, *i.e.* CF homozygotic (0-90 μg/L) and non-CF (> 90 μg/L) including both CF heterozygotic and normal, respectively.

4.Conclusions

By combining the specificity of biomolecular interactions with the tunability of quantum dot and organic dye optical properties, we have developed for the first time a detection system capable of cystic fibrosis prognosis, both qualitatively and quantitatively. The trypsin enzymatic activity was reported via FRET process, which mediates changes in the quantum dot emission spectra, between the organic dye TAMRA (λ_{em} = 575 nm) and green CdSe quantum dots (λ_{em} = 540 nm). Cross-reactivity and signal overlap were avoided by designing enzyme-specific peptidic sequences. The 2nanoSi proved to be a fast and highly sensitive single-step nanosensor, allowing the quantification of trypsin concentrations in a wide range (25-350 μg/L), which is clinically relevant for the diagnosis of cystic fibrosis (CF). This range covers different human genotypes, *i.e.* CF homozygotic (0-90 μg/L) and CF heterozygotic (91-349 μg/L), respectively. The biomarker has been shown to provide

significant prognostic information, and hence represents a promising system for proof-of-concept demonstration of the proposed approach. We anticipate the 2nanoSi system to be a starting point for non-invasive, easy-to-use and cost effective ratiometric fluorescence biomarker for recessive genetic diseases alike human cystic fibrosis.

This work was also part of the thesis of Dr. Ivan Castelló Serrano, but while his work was centered in the study of real samples, I prepared the material and did the studies shown in the annex of this chapter.

References

1. Steuerwald, N. Analysis of gene expression in single oocytes and embryos by real-time rapid cycle fluorescence monitored RT-PCR. *Mol. Hum. Reprod.* **5,** 1034–1039 (1999).

2. Murray, A. W., Solomon, M. J. & Kirschner, M. W. The role of cyclin synthesis and degradation in the control of maturation promoting factor activity. *Nature* **339,** 280–6 (1989).

3. Hennig, A., Bakirci, H. & Nau, W. M. Label-free continuous enzyme assays with macrocycle-fluorescent dye complexes. *Nat. Methods* **4,** 629–32 (2007).

4. Antunovic, S. S., Lukac, M. & Vujovic, D. Longitudinal cystic fibrosis care. *Clin. Pharmacol. Ther.* **93,** 86–97 (2013).

5. Schilling, O. & Overall, C. M. Proteome-derived, database-searchable peptide libraries for identifying protease cleavage sites. *Nat. Biotechnol.* **26,** 685–94 (2008).

6. Thomas, D. A. *et al.* A broad-spectrum fluorescence-based peptide library for the rapid identification of protease substrates. *Proteomics* **6,** 2112–20 (2006).

7. Sapsford, K. E. *et al.* Monitoring of enzymatic proteolysis on a electroluminescent-CCD microchip platform using quantum dot-peptide substrates. *Sensors Actuators B Chem.* **139,** 13–21 (2009).

8. Chalfie, M., Tu, Y., Euskirchen, G., Ward, W. & Prasher, D. Green fluorescent protein as a marker for gene expression. *Science (80-.).* **263,** 802–805 (1994).

9. Martin Chalfie, S. R. K. *Methods of Biochemical Analysis, Green Fluorescent Protein: Properties, Applications and Protocols*. (2005). at <http://eu.wiley.com/WileyCDA/WileyTitle/productCd-0471736821.html>

10. Algar, W. R. *et al.* Proteolytic activity at quantum dot-conjugates: kinetic analysis reveals enhanced enzyme activity and localized interfacial 'hopping'. *Nano Lett.* **12,** 3793–802 (2012).

11. Medintz, I. L., Uyeda, H. T., Goldman, E. R. & Mattoussi, H. Quantum dot bioconjugates for imaging, labelling and sensing. *Nat. Mater.* **4,** 435–46 (2005).

12. Ho, Y.-P. & Leong, K. W. Quantum dot-based theranostics. *Nanoscale* **2,** 60–8 (2010).

13. Medintz, I. L. & Mattoussi, H. Quantum dot-based resonance energy transfer and its growing application in biology. *Phys. Chem. Chem. Phys.* **11,** 17–45 (2009).

14. Zhang, H., Feng, G., Guo, Y. & Zhou, D. Robust and specific ratiometric biosensing using a copper-free clicked quantum dot-DNA aptamer sensor. *Nanoscale* **5,** 10307–15 (2013).

15. Chatterjee, S., Lee, J. B., Valappil, N. V, Luo, D. & Menon, V. M. Probing Y-shaped DNA structure with time-resolved FRET. *Nanoscale* **4,** 1568–71 (2012).

16. Chen, C.-Y. *et al.* Potassium ion recognition by 15-crown-5 functionalized CdSe/ZnS quantum dots in H2O. *Chem. Commun. (Camb).* 263–5 (2006). doi:10.1039/b512677k

17. Kim, G. B. & Kim, Y.-P. Analysis of Protease Activity Using Quantum Dots and Resonance Energy Transfer. *Theranostics* **2,** 127–138 (2012).

18. Medintz, I. L. *et al.* Self-assembled nanoscale biosensors based on quantum dot FRET donors. *Nat. Mater.* **2,** 630–8 (2003).

19. Yang, L. & Li, Y. Simultaneous detection of Escherichia coli O157:H7 and Salmonella Typhimurium using quantum dots as fluorescence labels. *Analyst* **131,** 394–401 (2006).

20. Alam, R., Zylstra, J., Fontaine, D. M., Branchini, B. R. & Maye, M. M. Novel multistep BRET-FRET energy transfer using nanoconjugates of firefly proteins, quantum dots, and red fluorescent proteins. *Nanoscale* **5,** 5303–6 (2013).

21. Zhang, H. & Zhou, D. A quantum dot-intercalating dye dual-donor FRET based biosensor. *Chem. Commun. (Camb).* **48,** 5097–9 (2012).

22. Ouadahi, K., Sbargoud, K., Allard, E. & Larpent, C. FRET-mediated pH-responsive dual fluorescent nanoparticles prepared via click chemistry. *Nanoscale* **4,** 727–32 (2012).

23. Algar, W. R. *et al.* Multiplexed tracking of protease activity using a single color of quantum dot vector and a time-gated Förster resonance energy transfer relay. *Anal. Chem.* **84,** 10136–46 (2012).

24. Lowe, S. B., Dick, J. A. G., Cohen, B. E. & Stevens, M. M. Multiplex sensing of protease and kinase enzyme activity via orthogonal coupling of quantum dot-peptide conjugates. *ACS Nano* **6,** 851–7 (2012).

25. Xavier, P. L., Chaudhari, K., Verma, P. K., Pal, S. K. & Pradeep, T. Luminescent quantum clusters of gold in transferrin family protein, lactoferrin exhibiting FRET. *Nanoscale* **2,** 2769–76 (2010).

26. Stoica, G. *et al.* Layered double hydroxides as carriers for quantum dots@silica nanospheres. *Nanoscale* **4,** 5409–19 (2012).

27. Heeley, A. & Watson, D. Cystic fibrosis--its biochemical detection. *Clin. Chem.* **29,** 2011–2018 (1983).

28. Midtvedt, T. *et al.* Increase of faecal tryptic activity relates to changes in the intestinal microbiome: analysis of Crohn's disease with a multidisciplinary platform. *PLoS One* **8,** 66074 (2013).

29. Leus, J., Van Biervliet, S. & Robberecht, E. Detection and follow up of exocrine pancreatic insufficiency in cystic fibrosis: a review. *Eur. J. Pediatr.* **159,** 563–568 (2000).

30. Beharry, S., Ellis, L., Corey, M., Marcon, M. & Durie, P. How useful is fecal pancreatic elastase 1 as a marker of exocrine pancreatic disease? *J. Pediatr.* **141,** 84–90 (2002).

31. Inc, P. DELFIA® Neonatal IRT Kit (S&S 903). (2009). at <http://www.perkinelmer.com/catalog/product/id/a005-110>

32. Lindau-Shepard, B. a. & Pass, K. a. Newborn screening for cystic fibrosis by use of a multiplex immunoassay. *Clin. Chem.* **56,** 445–450 (2010).

33. Mishra, A., Greaves, R. & Massie, J. The relevance of sweat testing for the diagnosis of cystic fibrosis in the genomic era. *Clin. Biochem. Rev.* **26,** 135–53 (2005).

34. Serrano, I. C., Ma, Q. & Palomares, E. QD-'Onion'-Multicode silica nanospheres with remarkable stability as pH sensors. *J. Mater. Chem.* **21,** 17673–17679 (2011).

35. Ma, Q., Serrano, I. C. & Palomares, E. Multiplexed color encoded silica nanospheres prepared by stepwise encapsulating quantum dot/SiO2 multilayers. *Chem. Commun.* **47,** 7071–7073 (2011).

36. Clapp, A. R. *et al.* Fluorescence resonance energy transfer between quantum dot donors and dye-labeled protein acceptors. *J. Am. Chem. Soc.* **126,** 301–10 (2004).

37. Barbero, G. J. Stool Trypsin and Chymotrypsin. *Am. J. Dis. Child.* **112,** 536–540 (1966).

38. Dandona, P., Hodson, M. E. & Batten, J. C. beta Cell reserve in cystic fibrosis patients and heterozygotes. *J. Clin. Pathol.* **36,** 790–792 (1983).

Annex I
Chapter 3

UNIVERSITAT ROVIRA I VIRGILI
SEMICONDUCTOR NANOPARTICLES AS PLATFORM FOR BIO-APPLICATIONS AND ENERGY RELATED SYSTEMS.
Alba María Matas Adams
Dipòsit Legal: T 55-2016

Analysis of trypsin activity using single colour quantum dot@silica-FRET nanosensors (1nanoSi): Proof-of-concept.

Figure A1 shows the photoluminescence (PL) absorption-emission profiles of the TAMRA dye and the QD_{540} quantum dots, respectively. The fluorescence emission from the QD_{540} overlaps very well with the absorption peak of TAMRA thus allowing the FRET process.[1,2]

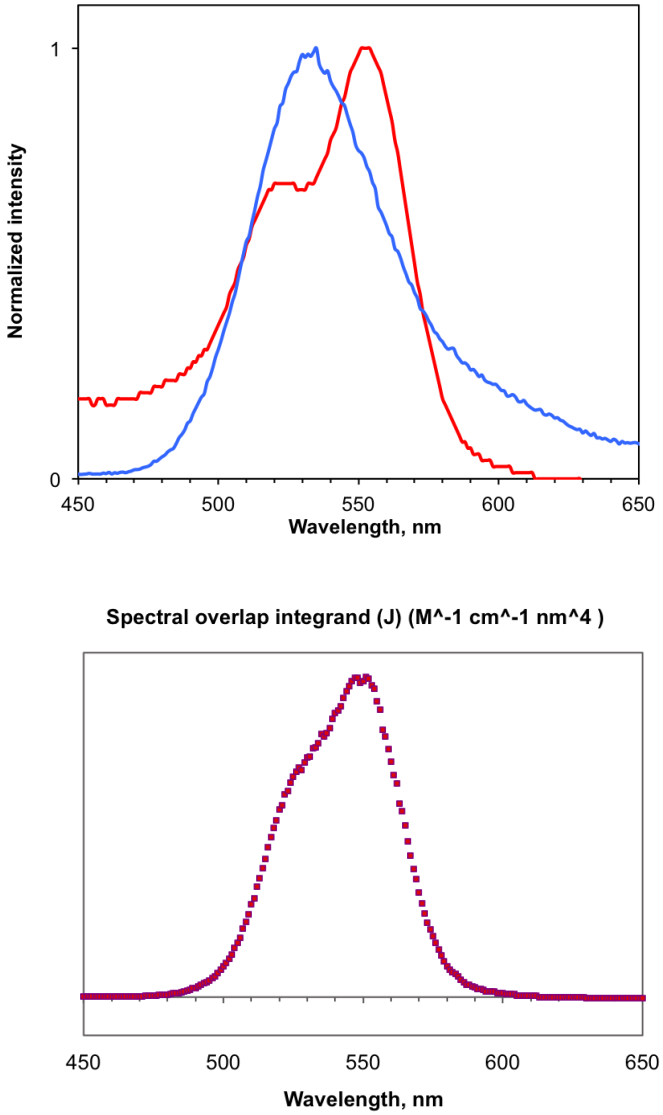

Figure A1. *Top, absorption of 5'-TAMRA (red) and emission spectra of QD_{540} quantum dots (blue), and their corresponding spectral overlap (bottom).*

Once the overlap between QD_{540} and the fluorescent dye was confirmed, we carried out the encapsulation of quantum dots and the assembling between the QD@silica nanospheres and the TAMRA-labelled peptide. Thereafter, we performed the enzyme

digestion using trypsin and read-out the emission of the 1nanoSi system. We used two different labelled peptides in order to obtain a control sample for our experiments.

On one hand, the "*pro-active*" labelled peptide has the following sequence: 3'-NH_2-Cys-Lys-Arg-Val-Lys-TAMRA-5'. Trypsin proteolytic activity is highly specific to the Lys-Arg-Val sequence and the enzyme digestions will cleave the peptide. On the other hand, our control sample, the "*in-active*" labelled peptide has the same chemical nature except for a change by Proline (Pro) instead of Arginine (Arg). Needless to say that trypsin cannot digest the small "*in-active*" peptide and the 1nanoSi fluorescence emission properties will remain the same.

The 1nanoSi system was incubated with trypsin for the peptide digestion, and the recorded emission spectra are shown in Fig. A2. The spectroscopic profiles further demonstrated the existence of FRET processes between the QD_{540}@silica nanospheres and the "*pro-active*" TAMRA-labelled peptide (Fig. A2a). Moreover, our control sample with the "*in-active*" 1nanoSi system, as expected, does not show any significant change in the fluorescence emission spectra (Fig. A2b).

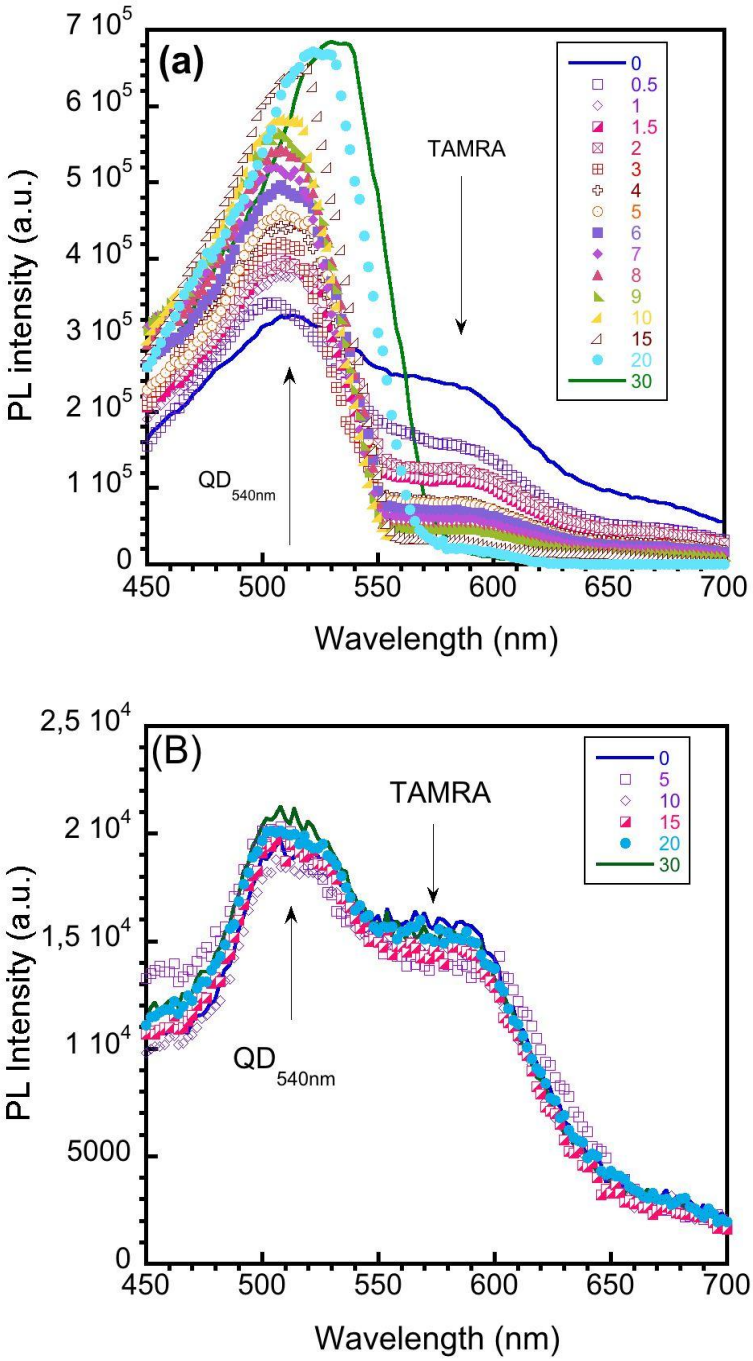

Figure A2. *Emission spectra of 5'TAMRA-labelled peptide-functionalized QD_{540}@silica nanospheres after trypsin digestion (a) the "pro-active" 1nanoSi and (b) the "in-active" 1nanoSi. The 1nanoSi system was incubated with trypsin (250 μg/mL) and the figure legends correspond to the enzymatic digestion time in minutes (0-30 min).*

Fig. A3 displays the emission spectra of the 2nanoSi nanospheres functionalized with different concentrations of the "*pro-active*" TAMRA-labelled peptide (400-4000 μg/L) in order to see how the amount of dye affects the emission of QDs. First, we would like to highlight the blue shift in the PL of QDs@silica in comparison to the pristine QDs in solution, i.e. 510 nm versus 540 nm, as observed previously[3–5], yet the original fluorescence is recovered after the trypsin digestion as shown later in this work.

Increasing the amount of TAMRA-labelled peptides on the QD_{540}@silica nanospheres surface leads to a decrease in the emission intensity between λ = 450 nm and 550 nm range, which corresponds to the fluorescence emission wavelength of the quantum dots, as mentioned above. The emission intensity drop is a direct evidence of efficient FRET between the QD_{540}@silica nanospheres and the TAMRA dye in the 2nanoSi system, as reported previously in analogous FRET systems.[6] However, at higher concentration of TAMRA-labelled peptide, that is above 1800 μg/L, the FRET process is saturated.

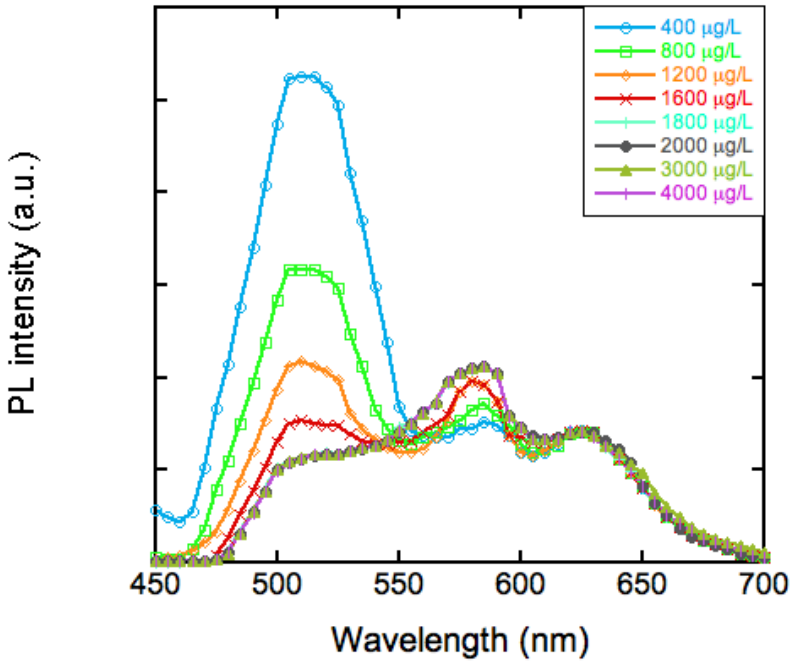

Figure A3. *Emission spectra of "pro-active" 2nanoSi system increasing the amount of TAMRA-labelled peptide at the surface of the nanosphere in the range 400-4000 μg/L.*

FRET measurements and calculations.

The FRET efficiency (*E*) is the quantum yield of the energy transfer transition, *i.e.* the fraction of energy transfer event occurring per donor excitation event.

The experimental efficiency, *E* is defined by the following equation:

$$E = (F_D - F_{DA})/F_D$$

where F_D and F_{DA} are the fluorescence intensities of the donor alone and the donor in the presence of acceptor[7,8], respectively.

The FRET efficiency relates to the quantum yield and the fluorescence lifetime of the donor molecule as follows:[9]

$$E = 1 - \tau'_D/\tau_D$$

where τ'_D and τ_D are the donor fluorescence lifetimes in the presence and absence of an acceptor, respectively.

Based on the fluorescence measurements in Figure A3, we obtained the following efficiencies for the 400-4000 μg/L concentrations range of the "*pro-active*" TAMRA-labelled peptide:

[peptide-TAMRA]	400	800	1200	1600	1800	2000	3000	4000
E (%)	20.45	47	59.61	68	72.83	72.96	72.90	72.96
n	0.3	1	1.67	2.36	3.03	3.05	3.04	3.05

Estimates of the QD donor–dye acceptor separation distance *r* were calculated via the Förster formalism by fitting the above experimental FRET efficiencies *E* using the expression:

$$E = 1/[1+(r/R_0)^6]$$

Where R_0 is the Förster distance designating the donor–acceptor separation at 50% energy transfer efficiency. R_0 (in Angstrom, Å) is expressed as[10]:

$$R_0 = 0.211(\kappa^2 n_D^{-4} Q_D J(\lambda))^{1/6}$$

where n_D is the refractive index of the medium, Q_D is the donor quantum yield in the absence of acceptor, $J(\lambda)$ is the spectral overlap integral, and κ^2 is the dipole orientation

factor. We use κ^2 = 2/3 corresponding to a random dipole orientation shown to be appropriate for our self-assembled QD–protein/peptide–dye conjugates, as detailed in reported previous studies.[6,8] This is based on the assumption that in a self assembled QD–peptide/protein–dye pair it is impossible to control the relative orientation of the dipoles. Each time a dye-labelled protein it is added to the conjugate, that dye will have a dipole orientation that does not correlate with the existing QD and dyes.

For our system, we obtained a R_0 = 4.982 nm and r = 5.10 nm at 47% energy transfer efficiency by fluorescence.

Dependence of *E* on the number of acceptors, *n*.

Supposing spherical symmetry of the dye-labelled peptides attached to the QDs@silica nanosphere surface, the number of acceptors *n* can be calculated following the Förster model[10]:

$$E = n/[n+(r/R_0)^6]$$

Considering the Förster distance R_0 = 4.982 nm and r = 5.10 nm, then the FRET efficiency of approx. 50% will correspond to a single donor-acceptor pair, while the FRET saturation (approx. 73%) is reached at three dye-labelled peptides on the surface of the QDs@silica nanosphere (Figure A4).

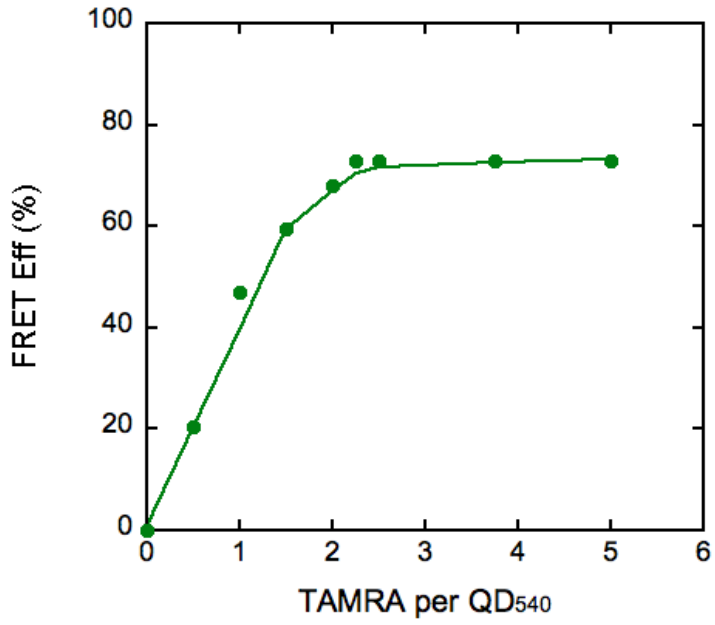

Figure A4. *Dependence of the FRET efficiency on the number of acceptors.*

As a consequence, the concentration of 800 μg/L of TAMRA-labelled peptide was chosen for all the enzymatic experiments as described in the main manuscript and the corresponding supporting information.

Michaelis-Menten kinetics.

Values for K_m and k_{cat} were determined from a conventional excess-substrate Michaelis-Menten (MM) plot as shown in Figure A5 and eq 1.

$$V = d[S]/dt = V[S]/(Km + [S]) = k_{cat}\,[E]_0\,[S] / (k_1^{-1}(k_{-1} + k_{cat}) + [S]) \quad (1)$$

The terms inlcude [*S*], the concentration of substrate; *V*, the máximum rate of catalysis; K_m, the Michaelis constant; k_{cat}, the turnover number; k_1 and k_{-1}, the rates for ES complex association and dissociation; and $[E]_0$, the total concentration of enzyme.[11,12]

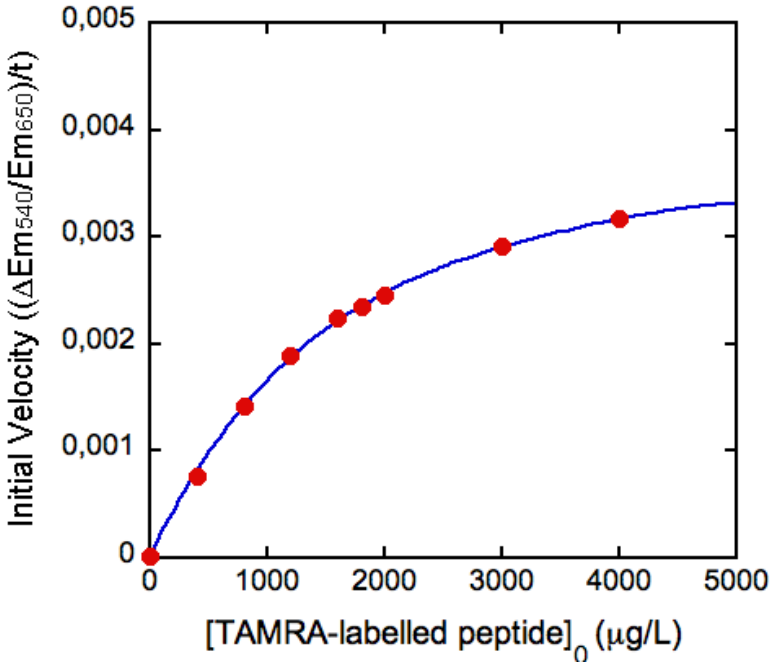

***Figure A5**. Michaelis-Menten (MM) plot for TAMRA-labelled peptides digestion (●), catalyzed by 150 ug/L of trypsin. The blue line is the fit to the integrated MM model.*

Each QDs@silica-TAMRA-labelled peptide substrate conjugate was digested with 150 μg/L of trypsin and the data was collected for 10 min. The MM kinetic parameters were determined as following:

$$K_m = 3.5 \text{ mM}$$

$$k_{cat} = 50.4 \text{ s}^{-1}$$

$$k_{cat}/K_m = 14.39 \text{ mM}^{-1} \text{ s}^{-1}$$

Taking into account the kinetic parameters for the natural substrate trypsinogen (K_m = 5.1 - 5.6 μM, k_{cat} = 2.12 - 4 s^{-1} and k_{cat}/K_m = 41 μM s^{-1})[13,14], our results are different. However, considering other kind of substrates, such as peptides, our results fit rather well with these studies relating the affinity of trypsin with the different peptidic sequences (K_m= 1.9 – 4.7 mM, k_{cat}= 7.1 - 290 s^{-1}).[15]

Supplementary figures and tables

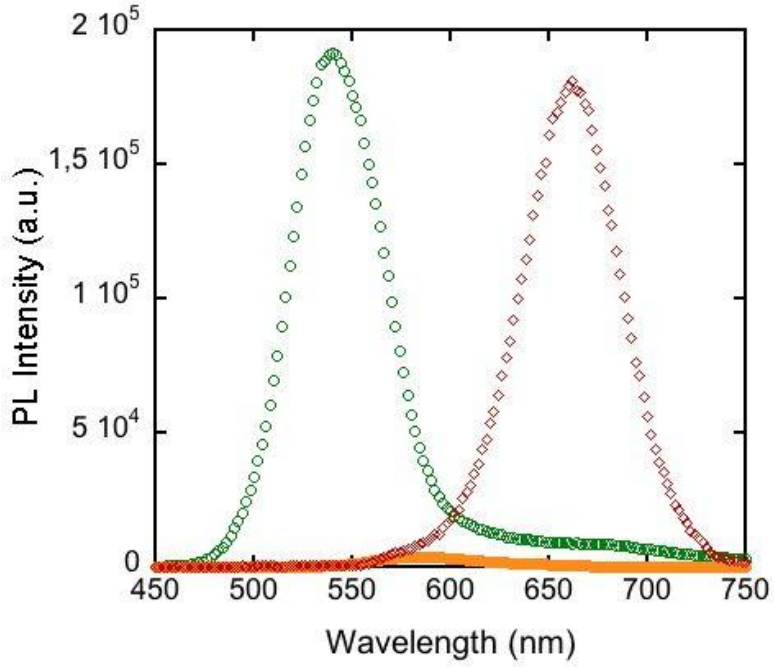

***Figure A6**. Emission spectra of control samples excited at 405 nm: $CdSe_{540}$@silica (green), $CdSe_{660}$@silica (red) and 5'-TAMRA (orange), respectively. All the samples were measured at the same window aperture conditions.*

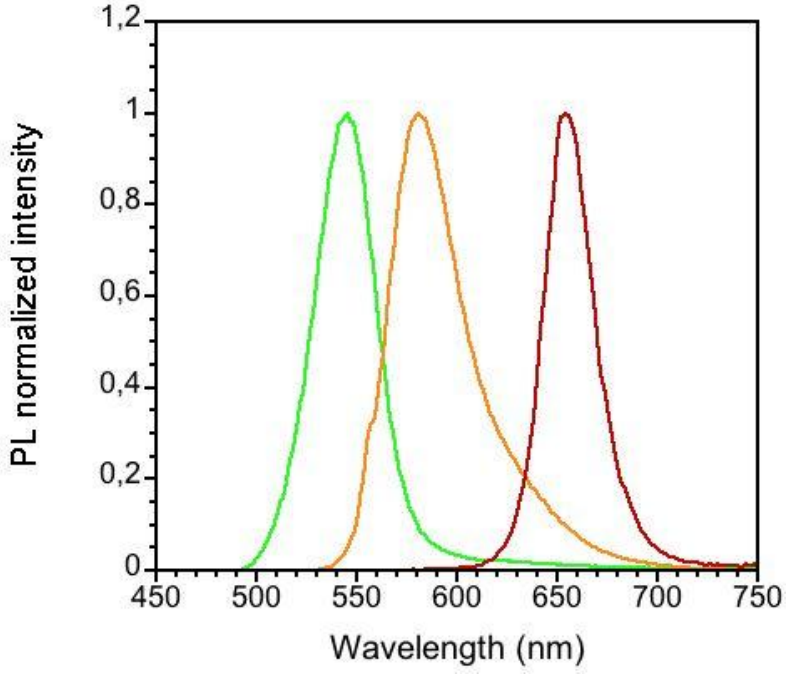

***Figure A7**. Emission spectra of QD_{540} (green), 5'-TAMRA (orange), and QD_{660} (red). The quantum dots were excited at 405 nm, while the TAMRA dye was excited at 535 nm.*

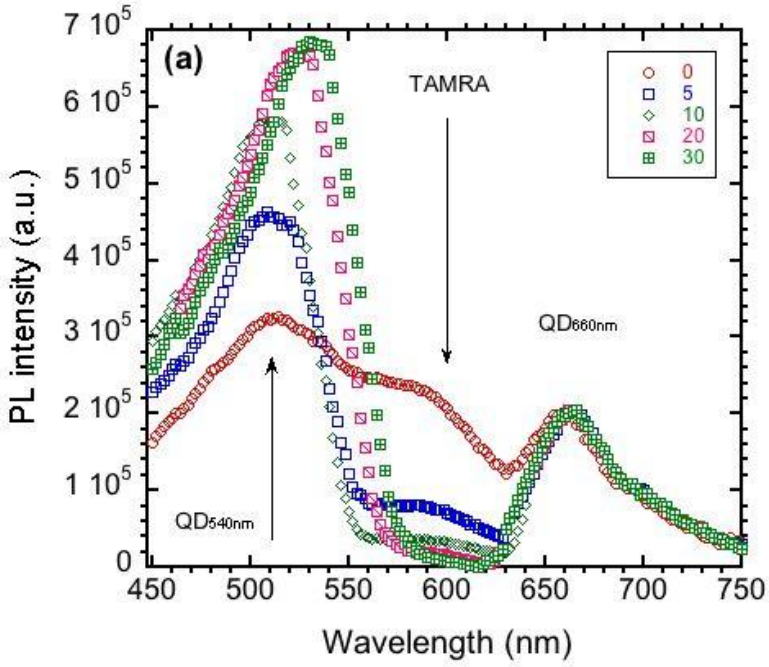

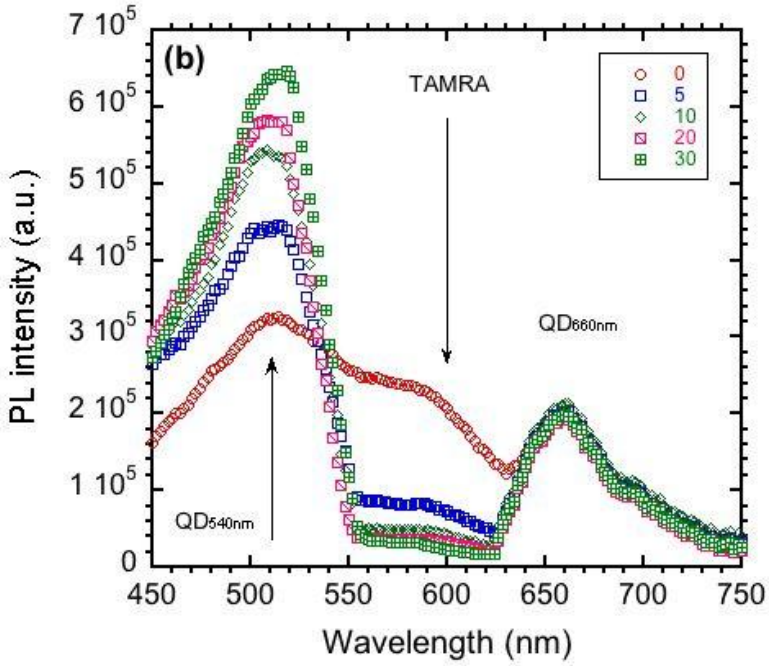

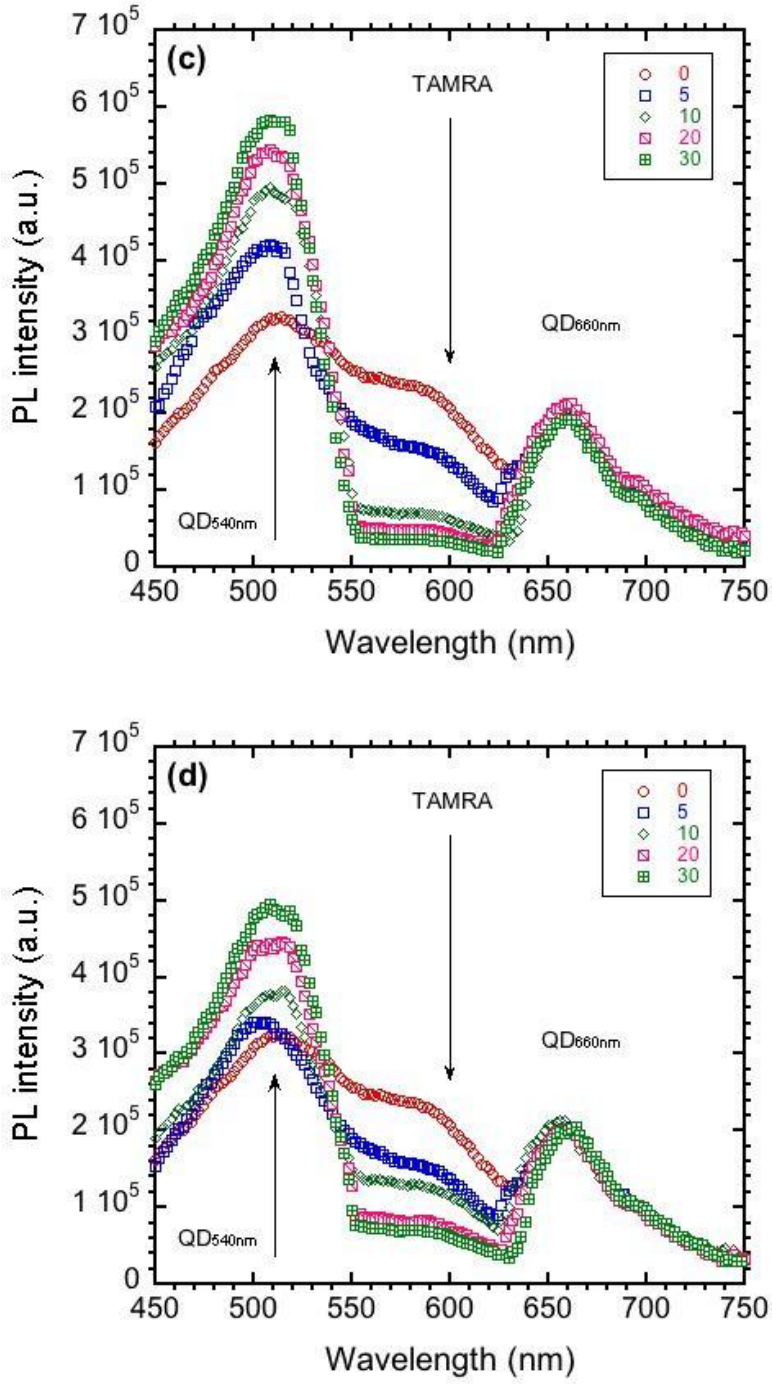

Figure A8. *Emission spectra of 5'TAMRA-labelled 2nanoSi nanospheres. Enzymatic digestion with different trypsin concentration: a) 250 μg/L, b) 200 μg/L, c) 100 μg/L, and d) 50 μg/L, respectively.*

References

1. Clegg, R. M. *Fret and Flim Techniques*. *Laboratory Techniques in Biochemistry and Molecular Biology* **33,** (Elsevier, 2009).

2. Somers, R. C. *et al.* A nanocrystal-based ratiometric pH sensor for natural pH ranges. *Chem. Sci.* **3,** 2980 (2012).

3. Calabretta, M. *et al.* Analytical ultracentrifugation for characterizing nanocrystals and their bioconjugates. *Nano Lett.* **5,** 963–967 (2005).

4. Serrano, I. C., Ma, Q. & Palomares, E. QD-'Onion'-Multicode silica nanospheres with remarkable stability as pH sensors. *J. Mater. Chem.* **21,** 17673–17679 (2011).

5. Ma, Q., Serrano, I. C. & Palomares, E. Multiplexed color encoded silica nanospheres prepared by stepwise encapsulating quantum dot/SiO2 multilayers. *Chem. Commun.* **47,** 7071–7073 (2011).

6. Dennis, A. M., Rhee, W. J., Sotto, D., Dublin, S. N. & Bao, G. Quantum dot-fluorescent protein FRET probes for sensing intracellular pH. *ACS Nano* **6,** 2917–24 (2012).

7. Medintz, I. L., Trammell, S. A., Mattoussi, H. & Mauro, J. M. Reversible modulation of quantum dot photoluminescence using a protein- bound photochromic fluorescence resonance energy transfer acceptor. *J. Am. Chem. Soc.* **126,** 30–1 (2004).

8. Medintz, I. L. *et al.* A fluorescence resonance energy transfer-derived structure of a quantum dot-protein bioconjugate nanoassembly. *Proc. Natl. Acad. Sci. U. S. A.* **101,** 9612–7 (2004).

9. Pawley, J. Handbook of Biological Confocal Microscopy. *Springer* (2006). at <http://www.springer.com/us/book/9780387259215>

10. Labowicz, J. R. *Principles of Fluorescence Spectroscopy* |. *Springer* (2006). at <http://www.springer.com/us/book/9780387312781>

11. Purich, D. *Enzyme Kinetics: Catalysis & Control*. *Elsevier* (2010). at <http://store.elsevier.com/Enzyme-Kinetics-Catalysis-and-Control/Daniel-Purich/isbn-9780123809247/>

12. Briggs, G. E. & Haldane, J. B. A Note on the Kinetics of Enzyme Action. *Biochem. J.* **19,** 338–9 (1925).

13. Castillo-Yáñez, F. J., Pacheco-Aguilar, R., García-Carreño, F. L. & Navarrete-Del Toro, M. de L. A. Isolation and characterization of trypsin from pyloric caeca of Monterey sardine Sardinops sagax caerulea. *Comp. Biochem. Physiol. B. Biochem. Mol. Biol.* **140,** 91–8 (2005).

14. Lu, D., Yuan, X., Zheng, X. & Sadler, J. E. Bovine Proenteropeptidase Is Activated by Trypsin, and the Specificity of Enteropeptidase Depends on the Heavy Chain. *J. Biol. Chem.* **272,** 31293–31300 (1997).

15. Caprioli, R. M. & Smith, L. Determination of Km and Vmax for tryptic peptide hydrolysis using fast atom bombardment mass spectrometry. *Anal. Chem.* **58,** 1080–1083 (1986).

UNIVERSITAT ROVIRA I VIRGILI
SEMICONDUCTOR NANOPARTICLES AS PLATFORM FOR BIO-APPLICATIONS AND ENERGY RELATED SYSTEMS.
Alba María Matas Adams
Dipòsit Legal: T 55-2016

UNIVERSITAT ROVIRA I VIRGILI
SEMICONDUCTOR NANOPARTICLES AS PLATFORM FOR BIO-APPLICATIONS AND ENERGY RELATED SYSTEMS.
Alba María Matas Adams
Dipòsit Legal: T 55-2016

Chapter 4

Tracking of Fc-γ receptors in platelets via new generation fluorescent materials

UNIVERSITAT ROVIRA I VIRGILI
SEMICONDUCTOR NANOPARTICLES AS PLATFORM FOR BIO-APPLICATIONS AND ENERGY RELATED SYSTEMS.
Alba María Matas Adams
Dipòsit Legal: T 55-2016

1. Introduction

Platelets were first described between 1865 and 1877 as particles present in the blood, smaller than leukocytes and erythrocytes, but without a real understanding of their origin and function.

Giulio Bizzozzero named in 1882 these particles as little plates, due to their shape, as well as established their role in haemostasis and in thrombosis.

Finally, the name platelets was given in 1910 by James Wright.[1]

Platelets are anucleate cells; fragments of cytoplasm with a biconvex discoid shape when they are unactivated, derived from megakaryocytes of the bone marrow of mammals[2]. They are the smallest elements present in blood with sizes ranging from 2-4 μm in diameter. Despite their small size and the fact that they are cell fragments, their primary function is to stop blood loss after tissue trauma and exposure of the subendothelial matrix[3], playing an important role in blood clotting. This is due to the proteins displayed on their surface, allowing them to stick to the blood vessel walls and to each other.

Their role is controlled by the many mobile transmembrane receptors present in their surface, including integrins, leucine-rich repeated receptors, tyrosine kinase receptors, and the object of our study, proteins belonging to the immunoglobulin superfamily with particular emphasis on the Fcγ receptors (FcγR), most importantly FcγRIIA.[4]

It is well known that most of the receptors play an important role in the hemostatic function of platelets, but also in other less well-understood functions as inflammation, tumor growth as well as metastasis.

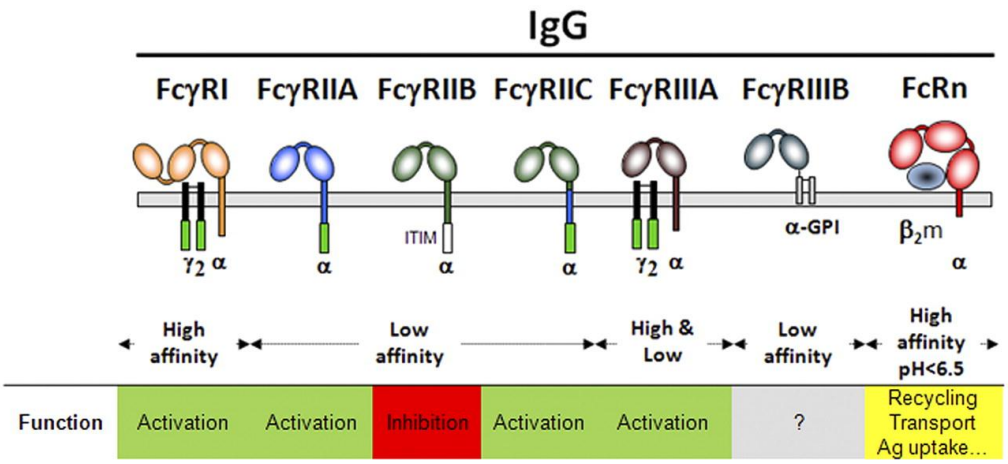

***Image 1**. Schematic representation of human IgG receptors at the cell membrane (grey bar) and their association or not to the FcRγ-chain dimer (black). Green boxes represent ITAMs; and the white box, the ITIM. Binding of a human IgG subclass is indicated between parentheses[5] Image used with the permission of the authors.*

In humans, the Fcγ system is the most complex, and it can be classified in: FcγRI, FcγRII and FcγRIII, as they present differences in the intracellular domains and cellular expression.[6] These families are categorized following the level of affinity to IgG and the signaling cascade it triggers. Image 1 shows that the low affinity receptors present two extracellular immunoglobulin-like domains, bent at a 50-55º angle and connected by a hinge region, while the high affinity ones present an extra immunoglobulin-like domain, which has been suggested to be important for this high affinity binding.

The case of our study (FcγRIIA) presents low to medium affinity to IgG and the crystal structure of this receptor complexed with IgG showed that it is a 1:1 stoichiometric interaction.[7,8]

For the formation of the platelet plug at the site of the vascular damage, a series of coordinated events have to take place.

First of all, platelet arrest onto the exposed tissue creating a monolayer of activated cells. This phase is known as the activation phase. For this step to take place, the platelets have to bind to fibrilar collagen, fibronectin and laminin present in the vessel wall, and of all of these ones, the most important are collagens I and III, that support platelet adhesion to the damaged vasculature.

The von Willebrand factor (VWF) that is immobilized in type I, III and VI collagen filaments, are the responsible of trapping the initial flowing platelets, while the collagen allows the formation of stable bond for firm adhesion as well as the platelet activation.[9]

The interaction is mediated by the GP VI immunoglobulin family member, and by integrin $\alpha_2\beta_1$.

GP VI is a platelet specific low affinity collagen receptor of high potency in the initiating signal generation and in fact, is complexed to the FcR γ-chain dimer, and it has been proven that without any of these two receptors the thrombus formation is reduced.[10,11]

The FcR γ-chain dimer present an immonoreceptor tyrosine-based activation motif (ITAM), that acts as the signal transducing subunit of the receptor, so when the GP VI receptor is bounded to the collagen there is a phosphorylation of the ITAM sequence allowing the activation of a downsteam signaling pathway that leads to a potent platelet activation.

Next step is the recruitment and activation of extra platelets so they stick to each other forming platelet aggregates, known as the extension phase. This is made possible due to the local accumulation of soluble agonists (ADP, thrombin and epinephrine) secreted by the previously activated platelets.

And finally, the stabilization phase, where the platelet plug is stabilized in order to prevent a premature disaggregation until the wound heals. The list of molecules that have a specific role in thrombus stabilization is far from complete, but it is known that the activated platelets in the plug are so close in contact that they allow the direct or indirect formation of bridges favoring the transfer of information as in a neurological synapse.

These three phases have to take place in a controlled way, to avoid the formation of uncontrolled thrombosis.

Fcγ receptors, most importantly, FcγRIIa (CD32), play a key factor in heparin-induced thrombocytopenia, a potentially devastating immune mediated adverse drug reaction, due to the treatment with heparin, which instead of preventing clot formation, promotes the adverse effect, producing also a low platelet count.[12]

The mechanism behind this unexpected clot formation in HIT has been investigated and it originates from the apparition of a complex between heparin and a platelet factor (PF4), which is then recognized by the body as a foreign object. Consequently, antibodies against this immune complex are formed. This union triggers the activation

of the platelets through the recognition of the immune complex (heparin-PF4-antibody) by the Fc-γ receptors on the surface of the platelet, ultimately producing the apparition of clots, as well as decreasing the platelet count.

Another important role of these receptors is as regulators of the immune response[6], due to their binding to the Fc part of the antibody attached to infected cells or invading pathogens. In the case of the FcγRIIA it does not require a γ chain for the phagocytic activity (as what happens for the other γ receptors), as they posses IgG binding and signal transduction capabilities in themselves.[13]

Until now, for the tracking of single molecules or a small number of molecules in living cells (including proteins), fluorescent dyes, latex beads or gold nanoparticles were used, but their applicability was restricted by the size of the probe or the photobleaching.[14]

Lately, these materials have been substituted by quantum dots (QDs), that have been widely used in the past few years as labeling and imaging agents[15] due to their narrower emission spectrum, larger photostability, and higher brightness. Besides, the emission spectrum is tunable by controlling the size during the synthesis, that ranges form 2-15 nm.[16] Moreover, their emission can be tracked for longer periods of time as they do not present photobleaching.

These systems have been used to determine the diffusion characteristics of individual receptors and their subcellular location over time[17–19], like the diffusion dynamics of Glycine Receptors (the main inhibitory neurotransmitter receptor in the adult spinal cord)[20], GABA (γ-aminobutyric acid) receptors[21], or even the rotation of the Fc receptors[22].

There are around 5000-8000 Fcγ receptors continuously on the platelets surface able to detect the immune complexes or the pathogens. Thus, an innovative strategy using long-fluorescence-lifetime labels allowing high-throughput screening and multiplexed detection on commercially available equipment is necessary.

Here we report, for the first time to our knowledge, a library of bioconjugated QDs for specific tracking of the FcγRIIA, using IgG and the Fc fragment of IgG, proteins with different molecular weights but the same specificity for Fc receptors.

2.Experimental

2.1 Bioconjugation of IgG and Fc to Quantum Dots. For the bioconjugation, 100 nM Carboxyl 605 nm QDs from ThermoFischer Scientific (605 QDs) were mixed with EDC in a 1:150 molar ratio at 4º for 30 min, then the proteins for each conjugation (IgG or Fc fragment against Fcγ receptor) in different molar ratios (from 1:0 to 1:16) were added, to a final volume of 250 µL with PBS in a shaker at 400 rpm at 20ºC for 2 hours (Table 1).

Molar ratio	[605QDs] (nM)	[Protein] (nM)
1:0	100	0
1:0.5	100	50
1:1	100	100
1:2	100	200
1:8	100	800
1:16	100	1600

Table 1. *Molar ratios used in the 605QDs conjugation to protein*

The mixture was then centrifuged at 4000g for 15 min in the Amicon Ultracentrifugal tubes (100 KDa filter), then resuspended in PBS and centrifuged again in the same conditions. The washing procedure was repeated three times in PBS, and finally the pellet was resuspended in PBS to a final volume of 250 µL.

2.2 Agarose Gel Electrophoresis (AGE). Gels were hand cast with agarose in Tris-Acetic-EDTA (TAE). For this, 0.5 g of agarose was briefly boiled in 100 mL of TAE buffer 1x (Mixing 4.8 g Tris-HCl, 1.14 g acetic acid and 2 mL of 0.5 M EthyleneDiamineTetraacetic Acid (EDTA) in a total volume of 1 L of deionized water), cooled and poured into a standard 7cm^2 gel tray.

AGE was performed with the Owl Easycast B1 (Thermo Scientific) in which gels were horizontally immersed in TAE buffer 1x for electrophoresis at different voltages and times. 20 mL of the samples were mixed with a loading buffer (Orange G 1%). Gels were imaged on a UV transilluminator (molecular imager Gel Doc XR+ (BioRad)) under UV excitation at 405 nm.

2.3 Incubation of bioconjugated QDs with platelets. Platelets (300.000 per μL) were isolated from blood of healthy patients as described elsewhere.[23]

For the incubation with the conjugates, 5 μL of platelets were diluted to a final volume of 55 μL in PBS (final concentration of around 30.000 platelets per μL).

The total volume was placed in a round Petri dish for 10 min for the platelets to settle, followed by washing with PBS to eliminate the unattached platelets.

Finally, 10 μL of the QD-protein (1:1) conjugate were added over the remaining platelets incubation. Images were recorded just after addition of the conjugates for different periods of time as well as after washing.

3. Results and discussion

3.1 Conjugation mechanism of IgG and Fc fragment to 605QDs

Activation of the carboxyl-functionalized 605QDs leads to the formation of a reactive ester by the crosslinking effect of EDC, as shown in Scheme 1, which can easily react with the free amino groups present in the protein.[24]

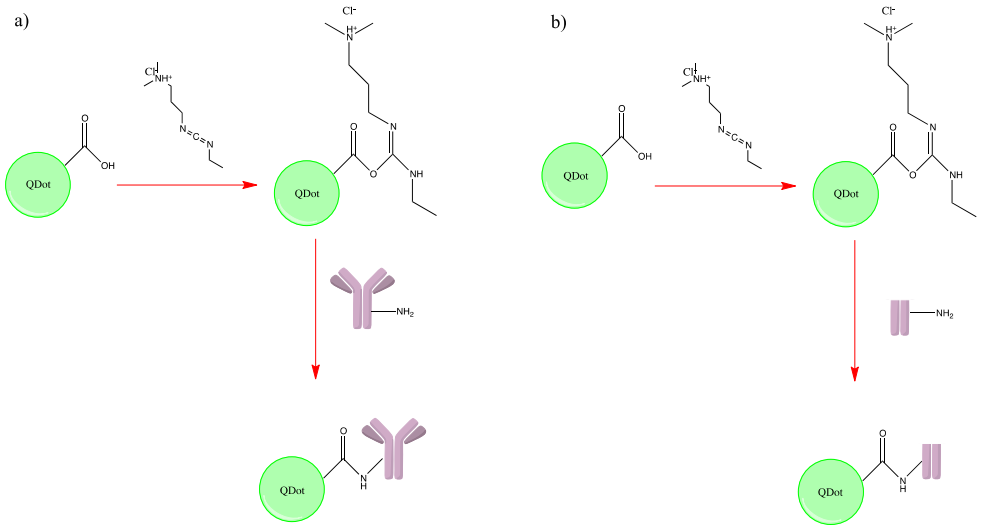

Scheme 1. *Conjugation of 605QD to a) IgG, b) Fc fragment.*

Once the activation and the conjugation took place, the final products corresponding to the different QD:protein ratio, were washed, and then an AGE electrophoresis was performed.

As shown in Figure 1, the fluorescence from the free 605QDs was visualized under UV light without the need of further staining.

Observing Figure 1a (605QDs-IgG) it can be seen thatLane 1 marks the fluorescence from the free QDs and that this signal remains in all of the lanes but slighter less intense.

As the molar ratio of the protein increases a faint new band appears for the 1:0.5 molar ratio in the case of Lane 2. This new band corresponds to the IgG conjugated to the QDs, but this conjugation is not 100% effective, even for the 1:16 (Lane 6), as free QDs could still be observed.

In the case of 605QDs-Fc something similar happens, most of the QDs are still free (as seen from the bands in the same position as free QDs), but in this case the band from the protein conjugated to the QDs are a lot lower as the molecular weight of the Fc fragment is a lot smaller than in the case of the IgG (150KDa vs 50KDa), so the conjugated band is quite close to the free QDs.

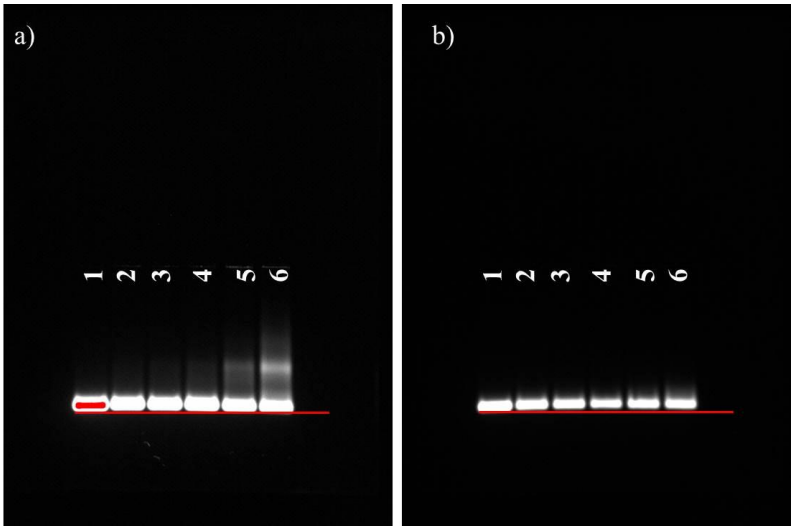

Figure 1. *AGE of a) 605QDs-IgG, b) 605QDs-Fc. Lanes: 1) Free 605 QDs, 2) 605QDs-Protein (1:0.5), 3) 605QDs-Protein (1:1), 4) 605QDs-Protein (1:2), 5) 605QDs-Protein (1:2), 6) 605QDs-Protein (1:16)*

3.2 Tracking of FcγRIIA receptors by bioconjugated QDs

The fluorescent conjugates (final concentration of 2nM of QDs) were incubated with the platelets, as previously described, and the images were recorded before and after the washing steps.

Along the chapter, only the images obtained after washing, using a Leica DMI 6000B Inverted Microscope, will be displayed.

Figure 2 shows the control experiments, that is the incubation of the platelets with free 605QDs (Figure 2a) and with 605QDs conjugated to BSA (Figure 2b).

From Figure 2a it is clear that free 605QDs interacted somehow with the cell staining the whole cell.

It could be explained as it has been seen that free QDs of any type are able to penetrate different cell lines membrane going inside the cells, but the reason behind this is not so well known (it could be due to size, charge, etc).[25,26]

This same phenomenon was observed after the incubation with 605QDs conjugated to BSA (Figure 2b) contrary to our expectations, as the BSA is quite a big protein and is surrounding in excess the QDs, it could not be able to penetrate the membrane. However, there is a fluorescent signal that could come from unspecific binding of BSA to the receptors in the surface[27], but if a competition assay was done with 605QDs-BSA and 605QDs-IgG it preferentially will uptake the 605QDs-IgG as shown in previous work by Neuwirth et al[28].

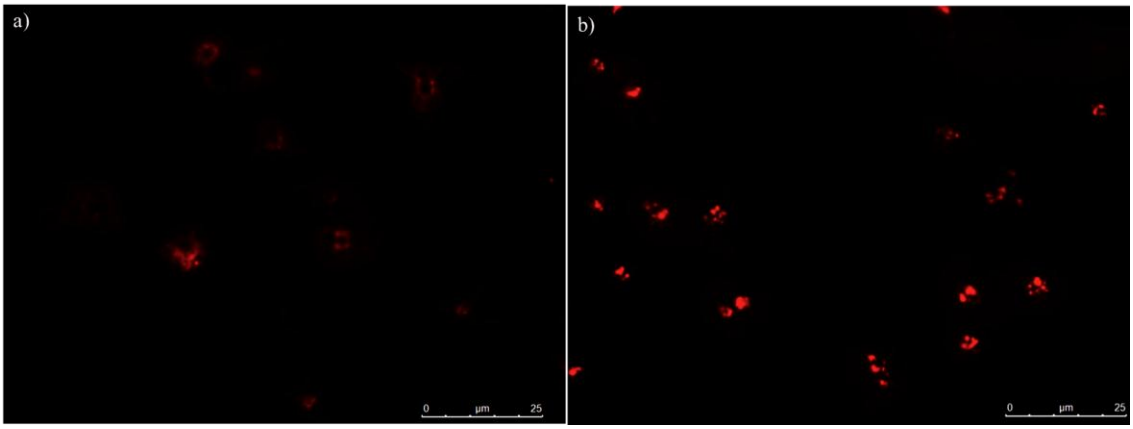

Figure 2. *Incubation of platelets with a) free 605QDs+platelets b) 605QDs-BSA (1:20)+ Platelets. QDs working concentration was 2nM.*

Comparing both controls, it could be noticed also, that the staining presents a different pattern for the free QDs, than the one for the QDs-BSA, so the interaction between the conjugates and the platelets have to differ.

A final control was done where the Fc receptors were blocked using an excess of free IgG (Scheme 2). 400.000 platelets were used, and as each platelet has around 5000 Fc receptors in the surface, there should be around $2x10^9$ receptors in our working cell volume, so free IgGs in a 1500 times excess were added to the platelets and incubated for 10 minutes and the wash the excess away.

As the receptors are blocked, after the incubation with the 605QDs-IgG and washing, no fluorescence should be observed.

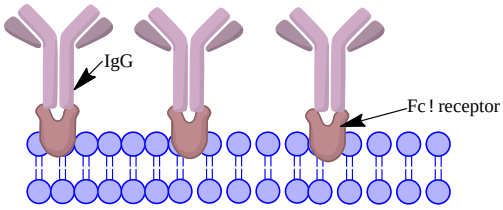

Scheme 2. *Blocking of the Fcg receptors with free IgG*

But what happened was not expected (Figure 3), fluorescence was observed and with the same patterning observed when the platelets were incubated with the 605QDs-IgG or 605 QDs-Fc, as shown later.

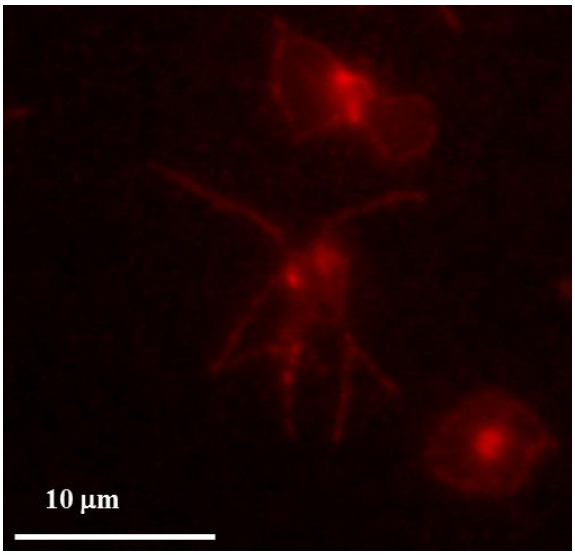

Figure 3. *Incubation of platelets with 1500 times excess of free IgG followed by incubation with 605QDs-IgG (1:1)*

A possible explanation for this unexpected fluorescence is that not all of the positions of the QDs are conjugated to the IgG, as the molar ratio for the conjugation used is 1 to 1, so they still can be some free positions in the QD that can bound to the IgG that has previously been attached to the Fcγ receptor to block the position as represented in Scheme 3.

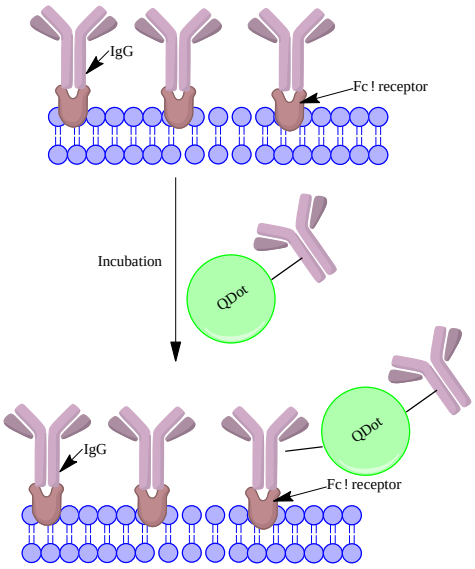

Scheme 3. *Possible explanation for the unexpected fluorescence after the blocking incubation.*

Scheme 4 illustrates the interaction of the conjugated 605QDs with the Fc receptors after incubation. The receptor detects and binds to the IgG (Scheme 4a) conjugated to the 605QD, which fluorescence is used to track the movement of receptor in the membrane over time. The same is done for the Fc fragment of IgG (Scheme 4b).

To be able to track this receptor, the platelets were incubated with the conjugated 605 QDs.

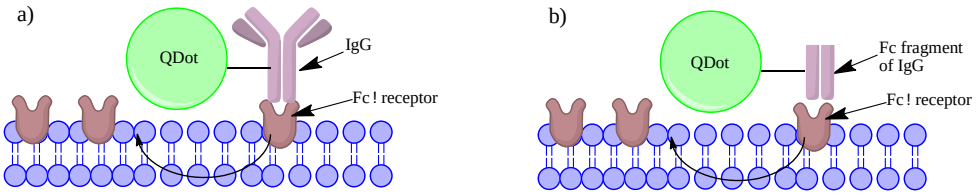

Scheme 4. *Tracking of the Fc receptor with a) 605QDs-IgG, b) 605QDs-Fc fragment.*

Figure 4 shows the result of the incubation of the conjugates (605QDs-IgG and 605QDs-Fc with the platelets for 5 min and washing, and it clearly demonstrates that the marking is different from the marking in the controls.

While in the controls the center body of the cells was the main focus of fluorescence, after the incubation with the conjugates, the same patterning of fluorescence is observed for both type of conjugates, the membrane as well as the center body of the cell is marked. This is in agreement with the expected, as the Fcγ receptors are in the membrane of the cell. The movement of the receptor is tracked mostly in the membrane;

specifically in the arm-like structure the platelet membrane develops when it gets activated by IgG or by the Fc fragment.

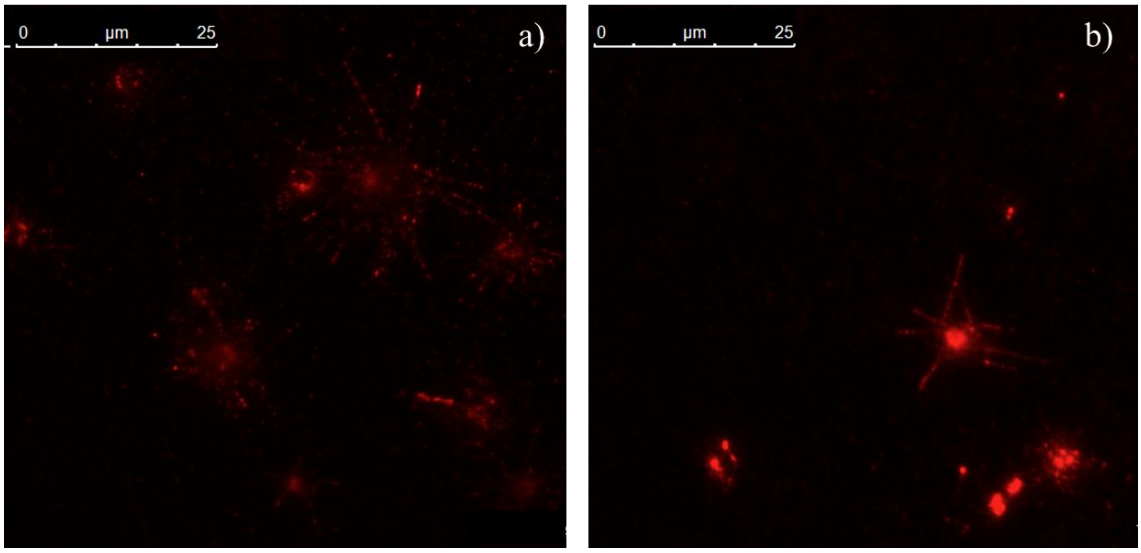

Figure 4. *Incubation of platelets with a) 605QDs-IgG, b) 605QDs-Fc fragment, working concentration was 100pM. Molar ratio 1:1*

After the incubation and washing, the images were recorded every 100 ms to a total of 2000 frames to track each 605QDs bonded to the Fc receptor and follow it.

Figure 5 depicts the movement of possibly a single Fc receptor after 100 ms, marked with an arrow it is seen how the fluorescent dot moves from its original position (Figure 5a) after 100 ms (Figure 5b). This movement has to be analyzed via Image J.

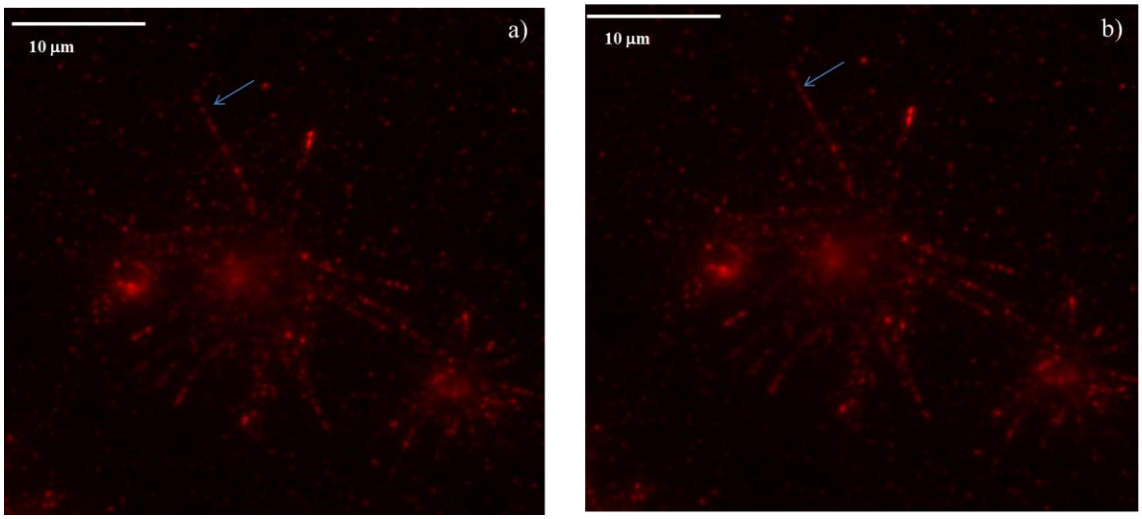

Figure 5. *Incubation of platelet with 605QDs-IgG (1:1). a) at time 0, b) after 100 ms.*

So it can be said that the single tracking of possible an Fc receptor in the surface of the platelet is possible, but more studies have to be done before this can be said for sure.

4. Conclusions

Platelets are cells that play an important role in the blood clot formation after a vessel injury, due to the multiple receptors present in the membrane, that are activated when there is danger. One of the receptors that play an important role at the beginning of this clot formation, and without its presence, it would not occur, are the Fc gamma receptors.

The object of this work is to analyse the movement of FcγRIIa (CD32) receptors using QDs, taking advantage of the properties of the QDs that are not present in the other materials previously used (non photobleaching, long lifetimes, narrow emission spectrum), and try to identify the pathway of single receptor, as well as to produce a library of QD-protein for the receptor.

First of all, incubation with the controls (free 605 QDs and QDs bounded to BSA) was performed, to avoid any possible false positives in fluorescence. Then, incubation of platelets with the QDs complexed to the IgG and Fc fragment against Fc receptor was also done for 5 min.

The first problem observed was that the incubation with the controls showed fluorescence, as well as after incubating with the complexes, but, the fluorescence pattern was different, so it is possible that the controls bind in a non specific way, while for the complexes, the proteins bind to the receptor, so the movement could be tracked.

Only an image is shown were it can be seen that the fluorescence spots that appear in the arms of the platelets after incubation with the QDs-IgG move after 100ms, what could be evidence of the movement of the receptor, but only with this information is impossible to be certain of the reason behind this difference, so more experiments have to be performed.

References

1. Brewer, D. B. Max Schultze (1865), G. Bizzozero (1882) and the discovery of the platelet. *Br. J. Haematol.* **133,** 251–258 (2006).

2. Machlus, K. R. & Italiano, J. E. The incredible journey: From megakaryocyte development to platelet formation. *J. Cell Biol.* **201,** 785–96 (2013).

3. Ruggeri, Z. M. & Mendolicchio, G. L. Adhesion mechanisms in platelet function. *Circ. Res.* **100,** 1673–85 (2007).

4. Rivera, J., Lozano, M. L., Navarro-Núñez, L. & Vicente García, V. Platelet receptors and signaling in the dynamics of thrombus formation. *Haematologica* **94,** 700–711 (2009).

5. Bruhns, P. Properties of mouse and human IgG receptors and their contribution to disease models. *Blood* **119,** 5640–9 (2012).

6. Nimmerjahn, F. & Ravetch, J. V. Fc gamma receptors as regulators of immune responses. *Nat. Rev. Immunol.* **8,** 34–47 (2008).

7. Kato, K., Fridman, W. H., Arata, Y. & Sautès-Fridman, C. A conformational change in the Fc precludes the binding of two Fcγ receptor molecules to one IgG. *Immunol. Today* **21,** 310–312 (2000).

8. Zhang, Y. *et al.* Crystal Structure of the Extracellular Domain of a Human FcγRIII. *Immunity* **13,** 387–395 (2000).

9. Savage, B., Ginsberg, M. H. & Ruggeri, Z. M. Influence of fibrillar collagen structure on the mechanisms of platelet thrombus formation under flow. *Blood* **94,** 2704–2715 (1999).

10. Kato, K. *et al.* The contribution of glycoprotein VI to stable platelet adhesion and thrombus formation illustrated by targeted gene deletion. *Blood* **102,** 1701–7 (2003).

11. Poole, A. *et al.* The Fc receptor gamma-chain and the tyrosine kinase Syk are essential for activation of mouse platelets by collagen. *EMBO J.* **16,** 2333–41 (1997).

12. Udeh Cl, Douglas A, Udeh BL, H. J. Heparin-induced thrombocytopenia: a clinical and economic review.OA Anaesthetics. *OA Anaesth.* **1,** 3 (2013).

13. McKenzie, S. E. *et al.* The role of the human Fc receptor Fc gamma RIIA in the immune clearance of platelets: a transgenic mouse model. *J. Immunol.* **162,** 4311–4318 (1999).

14. Baba, K. & Nishida, K. Single-molecule tracking in living cells using single quantum dot applications. *Theranostics* **2,** 655–67 (2012).

15. Bruchez Jr., M. Semiconductor Nanocrystals as Fluorescent Biological Labels. *Science (80-.).* **281,** 2013–2016 (1998).

16. Neeleshwar, S. *et al.* Size-dependent properties of CdSe quantum dots. *Phys. Rev. B* **71,** 201307 (2005).

17. Bats, C., Groc, L. & Choquet, D. The interaction between Stargazin and PSD-95 regulates AMPA receptor surface trafficking. *Neuron* **53,** 719–34 (2007).

18. Groc, L. *et al.* Differential activity-dependent regulation of the lateral mobilities of AMPA and NMDA receptors. *Nat. Neurosci.* **7,** 695–6 (2004).

19. Groc, L. *et al.* Surface trafficking of neurotransmitter receptor: comparison between single-molecule/quantum dot strategies. *J. Neurosci.* **27,** 12433–12437 (2007).

20. Dahan, M. *et al.* Diffusion dynamics of glycine receptors revealed by single-quantum dot tracking. *Science* **302,** 442–5 (2003).

21. Lévi, S. *et al.* Homeostatic regulation of synaptic GlyR numbers driven by lateral diffusion. *Neuron* **59,** 261–73 (2008).

22. Winter, P. W. *et al.* Rotation of Single Cell-Surface Fc Receptors Examined by Quantum Dot Probes. *Biophys. J.* **102,** 653–654 (2012).

23. Warkentin, T. E., Greinacher, A., Gruel, Y., Aster, R. H. & Chong, B. H. Laboratory testing for heparin-induced thrombocytopenia: a conceptual framework and implications for diagnosis. *J. Thromb. Haemost.* **9,** 2498–500 (2011).

24. Wang, S., Mamedova, N., Kotov, N. A., Chen, W. & Studer, J. Antigen/Antibody Immunocomplex from CdTe Nanoparticle Bioconjugates. *Nano Lett.* **2,** 817–822 (2002).

25. Fontes, A., Lira, R. B. De, Aparecida, M., Lopes, B. & Gomes, T. Quantum Dots in Biomedical Research. (2012).

26. Biju, V., Itoh, T. & Ishikawa, M. Delivering quantum dots to cells: bioconjugated quantum dots for targeted and nonspecific extracellular and intracellular imaging. *Chem. Soc. Rev.* **39,** 3031–56 (2010).

27. Kudolo, G. B. & Harper, M. J. Estimation of platelet-activating factor receptors in the endometrium of the pregnant rabbit: regulation of ligand availability and catabolism by bovine serum albumin. *Biol. Reprod.* **43,** 368–377 (1990).

28. Neuwirth, R. *et al.* Evidence for immunoglobulin Fc receptor-mediated prostaglandin2 and platelet-activating factor formation by cultured rat mesangial cells. *J. Clin. Invest.* **82,** 936–44 (1988).

2. Up Conversion Nanoparticles Introduction

UNIVERSITAT ROVIRA I VIRGILI
SEMICONDUCTOR NANOPARTICLES AS PLATFORM FOR BIO-APPLICATIONS AND ENERGY RELATED SYSTEMS.
Alba María Matas Adams
Dipòsit Legal: T 55-2016

2. Up Conversion Nanoparticles

2.1 Introduction

Most of the photoluminescence imaging techniques are based in the use of exogenous contrast agents as organic dyes, organically modified silica, fluorescent proteins or QDs. This agents use anti-Stokes-shifted emission, being excited in the UV or the blue-green spectral range, but present a number of limitations for biological applications, such as: low signal-to-background ratio due to autofluorescence from the biological tissue when they are excited at low wavelength, low penetration depth of the UV light in biological samples as well as possible DNA damage and cell death due to long term exposure to UV light and the toxicity of the heavy metals present in the QDs.

So, a few years ago, as an alternative, the use of cadmium free fluorescent nanoparticles was suggested, as an example it can be noticed the rare earth (RE)-derived materials.

These kinds of nanoparticles have a doped matrix with a sensitizer and an activator, and they can be divided in two groups: (i) down conversion nanoparticles (DCNP), and (ii) up-conversion nanoparticles (UCNP) as represented in Figure 1.[1]

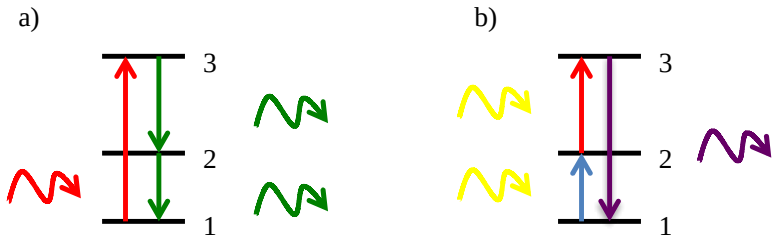

Figure 1. *Absorpiton and emission of a) DCNP and b) UCNP*

The difference between DCNP and UCNP arises from the dopant RE metal, which consequently determines the photoluminescent processes and properties displayed by nanoparticles (Table 1).[2]

In other words, when using as dopants RE metals like cerium (Ce) or terbium (Tb), these nanoparticles will be DCNP and the absorption will occur at lower wavelengths than the emission, as it is in the case of QDs.

When the RE metal is ytterbium (Yb), erbium (Er) or europium (Eu), they will be UCNP and the absorption of two or more photons under NIR excitation leads to the emission of one in a lower wavelength.

Host Matrix	Sensitizer/Activator	Emissions (nm)
Y_2O_3	Yb/Er	660
	Yb/Tm	450, 480
Gd_2O_3	Yb/Er	520-580,650-700
$LuPO_4$	Yb/Tm	476
LaF_3	Yb/Ho	541,643
YF_3	Yb/Tm	347,363,454,477
$NaYF_4$	Yb/Er	525,547,660
	Yb/Tm	450,476
$LiYF_4$	Yb/Tm	361,450,479,647

Table 1. *Emission of RENP*

UCNP maintain most of the properties of QDs, like the narrow emission spectrum, the large photostability and high brightness[3], but the emission wavelength is not related with the size of the nanoparticle.

These nanoparticles do not present quantum confinement, so different strategies have to be taken to tune the color of UCNP:

- Controlling dopant concentration or the different sensitizer/activators as seen in table 1. $NaYbF_4:Tm^{3+}$ (blue), $NaYbF_4:Ho^{3+}$ (green), $NaYbF_4:Er^{3+}$ (red) and $NaYbF_4:Yb^{3+}$(magenta).[4]
- Interparticle energy transfer or antenna effect (distance dependent)
- Manipulation of size and shape surface effects.[5,6] When decreasing the size of the UCNP the emission can be tuned, but as previously mentioned the quantum confinement effect is not available for the lanthanides and cannot be interpreted by quantum mechanics.[7]
- Use of core/shell designs.[8]
- Förster resonance energy transfer (FRET)[9] or luminescence resonance energy transfer (LRET)[10] between UCNP and dyes or QDs. The UCNP normally acts as the energy donor while the dye or QD is the energy acceptor. The difference

between FRET and LRET is that in LRET the energy transfer process is radiative while it is non radiative in FRET.

The shape of the nanoparticle plays an important role in the emission intensity, as well as the presence or not of a core/shell structure.[11]

The core/ shell structure can be:

a) Homogeneous, meaning that the nature of the core and shell is identical, i.e. $NaYF_4$ as the core as well as a thin layer of $NaYF_4$ as shell. For the case of $NaYF_4$: Yb^{3+},Er^{3+} @ $NaYF_4$, the fluorescence is enhanced 7.4 times. This shell eliminates the quenching sites on the surface of the core.

b) Heterogeneous, where the core and shell present different composition, but with the requirement of a low lattice mismatch between them. This structure presents the advantage of the incorporation of more imaging modalities as can be paramagnetism when a shell as $NaGdF_4$ is grown over the core.

c) Active core/shell structure. In this case, in the shell layer, a considerable concentration of lanthanide dopants (normally the sensitizer) are added. This structure also suppresses the surface deactivations as what happens for the homogeneous and heterogeneous structures, but also the extra ions are able to enhance the PL interacting with the lanthanide of the core. Capobianco et al. presented a core/shell structure as $NaGdF_4$: Yb^{3+},Er^{3+}@ $NaGdF_4$: Yb^{3+}.[12]

The PL intensity can also be enhanced by localized surface plasmon resonance (LSPR) as it has been seen for QDs (Chapter 1). The interaction between the UCNP and the metal can take place in three different ways: i) $NaYF_4$: Yb^{3+},Er^{3+} deposited over a metallic film of gold islands[13], dense metal nanoparticles[14,15] or over a 3D plasmonic antenna[16] could enhanced the photoluminescence by 5-310 fold optimizing the distance between the UCNP and the metal.

ii) Attachment of metal nanoparticles onto the surface of the UCNP as done by Schietinger et al.[17] when they coupled $NaYF_4$: Yb^{3+},Er^{3+} to a single gold nanosphere and the enhancement had an overall factor of 3.8.

iii) Forming a core/shell structure using metal/silica/UCNP (as done in Chapter 1 but with QDs), where the enhancement was 4-10 times higher, as the separation between the metal and the UCNP could be better controlled.[18]

The most used matrix is composed of $NaYF_4$, due to the higher emission it presents when crystalized in the hexagonal phase (β-$NaYF_4$), as it presents photoluminiscence, 4.4 times higher than the cubic phase (α-$NaYF_4$)[19], which is the predominantly obtained in the synthesis even though the more thermodynamically stable is the hexagonal one. This may due to the high energy required for the transformation of the cubic phase to the hexagonal one.

2.2 Internal mechanisms

Focusing in the upconversion term, it refers to the process of converting two or more photons of low energy into a higher energy radiation.

As it is a nonlinear process, it needs two or more metastable energy states to store the energy that leads to the emission of a higher energy photon; this is the reason why lanthanides have been used as dopants, because they present ladder-like energy levels. This process is different from the nonlinear multiphoton absorption that can take place in organic dyes and QDs, which involves simultaneous absorption of two or more photons through virtual states. [20] Adittionaly, it does not need from an ultrashort pulsed laser as the efficiency of the process is in general several orders of magnitud higher than other nonlinear multiphoton absorption processes.

The absorption processes [21] can be: a) Excited State Absorption (ESA), b) Energy Transfer Upconversion (ETU), c) cooperative sensitization upconversion (CSU), d) cross relaxation (CR) and e) photon avalanche (PA) as shown in Figure 2.

a) The ESA happens after a successive absorption of two photons. This is the only process were only a rear earth ion is needed, due to de ladder-like stricter of three level system. The first photon produces the promotion of an electron from the ground state (GS) to the first excitated state (ES1), if a second photon is absorbed during the lifetime of the electron, it can be promoted to the second excited state (ES2). These transitions only can take place on ions with a ladder like arrangement of the energy states such as Er^{3+}, Ho^{3+}, Tm^{3+} and Nd^{3+}.

b) The ETU process is quite different from the ESA, as in this case, two ions are involved. The first ion (known as sensitizer) absorbs a photon of low energy, promoting an electron from the GS to the ES1, then, it transfers the energy to the GS

and ES1 of ion 2 (known as activator), exciting ion 2 to the ES2, that can emit a photon of higher energy than the one absorbed.

The efficiency of this process depends on the distance between the sensitizer and the activator, determined by the dopants concentration.

For this process to take place, ion pairs like Yb^{3+}/Tm^{3+}, Yb^{3+}/Er^{3+} and $Yb^{3+}/Ho^{3+}$are used. [22,23] In this thesis, the pair Yb^{3+}/Er^{3+} is the one used.

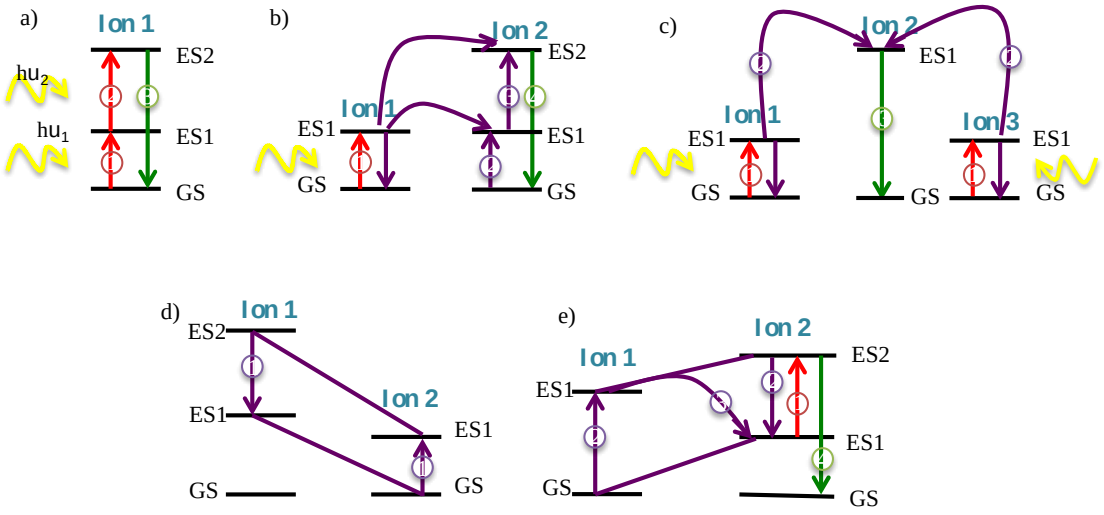

Figure 2. *Principal Up conversion processes for UCNPs: a) excited-state absorption (ESA), b) energy transfer upconversion (ETU), c) cooperative sensitization upconversion (CSU), d) cross relaxation (CR) and e) photon avalanche (PA). Red lines represent photon excitation, violet are the energy transfer processes and green is the emission process.*

c) The CSU involves three ion centers, where normally ion 1 and 3 are of the same type. It involves the absorption of a photon by both ion 1 and 3, and the corresponding energy transfer from the ES1 from both ions, to the ES1 of ion 2 (that presents higher energy than the other two ions). When ion 2 relaxes, it emits the upconverted photon. This process presents lower efficiency than ESA and ETU.

It has been reported the use of Yb^{3+}/Tb^{3+} [24], Yb^{3+}/Eu^{3+} [25] and Yb^{3+}/Pr^{3+} [26] ion pairs for this process.

d) Cross-relaxation is an energy transfer process, resulting from an ion-ion interaction. The ions can be of the same type or different.

In this case, ion 1 transfer's part of its energy from the ES2 to the ES1 of the ion 2, and the rest of the energy is used to stay in the ES1. The efficiency of the CR process

is tightly related to the dopant concentration, because if the concentration is high, this is a quenching mechanism.

e) Finally, the photon avalanche process only produces up conversion energy, above a certain limit of excitation power. It is a looping process that involves processes of ESA for excitation light and an efficient CR that produces feedback. Due to the complexity of the mechanism, it would not be explained.

2.3 Synthesis

To synthesize this nanoparticles there is a huge range of synthetic approaches such as co-precipitation method, thermal decomposition, hydro(solvo)thermal synthesis, sol-gel processing, as well Ostwald-ripening method.[3]

i) Co-precipitation method, where normally the nanoparticles precipitate with organic surfactants that control the size and prevent aggregation. This method is used for small nanoparticles. It is a friendly synthetic method as there are a small amount of toxic by products and the temperatures required for the synthesis are not extreme

Normally with this process, the cubic phase is produced, but with a thermal process, the hexagonal one can be achieved.

ii) Thermal decomposition is the most popular synthetic method to achieve UCNP and it employs organometallic compounds as precursors that decompose in a high boiling point organic solvent at high temperature. It requires the assistance of surfactants. The solvent normally is 1-octadecene (ODE), the surfactants can be oleic acid (OA), oleylamine (OM) or trioctylphosphine oxide (TOPO), as in the synthesis of QDs. Good dispersity and good cristalinity can be achieved with this method, but the reaction has to be very controlled as the nucleation can be really fast producing defects in the surface of the UCNP leading to a relatively low up converting quantum yield.

iii) Hydrothermal synthesis requires the use of an autoclave that produces high temperature and pressure to increase the solubility and reactivity of the inorganic compounds. Even though the temperatures used are high, they are lower than for the thermal decomposition. The size and shape can also be controlled using ligands.

iv) Sol-gel method is used to produce oxide or fluoride nanocrystals. The problem is that it also needs a step of calcination and there is a lack of monodispersity

v) Ostwald-ripening strategy offers short reaction times, nontoxic byproducts but the temperature of reaction is quite high (around 300ºC). In this process, the growth of larger particles is energetically favored at the expense of smaller ones.[27] It produces monodisperse nanoparticles normally with a hexagonal phase and with narrow size distribution and higher UC efficiency.

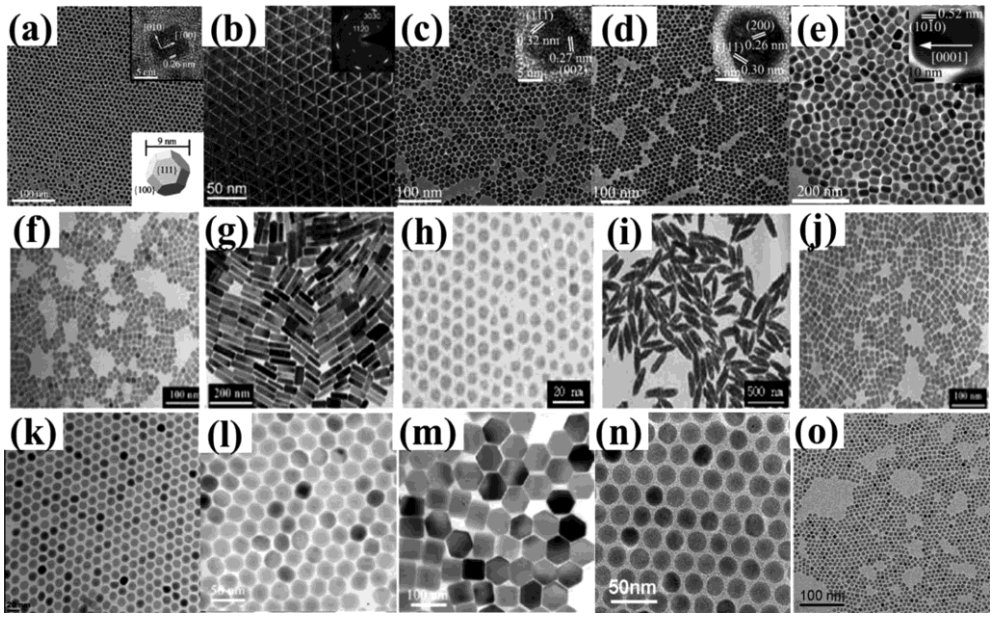

Figure 3. *TEM images of a) LuOF, b) LaF_3, c)α-$NaYF_4$, d)$NaYbF_4$, e)β-$NaEuF_4$ synthesized by the thermal decomposition method, f) α-$NaYF_4$:Yb^{3+}, Er^{3+}, g) β-$NaYF_4$:Yb^{3+}, Er^{3+}, h)LaF_3, i)YF_3, j) α-$NaYF_4$ synthesized by the hydro(solvo)thermal method and k-o) β-$NaYF_4$ or CaF_2 nanoparticles synthesized by the Ostwald ripening method. Imaged used with the authorization of the editorial.*[28]

Most of the UCNP produced by these methods are hydrophobic due to the capping ligands they present (OA, OM, TOP or TOPO), so they are not suitable for bio-applications.

A crucial step is the surface modification and functionalization to render them water-soluble and with reactive groups for the further functionalization steps.

As what happens with QDs, some of the strategies used are ligand exchange, ligand oxidation, silanization, and layer-by-layer assembly or simply perform the synthesis in water[29].

Of all, the most popular method is the ligand exchange, which replaces the hydrophobic ligand by other hydrophilic ones, without influencing the chemical and optical properties of the UCNP. The ligands choose are poly (acrylic acid) (PAA)[30], mercaptopropionic acid (MPA)[31], citrate[32]… Besides of rendering the nanoparticles water soluble, the ligands also contribute with functionalization.

The ligand oxidation process is limited to the presence of ligands with at least one insaturated bond, for example OA, that can be oxidized using ozone to hydrophilic azelaic acids ($HOOC(CH_2)_7COOH$) making the nanoparticles water soluble but with low yield of conversion.[33]

Another possibility, as for QDs, is the silica coating that presents a huge range of functional groups and it is biocompatible. This method presents the advantage that if the silica is mesoporous, then functional biomolecules and drugs can be immobilized inside the nanoporous for controlled release, as an example of applications.

And the layer-by-layer method is as explained in Chapter 2, the sequential adsorption of oppositely charged ions on the surface of the UCNPs.

Then, the nanoparticles require from bioconjugation to allow them to play a role in the bio-applications. There are two main ways to couple biomolecules to the UCNP that are:

a) Electrostatic interactions or physisorption, that is a straightforward approach but it is a weak interaction.

b) Covalent linkage resulting from a chemical reaction, this can be the formation of thiol bridges (resulting from the reaction of two thiols), amides (a carboxylic acid and an amine reaction) or an imine (after the reaction of an amide and a aldehyde) as shown in Figure 4.

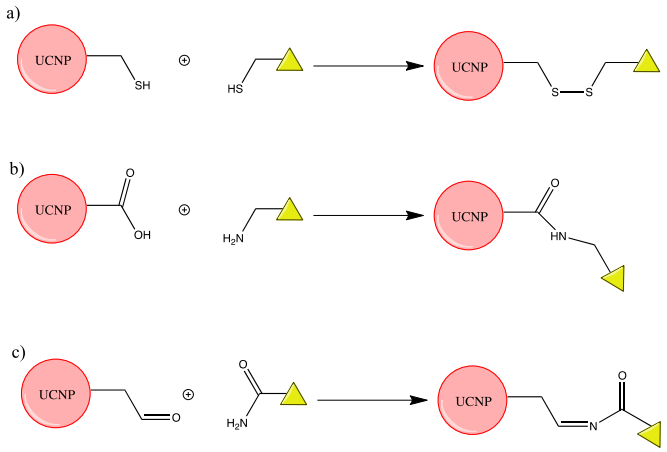

Figure 4. *Bioconjugation chemistry of the UCNP and different functional groups. a) Formation of a thiol bridge, b) formation of an amide, c) formation of an imine. The triangle represents the biomolecule.*

2.4 Applications

The advantages of the UCNP are many and even improve in some cases the advantages of QDs as can be: sharp emission bandwidth, large anti-Stokes shifts allowing the separation of the emission and absorption, long lifetime, high photostability and a high signal to noise ratio.

For bioapplications they present three main characteristics: low cytotoxicity, virtually zero background autofluorescence and most importantly, the strong penetration depth ability of the IR light in the skin and the consequent low photo damage to the cells or the tissue after long term irradiation.

The enhancement of the fluorescence is quite an important factor to take care of, as the highest reported by 2012 up conversion quantum yield at a 980 nm laser irradiation of 0.3W/cm^2 is of 0.6% for a core/shell structure[34], and the maximum permissible skin exposure of 980 nm irradiation is 0.73W/cm^2, so to be able to use it in vivo, the PL has to be improved.

Thanks to all of this, the UCNP are a promising alternative to dyes, fluorochromes and QDs for solar cells[35] (as the UCNP absorb in a part of the solar spectrum where QDs are not able to, the former started to be employed also for solar cells[36–38] just by themselves or mixed with QDs also, so there is a complete absorption of the sun spectrum), data storage[39], for in vitro and even, for in vivo use[40,41].

As previously mentioned, UCNP are excited with IR light that can penetrate the skin and avoids the scattering problem of the tissues with the UV light[42], consequently, if the nanoparticles are in the cells, the light can penetrate the skin and organs and excite the UCNP *in vivo*. Furthermore, the cytotoxicity of UCNP was tested by several groups and after incubation for more than 24 hours, the cellular viability was over 90%, concluding the low toxicity of these nanoparticles independently of the surface charge and functionalization[43–45], but the charge determines their cellular uptake efficiency.[46]

They have been used for temperature bio-sensing metal ions such in living cells taking advantage of quenching of the fluorescence due to the heavy metals such as Hg^{II}, Cu^{II}, Co^{II}, Ag^{I}…[47,48].
Also for the single-molecule imaging with long-time tracking capability, as their emission does not blink[49,50], as well as for imaging of small animals[10,51], for tumor targeting in cancer diagnosis and therapy[52] and for Magnetic Resonance Imaging (MRI)[53] using UCNP with magnetic properties that can also have a treatment role[54].

The low penetration depth of the UV light is a huge problem behind the use of QDs as donor agents in the Photodynamic Therapy (PDT), as well as directly as photosensitizer, as most of the QDs absorb at lower wavelengths that the IR, because of this, UCNP are highly exploited in photodynamic therapy as represented in Figure 5.[41,55] Tumor selectivity can be achieved by using ligands that will recognize receptors on the cancer cells, allowing the accumulation of the PDT system on cancer cells.
This tissue, will be destroyed, as the UCNP (in this case, the photosensitizer agent) attaches to it and generates ROS, as shown in Figure 5, the IR light from the source will excite the UCNP that automatically will emit visible light, being able to generate reactive oxygen species from the oxygen in the tissue.

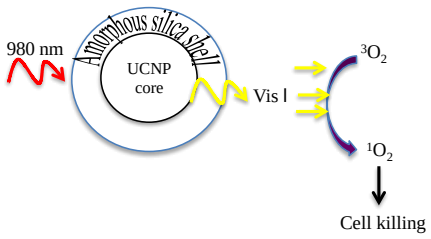

Figure 5. *Diagram of the photodynamic therapy.*

The problem with the direct use of UCNP as photosensitizer agents is the poor luminescence efficiency of the UCNP, so a possibility is to load other photosensitizer agents to the UCNP taking advantage of FRET from the UCNP to other molecules. An example is the union between the β-$NaYF_4$:Yb^{3+}, Er^{3+} with a meso-tetraphenylporphine photosensitizer and used to kill HeLa cells, with a 75% efficiency. [56]

These nanoparticles have even been used for in vivo PDT incorporating a photosensitizing porphyrin derivative chlorine 6 (Ce6) to a PEGylated amphiphilic polymer coated β-$NaYF_4$:Yb^{3+}, Er^{3+} nanoparticles, that were injected to the tumor site directly and after irradiation with a 980 nm laser a great tumor regression was observed.[57,58]

The main problem is that the loading efficiency of the photosensitizers on the UCNPs does not present a good efficiency, so to overcome this; an alternative is to coat the UCNP with a silica shell that allows higher loading of the photosensitizer agents.

Another use is as well as for the release of biomolecules[59,60], for this there are different approaches:

1) The use of hydro gels, that as shown in Figure 6, are degraded when the UCNP that have inside emit UV or visible light, liberating what has inside.

In this case there is no problem with the toxicity of the UCNP, as could happen with QDs.

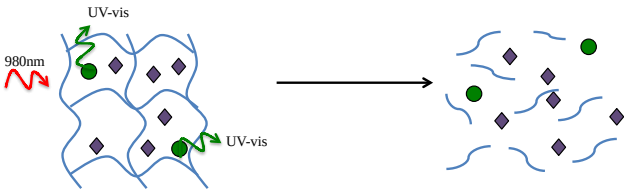

Figure 6. *Scheme of the liberation of drugs, molecule inside a hydrogel…*

2) Presence of hydrophobic pockets inside the UCNP surface where the drugs or biomolecules can be encapsulated using the hydrophobic-hydrophobic interaction. An example is the presence of PEGylated polymers where the drugs as doxorubicin (DOX) can be encapsulated, and could be released modifying the pH.[61]

3) Mesoporous silica shell where the drug can be deposited in the pores. For example ibuprofen can be deposited in the pores of the β-$NaYF_4$:Yb^{3+}, Er^{3+} system.[62]

References:

1. Auzel, F. Upconversion and anti-Stokes processes with f and d ions in solids. *Chem. Rev.* **104,** 139–73 (2004).

2. Chen, J. & Zhao, J. X. Upconversion nanomaterials: synthesis, mechanism, and applications in sensing. *Sensors* **12,** 2414–35 (2012).

3. Vennerberg, D. & Lin, Z. Upconversion Nanocrystals: Synthesis, Properties, Assembly and Applications. *Sci. Adv. Mater.* **3,** 26–40 (2011).

4. Ehlert, O., Thomann, R., Darbandi, M. & Nann, T. A four-color colloidal multiplexing nanoparticle system. *ACS Nano* **2,** 120–4 (2008).

5. Mai, H.-X., Zhang, Y.-W., Sun, L.-D. & Yan, C.-H. Highly Efficient Multicolor Up-Conversion Emissions and Their Mechanisms of Monodisperse NaYF 4 :Yb,Er Core and Core/Shell-Structured Nanocrystals. *J. Phys. Chem. C* **111,** 13721–13729 (2007).

6. Li, Z. & Zhang, Y. An efficient and user-friendly method for the synthesis of hexagonal-phase NaYF(4):Yb, Er/Tm nanocrystals with controllable shape and upconversion fluorescence. *Nanotechnology* **19,** 345606 (2008).

7. Chen, G., Yang, C. & Prasad, P. N. Nanophotonics and nanochemistry: controlling the excitation dynamics for frequency up- and down-conversion in lanthanide-doped nanoparticles. *Acc. Chem. Res.* **46,** 1474–86 (2013).

8. Kar, A. & Patra, A. Impacts of core-shell structures on properties of lanthanide-based nanocrystals: crystal phase, lattice strain, downconversion, upconversion and energy transfer. *Nanoscale* **4,** 3608–19 (2012).

9. Gorris, H. H., Ali, R., Saleh, S. M. & Wolfbeis, O. S. Tuning the dual emission of photon-upconverting nanoparticles for ratiometric multiplexed encoding. *Adv. Mater.* **23,** 1652–5 (2011).

10. Cheng, L., Yang, K., Shao, M., Lee, S. & Liu, Z. Multicolor In Vivo Imaging of Upconversion Nanoparticles with Emissions Tuned by Luminescence Resonance Energy Transfer. *J. Phys. Chem. C* **115,** 2686–2692 (2011).

11. Johnson, N. J. J. & van Veggel, F. C. J. M. Sodium lanthanide fluoride core-shell nanocrystals: A general perspective on epitaxial shell growth. *Nano Res.* **6,** 547–561 (2013).

12. Vetrone, F., Naccache, R., Mahalingam, V., Morgan, C. G. & Capobianco, J. A. The Active-Core/Active-Shell Approach: A Strategy to Enhance the Upconversion Luminescence in Lanthanide-Doped Nanoparticles. *Adv. Funct. Mater.* **19,** 2924–2929 (2009).

13. Saboktakin, M. *et al.* Metal-enhanced upconversion luminescence tunable through metal nanoparticle-nanophosphor separation. *ACS Nano* **6,** 8758–66 (2012).

14. Xu, W. *et al.* Ultra-broad plasma resonance enhanced multicolor emissions in an assembled Ag/NaYF4:Yb,Er nano-film. *Nanoscale* **4,** 6971–3 (2012).

15. Zhang, H., Xu, D., Huang, Y. & Duan, X. Highly spectral dependent enhancement of upconversion emission with sputtered gold island films. *Chem. Commun.* **47,** 979–81 (2011).

16. Paudel, H. P. *et al.* Enhancement of Near-Infrared-to-Visible Upconversion Luminescence Using Engineered Plasmonic Gold Surfaces. *J. Phys. Chem. C* **115,** 19028–19036 (2011).

17. Priyam, A., Idris, N. M. & Zhang, Y. Gold nanoshell coated NaYF4 nanoparticles for simultaneously enhanced upconversion fluorescence and darkfield imaging. *J. Mater. Chem.* **22,** 960–965 (2012).

18. Schietinger, S., Aichele, T., Wang, H.-Q., Nann, T. & Benson, O. Plasmon-enhanced upconversion in single NaYF4:Yb3+/Er3+ codoped nanocrystals. *Nano Lett.* **10,** 134–8 (2010).

19. Krämer, K. W. *et al.* Hexagonal Sodium Yttrium Fluoride Based Green and Blue Emitting Upconversion Phosphors. *Chem. Mater.* **16,** 1244–1251 (2004).

20. He, G. S., Markowicz, P. P., Lin, T.-C. & Prasad, P. N. Observation of stimulated emission by direct three-photon excitation. *Nature* **415,** 767–70 (2002).

21. Wang, M., Abbineni, G., Clevenger, A., Mao, C. & Xu, S. Upconversion nanoparticles: synthesis, surface modification and biological applications. *Nanomedicine* **7,** 710–29 (2011).

22. Sun, Y. *et al.* Controlled synthesis and morphology dependent upconversion luminescence of NaYF 4 :Yb, Er nanocrystals. *Nanotechnology* **18,** 275609 (2007).

23. Wang, G., Peng, Q. & Li, Y. Upconversion luminescence of monodisperse CaF2:Yb(3+)/Er(3+) nanocrystals. *J. Am. Chem. Soc.* **131,** 14200–1 (2009).

24. Liang, H. *et al.* Upconversion luminescence in Yb3+/Tb3+-codoped monodisperse NaYF4 nanocrystals. *Opt. Commun.* **282,** 3028–3031 (2009).

25. Dwivedi, Y., Thakur, S. N. & Rai, S. B. Study of frequency upconversion in Yb3+/Eu3+ by cooperative energy transfer in oxyfluoroborate glass matrix. *Appl. Phys. B* **89,** 45–51 (2007).

26. Pushkar', A. A., Uvarova, T. V. & Kiiko, V. V. Up-conversion multiwave (White) luminescence in the visible spectral range under excitation by IR laser diodes in the active BaY2F8:Yb3+,Pr3+ medium. *Opt. Spectrosc.* **111,** 273–276 (2011).

27. Voorhees, P. W. The theory of Ostwald ripening. *J. Stat. Phys.* **38,** 231–252 (1985).

28. Chen, G., Qiu, H., Prasad, P. N. & Chen, X. Upconversion nanoparticles: Design, nanochemistry, and applications in Theranostics. *Chem. Rev.* **114,** 5161–5214 (2014).

29. Wang, Z.-L. *et al.* Simultaneous synthesis and functionalization of water-soluble up-conversion nanoparticles for in-vitro cell and nude mouse imaging. *Nanoscale* **3,** 2175–81 (2011).

30. Cui, W., Ni, S., Shan, S. & Zhou, X. A Method to Improve the Up-Conversion Fluorescence of Polymer Modified NaYF 4 : Yb , Er (Tm) Nanocomposites. *World J. Nano Sci. Eng.* **2012,** 41–46 (2012).

31. Wawrzynczyk, D. *et al.* Optimisation of ligand exchange towards stable water suspensions of crystalline NaYF4: Er3+, Yb3+ nanoluminophors. *J. Nanosci. Nanotechnol.* **12,** 1886–91 (2012).

32. Cao, T. *et al.* Water-soluble NaYF4:Yb/Er upconversion nanophosphors: Synthesis, characteristics and application in bioimaging. *Inorg. Chem. Commun.* **13,** 392–394 (2010).

33. Zhou, H.-P., Xu, C.-H., Sun, W. & Yan, C.-H. Clean and Flexible Modification Strategy for Carboxyl/Aldehyde-Functionalized Upconversion Nanoparticles and Their Optical Applications. *Adv. Funct. Mater.* **19,** 3892–3900 (2009).

34. Chen, G. *et al.* (α-NaYbF4:Tm(3+))/CaF2 core/shell nanoparticles with efficient near-infrared to near-infrared upconversion for high-contrast deep tissue bioimaging. *ACS Nano* **6,** 8280–7 (2012).

35. Trupke, T., Green, M. A. & Würfel, P. Improving solar cell efficiencies by up-conversion of sub-band-gap light. *J. Appl. Phys.* **92,** 4117 (2002).

36. Zou, W., Visser, C., Maduro, J. A., Pshenichnikov, M. S. & Hummelen, J. C. Broadband dye-sensitized upconversion of near-infrared light. *Nat. Photonics* **6,** 560–564 (2012).

37. Pan, A. C. *et al.* Enhancement of up-conversion efficiency by combining rare earth-doped phosphors with PbS quantum dots. *Sol. Energy Mater. Sol. Cells* **94,** 1923–1926 (2010).

38. Bednarkiewicz, A., Nyk, M., Samoc, M. & Strek, W. Up-conversion FRET from Er 3+ /Yb 3+ :NaYF 4 Nanophosphor to CdSe Quantum Dots. *J. Phys. Chem. C* **114,** 17535–17541 (2010).

39. Zhang, C. *et al.* Luminescence modulation of ordered upconversion nanopatterns by a photochromic diarylethene: rewritable optical storage with nondestructive readout. *Adv. Mater.* **22,** 633–7 (2010).

40. Liu, J. *et al.* Ultrasensitive nanosensors based on upconversion nanoparticles for selective hypoxia imaging in vivo upon near-infrared excitation. *J. Am. Chem. Soc.* **136,** 9701–9709 (2014).

41. Idris, N. M. *et al.* In vivo photodynamic therapy using upconversion nanoparticles as remote-controlled nanotransducers. *Nat. Med.* **18,** 1580–5 (2012).

42. Cheng, L., Wang, C. & Liu, Z. Upconversion nanoparticles and their composite nanostructures for biomedical imaging and cancer therapy. *Nanoscale* **5,** 23–37 (2013).

43. Guller, A. E. *et al.* Cytotoxicity and non-specific cellular uptake of bare and surface-modified upconversion nanoparticles in human skin cells. *Nano Res.* **8,** 1546–1562 (2015).

44. Sun, Y., Feng, W., Yang, P., Huang, C. & Li, F. The biosafety of lanthanide upconversion nanomaterials. *Chem. Soc. Rev.* **44,** 1509–1525 (2015).

45. Gnach, A., Lipinski, T., Bednarkiewicz, A., Rybka, J. & Capobianco, J. A. Upconverting nanoparticles: assessing the toxicity. *Chem. Soc. Rev.* **44,** 1561–1584 (2015).

46. Jin, J. *et al.* Polymer-coated $NaYF_4$:Yb^{3+}, Er^{3+} upconversion nanoparticles for charge-dependent cellular imaging. *ACS Nano* **5,** 7838–47 (2011).

47. Saleh, S. M., Ali, R. & Wolfbeis, O. S. Quenching of the luminescence of upconverting luminescent nanoparticles by heavy metal ions. *Chemistry* **17,** 14611–7 (2011).

48. Hao, S., Chen, G. & Yang, C. Sensing using rare-earth-doped upconversion nanoparticles. *Theranostics* **3,** 331–45 (2013).

49. Park, Y. Il *et al.* Nonblinking and Nonbleaching Upconverting Nanoparticles as an Optical Imaging Nanoprobe and T1 Magnetic Resonance Imaging Contrast Agent. *Adv. Mater.* **21,** 4467–4471 (2009).

50. Nam, S. H. *et al.* Long-term real-time tracking of lanthanide ion doped upconverting nanoparticles in living cells. *Angew. Chem. Int. Ed. Engl.* **50,** 6093–7 (2011).

51. Jeong, S. *et al.* Multiplexed near-infrared in vivo imaging complementarily using quantum dots and upconverting NaYF4:Yb3+,Tm3+ nanoparticles. *Chem. Commun.* **47,** 8022–8024 (2011).

52. Xiong, L. *et al.* High contrast upconversion luminescence targeted imaging in vivo using peptide-labeled nanophosphors. *Anal. Chem.* **81,** 8687–94 (2009).

53. Chen, F. *et al.* Positive and Negative Lattice Shielding Effects Co-existing in Gd (III) Ion Doped Bifunctional Upconversion Nanoprobes. *Adv. Funct. Mater.* **21,** 4285–4294 (2011).

54. Fan, W. *et al.* Rattle-structured multifunctional nanotheranostics for synergetic chemo-/radiotherapy and simultaneous magnetic/luminescent dual-mode imaging. *J. Am. Chem. Soc.* **135,** 6494–503 (2013).

55. Zhang, P., Steelant, W., Kumar, M. & Scholfield, M. Versatile photosensitizers for photodynamic therapy at infrared excitation. *J. Am. Chem. Soc.* **129,** 4526–7 (2007).

56. Shan, J. *et al.* Pegylated Composite Nanoparticles Containing Upconverting Phosphors and meso-Tetraphenyl porphine (TPP) for Photodynamic Therapy. *Adv. Funct. Mater.* **21,** 2488–2495 (2011).

57. Wang, C., Tao, H., Cheng, L. & Liu, Z. Near-infrared light induced in vivo photodynamic therapy of cancer based on upconversion nanoparticles. *Biomaterials* **32,** 6145–54 (2011).

58. Wang, C. *et al.* Imaging-Guided pH-Sensitive Photodynamic Therapy Using Charge Reversible Upconversion Nanoparticles under Near-Infrared Light. *Adv. Funct. Mater.* **23,** 3077–3086 (2013).

59. Yan, B., Boyer, J.-C., Habault, D., Branda, N. R. & Zhao, Y. Near infrared light triggered release of biomacromolecules from hydrogels loaded with upconversion nanoparticles. *J. Am. Chem. Soc.* **134,** 16558–61 (2012).

60. Yang, Y. *et al.* Fabrication of and Drug Delivery by an Upconversion Emission Nanocomposite with Monodisperse LaF3:Yb,Er Core / Mesoporous Silica Shell Structure. *Eur. J. Inorg. Chem.* **2010,** 5195–5199 (2010).

61. Wang, C., Cheng, L. & Liu, Z. Drug delivery with upconversion nanoparticles for multi-functional targeted cancer cell imaging and therapy. *Biomaterials* **32,** 1110–20 (2011).

62. Hou, Z. *et al.* Electrospinning Preparation and Drug-Delivery Properties of an Up-conversion Luminescent Porous NaYF4:Yb3+, Er3+@Silica Fiber Nanocomposite. *Adv. Funct. Mater.* **21,** 2356–2365 (2011).

Chapter 5

Comparative study of the anion exchange of KYF_4: Yb^{3+}, Er^{3+} and CdTe in hydrotalcite

UNIVERSITAT ROVIRA I VIRGILI
SEMICONDUCTOR NANOPARTICLES AS PLATFORM FOR BIO-APPLICATIONS AND ENERGY RELATED SYSTEMS.
Alba María Matas Adams
Dipòsit Legal: T 55-2016

1. Introduction

Quantum dots (QDs) have been used in the past years as a potent agent for biomedical labelling or imaging[1] due to their narrow emission spectrum, larger photostability, and higher brightness when compared with the conventional organic dyes.

The main drawback when using QDs is the toxicity they present due to the heavy metals that compose them. In the case of the direct use of this type of QDs, the performed cytotoxicity studies showed low viability of the cells after a certain period of time.[2]
One way to avoid this problem is to infiltrate or surround the quantum dots by inert materials like polymers or silica,[3] that prevents the leakage and protect the core from harsh environments.

Another possibility, developed few years ago, is the use of cadmium free nanoparticles as the rare earth (RE)-derived materials. As explained in the general introduction, this kind of nanoparticles can be divided in two groups: (i) down conversion nanoparticles (DCNP), and (ii) up-conversion nanoparticles (UCNP). [4]
UCNP maintain most of the properties of QDs, like the narrow emission spectrum, the large photostability and high brightness [5], but the emission wavelength is not related with the size of the nanoparticle, only with the doping metals due to the energy levels they present, also, the shape of the nanoparticle plays an important role in the emission intensity.[6]
Another significant characteristic of the UCNP, as compared to QDs, is that as they are excited with IR light, it can penetrate the skin, unlike UV light.[7] Consequently, if the nanoparticles are in the cells, the light can penetrate the skin and organs and excite the UCNP *in vivo*.

One of the main concerns for the biological use of this UCNP is that usually the synthesis is done in organic media leading to nanoparticles with hydrophobic ligands needing a post functionalization or coating[8–10] to make bioconjugation possible.
An important part of bioconjugation is rendering the particles hydrophilic and therefore suitable for different biological environments and applications. Most of the possibilities are the same as with QDs mostly infiltration, but alternatively to the use of silica coating,[11] we present herein hydrotalcite-like materials encapsulating UCNP luminescent nanoparticles for the first time to our knowledge.

Hydrotalcite-like materials (HT), also known as layered double hydroxides (LDH), are anionic clays which general formula is $[M^{2+}_{1-x} M^{3+}_{x} (OH)_2]^{x+} A^{n-}_{x/n} * mH_2O$, where M^{2+} is a divalent cation, M^{3+} a trivalent cation, and A^{n-} the intercalated anion.

By varying the di- and/or trivalent cations, the LDH compositions vary leading to very interesting chemical combinations displaying a variety of properties. Depending on the final end of their applications, one can choose the appropriate metal combination.[12]

Hydrotalcites have been used mainly as catalysts[13], but also as loader of drugs, biomolecules[14], and imaging agents for biomedicine. In this sense, Mg/Al, Zn/Al or Ni/Al hydrotalcites were reported as host matrix for luminescent dyes but also for nanoparticles (QD, QOM, nanorods and lanthanides), enhancing their photoluminescence and stability.[15,16]

For this, the hydrotalcite is prepared by synthesis with these elements like lanthanadies, but the nanoparticles are introduced by anion exchange or delamination-restacking process (delaminating the hydrotalcite, mixing the nanoparticles with the delaminated hydrotalcite, and then, restacking the layers).

The ability of HT to be internalized into the cells has been reported[17], and some researchers say the mechanism may be a clathrin mediated endocytosis. While in the endosomes, due to the acidic pH, the HT dissolves, leaching what it has inside, as can be drugs, QDs, or UCNP as in our case.

We present herein the study of KYF_4: Yb, Er encapsulation by MgAl or CoAl hydrotalcites obtaining hybrid luminescent biocompatible nanomaterials. Additionally, by using cobalt-containing materials, the hybrids become magnetic. All these properties are highly employed in the field of biology and medicine, thus highlighting the benefits of the nanostructures reported in the present study.

A parallel study of CdTe quantum dots incorporation into MgAl or CoAl hydrotalcites will be presented as well to study if the materials incorporated vary the properties described.

Also, a parallel study will be performed to determine if the quenching effect of cobalt in QDs also affects the UCNP.

2.Experimental

2.1 Synthesis of KYF_4:Yb^{3+},Er^{3+}. KYF4: Yb^{3+}, Er^{3+} nanoparticles were synthesized following the method described by Kai et al.[18] with some modifications.

In a 50 ml round bottom flask, 12 mmol of KF were dissolved in 20 ml of methanol and the mixture was heated up to 65 ºC. In a separated flask, 3.89 mmol of YCl_3, 0.72 mmol of $YbCl_3$ and 0.24 mmol of $ErCl_3$ were dissolved in 10 mL of methanol and added dropwise to the first solution. The resulting solution was heated up to 65ºC for 2 hours under stirring. Finally, the resulting slurry was centrifuged and washed three times with methanol, and the precipitate was dried at 60ºC for 12 hours.

2.2 Synthesis of water soluble CdTe QDs. CdTe quantum dots were prepared following the method by Li. et al.[19].

In a 100 mL flask, 0.6 mmol of $CdCl_2$, 50 mL of H_20 and 66 µL of MPA were mixed and the pH was adjusted to 11 with NaOH 1 M. When reaching the desired pH, the flask was filled with Ar and the solution stirred for 30 min. At the same time, the NaHTe precursor was prepared in a 5 mL flask, mixing 0.1 mmol of Te, 1.9 mmol of $NaBH_4$ and 0.75 mL of H_20. Then an Ar flow was introduced and it was left stirring until it became colourless.

After 30 min, the temperature of the first flask was increased up to 100ºC and when the precursor was colourless, it was quickly injected.

Then, the synthesis was held for 30 min in order to achieve the desired quantum dot nanocrystals without further purification steps.

2.3 Synthesis of hydrotalcite. Mg/Al hydrotalcite with a molar Mg/Al ratio of 3 was synthesized by precipitation at constant pH 10. Briefly, aqueous solutions of $Mg(NO_3)_2$*$6H_2O$ (0.75 M) and $Al(NO_3)_3$*$9H_2O$ (0.25 M) were put in contact with the precipitating agent, i.e. NaOH and Na_2CO_3, 2 M each. The precipitate slurry was aged at room temperature for 12 h under mechanical stirring (500 rpm), followed by filtration, washing and drying at 60ºC for 12 h.[20]

The synthesis of Co/Al was done following the same ratio as for Mg/Al, but instead of $Mg(NO_3)_2$*$6H_2O$, $Co(NO_3)_2$*$6H_2O$ was used.

2.4 Incorporation of KYF_4: Yb^{3+},Er^{3+} in hydrotalcite by anion exchange. 50 mg of as-synthesized hydrotalcite (MgAl or CoAl) were mixed with 20 mL of KYF_4: Yb^{3+},Er^{3+} (1 mg/mL in a 1:1 v/v ethanol: water reaction medium) and stirred at 600 rpm for 48h at

ambient conditions. Then it was left to age at room temperature for 50 hours. After the ageing period, the mixtures were centrifuged in all the cases, and the pellets were washed with deionized water, then left to dry overnight.

2.5 Incorporation of CdTe in hydrotalcite by anion exchange. In parallel, 10 mL of CdTe were put in contact with 50 mg of as-synthesized hydrotalcite (MgAl or CoAl) and stirred at 600 rpm for 1 h, at ambient conditions. Then, the mixture was left aging at room temperature for 24 hours. After the ageing period, the mixtures were centrifuged in all the cases, and the pellets were washed with deionized water, then left to dry overnight.

3. Results and discussion

3.1 As-synthesized nanomaterials KYF_4: Yb^{3+},Er^{3+} up-conversion nanoparticles.

XRD analysis of the powder up-conversion nanoparticles showed (Figure 1) that all of the diffraction peaks matched the pattern from KYF_4 (JCPDS: 27-466), except for the peak at $2\theta=43^{o}$ belonging to KY_3F_{10} (JCPDS=27-465), that is quite normal in the UCNP synthesis. Besides, the peaks were quite sharp indicating that the sample is highly crystalline.

For the fluorescence measurements, KYF_4: Yb^{3+},Er^{3+} nanoparticles were excited at 980 nm under Ar (Figure 2). The emission spectrum presents two peaks, one centered at 540 nm (corresponding to $^4S_{3/2}$—>$^4I_{15/2}$ transition of Er ion) and the other at 660 nm ($^4F_{9/2}$—>$^4I_{15/2}$ transition of Er ion.) [21]

The Ytterbium absorbs one photon and the energy goes from the ground level $^2F_{7/2}$ to the excitated state $^2F_{5/2}$. Then an energy transfer takes place from this level to the $^4I_{11/2}$ of the erbium that relaxes nonradiatively to the $^4I_{13/2}$ and if erbium absorbs another photon, the eletron can promote from that level to $^4F_{9/2}$, where it can relax radiatively with a wavelength around 640-655 nm. Also a second energy transfer process can happen from Yb to the $^4F_{7/2}$ level of Er, the ion can relax to the $^2H_{11/2}$ and to $^4S_{3/2}$ without emitting, but from those states when it relaxes it emits at 525 and 540 nm respectively.

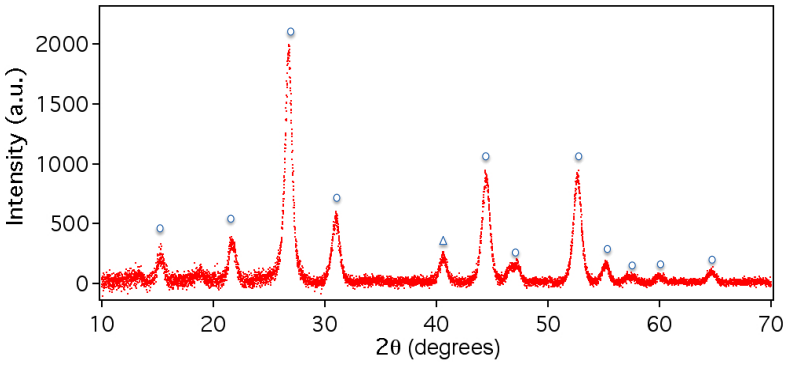

Figure 1. *XRD of KYF_4:Yb^{3+}, Er^{3+}. Legend: KYF_4 phase (dots), KY_3F_{10} phase (triangles).*

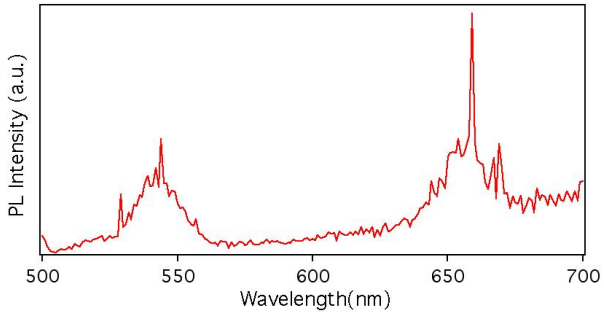

Figure 2. *Fluorescence spectrum of KYF_4: Yb^{3+}, Er^{3+} excited at 980 nm.*

When the infrared of KYF_4: Yb^{3+},Er^{3+} was studied (Figure 3), two vibration bands were the most predominant, one around 3400 cm^{-1} from the stretching of the H bonded from the –OH and the other one centered at 1630 cm^{-1} due to the bending mode of H-O-H from the water.

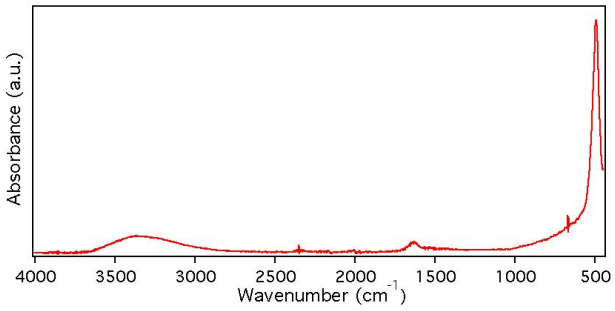

Figure 3. *IR of KYF_4: Yb^{3+}, Er^{3+}.*

The average size of KYF_4: Yb^{3+}, Er^{3+} nanoparticles as determined by electron microscopy was around 10 nm, ranging from 6 to 15 nm as can be seen in Figure 4, with a very low dispersity. This is in very good agreement with the XRD results with respect to the size of the particles.

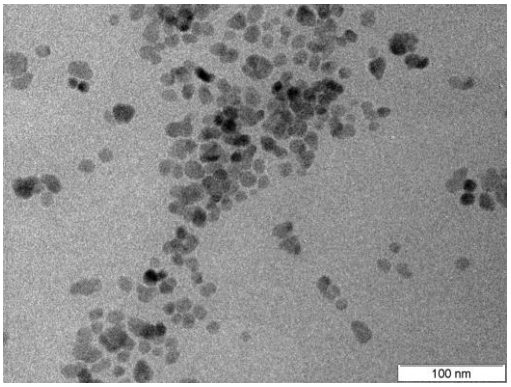

Figure 4. *TEM image of KYF_4: Yb^{3+}, Er^{3+}.*

Compositional study by EDX showed the presence of K, Y, F, Yb, Er in the main material.

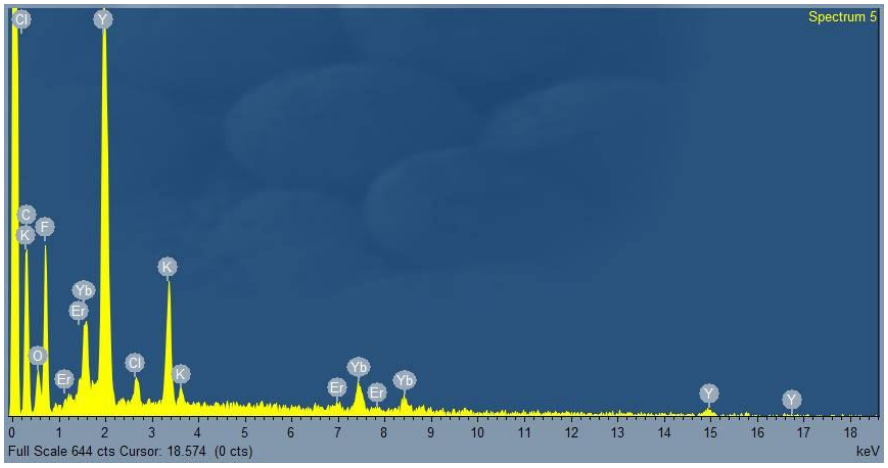

Figure 5. *EDX of KYF_4:Yb^{3+},Er^{3+}*

3.2 CdTe quantum dot nanocrystals

The maximum peak of emission is at 525 nm (Figure 6a) after excitation at 405 nm, corresponding with a green emission for the CdTe. The emission is in agreement with the size (Figure 6b) that is around 10nm.

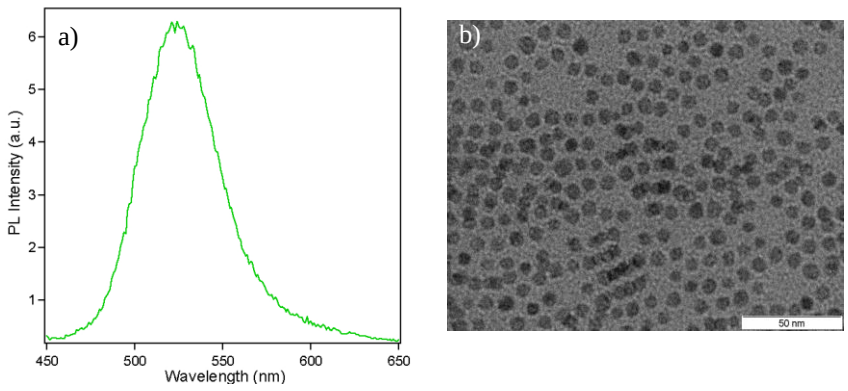

Figure 6. *a) Emission spectra of green CdTe QDs. b) TEM image of CdTe QDs*

3.3 Incorporation of $KYF_4:Yb^{3+},Er^{3+}$ or CdTe in MgAl hydrotalcite by anion exchange.

Figure 7 depicts the incorporation of CdTe quantum dots into MgAl hydrotalcite following the anion exchange process. When pouring the white MgAl hydrotalcite powder into the CdTe aqueous solution (Figure 7a), the mixture has a yellowish colour attributed to the presence of quantum dots. After 1 day uptake (Figure 7b), the reaction mixture became colorless and the host hydrotalcite adquired a yellow shading. These visual observations clearly indicate a total adsorption of the quantum dots by the hydrotalcite. Figure 7c supports the latter statement, indicating that only the precipitate (CdTe- MgAl HT) displays emission under the UV light. After the anion exchange, both the pellet and the supernatant were characterized.

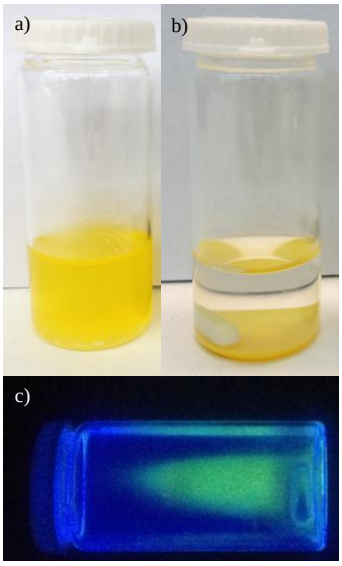

Figure 7*. Photograph of HT Mg/Al with CdTe. a) t= 0 min under daylight ,b) at 24 h under daylight , and c) t=24 h under UV light.*

In parallel, the up-conversion nanoparticles undergone the same procedure and characterization steps. However, the image of the UCNP- MgAl HT is not shown since the IR laser can not be used for safety reasons outside the fluorimeter for photography purposes.

Figure 8 comparatively illustrates the XRD patterns of the solids resulting from the treatment of MgAl hydrotalcite with the UCNP nanoparticles (Figure 8a) and CdTe quantum dots (Figure 8b), respectively. The X-ray diffraction confirmed the hydrotalcite (JCPDS 22- 700) as one of the crystalline phases in the precipitate as well as the UCNP and the CdTe.

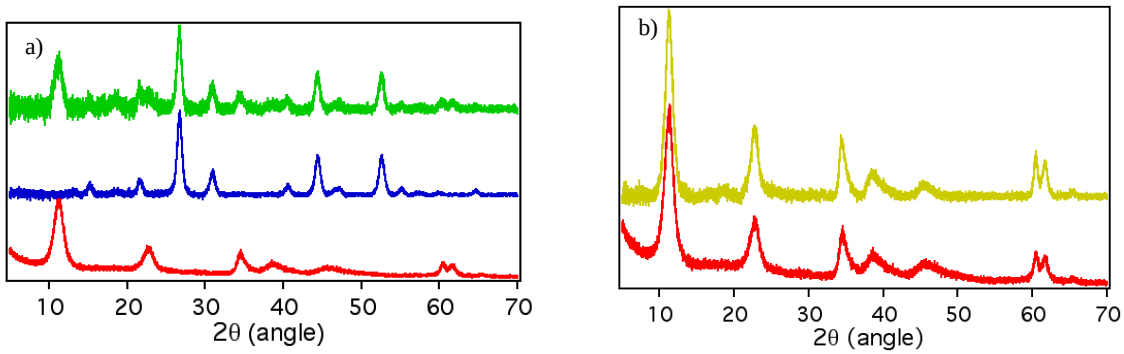

Figure 8. *XRD diffraction patterns of the solids resulting from the treatment of MgAl hydrotalcite with the UCNP nanoparticles (Figure 8a) and CdTe quantum dots (Figure 8b). Legend: MgAl HT (red), KYF_4: Yb^{3+}, Er^{3+} (blue), MgAl HT - KYF_4:Yb,Er (green), and MgAl HT - CdTe (yellow).*

Interestingly, upon the treatment of MgAl HT with the UCNP, MgAl HT - KYF_4:Yb^{3+},Er^{3+} succesfully displayed the hydrotalcite structure as shown in Figure 8a. To the best of our knowledge, this is the first time hydrotalcite was investigated as matrix for the up-conversion nanoparticles. Besides, reflections characteristic to the up-conversion material are visibile indicating the presence of UCNP in the interlayer space. In the case of CdTe QDs, as expected, MgAl HT – CdTe also exhibited the hydrotalcite structure. Previous studies in the literature demonstrated the incorporation of quantum dots into hydrotalcite either by anion exchange or delamination-restacking for imaging purposes or photovoltaics.[22]

Figure 9 shows the infrared spectrum of MgAl HT with characteristic vibration bands at 3450 cm^{-1} (O-H stretching), 1630 cm^{-1} (H-O-H bending from the water), 1465 and 1100 cm^{-1} (υ_3 vibrating mode of carbonate, antisymetric streching), 1380 cm^{-1} (symetric stretching of carbonate), 620 cm^{-1} (Mg-O translation modes) and 570 cm^{-1} (Al-O streching vibration). The infrared spectrum of MgAl HT - KYF_4:Yb^{3+},Er^{3+} in Figure 9a reveals new bands characteristic to KYF_4 at 1500 cm^{-1} (υ_2 H-O-H bending) and 1150 cm^{-1} (δ in plane vibration of O-H from the methanol), additionally to the hydrotalcite bands, which were preserved after the incorporation of the nanoparticles, in support to the XRD results.

Figure 9b shows the vibration bands of the mercaptopropionic acid MPA functionalized-CdTe QDs, which appear at 1550 cm^{-1} (asimetric stretching from the O-C-O of the acid that also can form a bridge with the metals of the HT) and 1280 cm^{-1} (wagging vibration of CH_2).[23]

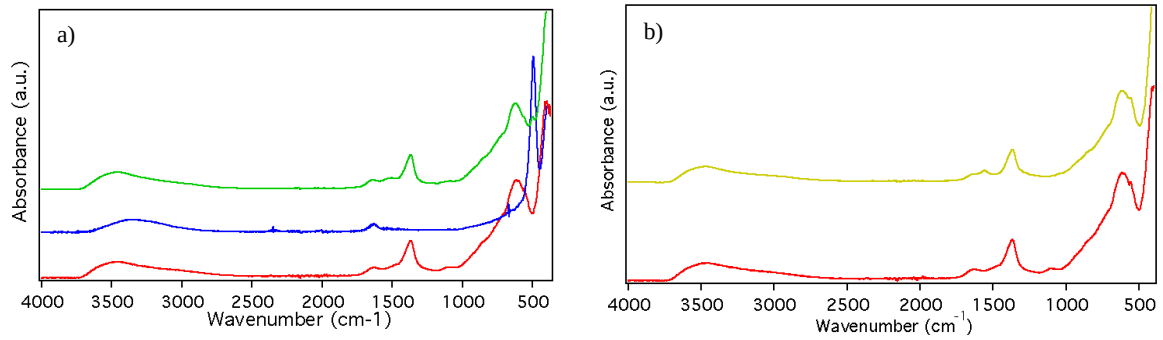

Figure 9. *Infrared of the solids after the treatment of MgAl hydrotalcite with the a) UCNP nanoparticles and b) CdTe quantum dots Legend: MgAl HT (red), KYF_4: Yb^{3+}, Er^{3+} (blue), MgAl HT - KYF_4:Yb^{3+},Er^{3+} (green), and MgAl HT - CdTe (yellow).*

The as-synthesized MgAl hydrotalcite featured the platelet-like morphology characteristic of these layered materials as revelead by the electron microscopy analysis. After the anion exchange procedure, the morphology of the hydrotalcite did not suffer any change (Figure 10). In addition to the laminar structure, UCNP nanoparticles (KYF_4:Yb^{3+},Er^{3+}) can be observed in Figure 10a, in agreemnt with the results obtained by X-ray diffraction and infrared. The same holds for CdTe-MgAl HT in Figure in 10b.

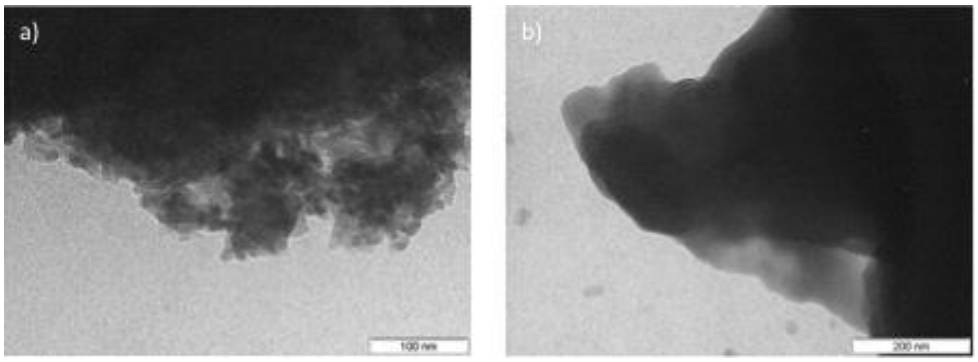

Figure 10. *TEM image of a) HT Mg/Al- KYF_4:Yb^{3+},Er^{3+} and b) HT Mg/Al-CdTe*

Finaly the photoluminescence spectra (Figure 11) were recorded to investigate the properties of the hybrid materials, UCNP - MgAl HT and CdTe - MgAl HT, respectively, with respect to the luminescent nanoparticles alone.

As shown in Figure 11, KYF_4: Yb^{3+},Er^{3+} – MgAl HT displays the same emission of KYF_4:Yb^{3+},Er^{3+} alone. The two emission peaks of the UCNP are still present (green line with peaks at 550 and 660 nm), with improved overall emission spectrum due to the protection effect to air and water offered by the hydrotalcite.

It has been previously reported that both, air and water affect the emission of the UCNP. To avoid this, normally the UCNP are encapsulated and for this needs previous functionalization.

Even though water and air do not affect QDs emission, for bio applications, normally they are embedded with silica, and for this, more functionalization has to be done.

In our case, the hydrotalcite acts as a protective shell so the host does not need further modification.

The supernatant obtained after separating and collecting KYF_4: Yb^{3+},Er^{3+} – MgAl HT did not show any emission (black line in Figure 11a).

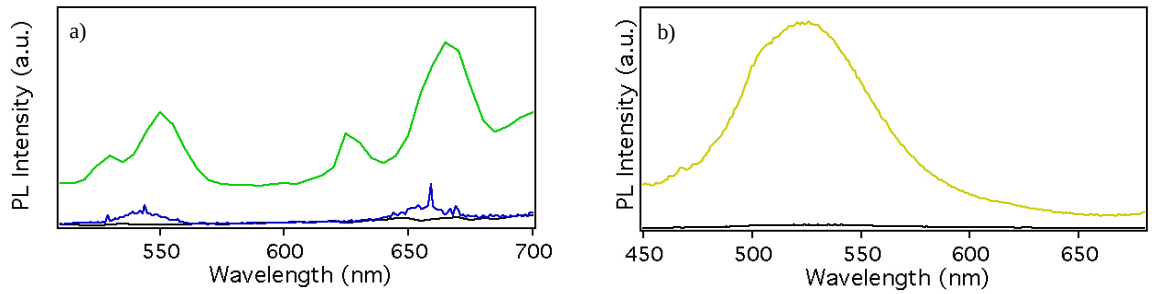

Figure 11. *Fluorescence comparision after the interaction of Mg/Al HT with a) UCNP and b) CdTe QDs. Legend: supernatants of the exchange (black), KYF_4: Yb^{3+}, Er^{3+} (blue), MgAl HT - KYF_4:Yb^{3+},Er^{3+} (green), and MgAl HT - CdTe (yellow).*

As expected, the photoluminescence of the solid CdTe - MgAl HT (Figure 11b) exhibited the same profile as the CdTe quantum dots in solution (maximum peak at 525 nm, Figure 6) confirming the presence of the emitting nanocrystals in the hydrotalcite structure.

The photoluminescence from the supernatant was also measured in both cases (black line in Figure 11b) and the emission was near to 0, what can be due to the fact that there was no UCNP or CdTe present.

3.4 Incorporation of KYF_4:Yb^{3+},Er^{3+} or CdTe in CoAl hydrotalcite by anion exchange

After succesfully demonstrating the incorporation of KYF_4: Yb^{3+},Er^{3+} into MgAl hydrotalcite, we envisaged a new system designed on the same layered material. The new approach started from CoAl hydrotalcite and KYF_4:Yb^{3+},Er^{3+} or CdTe, respectively. Thus, the generated hybrid materials would be biocompatible, luminescent and magnetic concomitantly.

In the last years, the scientists focused on developing nanomaterials that display more than one property of interest at the same time. Moreover, magnetic nanoparticles are highly required in different areas like imaging (MIR) and therapy for cancer (hyperthermia, magnetic gradients…).[24] So far, gold and iron-derived nanoparticles were highly investigated. Nevertheless, they require further functionalization toward bioapplications. Since the

hydrotalcite-like materials are biocompatible with the cellular membranes, no additional functionalization is required.

Figure 12 depicts the incorporation of CdTe quantum dots into CoAl hydrotalcite following the anion exchange process. Differently from MgAl HT which is white, the colour of CoAl HT is brown (Figure 12a). After 24 hours of contact (Figure 12b), the initial yellow colour of the solution (given by the quantum dots) disappears leading to a colourless supernatant indicating the QDs uptake by the hydrotalcite. However, when the reaction mixture, both precipitate and supernatant, were excited with UV light, no signal was visible (Figure 12c). This results differs from the CdTe-MgAl HT approach were the precipitate was luminescent as a consequence of the QDs uptake. The result obtained with the CoAl hydrotalcite suggests a change in the QDs photoluminescence, *i.e.* quenching, or alternatively, the absence of QDs.

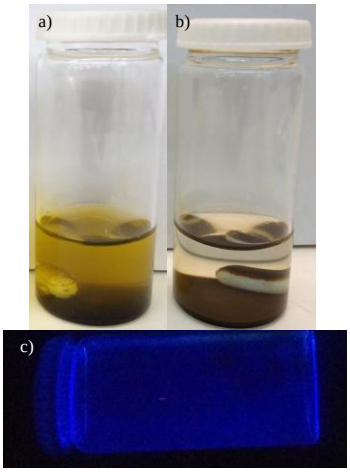

Figure 12. *Photograph of HT Co/Al with CdTe. a) t= 0 min under daylight ,b) at 24 h under daylight , and c) t=24 h under UV light.*

In parallel, the up-conversion nanoparticles undergone the same procedure and characterization steps. However, the image of the UCNP- CoAl HT for the same reasons as in the case with MgAl HT.

After the anion exchange, the pellet and the supernatant were characterized for the QDs and UCNP, respectively.

Figure 13 comparatively illustrates the XRD patterns of the solids resulting from the treatment of CoAl hydrotalcite with the UCNP nanoparticles (Figure 13a) and CdTe quantum dots (Figure 13b), respectively. The X-ray diffraction confirmed both the CoAl hydrotalcite (JCPDS 27-466) and the KYF_4: Yb^{3+},Er^{3+} nanoparticles are present. In the case of CdTe QDs, as expected, CoAl HT – CdTe also exhibited the hydrotalcite structure.

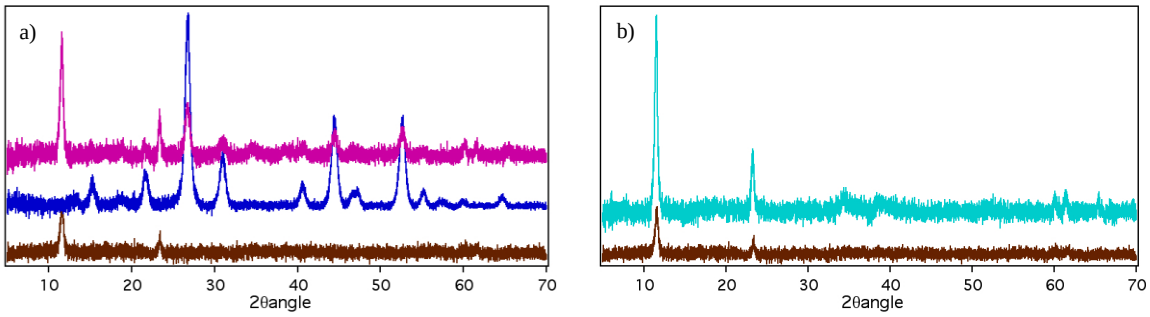

Figure 13. *XRD diffraction patterns of the solid after the treatment of Co/Al hydrotalcite with a) UCNP and b) CdTe QDs. Legend: HT Co/Al (brown), $KYF_4:Yb^{3+},Er^{3+}$ (blue), HT Co/Al-$KYF_4:Yb^{3+},Er^{3+}$ (pink) , and HT Co/Al-CdTe (light blue).*

Next, an infrared study was performed as shown in Figure 14. CoAl HT displayed the characteristic vibration spectrum of hydrotalcites: 3410, 3070 and 1630 cm^{-1} (O-H from the water and the methanol, as in MgAl HT), 1380 and 1220 cm^{-1} (υ_3 vibrating mode of carbonate, antisymetric steching), 570 cm^{-1} (Al-O streching vibration) and 770 cm^{-1} (Co-O streching vibration), that also appear in the final sample HT Co/Al-KYF_4: Yb^{3+},Er^{3+} and HT Co/Al-CdTe.

The infrared spectrum of CoAl HT - KYF_4: Yb^{3+},Er^{3+} in Figure 14a reveals new bands characteristic to KYF_4 at 1540 cm^{-1} (υ_2 H-O-H bending) and 1100 cm^{-1} (δ in plane vibration of O-H from the methanol), additionally to the hydrotalcite bands. Figure 14b shows the vibration bands from the MPA of the CdTe at 1570, and 1280 cm^{-1} as described previously. The results obtained from the infrared measurements confirm the presence of the nanoparticles in the hydrotalcite, in addition to the XRD.

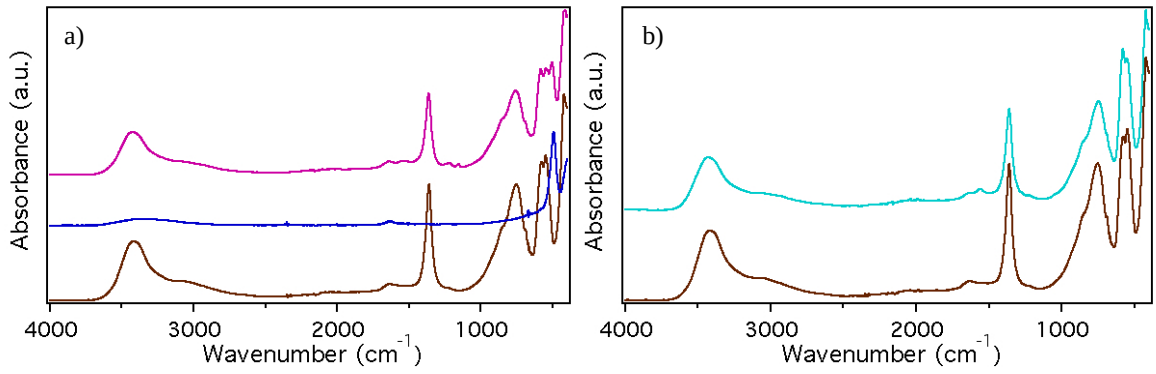

Figure 14. *Infrared peaks of the solid of HT Co/Al after treatment with a) UCNP and b) CdTe QDs. Legend: HT Co/Al (brown), $KYF_4:Yb^{3+},Er^{3+}$ (blue), HT Co/Al-$KYF_4:Yb^{3+},Er^{3+}$ (pink), HT Co/Al-CdTe (light blue)*

In line with the MgAl HT, the as-synthesized CoAl hydrotalcite featured the laminar morphology as revelead by the electron microscopy analysis in Figure 15. Besides, UCNP

nanoparticles (KYF_4:Yb^{3+},Er^{3+}) can be observed in Figure 15a, in agreement with the results obtained by X-ray diffraction and infrared. The same holds for CdTe-MgAl HT in Figure in 15b.

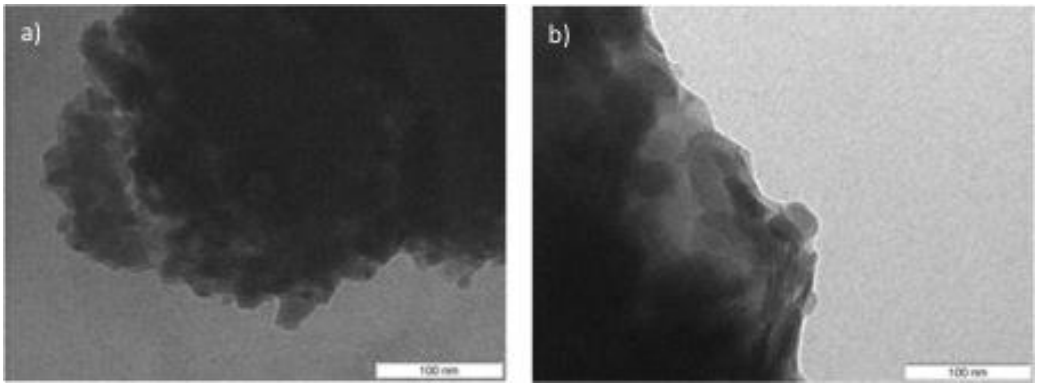

Figure 15. *TEM image of a) HT Co/Al- KYF_4: Yb^{3+},Er^{3+} and b) HT Co/Al-CdTe. Legend: UCNP (blue arrow), hydrotalcite layers (red arrow)*

The presence of UCNP or QDs between the layers of hydrotalcite was successfully confirmed by the previous techniques. However, the absence of any fluorescence under the UV lamp intrigued us to further investigate the precipitate and the supernatant samples.

As shown in Figure 16a, the emission profile of KYF_4: Yb^{3+},Er^{3+} – CoAl HT changed with respect to that of KYF_4: Yb^{3+},Er^{3+}. This indicates the high influence of the cobalt on the emission of the up-conversion nanoparticles. If the emission peak at 550 nm completely disappeared, the peak at 650 nm is slightly displayed, which could suggest a stronger influence of cobalt on the transitions responsible for the peak at 550 nm, it may affect the transition from Yb to the $^4F_{7/2}$ level of Er, or the relaxation from $^2H_{11/2}$ and to $^4S_{3/2}$. The quenching of UCNP by Co was previously demonstrated by Saleh et al. [25] The supernatant obtained after separating and collecting KYF_4: Yb^{3+},Er^{3+} – CoAl HT did not show any emission (Figure 16a).

The photoluminescence of CdTe - CoAl HT and the corresponding supernatant was also measured (Figure 16b) exhibiting no emission. These results clearly confirm the quenching of quantum dots in the presence of cobalt. Previous studies in the literature investigated the influence of several cations in solution on the emission of quantum dots and reported by Zhong et al.[26]

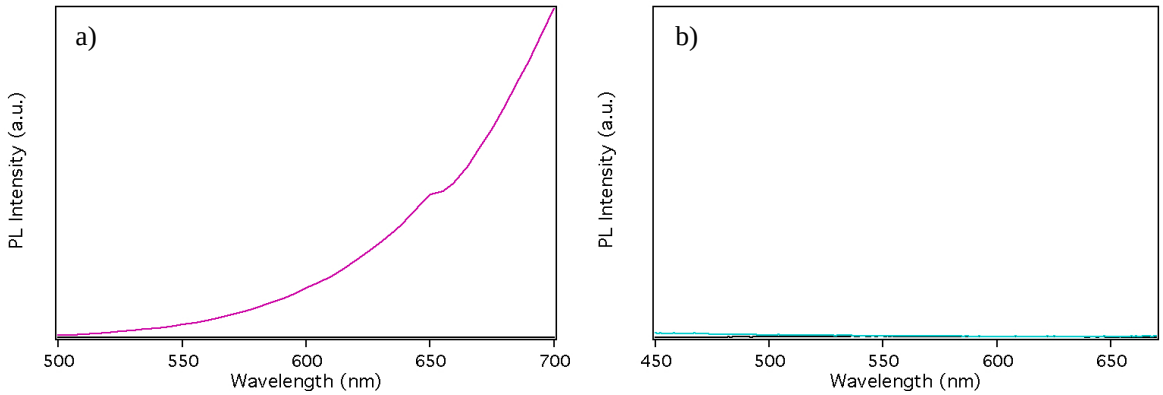

Figure 16. *Fluorescence comparision after the interaction of Co/Al HT with a) UCNP and b) CdTeQDs. Legend: supernatants of the exchange (black), HT Co/Al-KYF$_4$:Yb^{3+},Er^{3+} (pink), HT Co/Al-CdTe (light blue).*

4. Conclusion

After the anion exchange of UCNP and QD in Mg/Al and Co/Al HT, the resulting material was fully characterized, and for this, different techniques like IR, XRD, TEM, EDX and fluorescence were employed.

All was in agreement after the exchange, in the IR appeared peaks of the UCNP or the QD and the HT, as well as in XRD.

From TEM images, even the layers from the HT with the UCNP in between could be observed.

The only difference present after the exchange was for the fluorescence in the case of Co/Al HT.

The fluorescence in the case of Mg/Al HT for both, UCNP and QD, remained unchanged, but in the case of the Co/Al one, there was a quench for both hosts, but with a difference, for QD the quench was total, no emission was registered (not in the solid or in the supernatant), because the Cobalt traps the electrons from the excitation of the quantum dot, preventing the relaxation and the consequent emission.

However, for UCNP there is still present a slight peak of emission at 650 nm, that could be explained saying that the Cobalt only traps one of the electrons (maybe the one of the emission at 650) allowing the other one to relax and emit.

These materials could be used as a detector of Cobalt in water, or even in vivo, taking advantage of the internalization of the material in the cells,as well as for the photo-tracking of proteins in the body attaching antibodies to the UCNP or the QDs.

References

1. Bruchez Jr., M. Semiconductor Nanocrystals as Fluorescent Biological Labels. *Science.* **281,** 2013–2016 (1998).

2. Wang, L., Nagesha, D. K., Selvarasah, S., Dokmeci, M. R. & Carrier, R. L. Toxicity of CdSe Nanoparticles in Caco-2 Cell Cultures. *J. Nanobiotechnology* **6,** 11–26 (2008).

3. Serrano, I. C., Ma, Q. & Palomares, E. QD-'Onion'-Multicode silica nanospheres with remarkable stability as pH sensors. *J. Mater. Chem.* **21,** 17673–17679 (2011).

4. Auzel, F. Upconversion and anti-Stokes processes with f and d ions in solids. *Chem. Rev.* **104,** 139–73 (2004).

5. Chen, J. & Zhao, J. X. Upconversion nanomaterials: synthesis, mechanism, and applications in sensing. *Sensors* **12,** 2414–35 (2012).

6. Vennerberg, D. & Lin, Z. Upconversion Nanocrystals: Synthesis, Properties, Assembly and Applications. *Sci. Adv. Mater.* **3,** 26–40 (2011).

7. Cheng, L., Wang, C. & Liu, Z. Upconversion nanoparticles and their composite nanostructures for biomedical imaging and cancer therapy. *Nanoscale* **5,** 23–37 (2013).

8. Zou, W., Visser, C., Maduro, J. A., Pshenichnikov, M. S. & Hummelen, J. C. Broadband dye-sensitized upconversion of near-infrared light. *Nat. Photonics* **6,** 560–564 (2012).

9. Pan, A. C. *et al.* Enhancement of up-conversion efficiency by combining rare earth-doped phosphors with PbS quantum dots. *Sol. Energy Mater. Sol. Cells* **94,** 1923–1926 (2010).

10. Bednarkiewicz, A., Nyk, M., Samoc, M. & Strek, W. Up-conversion FRET from Er 3+ /Yb 3+ :NaYF 4 Nanophosphor to CdSe Quantum Dots. *J. Phys. Chem. C* **114,** 17535–17541 (2010).

11. Li, Z., Zhang, Y. & Jiang, S. Multicolor Core/Shell-Structured Upconversion Fluorescent Nanoparticles. *Adv. Mater.* **20,** 4765–4769 (2008).

12. P Nalawade, B Aware, V J Kadam, R. S. H. Layered double hydroxide: A review. *Layer. double hydroxides A Rev.* **68,** 267–272 (2009).

13. Li, F., Tan, Q., Evans, D. G. & Duan, X. Synthesis of carbon nanotubes using a novel catalyst derived from hydrotalcite-like Co-Al layered double hydroxide precursor. *Catal. Letters* **99,** 151–156 (2005).

14. Hong, C., Qi-dan, L., Wen-gong, Z. & Zheng-hua, L. Luminescent drug-containing hydrotalcite-like compound as a drug carrier. *Chem. Eng. J.* **185-186,** 358–365 (2012).

15. Stoica, G. *et al.* Layered double hydroxides as carriers for quantum dots@silica nanospheres. *Nanoscale* **4,** 5409–19 (2012).

16. Castelló Serrano, I., Stoica, G., Figuerola, A. & Palomares, E. Photoluminescent CdSe@CdS/2D as potential biocompatible materials. *J. Mater. Chem. B* **1,** 793–800 (2013).

17. Posati, T. *et al.* Selective internalization of ZnAl-HTlc nanoparticles in normal and tumor cells. A study of their potential use in cellular delivery. *Appl. Clay Sci.* **55,** 62–69 (2012).

18. Kai, C., Chao, G., Bo, P. & Wei, W. The Influence of SiO2 Shell on Fluorescent Properties of LaF3:Nd3+ /SiO2 Core/Shell Nanoparticles. *J. Nanomater.* **2010,** 1–5 (2010).

19. Li, L., Qian, H., Fang, N. & Ren, J. Significant enhancement of the quantum yield of CdTe nanocrystals synthesized in aqueous phase by controlling the pH and concentrations of precursor solutions. *J. Lumin.* **116,** 59–66 (2006).

20. Salomão, R., Milena, L. M., Wakamatsu, M. H. & Pandolfelli, V. C. Hydrotalcite synthesis via co-precipitation reactions using MgO and Al(OH)3 precursors. *Ceram. Int.* **37,** 3063–3070 (2011).

21. Patel, D. N. *et al.* Strong Visible Upconversion in Rare Earth Ion-Doped NaYF4 Crystals. in *Frontiers in Optics 2009/Laser Science XXV/Fall 2009 OSA Optics & Photonics Technical Digest* JWC13 (OSA, 2009). doi:10.1364/LS.2009.JWC13

22. Wang, X. *et al.* Investigation of the role of anions in hydrotalcite for quasi-solid state dye-sensitized solar cells application. *J. Mater. Chem. A* **1,** 4345–4351 (2013).

23. Castro, J. L., Lopez-Ramirez, M. R., Arenas, J. F. & Otero, J. C. Surface-enhanced Raman scattering of 3-mercaptopropionic acid adsorbed on a colloidal silver surface. *J. Raman Spectrosc.* **35,** 997–1000 (2004).

24. Kim, E., Lee, K., Huh, Y.-M. & Haam, S. Magnetic nanocomplexes and the physiological challenges associated with their use for cancer imaging and therapy. *J. Mater. Chem. B* **1,** 729–739 (2013).

25. Saleh, S. M., Ali, R. & Wolfbeis, O. S. Quenching of the luminescence of upconverting luminescent nanoparticles by heavy metal ions. *Chemistry* **17,** 14611–7 (2011).

26. Zhong, W., Liang, J. & Yu, J. Systematic study of the interaction of cobalt ions with different-sized CdTe quantum dots. *Spectrochim. Acta. A. Mol. Biomol. Spectrosc.* **74,** 603–6 (2009).

UNIVERSITAT ROVIRA I VIRGILI
SEMICONDUCTOR NANOPARTICLES AS PLATFORM FOR BIO-APPLICATIONS AND ENERGY RELATED SYSTEMS.
Alba María Matas Adams
Dipòsit Legal: T 55-2016

Chapter 6

Lanthanide-doped nanoparticles for specific recognition of toll-like receptor (TLR) in human neutrophils

UNIVERSITAT ROVIRA I VIRGILI
SEMICONDUCTOR NANOPARTICLES AS PLATFORM FOR BIO-APPLICATIONS AND ENERGY RELATED SYSTEMS.
Alba María Matas Adams
Dipòsit Legal: T 55-2016

1. Introduction

Neutrophils are an integral part of the human immune system and because of this they present important roles by engaging in early defense mechanisms against invasive microorganisms and pathogens.

Neutrophils rapidly can be found in the infection sites, limiting its spread and subsequently allowing recruitment and activation of other immune cells. As a result, pathogens are cleared and the immune response is triggered.[1,2] Moreover, neutrophils are able to discriminate between self and foreign molecules and microbial pathogens, a mechanism which relies on the evolutionary conserved family of the proteins called toll-like receptors (TLRs).

TLRs are type I transmembrane proteins comprising of an amino-terminal leucine-rich repeat (LRR) domain and a carboxyl-terminal Toll-interleukin-1 receptor (TIR) domain, wherein LRR domain is predominantly responsible for pathogen-associated microbial patterns (PAMP) recognition and the TIR domain is involved in intracellular signaling.[3,4] In mammalians, TLRs play a critical role in the early innate and adaptive immune responses through production of proinflammatory cytokines and chemokines, upregulation of co-stimulatory molecules and activation of antigen presentation by recognizing highly conserved structural motifs known as PAMPs, which include various bacterial cell wall components such as lipopolysaccharide (LPS),[5] peptidoglycan and lipopeptides, bacterial DNA and viral double-stranded RNA.[6,7]

To date, numerous luminescent materials, including fluorescent proteins,[8] organic dyes,[9] and semiconductor quantum dots (QDs),[10,11] have been developed as fluorescent probes for bio-imaging of TLR based on the single-photon excitation: emitting low energy fluorescence when excited by high energy light. In the last decade, rare-earth- or lanthanide-doped up-conversion nanoparticles (UCNP) are emerging as a promising alternative to the conventional fluorescent labels due to their unique photo-physical properties such as converse excitation and emission profiles wherein they are excited at near infrared (NIR) wavelength of 980 nm and emit at higher energy in the visible range or at shorter NIR wavelength.[12]

This phenomenon allows notable tissue penetration depth (>3.2 cm), a fluorescence of 6-8 orders of magnitude brighter than conventional fluorescence based imaging probes in two-photon processes, and use with minimal light scattering and

background from the surrounding biological tissue.[13,14] UCNP are being currently used in targeting and labeling of stem cells,[15] tumor derived cells,[16] cell surface antigens, diagnostic,[17] immunohistochemistry assays,[18] detection of pathogenic bacteria,[19] and reporters in nucleic acid microarrays.[20] Although the specific endocytic mechanism by which cells internalize nanoparticles such as UCNP is still a subject under debate, the mechanism of cellular uptake is important in the field of nanomedicine, cancer diagnosis, drug delivery and treatment.

The application of UCNP nanoparticles in bioimaging represents a versatile approach. It is known that UCNP exhibit fluorescence at both the original wavelength of 980 nm, in which case they require a novel laser diode emitting at 980 nm as excitation source, and at the second-harmonic wavelength of 488 nm, respectively.[21–23] The latter case implies the manipulation of UCNP on conventional imaging systems. This is attributed to the direct Er^{3+} excitation at the harmonic wavelength with indirect Yb^{3+} excitation, in contrast to the direct excitation of Yb^{3+} and the various up-conversion energy transfer processes at 980 nm.[23] The different probability of emitting wavelength (either green 540 nm or red 660 nm) is attributed to the smaller number of photons required to fill up the energy mismatch among the energy transfer processes (Scheme annex A1).[24]

The use of UCNP excited at 488 nm is similar to that of organic dyes or quantum dots in terms of photoluminescent processes involved. In contrast, UCNP display exceptionally longer luminescence lifetimes, i.e. microseconds versus nanoseconds.[25] This characteristic, together with the drawbacks of the organic dyes (poor photochemical stability, low quantum yield, easy deterioration in biological environments) or quantum dots (blinking, toxicity),[26,27] makes UCNP excellent candidates for cell imaging and tracking of molecules.

The immune system relies on a vast array of non-clonally expressed pattern recognition receptors for the detection of pathogens. Pattern recognition receptors bind conserved molecular structures shared by large groups of pathogens, termed pathogen-associated molecular patterns. The TLRs are a recently discovered family of pattern recognition receptors.

Herein, we report the conjugation of UCNP (KYF_4:Yb,Er) with streptavidin (Scheme 1) as the final coating element to recognize TLR in neutrophils through biotinylated lipopolysaccharide (LPS). This step is a prerequisite in elucidating unresolved

questions about the detailed molecular UCNP uptake mechanism by human neutrophils.

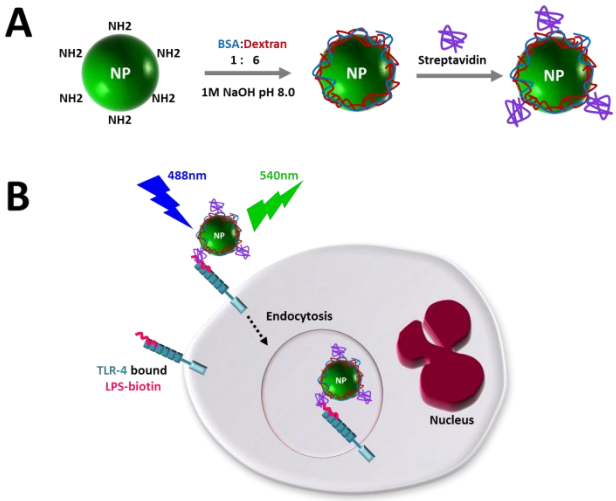

***Scheme 1**. a) Functionalization of UCNP (not to scale). b) Recognition of Biotin-LPS bound TLR4 and internalization of functionalized UCNP into neutrophils.*

2.Experimental

2.1 Synthesis of KYF_4:Yb,Er –APTMS. For the synthesis of KYF_4:Yb,Er 12 mmol KF were dissolved in 20 ml methanol, in a 50 ml round bottom flask, and heated up to 65ºC. In a separated flask, 3.89 mmol YCl_3•6 H_2O, 0.72 mmol $YbCl_3$•6 H_2O and 0.24 mmol $ErCl_3$•6 H_2O were dissolved in 10 mL methanol and added dropwise to the first solution. The resulting solution was kept at 65ºC with 800 rpm stirring for 2 hours. Further, the solution was centrifuged and washed three times with methanol.

For the addition of amino functional group, the method by Gorris et al. was followed[28] with some modifications. 80.5 mg KYF4:Yb,Er were dissolved in 13.5 ml toluene and 403 µL of APTMS (aminopropyltrimethyl sylane) were added. This was kept under N_2 with stirring for 24 hours. Then, the mixture was centrifuged for 20 min at 4000 rpm and washed three times with a mixture ethanol:acetone (1:1). The pellet was dried overnight at 60ºC.

2.2 Biofunctionalization of KYF_4:Yb,Er-APTMS with streptavidin. 1.2 mg of KYF_4:Yb,Er-APTMS were dissolved in a vial containing 1 mL Phosphate Buffer Saline (PBS). To this vial, 1 mL of glutaraldehyde (0.25 mg/mL) was added and the

mixture was stirred at 37ºC for 1 hour at 300 rpm. The resulting solution was centrifuged and the pellet washed three times with PBS.

5 mg of Bovine Serum Albumin (BSA) was mixed with 5 mg of Dextran in a molar ratio of 1:6 in water at pH 8.0 adding 0.1 mL of NaOH 1M in a total volume of 1 mL.[29] 0.5 mL of the mixture was added to 0.5 mL of glutaraldehyde-functionalized nanoparticles and stirred for 1 hour at 750 rpm. Then, the mixture was centrifuged and the BSA/Dextran-functionalized nanoparticles (BSA/Dex) were resuspended in 0.5 mL PBS.

Next, 0.5 mL of 0.1, 0.5, 1.0, 2.5 and 5.0 mg/mL of streptavidin, respectively, were added to UCNP-BSA-Dextran samples. The mixtures were stirred for 1 hour at 750 rpm, then centrifuged and washed three times with PBS, and stored in deionized water.

2.3 Agarose Gel Electrophoresis (AGE). Gels were hand cast with agarose in the appropriate buffers. 0.5 g of agarose was briefly boiled in 100 mL of TBE (Tris-Boric-EDTA) buffer 1x (Mixing 10 g of Tris-HCl, 5.5 g of boric acid and 4 mL of 0.5 M EDTA (Ethylene diamine tetraacetic acid) in a total volume of 1 L of deionized water), cooled and poured into a standard 7 cm^2 gel tray. Gels were horizontally immersed in TAE (Tris-Acetic-EDTA) (Mixing 4.8 g Tris-HCl, 1.14 g acetic acid and 2 mL of 0.5 M EDTA in a total volume of 1 L deionized water) buffer 1x for electrophoresis at 90 V for 90 min. Samples were diluted in 30% glycerol. For UCNP visualization, gels were placed on a UV transilluminator under UV excitation at 405 nm.

2.4 Isolation of neutrophils from human blood. Heparinized whole blood (20–30 mL) was collected from healthy human donors. After dextran sedimentation, granulocytes were isolated from the supernatant leukocyte-rich plasma by Ficoll-Hypaque gradient centrifugation and red blood cells were lysed with ammonium chloride solution.

2.5 Cellular uptake of the UCNP by neutrophils and Trypan Blue exclusion test for neutrophil viability. Neutrophils were incubated alone as a control of autofluorescence for 10 min (at 37ºC and 4ºC). For the rest of experiments, the neutrophils were incubated at 37ºC and 4ºC with 50 µL (1.2 mg/mL) of UCNP-APMTS or UCNP-BSA/dextran-Streptavidin in RPMI medium for 0, 2.5, 5 and 10

min in order to follow the uptake. In the case of the experiments for the specific recognition, neutrophils were preincubated with 0.1 mg/mL of biotinylated-LPS (from E. coli O111:B4) for 10 min at 4ºC.

For all the samples, the nucleus was stained with DRAQ5 dye (excitation at 633 nm and emission at 670 nm).

Imaging was performed by confocal microscopy (Olympus Fluoview FV 1000) with constant parameters throughout the experiments.

For quantitative image analysis ImageJ was used. Briefly, using ImageJ selection and drawing tools a region of interest was chosen on each cell in a background corrected confocal fluorescence image. Minimum of ten cells were analyzed in each image from a set of three separate images from three biological replicates and corrected total cell fluorescence was calculated. Neutrophil viability upon their incubation with UCNPs was determined by Trypan Blue dye exclusion test based on a previously established protocol.[29] Briefly, 1.2 mg/mL UCNP-APTMS and UCNP-APTMS-BSA/Dex-Strv were co-incubated with neutrophils in the absence and presence of biotinylated-LPS respectively for 10, 30, 60 and 180 min at 37ºC. After respective incubation time intervals neutrophils were washed and resuspended in RPMI media and were incubated with equal volume of 0.5% Trypan Blue solution. After three minutes unstained (viable) and stained (nonviable) neutrophil count was determined using a hemacytometer.

3. Results and discussion

3.1 Nanoparticle characterization and functionalization

Powder XRD analysis of the as-such KYF_4:Yb,Er up-conversion nanoparticles is shown in Fig. 1A. Two crystalline phases were identified: one corresponding to hexagonal KYF_4 (JCPDS 27- 466) and the second one to the cubic KY_3F_{10} form (JCPDS 27-465).[30] The high crystallinity of the sample is an indicative of small particles. This observation was also confirmed by the TEM measurements (Fig. 1B). The polyhedral crystals are uniform in size with very low dispersity (see inset). The average size of KYF_4:Yb,Er nanoparticles as indicated by the size histogram, determined from the electron microscopy analyses, was around 12 nm (Fig. 1C).

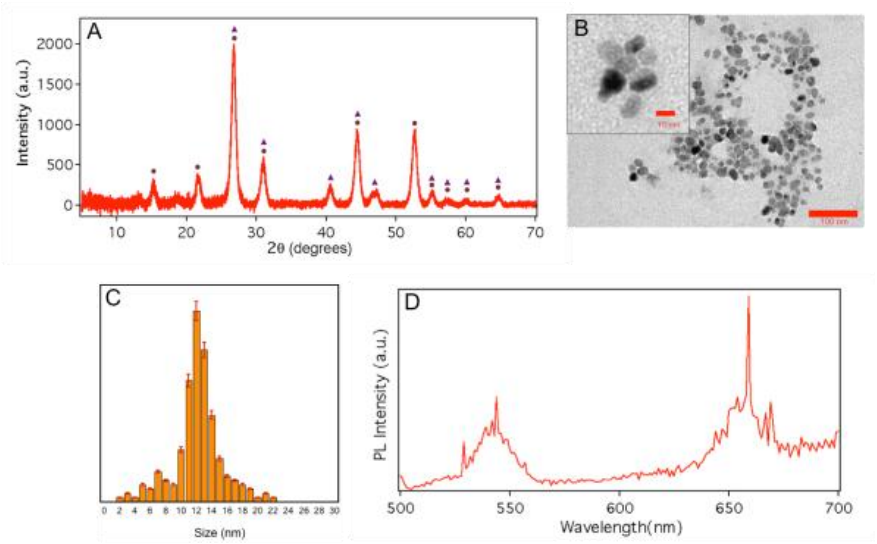

***Figure 1**. Nanoparticle characterization A) XRD pattern of KYF_4: Yb,Er. Symbols: KYF_4 (dots), KY_3F_{10} (triangles). B) TEM image of KYF_4:Yb, Er.(scale of image 100 nm and of inset 10 nm) C) Size histogram of KYF_4: Yb,Er. D) Fluorescence spectrum of KYF_4: Yb,Er nanoparticles; excitation under 980 nm light.*

The PL emission under 980 nm excitation presents two peaks (Fig. 1D), one centered at 540 nm, corresponding to the $^2H_{11/2} \rightarrow {}^4I_{15/2}$ and $^4S_{3/2} \rightarrow {}_4I_{15/2}$ transitions, and another one around 660 nm, corresponding to the $^4F_{9/2} \rightarrow {}^4I_{15/2}$ transitions, all of them transitions of Er^{3+}.[31] These two peaks are in good agreement with the emission wavelength in the energy level diagram in the Scheme annex A1. The lambda scan of UCNP excited using 488 nm laser by confocal laser scanning microscopy shows two emission peaks, i.e. 490-540 nm and 590-605 nm. In contrast to the predominant red emission at 660 nm obtained by excitation at 980 nm, excitation at the harmonic wavelength revealed a stronger green light emission, in agreement with previous studies using Yb,Er-doped nanocrystals at the same excitation wavelength.[32] The reason is that the electrons reach the $^4F_{7/2}$ level of Er^{3+} ion directly under 488 nm excitation, then they undergo a non-radiative process to reach the $^2H_{11/2}$ and $^4S_{3/2}$ levels, and only a few reach the $^4F_{9/2}$ level at the same time. Therefore, the strong green emission corresponding to the $^2H_{11/2}$, $^4S_{3/2} \rightarrow {}^4I_{15/2}$ transition and the weak red light corresponding to the $^4F_{9/2} \rightarrow {}^4I_{15/2}$ transition can be observed, respectively.[33]

The spectrum profile of the elemental mapping by EDX clearly shows the presence of the metals (Fig. A1). The detector measures the relative abundance versus their energy. The quantitative analysis gave the molecular weight of the nanoparticles, that summed up around 2000 g/mol, with a molar ratio Yb/Er = 3.43, which is in agreement with the theoretical ratio of Yb/Er = 3. The results demonstrate that the rare

earth metals (Yb,Er) were successfully incorporated during the synthesis step. The charge was determined by means of zeta potential measurements, giving a result of +14.34 meV for the KYF_4:Yb,Er-APTMS nanoparticles. Z-potential results were summarized in Table A1 of the annex.

Infrared spectra of the nanoparticles are shown in Fig. 2. After the functionalization of bare UCNP with APTMS, new bonds between the hydroxyl group from the UCNP and the Si from the APTMS are formed, corresponding to the doublet at 1000-1100 cm^{-1} (Si-O) and with the disappearance of the band at 3400cm^{-1} indicating the conjugation of the OH. Besides the formation of the Si-O bond, new bands can be observed by IR.

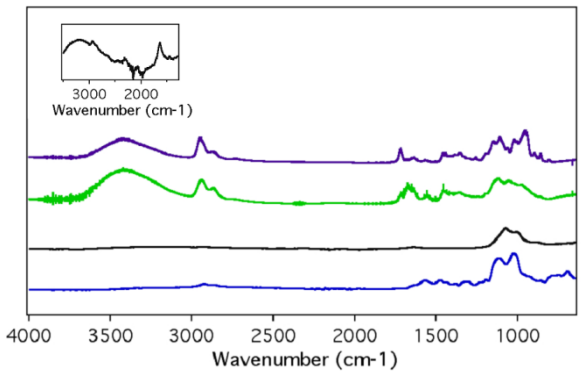

***Figure 2**. Infrared spectra of UCNP-APTMS (blue), UCNP-APTMS-Glutaraldehyde (black), UCNP-APTMS-Glutaraldehyde-BSA/Dex (green) and UCNP-APTMS-Glutaraldehyde-BSA/Dex-Strv (purple), respectively.*

The NH_2 terminal group of APTMS appears at 1570 cm^{-1} corresponding to the scissor vibration, while the bands at 1490 and 1610 cm^{-1} can be assigned to a symmetric deformation mode of NH_3^+. The propyl chain of APTMS is correlated with the stretching modes of C-H at 1380, 2850 and 2910 cm^{-1}, as well as with the stretching modes from the C-N at 1200 cm^{-1}.[34] The next step of functionalization implies the interaction of UCNP-APTMS nanoparticles with glutaraldehyde leading to UCNP-APTMS-Glutaraldehyde, forming an imine between the aldehyde from the glutaraldehyde and the free amine from the nanoparticles with the consequent apparition of a new band at 1638 cm^{-1}. The stretching mode of free aldehyde appears at 1700 cm^{-1}, as shown by the inset in Fig. 2. In addition, the bands from the N-H vibration and deformation decrease in intensity as the free amine reacts.[35] The next step of functionalization implies the interaction of UCNP-APTMS nanoparticles with

glutaraldehyde leading to UCNP- APTMS-Glutaraldehyde, forming an imine between the aldehyde from the glutaraldehyde and the free amine from the nanoparticles with the consequent apparition of a new band at 1638 cm^{-1}. The stretching mode of free aldehyde appears at 1700 cm^{-1}, as shown by the inset in Fig. 2. In addition, the bands from the N-H vibration and deformation decrease in intensity as the free amine reacts.[35] When UCNP-APTMS-Glutaraldehyde nanoparticles were incubated with BSA/Dextran, the free aldehyde groups of UCNP-APTMS-Glutaraldehyde interacted with the amine groups of BSA forming another imine. In consequence, the band at 1638 cm^{-1} gets more intense, while the bands from the free aldehyde in the glutaraldehyde disappeared. Additional vibration bands corresponding to the stretching of the free carboxy groups of the BSA (2800-3500 cm^{-1}), the stretching of the C=O (1717 cm^{-1}), and the deformation vibration of the C-OH (950 cm^{-1}) are also visible. At 1556 cm^{-1}, a peak from the amide groups of the BSA is present.

The final step of functionalization entailed the conjugation of the streptavidin to the BSA. The vibration bands of the proteins: peptide bond COOH to NH_2 between streptavidin and BSA can be observed at 1740 cm^{-1}.[36] Peaks representing amide bonds of streptavidin are detected near 1500 cm^{-1} and 1600 cm^{-1}. The very broad peak in the region 3100-3650 cm^{-1} indicates the presence of exchangeable protons from the amide peptide groups.[37]

Agarose gel electrophoresis was used to determine relative sizes and molecular weights of functionalized UCNP and to further investigate specific streptavidin labeling of the UNCPs. Fig. A2 annex shows the AGE results carried with the materials obtained after each functionalization step. UCNP-APTMS migrated toward the cathode due to their positive charge provided by the APTMS (Fig. A2 annex, lane 1). UCNP-APTMS nanoparticles functionalized with BSA (Fig. SI 2, lane 2), migrated still toward the cathode. Functionalized with dextran (Fig. A2 annex, lane 3), the nanoparticles migrated in both directions, to the cathode and anode, indicating that not all nanoparticles were functionalized. In both cases, with BSA and with dextran (Fig. A2 annex, lanes 2-3, respectively), we can see fluorescence in the well, as a result of NP that remained there.
This observation indicates they were not effectively functionalized and form large aggregates that are not able to migrate through the gel. After functionalization with a

mixture of BSA/Dex (ratio 1:6) (Fig. A2 annex, lane 4), we observed a very good functionalization and all the nanoparticles migrated towards the anode due to the negative charges provided by BSA/Dex. Further, adding streptavidin to the UCNP with BSA/Dex (Fig. A2 annex, lanes 5) resulted also in migration. The screening of the NP with different surface functionalization by AGE revealed UCNP-APTMS-BSA/Dex-Strv as the most effective in view of further cellular uptake experiments. Next step was to determine the optimal amount of streptavidin.

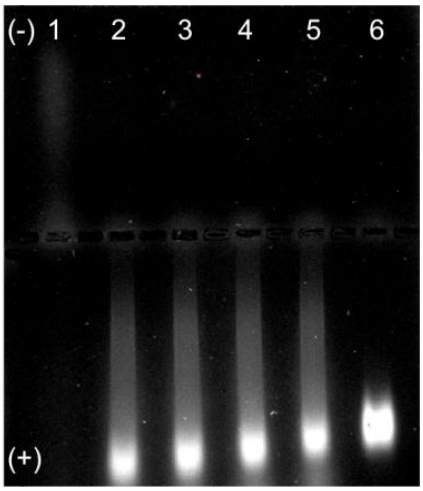

Figure 3. *Electrophoresis of UCNP before and after functionalization with proteins. Lane (1) corresponds to UCNP-APTMS, and lanes 2-6 to UCNP-APTMS-BSA/Dex-Strv, where the concentration of Streptavidin (Strv) is 0.1, 0.5, 1.0, 2.5 and 5.0 mg/mL, respectively. UCNP were revealed under 405 nm excitation wavelength.*

Taking this into account, different streptavidin concentrations in the range 0.1 - 5.0 mg/mL were used after BSA/Dex functionalization. Illustrated in Fig. 3, the as-such UCNP-APTMS still migrated toward the cathode due to their positive charge provided by the APTMS, but the rest of the samples migrated toward the anode due to their negative charge as a consequence of the functionalization. The higher is the amount of streptavidin; the lower is the migration of the nanoparticles due to the increase in weight. We observed that for BSA/Dex (Fig. SI 2) and BSA/Dex-Strv, due to lower concentrations of streptavidin (Fig. 3), there was a tail in the migration, indicating different net negative charge, in agreement with the results from zeta-potential measurements. However, at the highest concentration of streptavidin, all the nanoparticles were concentrated in the migrating band, as a result of their identical charge (Fig. 3, lane 6).

3.2 TLR specific recognition of UCNPs

Targeted imaging and tracking of labeled neutrophils were studied in order to elucidate whether the recognition of TLR was specific or non-specific. These cells perform multiple forms of endocytosis (see annex), including phagocytosis of pathogens and pinocytosis via clathrin-dependent and independent mechanisms.[38] All forms of endocytosis are active transport processes. They depend on the interactions between the endoskeletal proteins, motor proteins, plasma membrane and transport vesicles.[39] Endocytosis requires the movements of the cell cytoplasm to surround a given material, performing the endocytic vesicle. The movement of the cytoplasm around the extracellular molecule is dependent on changes in the cytoskeletal proteins and requires the cell energy. Thus, in extreme conditions, the cells will not perform endocytosis, as the energy will be used as primary source of cell survival.

We performed experiments at different temperatures in order to compare the normal behavior of neutrophils (37°C) and under stressing conditions (4°C) where the neutrophils do not take up anything from the environment. Scheme 1A depicts the final step of UCNP functionalization, i.e. with streptavidin. UCNP-streptavidin recognizes the biotinylated-LPS, previously attached to the cell membrane through specific recognition by TLR (Scheme 1B). Once the complex is formed, NP uptake takes place and membrane proteins such as TLRs that have been internalized into endosomes, are expected to be recycled. Confocal images of neutrophils incubated at 4°C with UCNP-APTMS-BSA/Dex-Strv and biotin-LPS (under 488 nm excitation) showed uptake in cells only after 5-10 min (Fig. 5). Fig. 4 shows the confocal images of the cells incubated with the nanoparticles at 37°C over time.

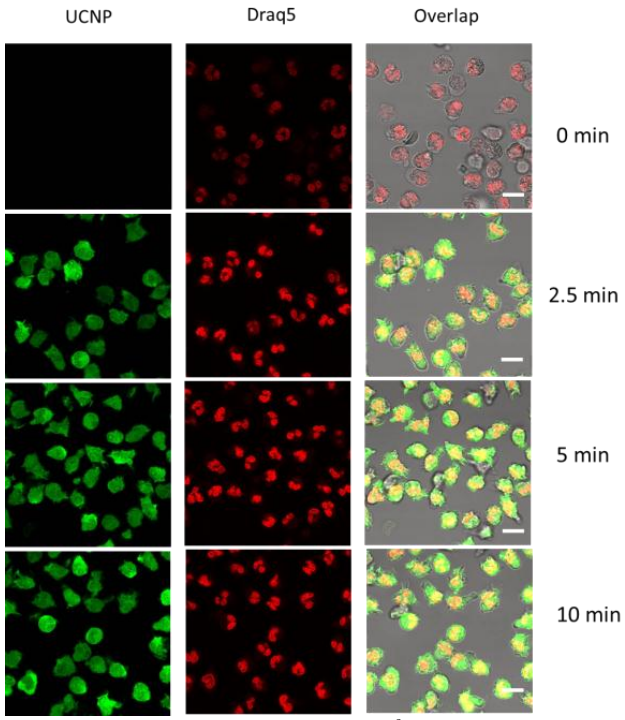

Figure 4. *Confocal images of neutrophils incubated at 37°C first with biotin-LPS and then with UCNP-APTMS-BSA/Dex-Strv5.0 under 488 nm excitation. From left to right, the images correspond to nanoparticles (green), Draq5 (red) and overlap (green and red), respectively. Incubation times (in minutes) are on the right hand side. Scale bars correspond to 10µm.*

No autofluorescence is detected in the control (neutrophils without nanoparticles) under 488 nm excitation wavelength. A fluorescence signal is observed from 2.5 min indicating an uptake of the nanoparticles. At longer incubation times (5 and 10 min), this signal becomes brighter. There is an uptake of every type of nanoparticles independently of their surface functionalization (see Fig. A3 annex). The uptake is increasing with the time and reaches a maximum at 10 min in the case of the UCNP-APTMS-BSA/Dex-Strv+biotin-LPS. Additionally, we showed using UCNP-Strv-Biotin-LPS nanoparticles (UCNP-APTMS-BSA/Dex-Strv5.0-Biotin-LPS0.1 prepared with 0.1mg/mL of Biotin-LPS added) that the uptake was lower compared with the uptake of UCNP by neutrophils incubated at 37ºC first with biotin-LPS and then with UCNP-APTMS-BSA/Dex-Strv5.0 (Fig. A4 annex), indicating that the two-step procedure that we applied to bind UCNP to neutrophils is a better option with respect to TLR4 activation and LPS internalization.

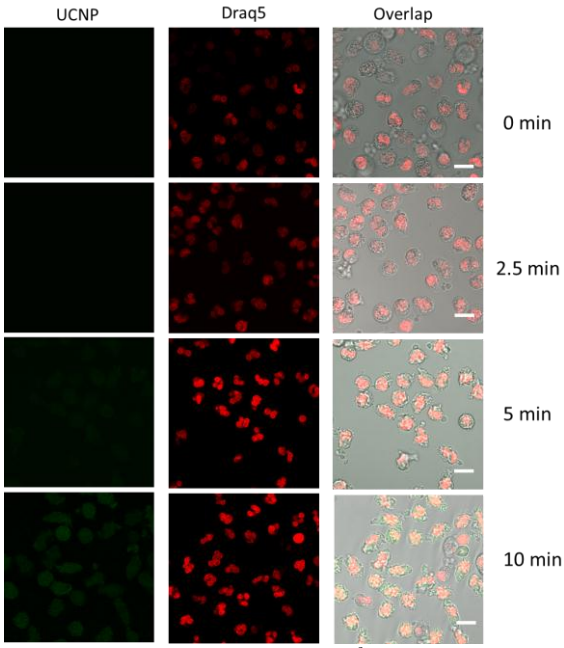

Figure 5. *Confocal images of neutrophils incubated at 4°C first with biotin-LPS and then with UCNP-APTMS-BSA/Dex-Strv5.0 under 488 nm excitation. From left to right, the images correspond to nanoparticles (green), Draq5 (red) and overlap (green and red), respectively. Incubation times (in minutes) are on the right hand side. Scale bars correspond to 10μm.*

To prove that the biotin-streptavidin interaction plays a vital role in the nanoparticle recognition by TLR4 receptors and their efficient internalization, we incubated the neutrophils directly with UCNP-APTMS-BSA/Dex-Strv5.0 without a previous incubation of the cells with Biotin-LPS. The results are shown in the Supporting Information (Fig. A5 annex). Comparing these results with those reported in Fig. 4 in the main manuscript, a higher uptake can be observed when the cells were previously treated with biotin-LPS (Fig. 4), followed by incubation with the UCNP-APTMS-BSA/Dex-Strv5.0. It is therefore clear that the union biotin-streptavidin plays a vital role in the nanoparticle recognition by TLR4 receptors and their efficient internalization. Confocal images of neutrophils incubated at 4°C with UCNP-APTMS-BSA/Dex-Strv and biotin-LPS (under 488 nm excitation) showed uptake in cells only after 5-10 min (Fig. 5). The fact that neutrophils uptake only the UCNP-APTMS-BSA/Dex-Strv nanoparticles in the presence of Biotin-LPS for the specific recognition by TLR (see Fig. A6 annex and Fig. 6), allows us to conclude that there is a specific recognition by TLR due to the formation of streptavidin-biotin complex. Higher rate of uptake at 37°C and a low uptake at 4°C shows that the internalization of the particles is an energy dependent process[40] and it also depends on the charged surface of the NP.[41] This is in good agreement with previously reported results, which demonstrated the effective internalization of UCNP coated with cationic polymers via

energy dependent endocytosis.[42,43] In the latter cases, the studies were performed with HeLa cell lines, differently from our investigation carried out with primary human neutrophils.

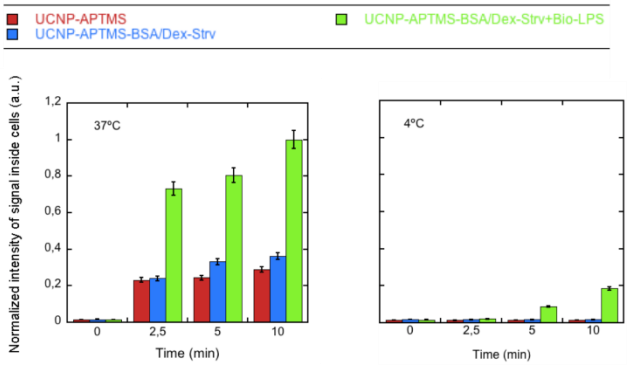

Figure 6. *Normalized fluorescence intensity of nanoparticles signal inside the cells from the grey scale at different times, at 37°C and 4°C, respectively. Legend: UCNP-APTMS (red), UCNP-APTMS-BSA/Dex-Strv5.0 (blue), UCNP-APTMS-BSA/Dex-Strv 5.0+Bio-LPS (green).*

Cell lines are immortal and might differ with respect to the primary cells in their nanoparticle uptake characteristics. In line with this, several researchers demonstrated that negatively charged nanoparticles were successfully internalized by neutrophils, while the cationic nanomaterials were trapped into extracellular structures,[41] in contrast with the results reported with the HeLa cell lines. Additionally, primary human blood phagocytes (i.e. macrophages, monocytes and neutrophil granulocytes) show comparable phagocytic activity *in vivo* and *in vitro*.[44] Therefore, neutrophils are ideal in vitro test platform for evaluation of the biological fate and consequences of nanoparticles in the human body. Moreover, endocytosis in neutrophils is a complex process involving fluid phase endocytosis and macropinocytosis[38,45] and there will be uptake of NPs, even when no receptors are targeted, as seen in Fig. A3 in the annex. We next investigated the viability of neutrophils coincubated with nonfunctionalized and functionalized UCNP at 37ºC in the absence and presence of biotin-LPS at 10, 30, 60 and 180 min by using Trypan Blue dye exclusion assay. We observed no significant decrease in neutrophil viability up to three hours of coincubation between control neutrophils and those incubated with UCNPs (Fig. A7 in the annex). The results from Trypan Blue dye exclusion viability assay indicate that neutrophil plasma membrane integrity is not compromised by prolonged incubation with UCNPs.

4.Conclusions

We reported the fabrication of up-conversion nanoparticles (UCNP) KYF_4:Yb,Er and their functionalization with BSA/Dex-Strv for the specific recognition by toll-like receptors (TLRs) in the presence of Biotin-LPS. Using highly fluorescent UCNP, we have monitored the uptake of functionalized UCNP in human neutrophils under normal (37°C) and stressing conditions (4°C). Uptake of the UCNP-APTMS-BSA/Dex-Strv nanoparticles in the presence of Biotin-LPS was proven to be faster and higher at 37°C compared to the uptake at 4°C.

These results indicate that an energy-dependent uptake process is the principal mechanism responsible for the UCNP internalization into human PMNs. Besides, negatively charged UCNP are required for cell uptake studies with PMNs in order to avoid extracellular nanoparticle trapping.

Excitation of the UCNP at the second-harmonic wavelength at 488 nm allows introducing new non-conventional detection imaging nanotools on commercially available imaging equipment.

The integrative *in vitro* approach proposed herein using the innovative UCNP imaging combined with the primary human blood neutrophils testing platform could be used *in vivo* to identify/evaluate the biological fate and consequences of nanoparticles in the human body. In addition, the applicability of these functionalized UCNP could be extended to other types of cells and to the recognition of other receptors involved in immune responses and to specific recognition of anti-cancer drugs since the mechanism of cellular uptake is important in the field of nanomedicine, cancer diagnosis, drug delivery and treatment.

References

1. Yamashiro, S. *et al.* Phenotypic and functional change of cytokine-activated neutrophils: inflammatory neutrophils are heterogeneous and enhance adaptive immune responses. *J. Leukoc. Biol.* **69,** 698–704 (2001).

2. Parker, L. C., Whyte, M. K. B., Dower, S. K. & Sabroe, I. The expression and roles of Toll-like receptors in the biology of the human neutrophil. *J. Leukoc. Biol.* **77,** 886–92 (2005).

3. Shi, Z. *et al.* Transcriptional regulation of the novel Toll-like receptor Tlr13. *J. Biol. Chem.* **284,** 20540–7 (2009).

4. Takeda, K., Kaisho, T. & Akira, S. Toll-like receptors. *Annu. Rev. Immunol.* **21,** 335–76 (2003).

5. Hajjar, A. M., Ernst, R. K., Tsai, J. H., Wilson, C. B. & Miller, S. I. Human Toll-like receptor 4 recognizes host-specific LPS modifications. *Nat. Immunol.* **3,** 354–9 (2002).

6. Takeda, K. & Akira, S. Microbial recognition by Toll-like receptors. *J. Dermatol. Sci.* **34,** 73–82 (2004).

7. Underhill, D. M. & Ozinsky, A. Toll-like receptors: key mediators of microbe detection. *Curr. Opin. Immunol.* **14,** 103–110 (2002).

8. Horvath, G., Young, S. & Latz, E. Toll-like receptor interactions imaged by FRET microscopy and GFP fragment reconstitution. *Methods Mol. Biol.* **517,** 33–54 (2009).

9. Latz, E. *et al.* Lipopolysaccharide rapidly traffics to and from the Golgi apparatus with the toll-like receptor 4-MD-2-CD14 complex in a process that is distinct from the initiation of signal transduction. *J. Biol. Chem.* **277,** 47834–43 (2002).

10. Dobrovolskaia, M. A. & McNeil, S. E. Immunological properties of engineered nanomaterials. *Nat. Nanotechnol.* **2,** 469–78 (2007).

11. Singh, R. & Lillard, J. W. Nanoparticle-based targeted drug delivery. *Exp. Mol. Pathol.* **86,** 215–23 (2009).

12. Auzel, F. Upconversion and anti-Stokes processes with f and d ions in solids. *Chem. Rev.* **104,** 139–73 (2004).

13. Frangioni, J. In vivo near-infrared fluorescence imaging. *Curr. Opin. Chem. Biol.* **7,** 626–634 (2003).

14. Hilderbrand, S. A. & Weissleder, R. Near-infrared fluorescence: application to in vivo molecular imaging. *Curr. Opin. Chem. Biol.* **14,** 71–9 (2010).

15. Zhao, L. *et al.* Stem Cell Labeling using Polyethylenimine Conjugated (α-NaYbF 4 :Tm 3+)/CaF 2 Upconversion Nanoparticles. *Theranostics* **3,** 249–257 (2013).

16. Yang, X. *et al.* Multifunctional core–shell upconversion nanoparticles for targeted tumor cells induced by near-infrared light. *J. Mater. Chem. B* **1,** 2757–2763 (2013).

17. Zijlmans, H. J. *et al.* Detection of cell and tissue surface antigens using up-converting phosphors: a new reporter technology. *Anal. Biochem.* **267,** 30–6 (1999).

18. Corstjens, P. L. A. M. *et al.* Infrared up-converting phosphors for bioassays. *IEE Proc. Nanobiotechnol.* **152,** 64–72 (2005).

19. Niedbala, R. S. *et al.* Detection of analytes by immunoassay using up-converting phosphor technology. *Anal. Biochem.* **293,** 22–30 (2001).

20. Van De Rijke, F. *et al.* Up-converting phosphor reporters for nucleic acid microarrays. *Nat. Biotechnol.* **19,** 273–6 (2001).

21. Song, F. *et al.* Three-photon phenomena in the upconversion luminescence of erbium–ytterbium-codoped phosphate glass. *Appl. Phys. Lett.* **79,** 1748 (2001).

22. Tkachuk, A. M. *et al.* Upconversion processes in Er3+:KPb2Cl5 laser crystals. *J. Lumin.* **125,** 271–278 (2007).

23. Hoang, J., Schwartz, R. N., Wang, K. L. & Chang, J. P. The effects of energy transfer on the Er3+ 1.54 μm luminescence in nanostructured Y2O3 thin films with heterogeneously distributed Yb3+ and Er3+ codopants. *J. Appl. Phys.* **112,** 063117 (2012).

24. Wong, H.-T., Chan, H. L. W. & Hao, J. Towards pure near-infrared to near-infrared upconversion of multifunctional GdF(3):Yb(3+),Tm(3+) nanoparticles. *Opt. Express* **18,** 6123–30 (2010).

25. Leblond, F., Davis, S. C., Valdés, P. A. & Pogue, B. W. Pre-clinical whole-body fluorescence imaging: Review of instruments, methods and applications. *J. Photochem. Photobiol. B.* **98,** 77–94 (2010).

26. Mancini, M. C., Kairdolf, B. A., Smith, A. M. & Nie, S. Oxidative quenching and degradation of polymer-encapsulated quantum dots: new insights into the long-term fate and toxicity of nanocrystals in vivo. *J. Am. Chem. Soc.* **130,** 10836–7 (2008).

27. Resch-Genger, U., Grabolle, M., Cavaliere-Jaricot, S., Nitschke, R. & Nann, T. Quantum dots versus organic dyes as fluorescent labels. *Nat. Methods* **5,** 763–75 (2008).

28. Gorris, H. H., Ali, R., Saleh, S. M. & Wolfbeis, O. S. Tuning the dual emission of photon-upconverting nanoparticles for ratiometric multiplexed encoding. *Adv. Mater.* **23,** 1652–5 (2011).

29. Strober, W. Trypan blue exclusion test of cell viability. *Curr. Protoc. Immunol.* **Appendix 3,** Appendix 3B (2001).

30. Schäfer, H., Ptacek, P., Zerzouf, O. & Haase, M. Synthesis and Optical Properties of KYF4/Yb, Er Nanocrystals, and their Surface Modification with Undoped KY 4. *Adv. Funct. Mater.* **18,** 2913–2918 (2008).

31. Wang, F. & Liu, X. Recent advances in the chemistry of lanthanide-doped upconversion nanocrystals. *Chem. Soc. Rev.* **38,** 976–89 (2009).

32. De la Rosa-Cruz, E. *et al.* Luminescence and visible upconversion in nanocrystalline ZrO2:Er3+. *Appl. Phys. Lett.* **83,** 4903 (2003).

33. Zhang, Q. Y. & Huang, X. Y. Recent progress in quantum cutting phosphors. *Prog. Mater. Sci.* **55,** 353–427 (2010).

34. Pasternack, R. M., Rivillon Amy, S. & Chabal, Y. J. Attachment of 3-(Aminopropyl)triethoxysilane on silicon oxide surfaces: dependence on solution temperature. *Langmuir* **24,** 12963–71 (2008).

35. Pandya, P. H., Jasra, R. V., Newalkar, B. L. & Bhatt, P. N. Studies on the activity and stability of immobilized α-amylase in ordered mesoporous silicas. *Microporous Mesoporous Mater.* **77,** 67–77 (2005).

36. Celej, M. S., Montich, G. G. & Fidelio, G. D. Protein stability induced by ligand binding correlates with changes in protein flexibility. *Protein Sci.* **12,** 1496–506 (2003).

37. Gaur, G., Koktysh, D. S. & Weiss, S. M. Immobilization of Quantum Dots in Nanostructured Porous Silicon Films: Characterizations and Signal Amplification for Dual-Mode Optical Biosensing. *Adv. Funct. Mater.* **23,** 3604–3614 (2013).

38. Uriarte, S. M. *et al.* Counterregulation of clathrin-mediated endocytosis by the actin and microtubular cytoskeleton in human neutrophils. *AJP Cell Physiol.* **296,** 857–867 (2009).

39. Paradisi, F., D'Onofrio, C., Pepe, G., Cifarelli, A. & Piccolo, D. Phagocytosis and cellular metabolism. *Ric. Clin. e Lab.* **9,** 47–60 (1979).

40. Detmers, P. A. *et al.* Potential role of membrane internalization and vesicle fusion in adhesion of neutrophils in response to lipopolysaccharide and TNF. *J. Immunol.* **157,** 5589–96 (1996).

41. Bartneck, M., Keul, H. A., Zwadlo-Klarwasser, G. & Groll, J. Phagocytosis independent extracellular nanoparticle clearance by human immune cells. *Nano Lett.* **10,** 59–63 (2010).

42. Jin, J. *et al.* Polymer-coated $NaYF_4$:Yb^{3+}, Er^{3+} upconversion nanoparticles for charge-dependent cellular imaging. *ACS Nano* **5,** 7838–47 (2011).

43. Ma, P. *et al.* Rational design of multifunctional upconversion nanocrystals/polymer nanocomposites for cisplatin (IV) delivery and biomedical imaging. *Adv. Mater.* **25,** 4898–905 (2013).

44. Schwarzer, E., Kuhn, H., Valente, E. & Arese, P. Malaria-parasitized erythrocytes and hemozoin nonenzymatically generate large amounts of hydroxy fatty acids that inhibit monocyte functions. *Blood* **101,** 722–8 (2003).

45. Lamb, F. S. *et al.* Endotoxin priming of neutrophils requires endocytosis and NADPH oxidase-dependent endosomal reactive oxygen species. *J. Biol. Chem.* **287,** 12395–404 (2012).

Annex II
Chapter 6

UNIVERSITAT ROVIRA I VIRGILI
SEMICONDUCTOR NANOPARTICLES AS PLATFORM FOR BIO-APPLICATIONS AND ENERGY RELATED SYSTEMS.
Alba María Matas Adams
Dipòsit Legal: T 55-2016

Mechanisms of nanoparticles cellular uptake.

Nanoparticles (NP) uptake by cells may occur through several different mechanisms, which can be classified into phagocytosis and pinocytosis. Pinocytosis includes macropinocytosis with uptake of particles with sizes > 1 μm, clathrin or caveolae-mediated endocytosis, or clathrin/caveolae independent endocytosis. Caveolae consist of plasma membrane invaginations of sizes between 50-80 nm containing cholesterol and sphingolipids, receptors and caveolins[1,2]. Endocytosis of various membrane receptors may also occur via lipid rafts[3]. Lipid rafts provide a platform for the assembly of receptors, adaptors, regulators, and other downstream proteins as a signaling complex, and may be joined with caveolae. Clathrin-coated pits of 100–200 nm have been shown to be associated with the key protein clathrin and other scaffold proteins such as AP-2 and eps15[4]. Macropinocytosis is a form of endocytosis related to cell surface ruffling and provides a route for non-selective endocytosis of solute macromolecules. Macropinosomes are more than 0.2 μm in diameter, and may be as large as 5 μm.[5] Specialized phagocytosis via protease activation receptor 2 occurs in HEK that up take melanosomes from adjacent melanocytes. It is possible that NP may be uptaken by cells *via* their size selectivity that may match those of endocytic pits. Neutrophils granulocytes mainly trap nanoparticles via extracellular networks.[6,7]

NP endocytosis by cells not only depends on the size of the NP, but also on the surface coating and charge[7]. Carboxydextran-coated superparamagnetic iron oxide nanoparticles (SPION) were internalized by human mesenchymal stem cells, and the efficiency of uptake was correlated with the amount of carboxyl groups on the NP surface.[8] Cationic D,L-polylactide (PLA)-NP entered HeLa cells in greater amounts than anionic PLA-NP.[9,10] NP uptake may also depend on the length of the surface coating[11], or the type of cells.[12]

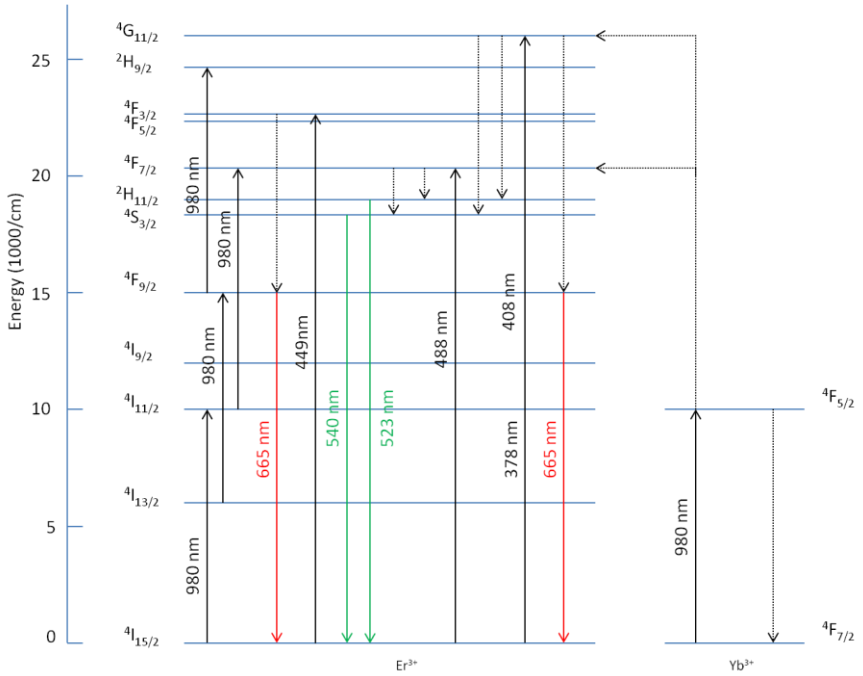

Scheme A1. *Energy transfer processes of Er^{3+} and Yb^{3+} at different excitation wavelengths.*

Sample	Charge (meV)	s.d
UCNP-APTMS	+14.34	0.59
UCNP-APTMS-Glutaraldehyde	+32.3	0.97
UCNP-APTMS-BSA	+7.38	0.37
UCNP-APTMS-Dex	+7.09	0.25
UCNP-APTMS-BSA/Dex	-22.93	0.83
UCNP-APTMS-BSA/Dex-Strv0.5	-24.18	0.62
UCNP-APTMS-BSA/Dex-Strv5.0	-28.6	1.07

Table A1. *Zeta-potential data from the UCNP after each functionalization step. Numbers in the name of the sample correspond to mg/mL of biomolecules added.*

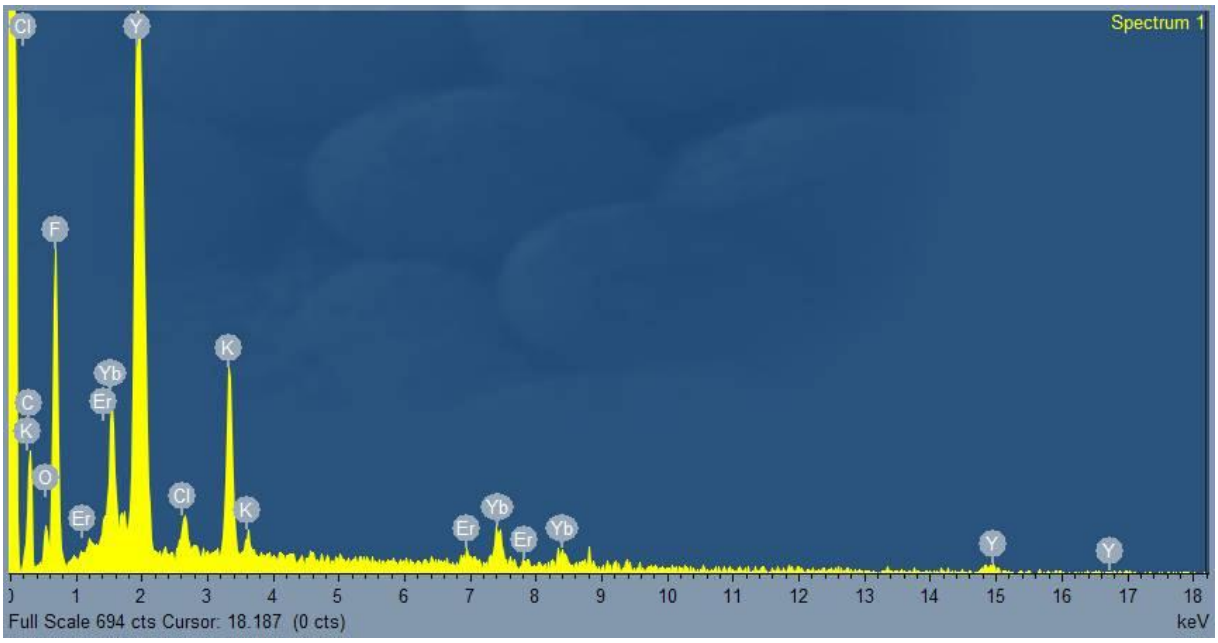

***Fig. A1**. Elemental mapping with EDX of KYF_4:Yb,Er.*

***Fig. A2**. Electrophoresis of UCNP before and after functionalization. Lanes correspond to samples (1) UCNP-APTMS, (2) UCNP-APTMS-BSA, (3) UCNP-APTMS-Dex, (4) UCNP-APTMS-BSA/Dex, and (5) UCNP-APTMS-BSA/Dex-Strv5.0. UCNP were revealed under 405 nm excitation wavelength.*

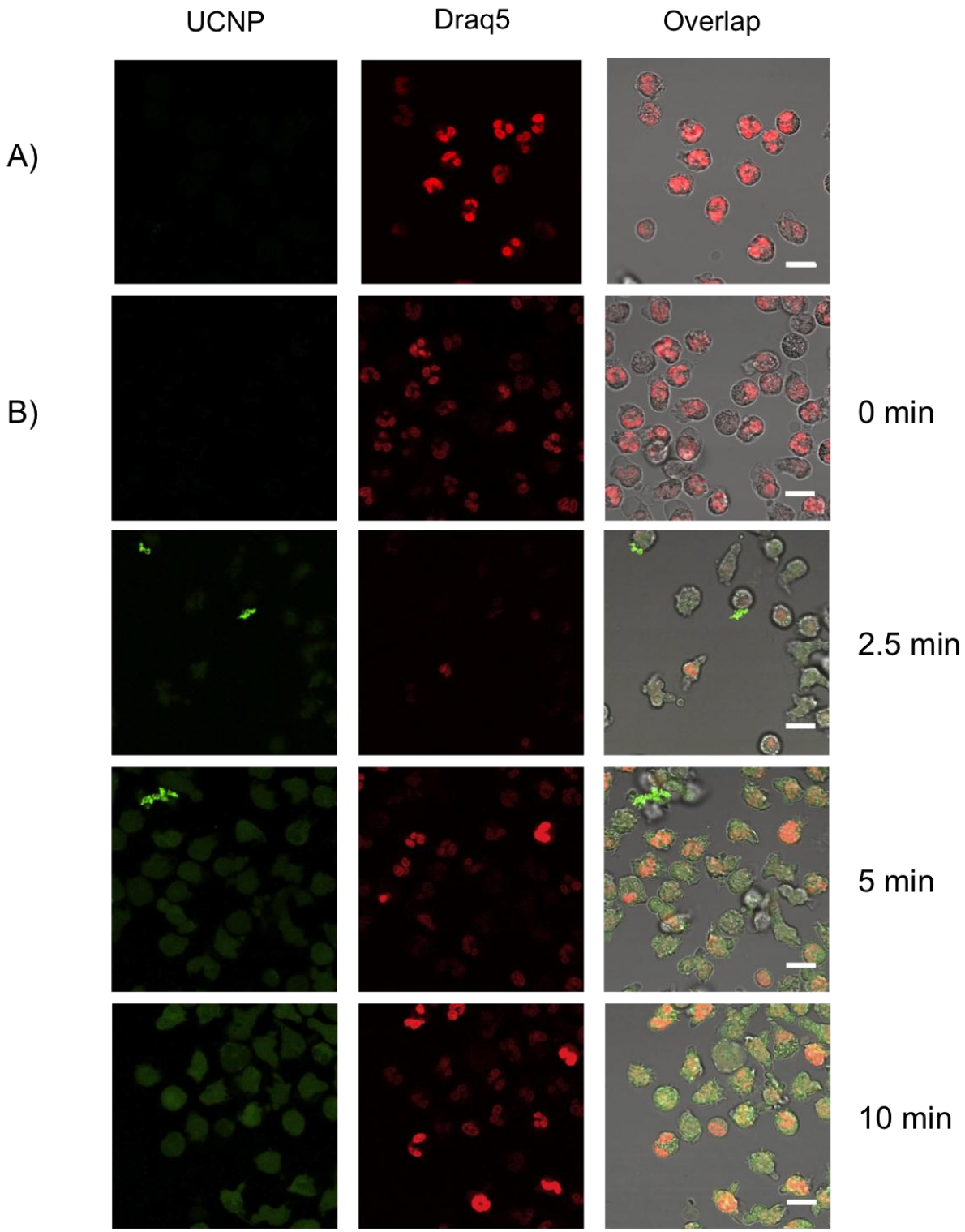

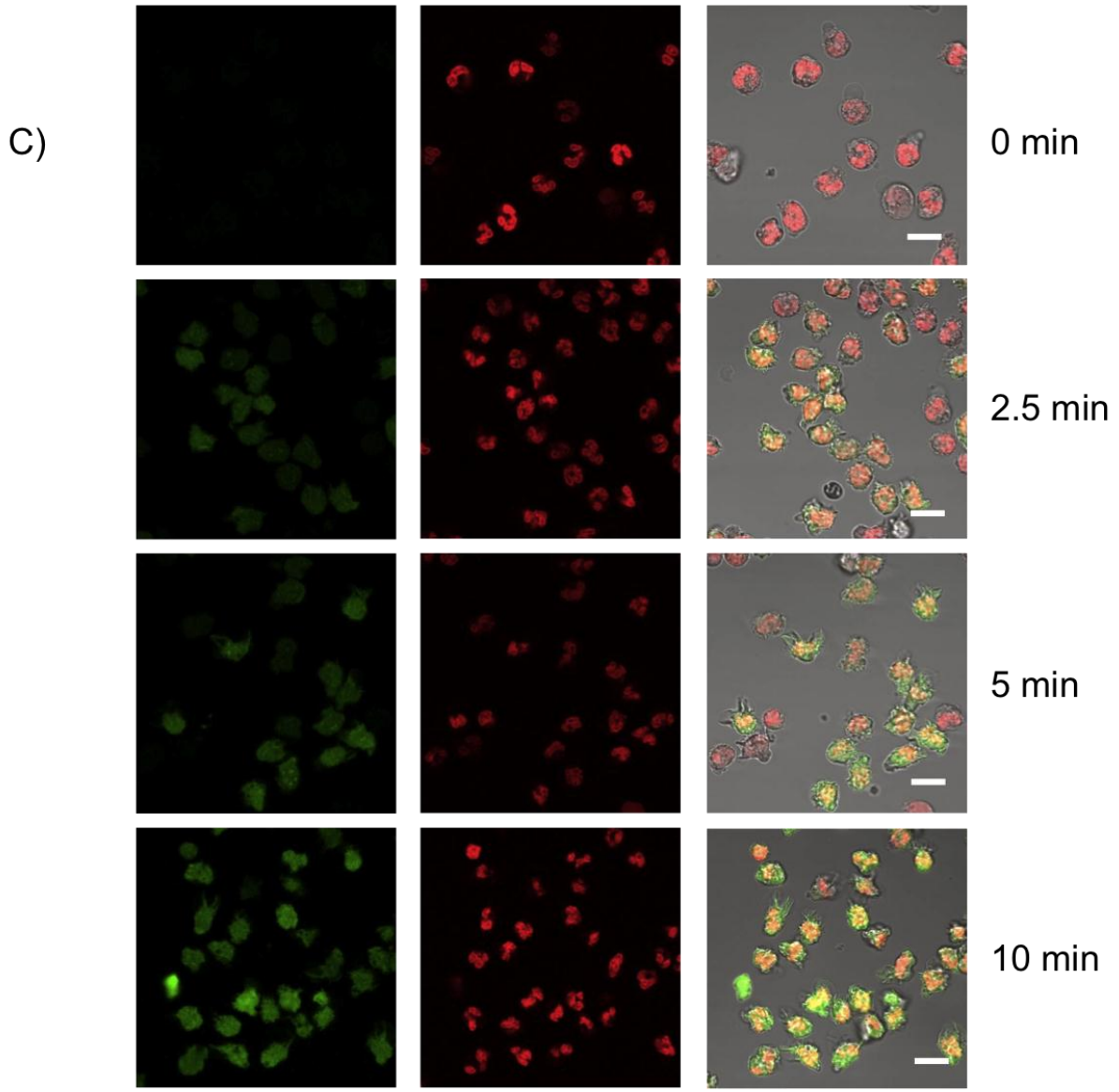

***Fig. A3**. Confocal images of A) neutrophils without UCNP, B) neutrophils with UCNP-APTMS and C) neutrophils with UCNP-APTMS-BSA/Dex-Strv5.0 under 488 nm excitation incubated at 37 ºC. Neutrophils were first treated with biotin-LPS. From left to right, the images correspond to nanoparticles (green), Draq5 (red) and overlap (green and red), respectively. Incubation times (in minutes) are on the right hand side. Scale bar corresponds to 10 µm.*

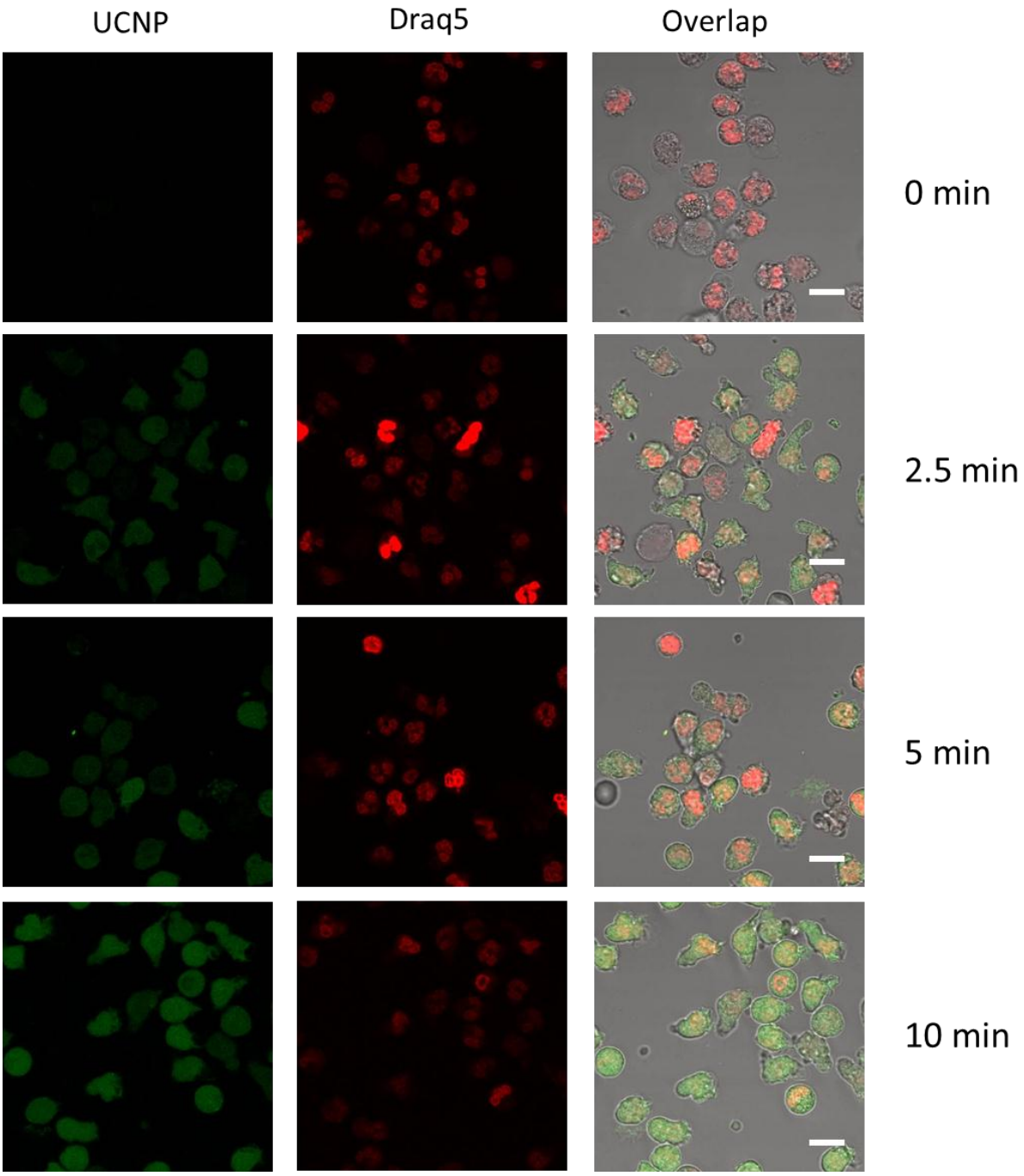

***Fig. A4**. Confocal images of neutrophils incubated at 37ºC with UCNP-APTMS-BSA/Dex-Strv5.0-Biotin-LPS0.1 (0.1mg/mL of Biotin-LPS added) under 488 nm excitation. From left to right, the images correspond to nanoparticles (green), Draq5 (red) and overlap (green and red), respectively. Incubation times (in minutes) are on the right hand side. Scale bars correspond to 10 µm.*

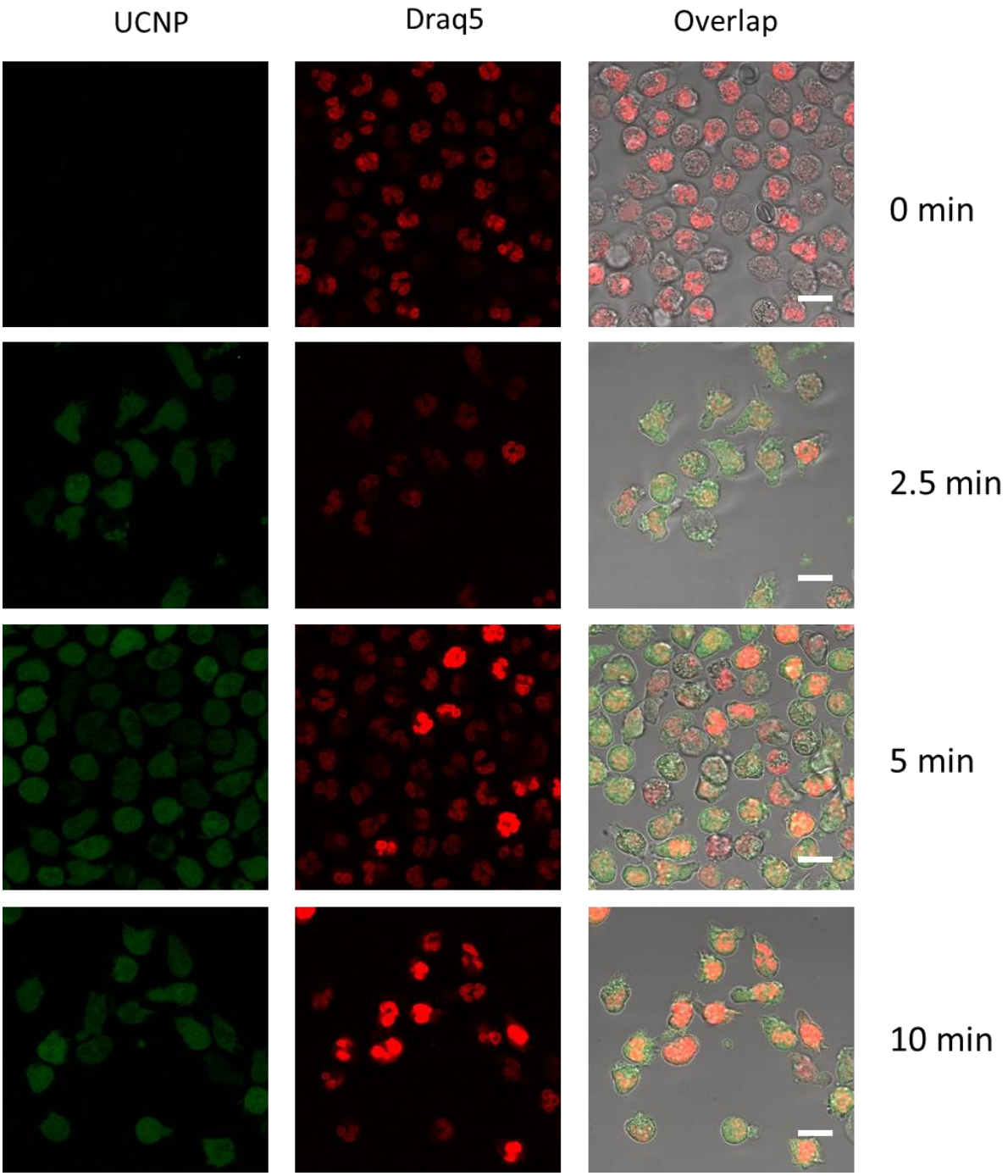

Fig. A5. *Confocal images of neutrophils incubated at 37ºC with UCNP-APTMS-BSA/Dex-Strv5.0 under 488 nm excitation. From left to right, the images correspond to nanoparticles (green), Draq5 (red) and overlap (green and red), respectively. Incubation times (in minutes) are on the right hand side. Scale bars correspond to 10 μm.*

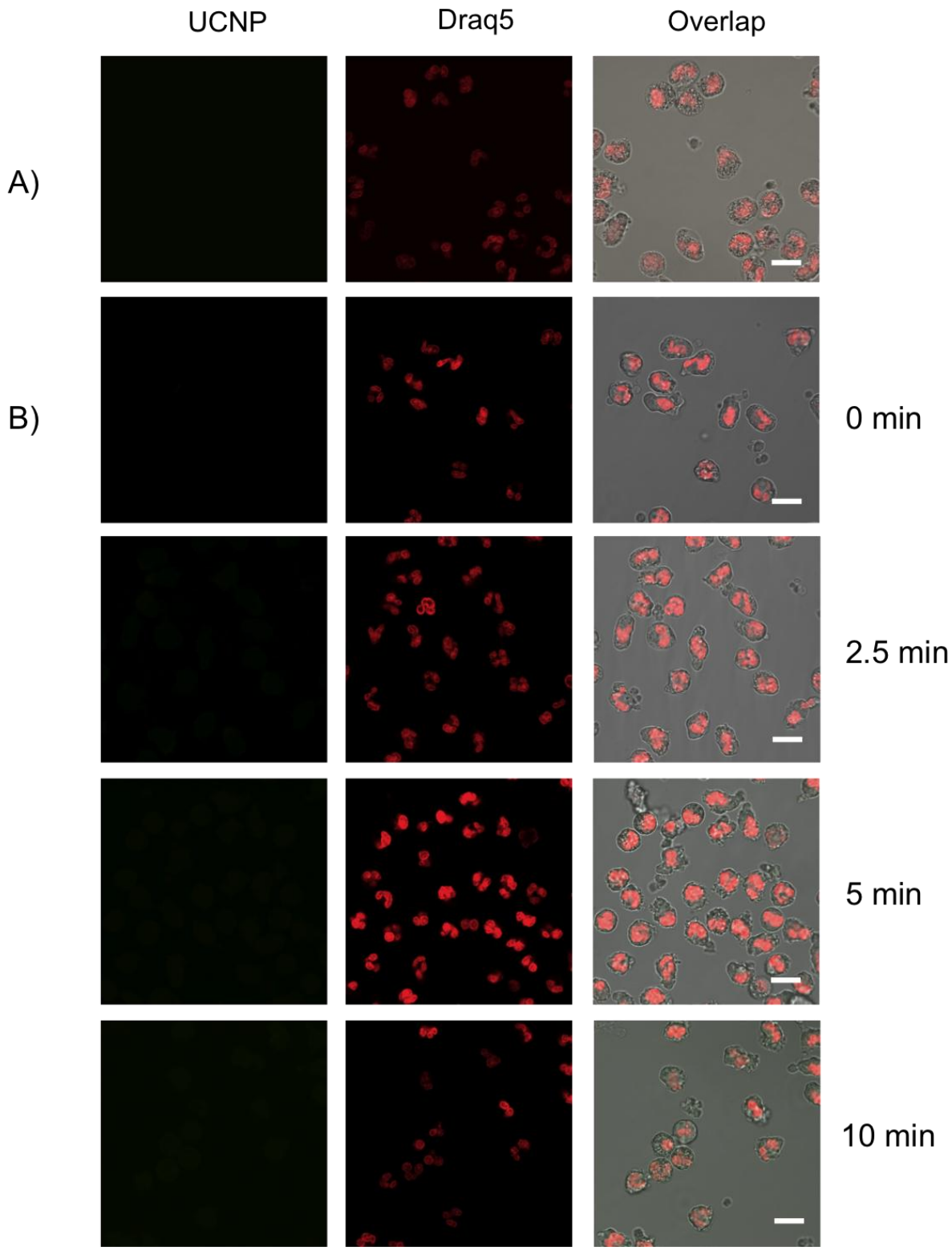

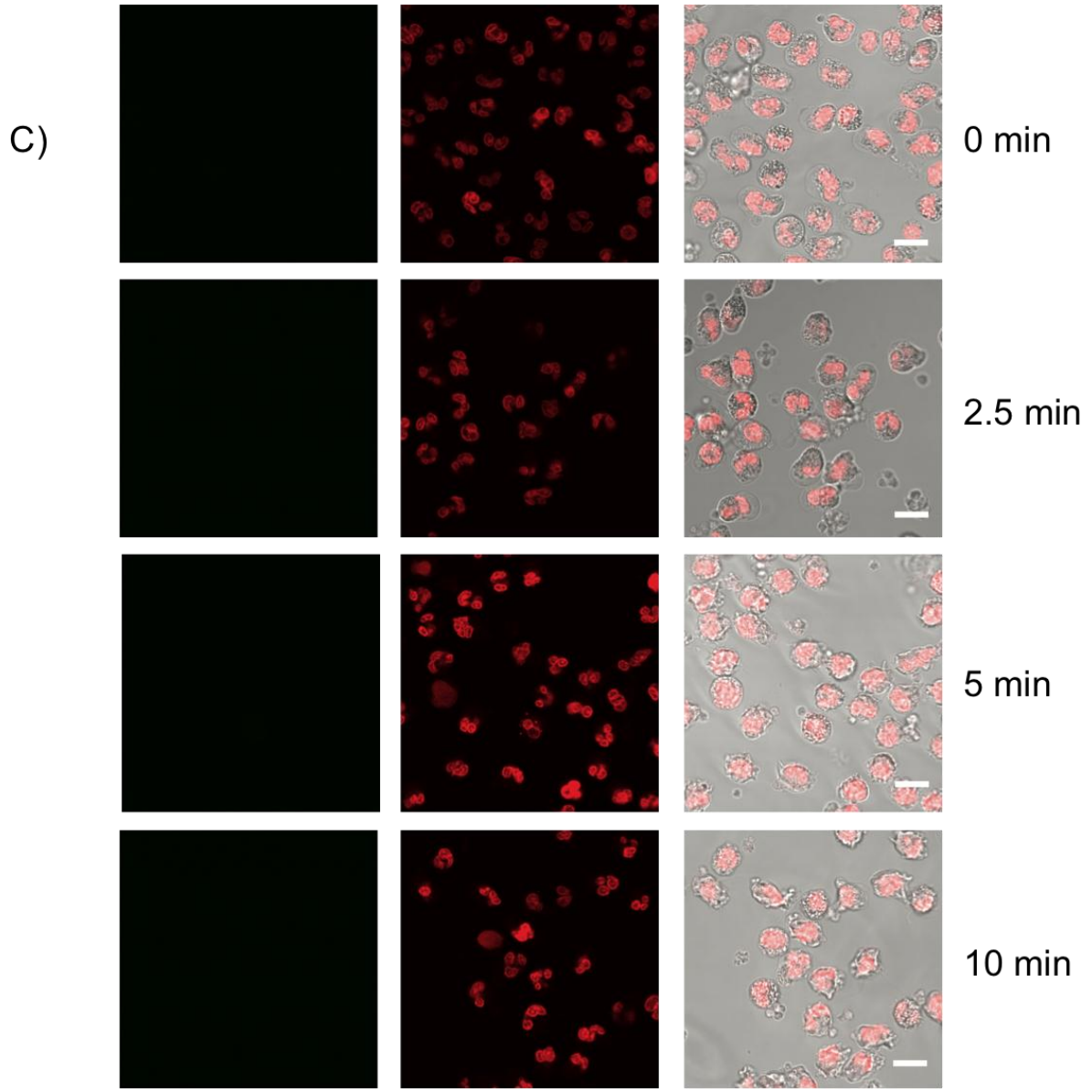

***Fig. A6**. Confocal images of A) neutrophils without UCNP, B) neutrophils with UCNP-APTMS and C) neutrophils with UCNP-APTMS-BSA/Dex-Strv5.0 under 488 nm excitation incubated at 4ºC. Neutrophils were first treated with biotin-LPS. From left to right, the images correspond to nanoparticles (green), Draq5 (red) and overlap (green and red), respectively. Incubation times (in minutes) are on the right hand side. Scale bar corresponds to 10 μm.*

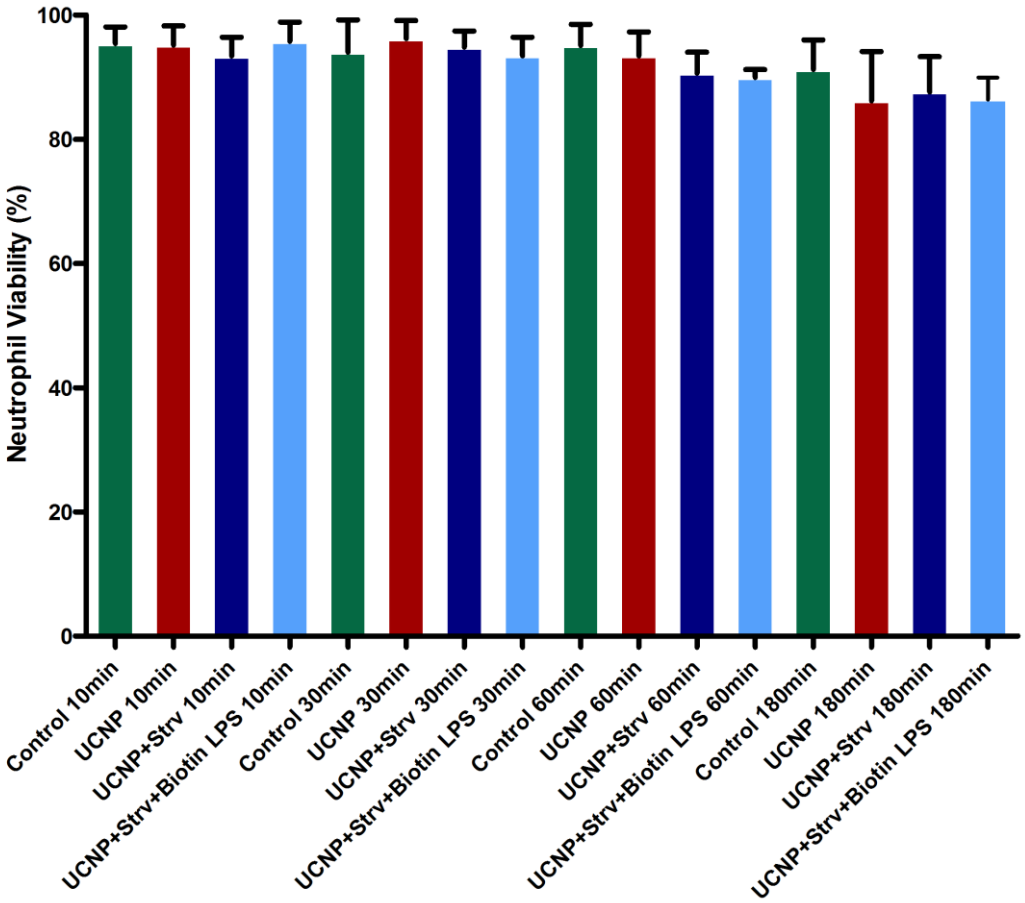

Fig. A7. *Trypan Blue exclusion test for neutrophil viability testing at 10, 30, 60 and 180 min coincubation in the presence of UCNPs.*

References

1. Lajoie, P., Goetz, J. G., Dennis, J. W. & Nabi, I. R. Lattices, rafts, and scaffolds: domain regulation of receptor signaling at the plasma membrane. *J. Cell Biol.* **185,** 381–5 (2009).

2. Pelkmans, L. & Helenius, A. Endocytosis via caveolae. *Traffic* **3,** 311–20 (2002).

3. Nichols, B. Caveosomes and endocytosis of lipid rafts. *J. Cell Sci.* **116,** 4707–14 (2003).

4. Ehrlich, M. *et al.* Endocytosis by random initiation and stabilization of clathrin-coated pits. *Cell* **118,** 591–605 (2004).

5. Swanson, J. A. & Watts, C. Macropinocytosis. *Trends Cell Biol.* **5,** 424–8 (1995).

6. Brinkmann, V. *et al.* Neutrophil extracellular traps kill bacteria. *Science* **303,** 1532–5 (2004).

7. Bartneck, M., Keul, H. A., Zwadlo-Klarwasser, G. & Groll, J. Phagocytosis independent extracellular nanoparticle clearance by human immune cells. *Nano Lett.* **10,** 59–63 (2010).

8. Mailänder, V. *et al.* Carboxylated superparamagnetic iron oxide particles label cells intracellularly without transfection agents. *Mol. Imaging Biol.* **10,** 138–46

9. Dausend, J. *et al.* Uptake mechanism of oppositely charged fluorescent nanoparticles in HeLa cells. *Macromol. Biosci.* **8,** 1135–43 (2008).

10. Harush-Frenkel, O., Debotton, N., Benita, S. & Altschuler, Y. Targeting of nanoparticles to the clathrin-mediated endocytic pathway. *Biochem. Biophys. Res. Commun.* **353,** 26–32 (2007).

11. Chang, E., Thekkek, N., Yu, W. W., Colvin, V. L. & Drezek, R. Evaluation of quantum dot cytotoxicity based on intracellular uptake. *Small* **2,** 1412–7 (2006).

12. Xia, T., Kovochich, M., Liong, M., Zink, J. I. & Nel, A. E. Cationic polystyrene nanosphere toxicity depends on cell-specific endocytic and mitochondrial injury pathways. *ACS Nano* **2,** 85–96 (2008).

UNIVERSITAT ROVIRA I VIRGILI
SEMICONDUCTOR NANOPARTICLES AS PLATFORM FOR BIO-APPLICATIONS AND ENERGY RELATED SYSTEMS.
Alba María Matas Adams
Dipòsit Legal: T 55-2016

UNIVERSITAT ROVIRA I VIRGILI
SEMICONDUCTOR NANOPARTICLES AS PLATFORM FOR BIO-APPLICATIONS AND ENERGY RELATED SYSTEMS.
Alba María Matas Adams
Dipòsit Legal: T 55-2016

3. Other Materials Introduction

UNIVERSITAT ROVIRA I VIRGILI
SEMICONDUCTOR NANOPARTICLES AS PLATFORM FOR BIO-APPLICATIONS AND ENERGY RELATED SYSTEMS.
Alba María Matas Adams
Dipòsit Legal: T 55-2016

3. Other materials

The main focus of this last introduction will be to briefly descript the materials used in the last two chapters of the thesis (bismuth sulfide, titanium oxide and perovskite), their synthesis and the importance of their different applications.

It moves away from the luminescent properties of the first chapters, but it shows the versatility of the different material synthesized and shown in the thesis.

3.1 Bismuth sulfide.

Other semiconductor nanocrystals besides QDs and UCNP have attracted increasing attention in the last few years, being bismuth sulfide a clear example of that.

One of the advantages of this material is that it is environmentally friendly and considerably cheap (in comparison with other semiconductor that present heavy metals, lanthanides or precious metals).

Due to the band gap (1.3 eV for the bulk)[1] they present they are able to absorb in the near IR, which gives this material potential use in different areas such as photovoltaics[2,3], photosensing[4] or photocatalisis[5].

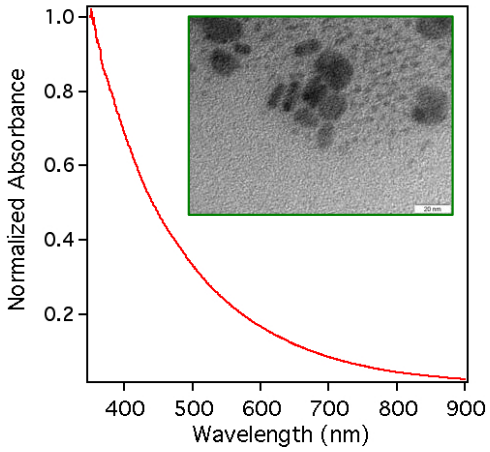

Figure 1. *Absorbance and TEM image of Bi_2S_3*

Different shaped Bi_2S_3 nanomaterials can be synthesized using different techniques as solvothermal synthesis, hydrothermal, chemical vapor deposition, hot injection…to obtain different shapes as nanowires, nanotubes, nanorods, nanoflowers… [6–8], that will modify the band gap.

In the thesis, we will focus on the use of bismuth sulfide nanorods for photocatalysis in organic reactions, but normally other bismuth chalcogenides as Bi_2O_3 are used.[9] We will compare the use of Bi_2O_3 to Bi_2S_3 in chapter 7.

3.2 Titania and Perovskite

The commercial produce of titanium oxide started in the twentieth century, and since then it has advanced a long way. They present a vast range of applications, since their use as pigments[10], in sunscreens[11,12], paints[13,14] to thoohpaste[15,16]… but the main interest for the investigation development was the discovery in 1972 by Fujisjima and Honda of the photocatalytic phenomenon of water splitting on a TiO_2 electrode under UV light.[17] The different applications developed since then depended on the modifications of the titanium oxide and on the interactions with the environment.
Also, when the synthesis allowed to decrease the size of the material, new physical and chemical properties emerged as a specific surface area and surface to volume ratio that increased with the size decrease of the TiO_2.

The synthesis methods can be divided in:

- Sol-gel method is used to synthesis different ceramic materials including titania. In the typical process, a colloidal suspension (also called sol), is formed from the hydrolysis and polymerization of the precursors such as inorganic metal salts or metal organic compounds. Depending on the method used for the formation, different properties can be obtained (thin films, dense ceramic, porous material...).[18,19] If it is a based catalyzed synthesis highly crystalline anatase TiO_2 nanoparticles are obtained.

  Different morphologies can be obtained as cuboidal shape, nanorods, and nanowires changing the conditions of the reaction.
- Micelle and inverse micelle methods are a commonly used to synthesize TiO_2, but normally present amorphous structure and calcination is needed for cristallinity. [20–22]
- Sol methods involve the reaction of titanium chloride with different oxygen donor molecules; also, surfactants have been used to obtain good size distribution and dispersity. [23,24]

- Hydrothermal methods normally take place inside a steel pressure vessel (autoclave) where the temperature and/or the pressure can be controlled.[25]
  This method is widely used in the ceramic industry to obtain small size particles. The reaction takes place in water in the presence of a titanium precursor with peptizing agents to obtain nanoparticles, nanorods, nanotubes and nanowires.
- Solvothermal is similar to the hydrothermal synthesis, but it allowes higher temperatures as the solvent is non-aqueous.[26]
- Direct oxidation of titanium metal using oxidants or anodization is another alternative to obtain TiO_2 nanoparticles.[27]
- Chemical vapor deposition methods are normally used to form coatings, films or fibers. A vacuum chamber is needed for this formation.[28]
- Electrodeposition methods are also used to form coatings on a surface by the reduction at the cathode.[29]
- Microwave radiation is used to prepare different TiO_2 nanoparticles.[30]

To obtain meso- or nanoporous TiO_2 Barbe et al. used the hydrothermal method and by controlling the precipitation pH, hydrolysis rate and autoclaving temperature, they obtained different morphologies and sizes.[31] Other methods to obtain mesoporous titania are the sol-gel method[32] or ultrasound without the need of surfactancts[33].

Regarding the crystal structure, Hwu et al. found that it largely depends on the synthetic method.[34] Even though rutile is the most thermodynamically stable phase at high temperatures, for small nanoparticles (of less than 50 nm) the stable phase is anatase, and it is only transformed to rutile at temperatures higher than 700ºC. Also, in the synthesis of ultrafine titania, the majority product is anatase or brookite (brookite is a minority product in most of the synthesis).[35]

TiO_2 can be used for photocatalytic applications in relation with an application of bismuth sulfide, as it absorbs a photon (with larger energy than its band gap) and a electron-hole pair is created, then the carriers migrate to the surface and react with the species adsorbed on the surface, the problem is that they only can use a small percentage of sun light for the catalysis.

In this thesis, specifically in Chapter 8, we will talk about the synthesis and application of mesoporous TiO_2 as scaffolds for solar cells with a wide direct band gap of around 4.2 eV. If the TiO_2 is modified by doping with different elements[36,37] or sensitizing with dyes[38,39], QDs[40,41]… then, the band gap can be tuned and the optical properties will change.

The titanium oxide will only act as scaffold, so the free carriers won´t be formed in the titania, but in the Perovskite.

This perovskite is an inorganic material used in the last couple of years as a photoactive material in solar cells, which has been giving good efficiencies results, up to 21% (similar range as the silicon solar cells).

Perovskite present an ABX_3 crystal structure where X is the anion (a halogen as Cl^-, Br^- or I^-) and A and B are cations where A is larger than B.[42]

The lager A cation is organic (normally methylammonium[43,44] but it also can be ethylammonium[45] or formamidinium[46]) and B is lead, but in the last year reports have appear where lead was substituted by tin.[47]

$CH_3NH_3PbX_3$, is the most used structure where X is an halogen with a band gap ranging from 2.3 to 1.6 eV.

The electrons generated in the perovskite are transferred to the mesoporous TiO_2 layer and the holes go to the Hole Transporting Material (HTM).

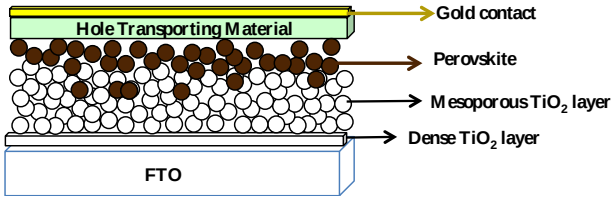

***Figure 2**. Perovskite cell structure*

The advantage that the perovskite material presents compared to other light-absorbers is that the range of absorption is higher than other organic materials (up to 800 nm), on the other hand, the main problem that these cells present right now is the toxicity that arises from the lead.

We will try to understand the interaction between the titanium oxide scaffold and the perovskite, modifying the properties of the scaffold in chapter 8.

References

1. Vogel, R., Hoyer, P. & Weller, H. Quantum-Sized PbS, CdS, Ag2S, Sb2S3, and Bi2S3 Particles as Sensitizers for Various Nanoporous Wide-Bandgap Semiconductors. *J. Phys. Chem.* **98,** 3183–3188 (1994).

2. Solís, M., Rincón, M. E., Calva, J. C. & Alvarado, G. Bismuth sulfide sensitized TiO2 arrays for photovoltaic applications. *Electrochim. Acta* **112,** 159–163 (2013).

3. Im, J.-H., Chung, J., Kim, S.-J. & Park, N.-G. Synthesis, structure, and photovoltaic property of a nanocrystalline 2H perovskite-type novel sensitizer (CH3CH2NH3)PbI3. *Nanoscale Res. Lett.* **7,** 353 (2012).

4. Liu, J. *et al.* Bismuth sulfide nanorods as a precision nanomedicine for in vivo multimodal imaging-guided photothermal therapy of tumor. *ACS Nano* **9,** 696–707 (2015).

5. Wu, T., Zhou, X., Zhang, H. & Zhong, X. Bi2S3 nanostructures: A new photocatalyst. *Nano Res.* **3,** 379–386 (2010).

6. Shi, L. *et al.* Synthesis of monodispersed ultrafine Bi2S3 nanocrystals. *J. Alloys Compd.* **509,** 9382–9386 (2011).

7. Zhang, H., Huang, J., Zhou, X. & Zhong, X. Single-crystal Bi2S3 nanosheets growing via attachment-recrystallization of nanorods. *Inorg. Chem.* **50,** 7729–34 (2011).

8. Cademartiri, L., Guerin, G., Bishop, K. J. M., Winnik, M. A. & Ozin, G. A. Polymer-like conformation and growth kinetics of Bi2S3 nanowires. *J. Am. Chem. Soc.* **134,** 9327–34 (2012).

9. Zhao, H., Tian, F., Wang, R. & Chen, R. A Review on Bismuth-Related Nanomaterials for Photocatalysis. *Rev. Adv. Sci. Eng.* **3,** 3–27 (2014).

10. Braun, J. H., Baidins, A. & Marganski, R. E. TiO2 pigment technology: a review. *Prog. Org. Coatings* **20,** 105–138 (1992).

11. Smijs, T. G. & Pavel, S. Titanium dioxide and zinc oxide nanoparticles in sunscreens: focus on their safety and effectiveness. *Nanotechnol. Sci. Appl.* **4,** 95–112 (2011).

12. Zallen, R. & Moret, M. P. The optical absorption edge of brookite TiO2. *Solid State Commun.* **137,** 154–157 (2006).

13. Pfaff, G. & Reynders, P. Angle-Dependent Optical Effects Deriving from Submicron Structures of Films and Pigments. *Chem. Rev.* **99,** 1963–1982 (1999).

14. *DuPont Ti-Pure titanium dioxide. Titanium dioxide for coatings.* at <https://www.chemours.com/Titanium_Technologies/en_US/tech_info/literature/Coatings/CO_B_H_65969_Coatings_Brochure.pdf>

15. Yuan, S., Chen, W. & Hu, S. Fabrication of TiO2 nanoparticles/surfactant polymer complex film on glassy carbon electrode and its application to sensing trace dopamine. *Mater. Sci. Eng. C* **25,** 479–485 (2005).

16. Toothpaste Ingredients, Colgate | Colgate Total®. at <http://www.colgatetotal.com/health-benefits/toothpaste-ingredients>

17. Fujishima, A. & Honda, K. Electrochemical Photolysis of Water at a Semiconductor Electrode. *Nature* **238,** 37–38 (1972).

18. Bessekhouad, Y., Robert, D. & Weber, J. V. Synthesis of photocatalytic TiO2 nanoparticles: optimization of the preparation conditions. *J. Photochem. Photobiol. A Chem.* **157,** 47–53 (2003).

19. Chemseddine, A. & Moritz, T. Nanostructuring Titania: Control over Nanocrystal Structure, Size, Shape, and Organization. *Eur. J. Inorg. Chem.* **1999,** 235–245 (1999).

20. Mori, Y., Okastu, Y. & Tsujimoto, Y. Titanium Dioxide Nanoparticles Produced in Water-in-oil Emulsion. *J. Nanoparticle Res.* **3,** 219–225 (2001).

21. Hong, S.-S., Lee, M. S., Park, S. S. & Lee, G.-D. Synthesis of nanosized TiO2/SiO2 particles in the microemulsion and their photocatalytic activity on the decomposition of p-nitrophenol. *Catal. Today* **87,** 99–105 (2003).

22. Kim, K. Do, Kim, S. H. & Kim, H. T. Applying the Taguchi method to the optimization for the synthesis of TiO2 nanoparticles by hydrolysis of TEOT in micelles. *Colloids Surfaces A Physicochem. Eng. Asp.* **254,** 99–105 (2005).

23. Niederberger, M., Bartl, M. H. & Stucky, G. D. Benzyl Alcohol and Titanium TetrachlorideA Versatile Reaction System for the Nonaqueous and Low-Temperature Preparation of Crystalline and Luminescent Titania Nanoparticles. *Chem. Mater.* **14,** 4364–4370 (2002).

24. Trentler, T. J., Denler, T. E., Bertone, J. F., Agrawal, A. & Colvin, V. L. Synthesis of TiO 2 Nanocrystals by Nonhydrolytic Solution-Based Reactions. *J. Am. Chem. Soc.* **121,** 1613–1614 (1999).

25. Yang, J., Mei, S. & Ferreira, J. M. F. Hydrothermal synthesis of TiO2 nanopowders from tetraalkylammonium hydroxide peptized sols. *Mater. Sci. Eng. C* **15,** 183–185 (2001).

26. Wen, B., Liu, C. & Liu, Y. Bamboo-shaped Ag-doped TiO2 nanowires with heterojunctions. *Inorg. Chem.* **44,** 6503–5 (2005).

27. Peng, X. & Chen, A. Aligned TiO2 nanorod arrays synthesized by oxidizing titanium with acetone. *J. Mater. Chem.* **14,** 2542 (2004).

28. Seifried, S., Winterer, M. & Hahn, H. Nanocrystalline Titania Films and Particles by Chemical Vapor Synthesis. *Chem. Vap. Depos.* **6,** 239–244 (2000).

29. Lei, Y., Zhang, L. D. & Fan, J. C. Fabrication, characterization and Raman study of TiO2 nanowire arrays prepared by anodic oxidative hydrolysis of TiCl3. *Chem. Phys. Lett.* **338,** 231–236 (2001).

30. Dar, M. I., Chandiran, A. K., Grätzel, M., Nazeeruddin, M. K. & Shivashankar, S. A. Controlled synthesis of TiO2 nanoparticles and nanospheres using a microwave assisted approach for their application in dye-sensitized solar cells. *J. Mater. Chem. A* **2,** 1662–1667 (2014).

31. Barbe, C. J. *et al.* Nanocrystalline titanium oxide electrodes for photovoltaic applications. *J. Am. Ceram. Soc.* **80,** 3157–3171 (1997).

32. Liu, C., Fu, L. & Economy, J. A simple, template-free route for the synthesis of mesoporous titanium dioxide materials. *J. Mater. Chem.* **14,** 1187–1189 (2004).

33. C. Yu, J., Zhang, L. & Yu, J. Rapid synthesis of mesoporous TiO2 with high photocatalytic activity by ultrasound-induced agglomeration. *New J. Chem.* **26,** 416–420 (2002).

34. Hwu, Y., Yao, Y. D., Cheng, N. F., Tung, C. Y. & Lin, H. M. X-ray absorption of nanocrystal TiO2. *Nanostructured Mater.* **9,** 355–358 (1997).

35. Zhang, H. & Banfield, J. F. Thermodynamic analysis of phase stability of nanocrystalline titania. *J. Mater. Chem.* **8,** 2073–2076 (1998).

36. Burda, C. *et al.* Enhanced Nitrogen Doping in TiO 2 Nanoparticles. *Nano Lett.* **3,** 1049–1051 (2003).

37. Yu, Y. *et al.* Enhancement of photocatalytic activity of mesoporous TiO2 by using carbon nanotubes. *Appl. Catal. A Gen.* **289,** 186–196 (2005).

38. Clifford, J. N. *et al.* Molecular control of recombination dynamics in dye-sensitized nanocrystalline TiO2 films: free energy vs distance dependence. *J. Am. Chem. Soc.* **126,** 5225–33 (2004).

39. Joly, D. *et al.* A Robust Organic Dye for Dye Sensitized Solar Cells Based on Iodine/Iodide Electrolytes Combining High Efficiency and Outstanding Stability. *Sci. Rep.* **4,** 4033 (2014).

40. Robel, I., Subramanian, V., Kuno, M. & Kamat, P. V. Quantum dot solar cells. harvesting light energy with CdSe nanocrystals molecularly linked to mesoscopic TiO2 films. *J. Am. Chem. Soc.* **128,** 2385–93 (2006).

41. Zewdu, T., Clifford, J. N., Hernández, J. P. & Palomares, E. Photo-induced charge transfer dynamics in efficient TiO2/CdS/CdSe sensitized solar cells. *Energy Environ. Sci.* **4,** 4633–4638 (2011).

42. Li, C. *et al.* Formability of ABX3 (X = F, Cl, Br, I) halide perovskites. *Acta Crystallogr. B.* **64,** 702–7 (2008).

43. Swainson, I. P., Hammond, R. P., Soullière, C., Knop, O. & Massa, W. Phase transitions in the perovskite methylammonium lead bromide, CH3ND3PbBr3. *J. Solid State Chem.* **176,** 97–104 (2003).

44. Leguy, A. M. A. *et al.* The dynamics of methylammonium ions in hybrid organic-inorganic perovskite solar cells. *Nat. Commun.* **6,** 7124 (2015).

45. Hsu, H.-L. *et al.* High-performance and high-durability perovskite photovoltaic devices prepared using ethylammonium iodide as an additive. *J. Mater. Chem. A* **3,** 9271–9277 (2015).

46. Koh, T. M. *et al.* Formamidinium-Containing Metal-Halide: An Alternative Material for Near-IR Absorption Perovskite Solar Cells. *J. Phys. Chem. C* **118,** 16458–16462 (2014).

47. Umari, P., Mosconi, E. & De Angelis, F. Relativistic GW calculations on CH3NH3PbI3 and CH3NH3SnI3 perovskites for solar cell applications. *Sci. Rep.* **4,** 4467 (2014).

Chapter 7

Light-Driven organophotocatalysis using cheap, non-toxic Bi_2O_3 as catalyst

UNIVERSITAT ROVIRA I VIRGILI
SEMICONDUCTOR NANOPARTICLES AS PLATFORM FOR BIO-APPLICATIONS AND ENERGY RELATED SYSTEMS.
Alba María Matas Adams
Dipòsit Legal: T 55-2016

1. Introduction

Chemical transformations promoted by sunlight are currently the subject of intense research.[1–5] Photocatalytic methods have shown promising potential for bulk production and are widely accepted and popular as convenient strategies in the area of asymmetric catalysis.[6–9] In a pioneering effort, MacMillan and co-workers merged organo- and photoredox catalysis to promote a direct asymmetric α-alkylation of aldehydes[10] through a process catalyzed by $[Ru(bpy)_3]^{2+}$.[11]
Since then, much effort has been devoted to the development of more convenient reaction conditions.[12,13]

In view of the future substantial use of such reactions, the "Achilles' heel" of these methods is their dependence on ruthenium. This is a scarce and expensive metal with rather low production (approximately twelve tons of ruthenium are mined every year) and very limited estimated world reserves (5000 tons). Furthermore, ruthenium compounds are highly toxic and suspected carcinogens. For these reasons, the identification of more convenient visible-light photocatalysts, replacing $[Ru(bpy)_3]^{2+}$ catalyst, has become an area of intense research.
In this regard, heterogeneous semiconductors[14] as well as organic dyes[15,16] have been applied to the asymmetric α-alkylation of aldehydes to avoid the use of expensive ruthenium and the presence of traces of ruthenium in the final products.

Photocatalysts that are based on heterogeneous semiconductors[17–20] have found some applications in the catalysis of organic reactions.[14,21–25] Among them, TiO_2 is by far the most used because of its low toxicity, low cost, and high reactivity.[26] However, its wide band gap (>3 eV) makes the use of UV light for its photoexcitation necessary, which should limit its use in visible-light-driven photocatalysis. In spite of this, several carbon–carbon, carbon–hydrogen, or carbon–heteroatom bond formation reactions[27–29] and even asymmetric α-alkylation reactions of aldehydes that are promoted by visible light in the presence of TiO_2 have been reported, but they proceed with low efficiency.[14] In turn, low-band-gap semiconductors such as $PbBiO_2Br$ have been revealed to be efficient visible-light photocatalysts for the asymmetric α-alkylation of aldehydes when they were employed either as a bulk material or in nanocrystalline form.[14] In any case, the toxicity of this material, associated with the presence of lead, severely limits its practical use.

Inspired by these results, we have focused our research on the identification of photocatalytic materials that fulfill a series of basic requirements in view of large-scale applications: They should be characterized by a low band gap (<1.5 eV) to ensure successful photoexcitation by visible light, and they should be abundant and nontoxic. Among the possible candidates, we identified bismuth sulfide (Bi_2S_3) and bismuth oxide (Bi_2O_3) as the most promising. These compounds are semiconductors with a low band gap (ca. 1.3 eV). Although Bi is ranked as the 69th most abundant element in the earth′s crust (Ru is ranked 74th), a large amount of bismuth is obtained each year as a side product in the refining of different metals, such as copper, lead, tin, and tungsten,[30] and the estimated world reserves exceed 320 000 tons. Therefore, bismuth and its compounds are rather inexpensive.

Moreover, bismuth and most of its derivatives are nontoxic, noncarcinogenic, and non-bioaccumulative, with low solubility in blood and water.[31] Binary bismuth(III) compounds have found applications in organic synthesis,[32,33] but they have never been used in the context of dual organo-photocatalysis.

We accordingly decided to study the photocatalytic activity of Bi_2S_3 and Bi_2O_3 and compare it with $[Ru(bpy)_3]^{2+}$. In particular, we herein report the successful application of these materials to promote the asymmetric alkylation of aldehydes with α-bromocarbonyl derivatives. Furthermore, we wanted to evaluate the influence of the physical state of these materials (nanostructured or bulk) on its catalytic behavior.

2. Experimental.

$Ru(bpy)_3Cl_2·6H_2O$ and Bi_2O_3 powder were purchased form Sigma Aldrich and used without any purification steps. Dr. Paola Riente prepared the molecules used for the catalysis.

For the characterization of the materials:

ATR spectra were recorded on Bruker Optics FTIR Alpha spectrometer equipped with a DTGS detector.

Catalytic experiment were analyzed in an Agilent 6890N gas chromatograph coupled to a mass selective detector with ionization by electronic impact and in an Agilent 6890N with a FID detector using dodecane as a internal standard.

Transmission Electron Microscopy (TEM) was carried out in a JEOL JEM-1011 microscope operating at 100 kV and equipped with a SIS Megaview III CCD camera.

A few droplets of the sample suspended in ethanol were placed on a carbon-coated copper grids followed by evaporation at ambient conditions.

Powder X-ray diffraction patterns (XRD) were measured in a Bruker AXS D8 Advance diffractometer equipped with a Cu tube, a Ge(111) incident beam monochromator, and a Vantec-1 PSD. Data were recorded in the range 5–70º 2θ with an angular step size of 0.016º and a counting time of 6 s per step.

UV-Vis measurements in solution were carried out on a Shimadzu UV-1700PC spectrophotometer equipped with a photomultiplier detector, double beam optics, and D2 and W light source. For the solid samples an ISR-240A was integrating sphere accessory used mixing the sample with $BaSO_4$.

All products that are known were characterized by comparison of their physical and spectroscopic properties with those described in the literature.

2.1 Synthesis of Bi_2S_3 nanoparticles. Following the synthesis described by Martinez et al[34], bismuth acetate (5.4 mmol, 2.09 g) was mixed with oleic acid (OA) (34 mmol, 10.72 mL) and 1-octadecene (ODE) (34 mmol, 10.88 mL) in a 50 ml flask, degassed and heated at 100 ºC overnight. After this time, the temperature was raised up to 170 ºC. In another flask a dilution of hexamethyldisilathiane (1.2 mmol, 0.253 mL) in 10 ml of ODE was made, and when the first flask reached 170 ºC, this solution was quickly injected and the mixture turned black. Following this, the reaction temperature was turned down to 100 ºC and left at these conditions for 2 hours. The reaction was stopped removing the heating mantle, and adding cold and anhydrous toluene (20 mL) and cold methanol (40 mL). The Bi_2S_3 nanoparticles were isolated by centrifugation. The purification of the particles was performed by successive dispersion and precipitation in toluene/methanol solution.

2.2α-alkylation of aldehydes. A sealed vial containing **3** (0.09 mmol, 0.2 equiv), the corresponding bromocarbonyl compound (0.45 mmol, 1 equiv), and the photocatalyst (0.01 mmol or 5 mg for Bi_2S_3 nanoparticles) was purged with argon, and anhydrous DMF (1 mL) was added through a septum.

The aldehyde (0.9 mmol, 2 equiv) and 2,6-lutidine (0.9 mmol, 2 equiv) were added to this suspension via syringe, and the mixture was degassed for 10 minutes by bubbling argon through the reaction medium. Then, the inlet and outlet needles were removed; the vial was sealed (parafilm) and placed at a distance of 10 cm from a household

bulb lamp.

When the reaction was complete according to TLC analysis or ^{1}H NMR spectroscopy, the crude reaction mixture was poured into a funnel containing diethyl ether (5 mL) and H_2O (5 mL). The layers were separated; the aqueous phase was extracted with diethyl ether (3x5 mL), and the combined organic phases were dried over $MgSO_4$ and concentrated. The resulting residue was purified by column chromatography on silica gel (hexane/EtOAc, 90:10) to afford the corresponding product.

3. Results and Discussion

The morphology of the Bi_2S_3 nanoparticles was determined by TEM (Figure 1). The main morphology present was round nanocrystals similar to dots, but there were also present nanorods, with a diameter of around 5-6 nm and a length of 15-20 nm.

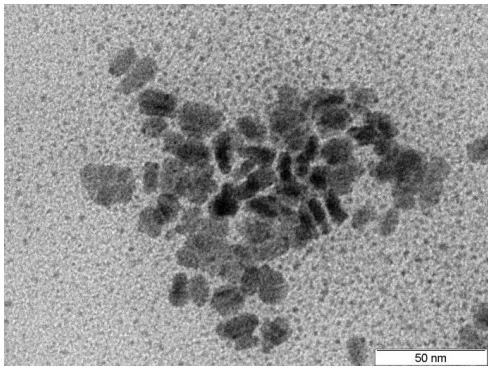

Figure 1. *TEM image of Bi_2S_3 nanocrystal.*

Additionally, the absorption was measured and was in good agreement with the one obtained by Rath et al,[35] with an absorption ranging from 800 nm to less than 300 nm. In Figure 2 the absorption of Bi_2S_3, Bi_2O_3 and $Ru(bpy)_3Cl_2 \cdot 6H_2O$ is depict and compared, to emphasized in the different range of absorption of the three materials. The wider absorption range is for Bi_2S_3, while the narrower corresponds to Bi_2O_3.

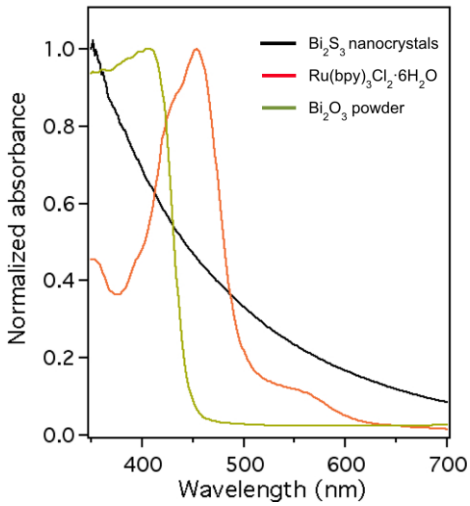

Figure 2. *Comparative UV-vis spectrum of Bi_2S_3 nanocrystals, $Ru(bpy)_3Cl_2·6H_2O$ and Bi_2O_3 powder.*

To be certain that the nanocrystals were covered by oleic acid, an infrared spectroscopy of both, oleic acid and the product was recorded (Figure 3). All the peaks, except at 1700 cm^{-1} (C=O), appear in the final product. This can be due to union between the acid from the oleic acid, and bismuth sulfide. The same happened with the peaks from 1250-1300 cm^{-1} that comes from the C-O of the acid, that also disappear, showing the correct functionalization.

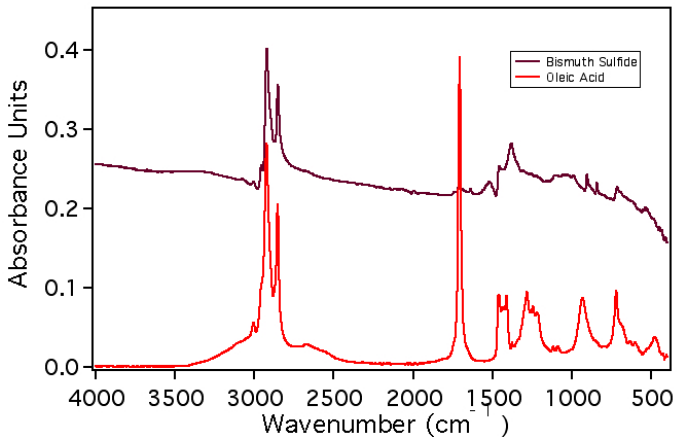

Figure 3. *IR spectrum of Bi_2S_3-capped with OA and OA.*

The diffraction peaks from the sample were recorded, the pattern for bismuth sulfide has two JCPD codes: 17-320 and 43-1471. The 2θ□angles recorded were in agreement with the theoretical, but due to detection limits not all the peaks that had to appear did (Figure 4).

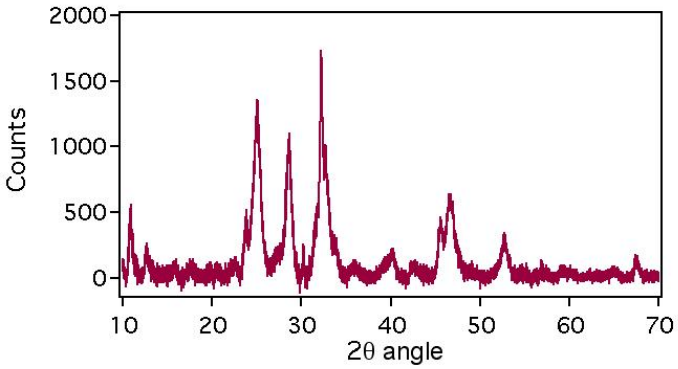

Figure 4. *XRD spectrum of Bi_2S_3.*

As the test reaction for process optimization, we selected the α-alkylation of hydrocinnamaldehyde with diethyl bromomalonate in the presence of MacMillan catalyst **3** (Table 1).

Different catalyst were used, the first studied were Bi_2S_3 (entries 1–4), and a nanostructured material (15 nm long and 5 nm wide) was our initial catalyst of choice (entry 1). Quite gratifyingly, full conversion was achieved in only one hour (entry 1) by irradiating with a 15 W fluorescent-bulb lamp, and the alkylated product **4** was obtained with excellent enantioselectivity (93 % *ee*).

If the lamp power was changed to 23 W, Product **4** could be isolated in a slightly improved yield (80 %) (entry 2), which was thus used for the rest of the study. As anticipated, the reaction did not proceed in the dark (entry 3).

With respect to the effect of the particle size on the performance of the photoredox catalyst, it was found that a reaction performed with commercial bulk Bi_2S_3 (entry 4) showed only minor erosion in catalytic activity and enantioselectivity.

Table 1. α-Alkylation of hydrocinnamaldehyde with diethyl bromomalonate using a second generation MacMillan catalyst and semiconductors.[a]

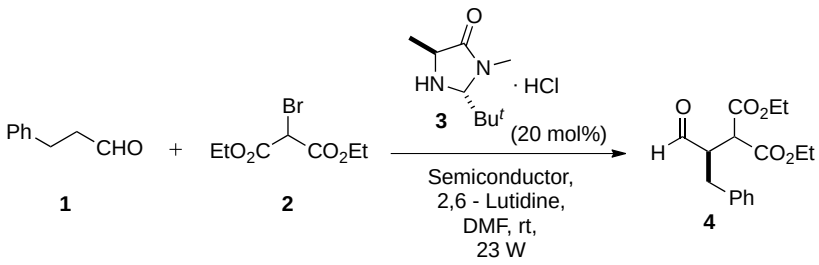

Entry	Semiconductor	t (h)	Conv. (%)[b]	Yield (%)[c]	ee (%)[d]
1	Bi_2S_3[e]	1	100	71	93
2	Bi_2S_3	1	100	80	93
3	Bi_2S_3[f]	12	2	nd	nd
4	Bi_2S_3[g]	3	98	54	85
5	Bi_2O_3[g]	1	100	86	93
6	Bi_2O_3[f]	48	-	-	-
7	Bi_2O_3[h]	3	99	81	72
8	Bi_2O_3[i]	1	100	80	93
9	Fe_2O_3[g]	72	96	45	78
10	TiO_2[j]	1	0.1	nd	nd
11	-	1	0.1	nd	nd

[a] Hydrocinnmaldehyde (0.90 mmol), diethyl bromomalonate (0.45 mmol), 2,6-lutidine (0.90 mmol), **3** (0.09 mmol), semiconductor (0.011 mmol), DMF (1 mL), 23 W fluorescent bulb lamp as light source. The reactions were performed in pyrex glassware, and the reaction mixture was degassed before irradiation was started. [b] By ^{1}H NMR. [c] Isolated yield. [d] By ^{1}H NMR on the derived diastereomeric acetals with (2*S*,4*S*)-2,4-pentanediol. [e] A 15 W fluorescent bulb lamp was used. [f] Reaction carried out in the dark. [g] Commercially available powder. [h] The reaction mixture was not degassed. [i] Reaction promoted by sunlight. [j] P25 degussa, mixture of rutile and anatase.

We next explored the use of commercial Bi_2O_3 powder in the reaction (entries 5–8). Under the previously optimized reaction conditions (23W lamp), complete conversion was recorded after one hour (entry 5), and the alkylated aldehyde **4** was obtained with excellent yield (86 %) and enantioselectivity (93 % *ee*). Control experiments showed that the reaction did not proceed in the dark (entry 6), and that the presence of dissolved oxygen had a negative effect on the process (entry 7).

Most gratifyingly, the reaction proceeded to completion in one hour with high efficiency when the reaction vial was exposed to the morning sunlight on a clear September day in Tarragona, Spain (entry 8).

For comparison, titanium dioxide[14] was tested under the optimized conditions for Bi_2O_3 (entry 9). As anticipated from band-gap considerations, a rather low conversion was recorded (12 %). The even cheaper semiconductor Fe_2O_3 was also tested as a photoredox catalyst of this transformation (entry 10). In this case, a much longer reaction time (72 h) was required for complete conversion, and the alkylated product was obtained with lower yield (45 %) and moderate enantioselectivity (78 % *ee*).

Finally, we wanted to test the viability of the reaction in the absence of a photocatalyst. When the reaction mixture was irradiated for one hour in the absence of a semiconductor (entry 11), only 8 % conversion was observed. These last results (entries 9–11) clearly show that the bismuth derivatives employed in this study are

real photocatalysts under irradiation with visible light, with efficiencies that are in accordance with their low band gaps.

To establish the scope of the asymmetric α-alkylation of aldehydes enabled by bismuth-based semiconductors as photocatalysts, of aldehyde substrates was selected and reacted them with different compounds in the presence of either Bi_2S_3 nanoparticles or bulk Bi_2O_3 and the second-generation MacMillan catalyst **3** under the previously optimized reaction conditions.

The results obtained with Bi_2O_3 showed much higher reproducibility than those obtained with Bi_2S_3 nanoparticles. This is most probably due to the fact that nanostructured Bi_2S_3 is almost completely insoluble in the reaction medium, and changes in aggregation between different batches of this material lead to substantial differences in catalytic behavior. Bismuth oxide, in turn, dissolves in the reaction media as the reaction proceeds. Thus, reactions mediated by Bi_2O_3 are essentially homogeneous and hence are not influenced by the physical state of the photoredox catalyst.

By comparison with the seminal contribution of Nicewicz and MacMillan, which illustrated the potential of $[Ru(bpy)_3]^{2+}$ in this transformation, some important advantages (as well as some limitations) that are associated with the use of bismuth-based semiconductors as photocatalysts became evident. First, the reactions with bromomalonate alkylating agents are much faster (1–3 h vs. 5–7 h) and slightly more enantioselective with the bismuth-based photoredox catalysts than with $[Ru(bpy)_3]^{2+}$. In contrast, for processes that involve α-bromocarbonyl alkylating agents, the reactions mediated by Bi_2X_3 required substantially more time to reach completion, although the enantioselectivities remained high (ca. 90 % *ee*).

4. Conclusions

In summary, the feasibility of using Bi_2O_3 and Bi_2S_3 semiconductors as photocatalysts for the direct asymmetric α-alkylation of aldehydes with α-bromocarbonyl compounds under organo-photocatalytic conditions has been established. Aside from the advantages of bismuth compounds in terms of their low cost and nontoxicity, we have found that bulk, commercial Bi_2O_3 is an even more active catalyst of this process than nanostructured Bi_2S_3, which appears to be due to the solubility of the oxide in the

reaction medium. Both bismuth compounds are catalytically active at low concentrations under irradiation with white light from a standard-illumination fluorescent bulb or under simple exposure to sunlight. The findings reported in this communication pave the way for future applications of these environmentally friendly materials in photocatalyzed organic reactions.

References

1. Yoon, T. P., Ischay, M. A. & Du, J. Visible light photocatalysis as a greener approach to photochemical synthesis. *Nat. Chem.* **2,** 527–32 (2010).

2. Narayanam, J. M. R. & Stephenson, C. R. J. Visible light photoredox catalysis: applications in organic synthesis. *Chem. Soc. Rev.* **40,** 102–13 (2011).

3. Prier, C. K., Rankic, D. A. & MacMillan, D. W. C. Visible light photoredox catalysis with transition metal complexes: applications in organic synthesis. *Chem. Rev.* **113,** 5322–63 (2013).

4. Schultz, D. M. & Yoon, T. P. Solar synthesis: prospects in visible light photocatalysis. *Science.* **343,** 1239176 (2014).

5. Hopkinson, M. N., Sahoo, B., Li, J.-L. & Glorius, F. Dual catalysis sees the light: combining photoredox with organo-, acid, and transition-metal catalysis. *Chemistry* **20,** 3874–86 (2014).

6. Xuan, J., Lu, L.-Q., Chen, J.-R. & Xiao, W.-J. Visible-Light-Driven Photoredox Catalysis in the Construction of Carbocyclic and Heterocyclic Ring Systems. *European J. Org. Chem.* **2013,** 6755–6770 (2013).

7. Reckenthäler, M. & Griesbeck, A. G. Photoredox Catalysis for Organic Syntheses. *Adv. Synth. Catal.* **355,** 2727–2744 (2013).

8. Bergonzini, G., Schindler, C. S., Wallentin, C.-J., Jacobsen, E. N. & Stephenson, C. R. J. Photoredox Activation and Anion Binding Catalysis in the Dual Catalytic Enantioselective Synthesis of β-Amino Esters. *Chem. Sci.* **5,** 112–116 (2014).

9. Nguyen, T. M., Manohar, N. & Nicewicz, D. A. anti-Markovnikov hydroamination of alkenes catalyzed by a two-component organic photoredox system: direct access to phenethylamine derivatives. *Angew. Chem. Int. Ed. Engl.* **53,** 6198–201 (2014).

10. Vignola, N. & List, B. Catalytic asymmetric intramolecular alpha-alkylation of aldehydes. *J. Am. Chem. Soc.* **126,** 450–1 (2004).

11. Nicewicz, D. A. & MacMillan, D. W. C. Merging photoredox catalysis with organocatalysis: the direct asymmetric alkylation of aldehydes. *Science* **322,** 77–80 (2008).

12. Shih, H.-W., Vander Wal, M. N., Grange, R. L. & MacMillan, D. W. C. Enantioselective α-benzylation of aldehydes via photoredox organocatalysis. *J. Am. Chem. Soc.* **132,** 13600–3 (2010).

13. Pirnot, M. T., Rankic, D. A., Martin, D. B. C. & MacMillan, D. W. C. Photoredox activation for the direct β-arylation of ketones and aldehydes. *Science* **339,** 1593–6 (2013).

14. Cherevatskaya, M. *et al.* Visible-light-promoted stereoselective alkylation by combining heterogeneous photocatalysis with organocatalysis. *Angew. Chem. Int. Ed. Engl.* **51,** 4062–6 (2012).

15. Neumann, M., Füldner, S., König, B. & Zeitler, K. Metallfreie kooperative asymmetrische Organophotoredoxkatalyse mit sichtbarem Licht. *Angew. Chemie* **123,** 981–985 (2011).

16. Fidaly, K. *et al.* Visible light photoredox organocatalysis: a fully transition metal-free direct asymmetric α-alkylation of aldehydes. *Green Chem.* **14,** 1293–1297 (2012).

17. Hoffmann, M. R., Martin, S. T., Choi, W. & Bahnemann, D. W. Environmental Applications of Semiconductor Photocatalysis. *Chem. Rev.* **95,** 69–96 (1995).

18. Rajeshwar, K., de Tacconi, N. R. & Chenthamarakshan, C. R. Semiconductor-Based Composite Materials: Preparation, Properties, and Performance. *Chem. Mater.* **13,** 2765–2782 (2001).

19. Kisch, H. Semiconductor photocatalysis--mechanistic and synthetic aspects. *Angew. Chem. Int. Ed. Engl.* **52,** 812–47 (2013).

20. Serpone, N. & Emeline, A. V. Semiconductor Photocatalysis — Past, Present, and Future Outlook. *J. Phys. Chem. Lett.* **3,** 673–677 (2012).

21. Zeug, N., Buecheler, J. & Kisch, H. Catalytic formation of hydrogen and carbon-carbon bonds on illuminated zinc sulfide generated from zinc dithiolenes. *J. Am. Chem. Soc.* **107,** 1459–1465 (1985).

22. Ohtani, B., Kusakabe, S., Nishimoto, S., Matsumura, M. & Nakato, Y. Improvement of Photocatalytic Activity and Product Selectivity by Cadmium Metal Deposited in situ on Suspended Cadmium(II) Sulfide Particles. *Chem. Lett.* **24,** 803–804 (1995).

23. Marinković, S. & Hoffmann, N. Diastereoselective Radical Tandem Addition-Cyclization Reactions of Aromatic Tertiary Amines by Semiconductor-Sensitized Photochemical Electron Transfer. *European J. Org. Chem.* **2004,** 3102–3107 (2004).

24. Mitkina, T. *et al.* Visible light mediated homo- and heterocoupling of benzyl alcohols and benzyl amines on polycrystalline cadmium sulfide. *Org. Biomol. Chem.* **10,** 3556–61 (2012).

25. Lang, X., Chen, X. & Zhao, J. Heterogeneous visible light photocatalysis for selective organic transformations. *Chem. Soc. Rev.* **43,** 473–86 (2014).

26. Chen, X. & Mao, S. S. Titanium dioxide nanomaterials: synthesis, properties, modifications, and applications. *Chem. Rev.* **107,** 2891–959 (2007).

27. Ho, X.-H., Kang, M.-J., Kim, S.-J., Park, E. D. & Jang, H.-Y. Green organophotocatalysis. TiO2-induced enantioselective α-oxyamination of aldehydes. *Catal. Sci. Technol.* **1,** 923–926 (2011).

28. Vila, C. & Rueping, M. Visible-light mediated heterogeneous C–H functionalization: oxidative multi-component reactions using a recyclable titanium dioxide (TiO2) catalyst. *Green Chem.* **15,** 2056–2059 (2013).

29. Rueping, M. *et al.* Light-mediated heterogeneous cross dehydrogenative coupling reactions: metal oxides as efficient, recyclable, photoredox catalysts in C-C bond-forming reactions. *Chemistry* **18,** 3478–81 (2012).

30. Mineral Commodity Summaries 2012. at <http://minerals.usgs.gov/minerals/pubs/mcs/2012/mcs2012.pdf>

31. Briand, G. G. & Burford, N. Bismuth Compounds and Preparations with Biological or Medicinal Relevance. *Chem. Rev.* **99,** 2601–2658 (1999).

32. Leonard, N. M., Wieland, L. C. & Mohan, R. S. Applications of bismuth(III) compounds in organic synthesis. *Tetrahedron* **58,** 8373–8397 (2002).

33. Aggen, D. H., Arnold, J. N., Hayes, P. D., Smoter, N. & Mohan, R. S. Bismuth compounds in organic synthesis. Bismuth nitrate catalyzed chemoselective synthesis of acylals from aromatic aldehydes. *Tetrahedron* **60,** 3675–3679 (2004).

34. Martinez, L. *et al.* Hybrid solution-processed bulk heterojunction solar cells based on bismuth sulfide nanocrystals. *Phys. Chem. Chem. Phys.* **15,** 5482–7 (2013).

35. Rath, A. K. *et al.* Solution-processed inorganic bulk nano-heterojunctions and their application to solar cells. *Nat. Photonics* **6,** 529–534 (2012).

Chapter 8

The influence of the mesoporous TiO_2 scaffold in the performance of Methyl Ammonium Lead Iodide (MAPI) Perovskite solar cells: charge injection, charge recombination and solar cell efficiency relationship.

UNIVERSITAT ROVIRA I VIRGILI
SEMICONDUCTOR NANOPARTICLES AS PLATFORM FOR BIO-APPLICATIONS AND ENERGY RELATED SYSTEMS.
Alba María Matas Adams
Dipòsit Legal: T 55-2016

1.Introduction

The research of earth abundant and inexpensive materials for solar cells such as MAPI[1,2], SnS[3] and CZTS[4] is attracting much attention and hold the promise to fill the gap of the terawatt solar energy production.[5]

In less than 5 years the reported efficiency for MAPI perovskite solar cells has arrived to overpass 20% under standard conditions (100mW/cm^2 sun-simulated 1.5 AM G). [6]

Although the interest in MAPI, as photoactive material, in solar cells has derived in multiple solar cell configurations[7], with solar cell efficiencies superior to other related energy conversion devices such as dye sensitized solar cells, organic solar cells and quantum dot solar cells, the most utilised configuration is the one that uses mesoporous TiO_2 ($mpTiO_2$) as scaffold and/or contact electrode. In fact, the best reported efficiencies have been published with the following device configuration: FTO/$dTiO_2$/$mTiO_2$/MAPI or MAPIC/ HTM/Au where FTO is fluorine doped tin oxide, $dTiO_2$ is a thin and dense layer of TiO_2, $mpTiO_2$ is the mesoporous layer of TiO_2, MAPI or MAPIC is the methyl ammonium lead iodide without or with chloride, respectively, HTM is the hole transport material and Au is the gold metal contact.

Mesoporous TiO_2 has been widely used in different areas such as catalysis[8], sensing[9] and energy[10]. In the later area of research, energy, the TiO_2 is paramount in so called Grätzel solar cells[11] or dye sensitized solar cells (DSSC) with an outstanding number of reports on the properties of the $mpTiO_2$ and its effects over the DSSC performance.[12–14] In contrast, in MAPI solar cells the number of such studies is scarce for several reasons; including the considerable recent discover of MAPI solar cells and the fact that MAPI solar cells can also be constructed without the use of $mpTiO_2$ with a noteworthy efficiency.[15,16] Nonetheless, there are important scientific questions that are still under debate in relation with the role of the nanocrystalline TiO_2 nanoparticles and, hence, the $mpTiO_2$ layer over the MAPI device function. For example, taking into account that MAPI solar cells also work well using $mpAl_2O_3$ as scaffold and the Al_2O_3 is a well-known wide band-gap insulator, is not clear if it is really necessary an efficient electron transfer reaction from the MAPI perovskite

material to the TiO_2 conduction band, TiO_2 CB; (so called charge injection in a parallelism with the charge transfer from the dye excited state to the TiO_2 CB in DSSC) or if the electron accumulation at the $mpTiO_2$ plays a role on the MAPI solar cell voltage at all.

In this work we aim to study how different $mpTiO_2$ layers fabricated using different synthetic routes effect a change on the MAPI solar cell parameters: short circuit current (Isc), open circuit voltage (Voc) , fill factor (FF) and the overall efficiency (η). The synthetic routes differ on the pH synthetic conditions leading to an acid route and a basic route and their respective acid or basic TiO_2 pastes used to fabricate the $mpTiO_2$. Moreover, we examined the electrical differences of the different MAPI perovskite solar cells in terms of charge density (defined as the total accumulated charge at the solar cell) as a function of light bias (cell voltage due to external applied light at different and controlled light intensities) and its relation with capacitance and carrier recombination lifetime measured under solar cell working conditions.

2.Experimental Section

2.1Nanocrystalline TiO_2 nanoparticles ($ncTiO_2$) synthesis. The colloids of titanium dioxide nanoparticles were obtained starting from the same precursor (titanium isopropoxide), but different peptidization agents were used to modify the surface charge. Two different synthetic routes were followed as previously reported by Hore et al.[12]

Acid Route

The acid preparation of TiO_2 nanocrystalline nanoparticles consisted on 20mL of anhydrous titanium isopropoxide (Sigma Aldrich© 97%) mixed under argon atmosphere with 5.5 mL of glacial acetic acid (Panreac©) and stirred for 10 minutes.
In a separated Erlenmeyer, 120 mL of a 0.1 M nitric acid solution (Scharlau, 69.5%) in distilled water was degassed with argon.
The TiO_2 colloidal solution was injected dropwise at room temperature while stirring.
The final mixture was stirred vigorously under argon at 1500 rpm for 10 minutes, and finally heated in air for 8 hours at 80^{o}C, followed by room temperature cooling over night.

Next, the solution was filtrated at room temperature using a 0.45 μm syringe filter.
To allow the $ncTiO_2$ to grow into the desired particle size, 5% in weight of the $ncTiO_2$ solution was autoclaved at 220°C for 12 hours and later allowed to cool down to room temperature. The obtained particles sizes were between 15-20nm.
The colloids were dispersed with a 60 seconds cycle burst using a sonic probe horn, and concentrated to 12.5% in TiO_2 weight to prepare the acid $mpTiO_2$ paste for the MAPI perovskite solar cell fabrication.

Basic Route

A similar procedure was followed for the basic peptidization, but instead of mixing the titanium isopropoxide with acetic acid the 20 mL were injected dropwise into a 0.1M solution of tetramethylammonium hydroxide (Sigma Aldrich©, 25wt% in H_2O) in distilled water previously degassed with argon. The solution was vigorously stirred at 1500 rpm for 10 minutes and then heated at 80°C, 500 rpm for 8h.
Next, the solution was left to cool down over night, filtrated as mentioned above and recovered.
For the basic route, the procedure to grow the nanoparticles is alike the acid route but the autoclave temperature is set to 180°C
In both cases, to form the titanium dioxide pastes from the $ncTiO_2$, we added 6.2 w% of Poly (ethylene oxide) (Sigma Aldrich©, molecular weight (Mw)≈300000) to the final suspension.

2.2 Nanocrystalline TiO_2 nanoparticles characterization.

The nanocrystalline TiO_2 particles were characterized using XRD (X-ray powder diffraction), TEM (transmission electron microscopy), nitrogen isotherms (Brunauer-Emmett-Teller) and Z potential measurements as shown.

Powder XRD was measured in a Bruker© AXS D8 Advance diffractometer equipped with a Cu tube, a Ge (111) incident beam monochromator, and a Vantec-1 PSD. Data were recorded in the range 5-70° 2θ with an angular step size of 0.016° and a counting time of 6 seconds per step.

Transmission Electron Microscopy (TEM) was carried out in a JEOL JEM-1011 microscope operating at 100 kV and equipped with a SIS Megaview III CCD camera.

A 5µL of the sample suspended in ethanol were placed on a carbon-coated copper grids followed by evaporation at ambient conditions.

Zeta potential (ζ-potential) was measured with a NanoSizer (MALVERN© Nano-ZS) using dynamic light scattering (DLS) and the Smoluchowski equation. All measurements were performed at 25^{o}C.

Nitrogen isotherms (BET) measurements were carried out at 77K on a Quantachrome Autosorb© iQ analyser. Prior to the analysis, the samples were degassed in a vacuum at 300 ^{o}C for 5h. The BET theory was applied to calculate the total surface area.

2.3 MAPI perovskite solar cell fabrication and characterization

The device presents the following architecture: FTO/d-TiO_2/mp-TiO_2/MAPI/OMeTAD/gold, and for its preparation a thin (50 nm) and dense titanium oxide layer (d-TiO_2) was deposited by spin-coating onto the Fluorine doped Tin Oxide glass (FTOs) with a resistance of 8 Ω/cm^2 as previously described.[17]

To homogenize this layer, the substrates were immersed in a 40mM $TiCl_4$ solution at 70^{o}C for 30 minutes and annealed at 500^{o}C for 20 minutes.

Next, the mesoporous titanium oxide layer (mp-TiO_2) was spin-coated, and in this case, three different pastes of titanium oxide were used: Commercial paste (Ti Nanoxide HT/SP Solaronix©), Acid paste and Basic Paste, in different proportions of paste: ethanol, to obtain a mesoporous TiO_2 layer of 400 nm. The substrates were then heated at 325^{o}C for 30 minutes, 375^{o}C for 5 minutes, 450^{o}C for 15 minutes and at 500^{o}C for 30 minutes.

For the MAPI perovskite preparation, methyl ammonium iodide (MAI) synthesized as described previously[18] was mixed with lead chloride ($PbCl_2$) (Sigma Aldrich©, 98%) in a 3:1 molar ratio in DMF (anhydrous dimethyl formamide) and deposited over the different mp-TiO_2 film in a glove box ([H_2O]<0.1ppm and [O_2]<100ppm) at 2000 rpm for 60 seconds.

Next, the film was annealed at 100^{o}C for 1 hour.

The Hole Transport Material (HTM) spiro-OMeTAD (1-Material©) was dissolved in chlorobenzene (70mg/mL). Bis (trifluoromethane)-sulfonimide lithium salt (520mg/mL) and 4-tertbutylpiridine were used as chemical additives.

For all different devices we kept identical spin-coating conditions.

Finally, an 80 nm layer of gold was evaporated as anode by thermal evaporation at a pressure close to $1X10^{-6}$ mbar.

2.4 Photo-induced characterization.

Several techniques have been used to characterise either mpTiO_2/MAPI and mpTiO_2/MAPI/OMeTAD thin films or complete MAPI perovskite solar cells.

Picosecond-nanosecond Time Correlated Single Photon Counting (ps-ns TCSPC) was used to estimate charge injection and measure the radiate recombination lifetime. The system used was an Edinburgh Instruments© LifeSpec-II spectrometer with a PMT detector and a laser excitation source with a nominal wavelength of 470 nm and an IR (Instrument Response) measured at FWHM (Full width at half maximum) of 400 ps.

Photo-induced charge recombination kinetics in thin films was carried out using a home-build L-TAS system (Laser Transient Absorption Spectroscopy) that consist in a Nd-YAG excitation source in line with an optical parametric oscilator (OPO) to tune the excitation wavelength with a laser pulse energy of 75microJ/cm^2. The probe wavelength is a 150 W lamp that is filtered through two monochromators from Dongwoo Optron (DM500i model) positioned in front and behind the sample holder. The signal is recorded using an InGAs photodiode for the IR region.

Photo-induced differential charging (PIDC) was used to register the charge accumulated at the solar cell under different light bias. The PIDC technique was used as described before[17]. In brief, PIDC uses the photo-induced transient photocurrent decay (PIT-PC) and the PIT-PV decays to calculate the solar cell capacitance assuming two caveats: (1) the charge losses at short circuit in the solar cell under illumination are negligible and (2) the solar cell Isc value is linear with the increase of sun-simulated light intensity. The first caveat can be tested by measuring PIT-PC in the dark and at 1 sun conditions and compare that there are not critical differences in both decays. The second caveat can be tested measuring the MAPI solar cell under different light intensity conditions and registering the Isc. The relationship between Isc and light intensity (LI)

must be close to a=1 where a is the exponential factor in the power law relationship P α LI

The photo-induced transient photovoltage (PIT-PV) was measured using a rig of white LEDs plus a nanosecond PTI GL- 3300 N_2 dye laser.[19] Once the MAPI solar cell voltage has arrived to equilibrium, for a given light bias, a short laser pulse given by the N_2 dye laser produced a small charge in Voc (usually less than 20mV). The original Voc is restored after the N2 dye laser pulse. The generated voltage decay, thus, represents a small DV at a given light bias that can be directly correlated with the device charge measured at the same given light bias (Voc).

3. Results and discussion

3.1 Nanocrystalline TiO_2 nanoparticles ($ncTiO_2$).

Figure 1 illustrates the TEM (Transmission Electron Microscopy) images for the acid, the basic and a commercial sample of $ncTiO_2$ particles. As can be seen, the acid route leads to smaller $ncTiO_2$ with a more spherical shape than the presented in the case of the basic nanoparticles that have a rod-like shape and bigger size.

The X-ray diffraction (XRD) measurements (Figure 2) shows clear diffraction peaks at 2 tetha angle (2θ) at 25^o and 48^o indicating TiO_2 anatase phase, in good agreement with the standard spectrum (JCPDS: 84-1286). Moreover, it can be seen that for the basic $ncTiO_2$ the diffraction pattern is more resolved in sharp peaks in contrast with the acid $ncTiO_2$ samples but in this particular case was due to the small size of the acid TiO_2 nanoparticles.

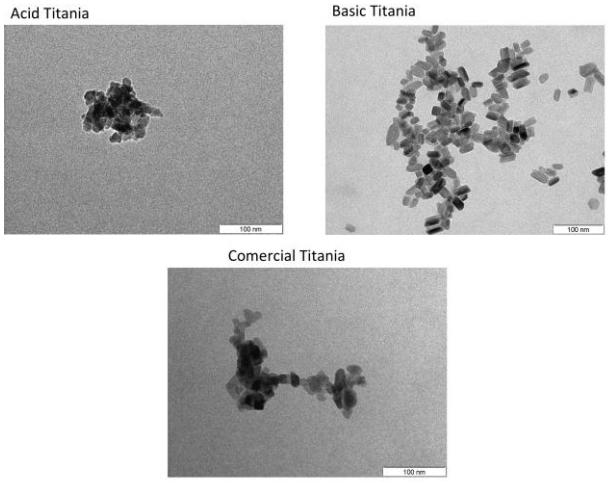

Figure 1. *TEM images of ncTiO2 from different synthetic routes. The scale bar is 100nm.*

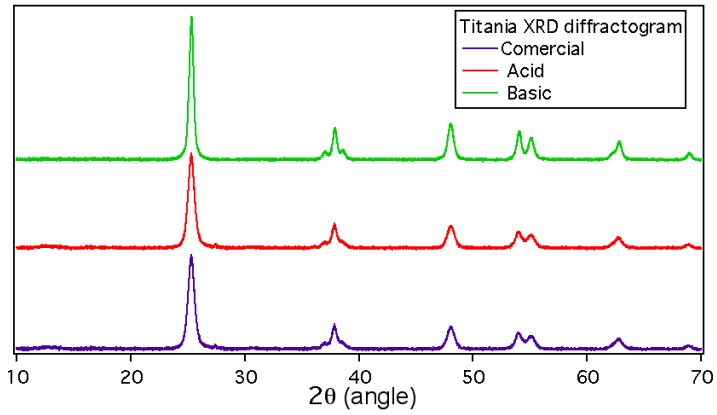

***Figure 2**. XRD measurements for $ncTiO_2$ acid samples (red), $ncTiO_2$ basic samples (green) and commercial $ncTiO_2$ (purple).*

We carried out further analysis of the samples measuring the zeta potential and the surface area. The zeta potential is a key measurement to evaluate the different charge at the surface of the $ncTiO_2$ particles. Table 1 shows the different properties for the $ncTiO_2$ samples studied in the present work.

Table 1. NcTiO2 characterisation parameters.

	Size (nm)	S_{BET} (m^2/g)	V_{pore} (cm^3/g)	PSD (nm)	Zpot (mV)
Acid	**10-20**	**92**	**0.2**	**8.46**	**-14.6**
Basic	**15-30**	**49**	**0.11**	**9.33**	**-24.8**
Com	**10-20**	**85**	**0.48**	**22.6**	**-3.53**

S_{BET}= Surface area measurement. V_{pore} = Pore volume. PSD=Pore Size Distribution. Zpot= Zeta potential. Com= commercial sample.

Thus, as can be seen from Figure 1 and Figure 2, as well as, from the parameters listed in Table 1 there are important differences on the $ncTiO_2$ particles depending on the synthetic route. For example, the different Z potential can be correlated with different pH values for the $mpTiO_2$ paste as demonstrated before.[20] The acid paste with a -14.6 mV will correspond to a pH value of 6.5, while for the case of the basic paste, -24.8mV corresponds to a pH of 7.5, which is neutral pH.

Once the $ncTiO_2$ were characterised we prepared $mpTiO_2$ thin films alike those ones that will be used for the fabrication of the solar cells and performed the initial characterization of two of the interfacial charge transfer reactions that occur at the solar cell as detailed in the next point.

3.2 Charge injection in mpTiO$_2$/MAPI thin films and charge recombination in mpTiO2/MAPI and mp/TiO2/OMeTAD thin films.

On the one hand, we measured the charge injection from the MAPI perovskite into the TiO_2 CB using TCSPC as detailed in the Experimental section. The TCSPC is commonly used to scrutinize the radiative recombination lifetime in MAPI and MAPIC thin films[21,22] and has been useful to evaluate the radiative charge recombination order[23]. Here we used the TCSPC measurements to measure the changes on the MAPI perovskite radiative recombination lifetime. Figure 3 illustrates the different photoluminescence decays for the different mpTiO$_2$/MAPI films.

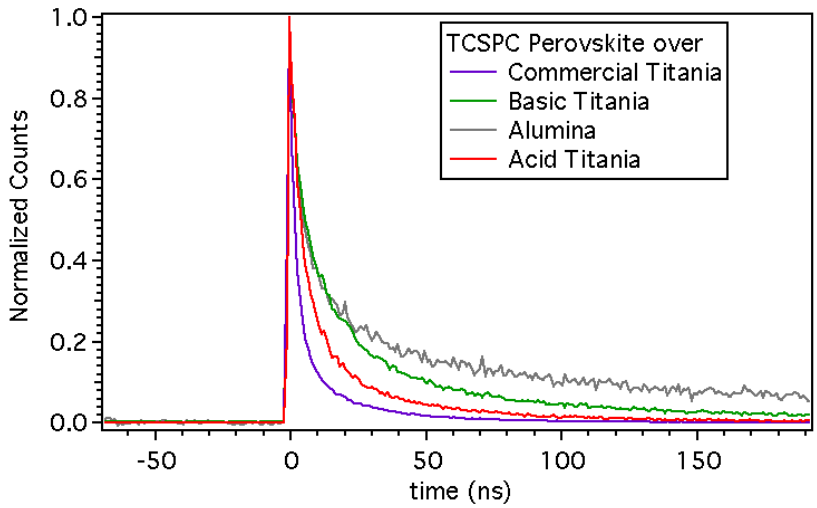

Figure 3. *Normalised photoluminescence decays measured after excitation at □=470nm under nitrogen and monitoring at 750 nm.*

As can be appreciated the MAPI perovskite radiative recombination lifetime is greatly affected upon the different mpTiO$_2$ film. It is worthy to mention that we have also used mpAl$_2$O$_3$ for comparison purposes and all films have equivalent absorbance at the excitation wavelength (λex=470nm).

The slower decay lifetime for the pastes corresponds to the basic mpTiO$_2$ with a value of τ1=47ns and τ2=6ns, in contrast with the acid mpTiO$_2$ that has a decay lifetime of τ1=30ns and τ2=5ns. These values appear to be faster than those values reported for other MAPI films.

On the other hand, we used IR L-TAS to measure the interfacial charge recombination in mpTiO$_2$/MAPI/spiro-OMeTAD films. Upon light excitation

the MAPI perovskite generates free carriers (electrons and holes) and can transfer an electron to the TiO_2 CB or, alternatively, can transfer an electron to a TiO_2 surface state (TiO_2-ss). While the latter case results in a charge loss, the former case can lead to electrical work if the charge is transported efficiently to the contact. However, it is also likely that the electron can undergo back electron transfer to the MAPI perovskite or to the spiro-OMeTAD film. Last but not least, it is also feasible that upon light excitation and carrier generation an electron can be directly transferred from the MAPI perovskite CB to the HTM spiro-OMeTAD. Scheme 1 shows a representation of the interfacial charge transfer described above. Needless to say that we have not included other charge transfer reactions (ie: radiative and non radiative charge transfer reactions within the MAPI perovskite) to simplify the graphical representation.

Interfacial electron transfer reaction (4) in Scheme 1 is still under debate as it implies that electrons must be transported through the perovskite material to recombine with holes at the HTM, in this case the spiro-OMeTAD.[24] This process can be possible if charges have excellent mobility at the MAPI perovskite and also may occur if the perovskite overlayer on top of the mpTiO_2 presents micropores where the spiro-OMeTAD can penetrate and get closer to the TiO_2. In any case, early work by Moser and co-workers have already measured this electron transfer reaction, which supposes a non radiative carrier recombination pathway that minimised the solar cell efficiency[25]. Yet, we must consider that these measurements and the ones described herein below are registered in dark conditions (without any light bias) and may differ from charge transfer reactions under light irradiation conditions.[26]

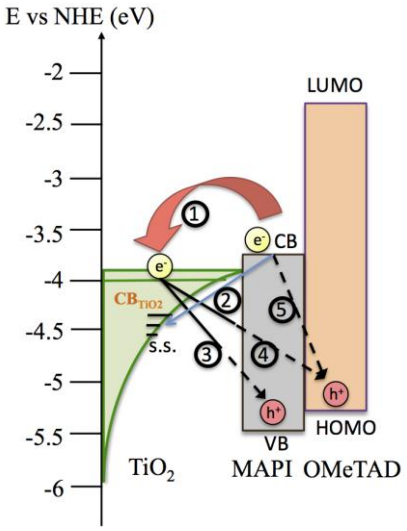

Scheme 1. *Interfacial charge transfer reactions upon light excitation in mpTiO$_2$/MAPI/spiro-OMeTAD. (1) Electron injection from the MAPI perovskite CB to the TiO$_2$ CB. (2) Charge transfer from the MAPI perovskite CB to the TiO$_2$ surface states. (3) Back-electron transfer from the TiO$_2$ to the MAPI perovskite VB (valence band). (4) Back-electron transfer from the TiO$_2$ to the spiro-OMeTAD and (5) electron transfer from the MAPI perovskite to the spiro-OMeTAD.*

Figure 4 shows the IR L-TAS interfacial charge recombination reaction, reaction 4 at Scheme 1, for our different mpTiO$_2$/MAPI/spiro-OMeTAD thin films. We registered the measurement at λ_{probe}=1400nm that corresponds to the wavelength near the maximum absorption of the spiro-OMeTAD positive polarons (spiro-OMeTAD$^+$) as reported before.[24] Figure 4 illustrates the IR L-TAS spectrum for the mpTiO$_2$/MAPI/spiro-OMeTAD upon excitation at λex=580nm under nitrogen at 25^o C.

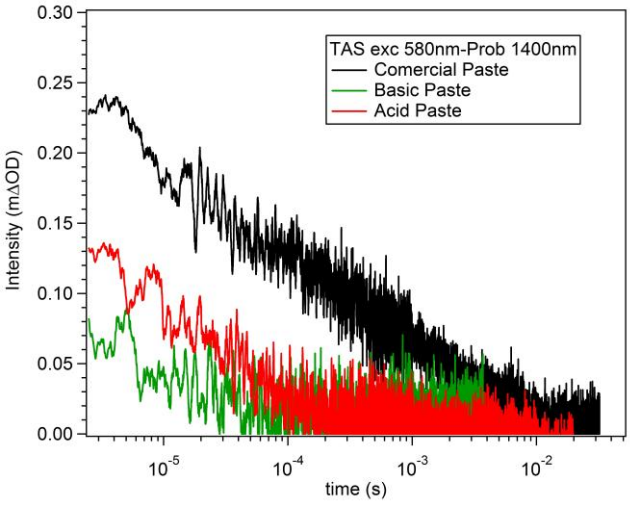

Figure 4. *Photo-induced interfacial charge recombination decays for the mpTiO$_2$ acid (red), mpTiO$_2$ basic (green) and the mpTiO$_2$ commercial pastes with the MAPI perovskite and the spiro-OMeTAD layers alike in a functional solar cell. The excitation wavelength was λ_{ex}=580nm and the probe wavelength was λ_{probe}=1400nm.*

As can be seen in Figure 4, the most striking observation is the low signal amplitude for the basic mpTiO_2 sample in comparison with the acid mpTiO_2 and the commercial mpTiO_2 paste. As all samples have alike absorption at 580nm, this results implicates that for the basic mpTiO_2 there is much less yield of electron injection from the MAPI perovskite to the TiO_2 CB. On the contrary, the signal amplitude for the commercial mpTiO_2 /MAPI/spiro-OMeTAD film denotes a greater yield for the electron injection (reaction 1 at Scheme 1) process.

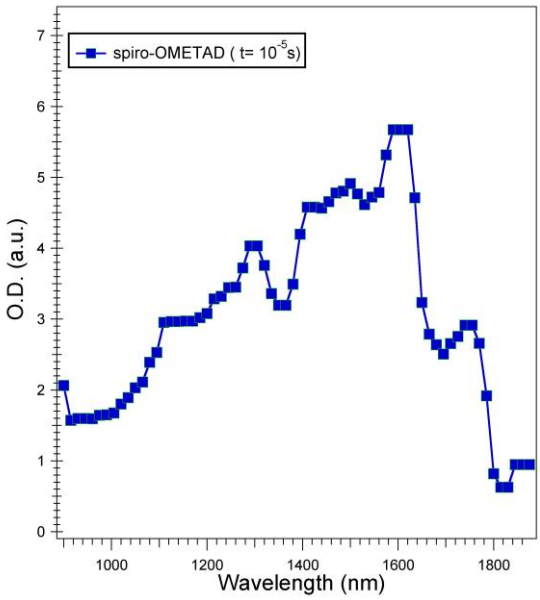

***Figure 5**. Photo-induced IR-LTAS spectrum for a mpTiO_2/MAPI/spiro-OMeTAD film (mpTiO_2 commercial) registered after 10 microseconds of laser excitation (laser power 70microJ/cm^2) at λex=580nm under ambient conditions.*

The IR L-TAS measurements are in good agreement with the measurements carried out using TCSPC and shown in Figure 3, where the mpTiO_2/MAPI basic film shows the slowest radiative recombination decay for TiO_2 samples and the electron injection in this particular film is not efficient. Thus, we can establish that the order for efficient electron injection in our different mpTiO_2 films is commercial>acid>basic ncTiO_2 nanoparticles. Moreover, other important feature that can be seen in Figure 5 is the different decay half-lifetimes (measured at the decay half maximum of its signal amplitude) for the acid and the commercial mpTiO_2/MAPI/spiro-OMeTAD films. The former has a $\tau_{1/2}$=26ms and the later a $\tau_{1/2}$=170ms, respectively. As the laser power intensity was kept constant and the MAPI perovskite absorption at the

excitation wavelength was alike the first hypothesis for the observed difference in decay lifetime is that the electrons at the acid mpTiO_2 are deeply trapped while in the commercial mpTiO_2 the electrons are in shallow traps and can more easily migrate to the surface.

To complete our study, we now turned into the fabrication and characterization of the MAPI perovskite solar cells using the different mpTiO_2 films.

3.3 MAPI perovskite solar cells characterization.

We fabricate the MAPI perovskite solar cells as detailed at the Experimental Section. Figure 6 shows the measured IV curves (current vs. voltage) under standard 1 sun measuring conditions (100mW/cm^2 sun-simulated 1.5.AM G spectrum).

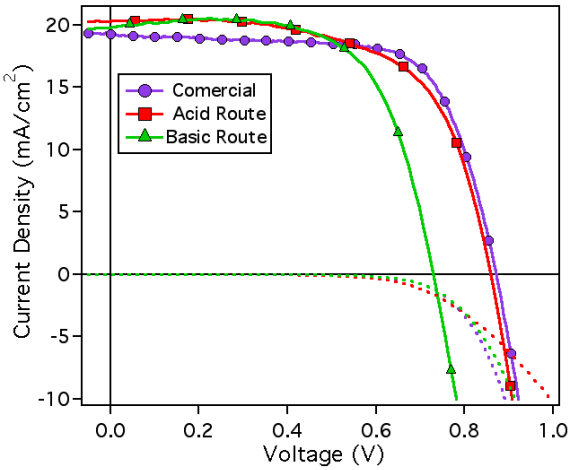

Figure 6. *The current vs. voltage curves measured under 1sun (1.5 AM G sun simulated irradiation, lines with markers) and under dark. The solar cells have an area of 0.25cm^2.*

The most relevant parameters from the measured MAPI perovskite solar cells are listed in Table 2. The solar cells fabricated with the basic mpTiO_2 show almost identical Jsc (≈20mA/cm^2), however, the Voc (730mV) is systematically lower in these devices. On the other hand, the acid mpTiO_2 film shows almost alike performance as the commercial TiO_2 paste.

Table 2. Most relevant parameters for the MAPI perovskite solar cells measured in this work.

	Jsc (mA)	Voc (mV)	FF (%)	η (%)	Rs (Ω)	Rsh (Ω)
Basic	19.8	733	66.56	9.62	9	4.25e4
Acid	20.10	870	63.25	11.06	22	1.3e5
Com	19.35	870	69.14	11.64	6.6	8.1e4

Jsc= Photocurrent density. Voc = Open circuit voltage. FF=Fill Factor. η = Efficiency .Rs= Series Resistance. Rsh = Shunt resistance.

To study further the reasons for the differences between the acid and the basic $mpTiO_2$ films in MAPI perovskite solar cells we carried out, as detailed below, photo-induced time resolved advanced spectroscopy such as PIDC and PIT-PV.

3.4 Photo-induced differential charging (PIDC) and photo-induced transient photo-voltage (PIT-PV)

The PIDC technique has been previously applied in OPV and QDSC (quantum dot solar cells) and more recently in MAPI perovskite solar cells to measure the charge density at different light bias[17]. As can be seen in Figure 7 the PIDC data at different light bias leads to a different exponential distribution of the charges. The PIDC data is the result of the accumulated charge at the different materials including the $mpTiO_2$, the MAPI perovskite and the HTM.

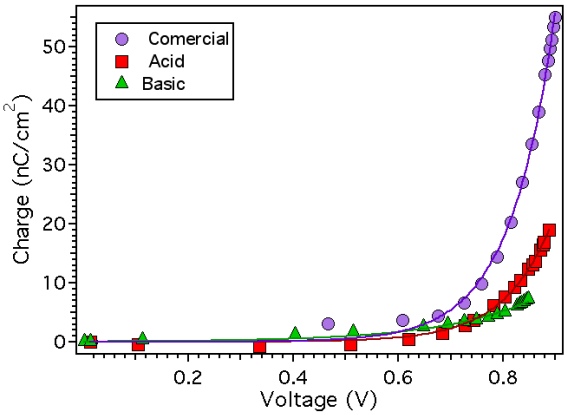

***Figure 7**. Charge measured using PIDC at different light bias for the different $mpTiO_2$ MAPI perovskite solar cells.*

In previously $mpTiO_2$ based MAPI perovskite solar cells PIDC was correlated to the electronic charge at solar cell and, moreover, it was possible to obtain the recombination current value Jrec for the devices with good agreement with the measured Jsc. However, the Jrec values were only meaningful when the fastest component of the PIT-PV decay was considered.

We carried out the PIT-PV measurements (Figure 8), as described before, leaving the MAPI solar cell under different illumination intensities to stabilize its Voc.

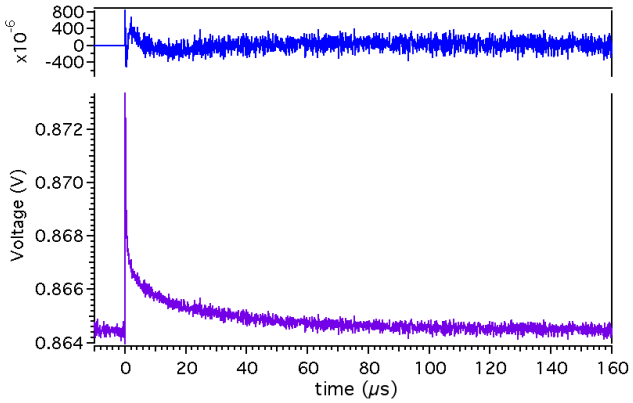

***Figure 8**. The PIT-PV decay at 1sun (solar cell Voc= 0.870V) for the MAPI solar cells fabricated using the commercial mpTiO$_2$. The top figure shows the residual plot for the decay fitting to a bi-exponential equation.*

For all MAPI solar cells, independently of the mpTiO$_2$ used the PIT-PV decay cannot be fitted to a single mono-exponential equation but to a double-exponential equation instead. These results are in good agreement with previous measurements.[17,19]

In Figure 9, we compare the fastest component of the PIT-PV decay at the same charge measured by PIDC.

As can be seen, the slowest decay lifetime corresponds to the commercial mpTiO$_2$ MAPI perovskite solar cells in clear contrast with the basic TiO$_2$ based devices.

On the one hand, the faster lifetime component of the decay for the basic mpTiO$_2$ MAPI perovskite solar cells can explain the lower Voc observed for these devices. This fast component is related to the electronic charge in the solar cell and the carrier recombination kinetics. Moreover, the slope of the charge vs. the decay lifetime for the basic mpTiO$_2$ (α = 2.4) implicates that small changes on the light bias leads to a greater increase of the decay kinetics in comparison with the acid or the commercial mpTiO$_2$ MAPI perovskite solar cells, which present an α= 0.96 and α= 0.7 respectively. On the other hand, the charge vs. decay lifetime for the acid mpTiO$_2$ MAPI perovskite solar cell is not much different when compared to the commercial mpTiO$_2$ device, which is in good agreement with the measured Voc (Figure 6).

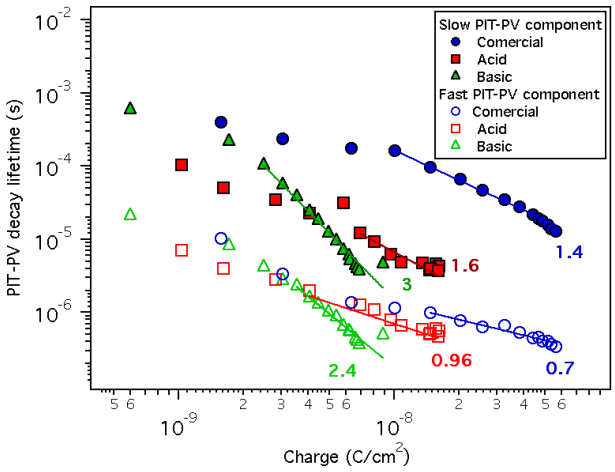

***Figure 9**. Charge vs. PIT-PV decay lifetimes. Filled and empty symbols correspond to the slow and the fast decay components, respectively.*

4. Conclusions

In overall, we have demonstrated that different synthetic routes to achieve nanocrystalline TiO_2 nanoparticles lead to substantial differences in the solar-to-energy conversion efficiency of mesoporous TiO_2/ MAPI based solar cells. The differences observed are more accentuated in the solar cells open-circuit voltage value. A complete study of the charge transfer reactions in complete devices, illustrates that for the solar cells based on the mpTiO_2 from the basic route the electron transfer from the MAPI conduction band to the TiO_2 conduction band is less favoured. This can be understood in terms of TiO_2 conduction band energy position. It is well established that the TiO_2 conduction band can be shifted towards higher energy values, which makes the charge transfer less favourable. For example, in DSSC the use of pyridine in the liquid electrolyte shifts the TiO_2 CB and decreases the electron injection from the dye excited state (and hence the device photocurrent). In MAPI solar cells, since MAPI can transport effectively electrons and holes within the same material, there is no need of mesoporous TiO_2 to transport the electrons to the contact. Thus, even though the electron transfer process is less efficient in the basic TiO_2 it is still feasible to achieve high currents alike in Al_2O_3 mesoporous based MAPI solar cells[27]. This result is further confirmed by L-TAS where the decay amplitude, which is related to the population of polarons in the spiro-OMETAD as a result of the charge transfer process between the MAPI and the spiro-OMETAD, is also much lower for the basic mpTiO_2/MAPI solar cell.

Moreover, the analysis of the charges at the solar cells, under different illumination conditions using PIDC, shows that for a given voltage, close to sun-simulated illuminations of 1 sun, the acid and the basic mpTiO_2 show similar values in contrast to the commercial mpTiO_2/MAPI that has higher charge density. In other type of solar cells[28], the accumulated charge is related to the splitting of the quasi Fermi levels in the different materials that lead to the solar cell junction. The energy difference between the quasi Fermi levels is directly related to the solar cell open-circuit voltage. Hence, the more charge accumulated, the greater the difference in energy between the quasi Fermi levels and higher is the Voc. Furthermore, the analysis of the PIT-PV decay kinetics (Figure 9) indicates that it is faster for the basic TiO_2, when comparing the data at the same charge density, and these faster kinetics are related to the lower measured Voc because the analysis of the charge density for the acid and the basic TiO_2 (Figure 7) shows that are almost identical despite the larger Voc measured for the acid TiO_2. Thus, we have demonstrated that the efficiency of MAPI solar cells, based on mesoporous TiO_2, not only depends on the MAPI itself as photoactive material but also on the nature of the TiO_2 nanocrystalline particles that effects important changes on the interfacial charge transfer process that limit the solar cell efficiency.

References

1. Boix, P. P., Nonomura, K., Mathews, N. & Mhaisalkar, S. G. Current progress and future perspectives for organic/inorganic perovskite solar cells. *Mater. Today* **17,** 16–23 (2014).

2. Gao, P., Grätzel, M. & Nazeeruddin, M. K. Organohalide lead perovskites for photovoltaic applications. *Energy Environ. Sci.* **7,** 2448–2463 (2014).

3. Ramakrishna Reddy, K. T., Koteswara Reddy, N. & Miles, R. W. Photovoltaic properties of SnS based solar cells. *Sol. Energy Mater. Sol. Cells* **90,** 3041–3046 (2006).

4. Katagiri, H. *et al.* Development of CZTS-based thin film solar cells. *Thin Solid Films* **517,** 2455–2460 (2009).

5. Smalley, R. E. Future Global Energy Prosperity: The Terawatt Challenge. *MRS Bull.* **30,** 412–417 (2005).

6. Yang, W. S. *et al.* High-performance photovoltaic perovskite layers fabricated through intramolecular exchange. *Science* . **348,** 1234–1237 (2015).

7. Stranks, S. D. & Snaith, H. J. Metal-halide perovskites for photovoltaic and light-emitting devices. *Nat. Nanotechnol.* **10,** 391–402 (2015).

8. Nakata, K. & Fujishima, A. TiO2 photocatalysis: Design and applications. *J. Photochem. Photobiol. C Photochem. Rev.* **13,** 169–189 (2012).

9. Haidry, A. *et al.* Hydrogen gas sensors based on nanocrystalline TiO2 thin films. *Open Phys.* **9,** 1351–1356 (2011).

10. Mathew, S. *et al.* Dye-sensitized solar cells with 13% efficiency achieved through the molecular engineering of porphyrin sensitizers. *Nat. Chem.* **6,** 242–7 (2014).

11. O'Regan, B. & Grätzel, M. A low-cost, high-efficiency solar cell based on dye-sensitized colloidal TiO2 films. *Nature* **353,** 737–740 (1991).

12. Hore, S. *et al.* Acid versus base peptization of mesoporous nanocrystalline TiO2 films: functional studies in dye sensitized solar cells. *J. Mater. Chem.* **15,** 412 (2005).

13. Fabregat-Santiago, F. *et al.* The origin of slow electron recombination processes in dye-sensitized solar cells with alumina barrier coatings. *J. Appl. Phys.* **96,** 6903 (2004).

14. Palomares, E., Clifford, J. N., Haque, S. A., Lutz, T. & Durrant, J. R. Control of charge recombination dynamics in dye sensitized solar cells by the use of

conformally deposited metal oxide blocking layers. *J. Am. Chem. Soc.* **125,** 475–82 (2003).

15. Xue, Q. *et al.* Metallohalide perovskite–polymer composite film for hybrid planar heterojunction solar cells. *RSC Adv.* **5,** 775–783 (2015).

16. Im, S. H., Heo, J.-H., Han, H. J., Kim, D. & Ahn, T. 18.1 % hysteresis-less inverted CH3NH3PbI3 planar perovskite hybrid solar cells. *Energy Environ. Sci.* **8,** 1602–1608 (2015).

17. O'Regan, B. C. *et al.* Optoelectronic Studies of Methylammonium Lead Iodide Perovskite Solar Cells with Mesoporous TiO_2 : Separation of Electronic and Chemical Charge Storage, Understanding Two Recombination Lifetimes, and the Evolution of Band Offsets during J-V Hysteresis. *J. Am. Chem. Soc.* **137,** 5087–99 (2015).

18. Im, J.-H., Lee, C.-R., Lee, J.-W., Park, S.-W. & Park, N.-G. 6.5% efficient perovskite quantum-dot-sensitized solar cell. *Nanoscale* **3,** 4088–93 (2011).

19. Marin-Beloqui, J. M., Hernández, J. P. & Palomares, E. Photo-induced charge recombination kinetics in MAPbI 3−x Cl x perovskite-like solar cells using low band-gap polymers as hole conductors. *Chem. Commun.* **50,** 14566–14569 (2014).

20. Suttiponparnit, K. *et al.* Role of Surface Area, Primary Particle Size, and Crystal Phase on Titanium Dioxide Nanoparticle Dispersion Properties. *Nanoscale Res. Lett.* **6,** 1–8 (2011).

21. De Bastiani, M., D'Innocenzo, V., Stranks, S. D., Snaith, H. J. & Petrozza, A. Role of the crystallization substrate on the photoluminescence properties of organo-lead mixed halides perovskites. *APL Mater.* **2,** 081509 (2014).

22. Roiati, V. *et al.* Investigating charge dynamics in halide perovskite-sensitized mesostructured solar cells. *Energy Environ. Sci.* **7,** 1889–1894 (2014).

23. Yamada, Y., Nakamura, T., Endo, M., Wakamiya, A. & Kanemitsu, Y. Photocarrier recombination dynamics in perovskite CH3NH3PbI3 for solar cell applications. *J. Am. Chem. Soc.* **136,** 11610–3 (2014).

24. O'Mahony, F. T. F. *et al.* Improved environmental stability of organic lead trihalide perovskite-based photoactive-layers in the presence of mesoporous TiO 2. *J. Mater. Chem. A* **3,** 7219–7223 (2015).

25. Marchioro, A. *et al.* Unravelling the mechanism of photoinduced charge transfer processes in lead iodide perovskite solar cells. *Nat. Photonics* **8,** 250–255 (2014).

26. Gottesman, R. *et al.* Photoinduced Reversible Structural Transformations in Free-Standing CH3NH3PbI3 Perovskite Films. *J. Phys. Chem. Lett.* **6,** 2332–2338 (2015).

27. Lee, M. M., Teuscher, J., Miyasaka, T., Murakami, T. N. & Snaith, H. J. Efficient Hybrid Solar Cells Based on Meso-Superstructured Organometal Halide Perovskites. *Science.* **338,** 643–647 (2012).

28. Bisquert, J. & Garcia-Belmonte, G. On Voltage, Photovoltage, and Photocurrent in Bulk Heterojunction Organic Solar Cells. *J. Phys. Chem. Lett.* **2,** 1950–1964 (2011).

UNIVERSITAT ROVIRA I VIRGILI
SEMICONDUCTOR NANOPARTICLES AS PLATFORM FOR BIO-APPLICATIONS AND ENERGY RELATED SYSTEMS.
Alba María Matas Adams
Dipòsit Legal: T 55-2016

Summary and Perspective

UNIVERSITAT ROVIRA I VIRGILI
SEMICONDUCTOR NANOPARTICLES AS PLATFORM FOR BIO-APPLICATIONS AND ENERGY RELATED SYSTEMS.
Alba María Matas Adams
Dipòsit Legal: T 55-2016

Summary

In the last few decades the investigation of semiconductor fluorescent materials has been a hot topic due to their advantages and their multidisciplinary use.

This thesis is divided in three sections as the semiconductors present different nature and use.

Section 1 includes the 4 first chapters dedicated to Quantum dots (QDs), nanoparticles with sizes below 10 nm.

Due to quantum confinement effects, the size is related to the wavelength of emission (the smaller the size, the bluer the emission).

The different advantages compared with other fluorescent compounds as dyes, has provoked them to be the best substitutes and their massive applications include the direct use as fluorescent tags for different molecules, antibodies, to detect pathogens and toxins as well as to track single cell receptors as explained in Chapter 4.

The main problem with these QDs is their toxicity that arises from the heavy metals present in the structure. To overcome this problem one of the best alternatives is the protection of the core QD with silica or an inert polymer as can be polystyrene.

The coating step beside of decreasing the toxicity also allows the development of other hybrid structures at it supplies functionalization. In Chapter 1, we took advantage of the functionalization delivered by the silica to grow gold nanoparticles in the surface and study the distance effect on the fluorescence after the interaction QDs –metal.

This extra functionalization after the silica coating could also be done after protecting the QDs with other polymers, as can be seen in Chapter 2, where the QDs are covered by polymers following a layer-by layer approach leading to a carboxyl functionalization that allows for further attachments, for example a dye as TAMRA. This system was developed for the use as controls in flow cytometry, as the size is smaller than the normal blanks used and the fluorescence coming from the QDs present a higher PLQY than the dyes and molecules used until now.

A phenomenon that takes place and involves QDs is the Förster Resonance Energy Transfer (FRET), in which a red QD inside a silica sphere act as reference, a green QD acts as the donor and a TAMRA molecule in the surface of the silica acts as the acceptor as explained in Chapter 3. The distance between the QDs and TAMRA had

to be controlled to avoid quenching effects. Taking advantage of this effect, the system was used to detect cystic fibrosis both qualitatively and quantitatively using an active peptide between the silica and TAMRA, which after conjugation with trypsin was cut, preventing the energy transfer.

Another way to avoid the cytotoxicity of QDs is to use fluorescent nanoparticles that do not contain heavy metals, and in exchange contain for example rear earth elements, as is the case of the nanoparticles synthesized for the second section of the thesis.
This rear earth nanoparticles were divided in two groups depending on wavelength of the absorption, while the down conversion nanoparticles (DCNP) present the absorption at lower wavelengths than the emission (the anti-Stokes shift is bigger than for dyes and even than the one present in QDs) or, the up conversion nanoparticles (UCNP), that behave the other way around, the absorption is at higher wavelengths than the emission.
This section is focused in the synthesis and applications of the UCNP as they present similar properties than QDs: narrow emission, low photobleaching and high photostability, but in addition it presents low noise-to-signal ratio, larger anti-Stokes shift than QDs and are excited in the IR and that wavelength present a bigger penetration depth than UV light that is used to excite QDs.

Chapter 5 and 6 talk about possible applications of the UCNP due to the magnificent properties displayed. In Chapter 5, a comparison study of the incorporation of UCNP and QDs into two different layered double hydroxides (hydrotalcite) shows that while in the Mg/Al hydrotalcite the fluorescence remains unchanged (for both QDs and UCNP), in the case of the Co/Al hydrotalcite, the fluorescence is quenched as the cobalt is able to trap the electros from the QD preventing the relaxation, and for UCNP the emission is not fully quenched as it is a two electron process. This led us to think that UCNP could be used to detect cobalt not only in water, but even for in vivo.
The main issue present with the use of UCNP is that a 980 nm laser is required (in the case of KYF_4: Yb^{3+}, Er^{3+}, and not all the labs possess one or equipment equipped with one).
In our case, to measure simple fluorescence we modified the spectrophotometer to attach the 980 nm laser and we were able to measure the fluorescence directly, but in the case of confocal imaging it is more difficult.

In Chapter 6 the specific recognition of toll-like receptors in human neutrophils used also lanthanide doped nanoparticles, but for the imaging of cells the microscope did not have a 980 nm laser which is the main draw back for this type of materials, so as a solution, the second harmonic wavelength was used (490 nm), to monitor the uptake of functionalized UCNP in neutrophils at 37ºC and at 4ºC, and differences were observed indicating an energy dependent uptake process.

The final section of the thesis is entitled "Other materials" and includes two semiconductor materials that are not QDs or UCNP but present photo-related properties, emphasizing on the multidisciplinary topics of this thesis.
One of the topics is bismuth sulfide that is used in Chapter 7 as photocatalyst for the direct asymmetric α-alkylation of aldehydes. It is compared with two other catalysts as are ruthenium and bismuth oxide, and it was seen that bismuth oxide is a more active catalyst that bismuth sulfide, but the reason behind can be the solubility, but this paves the way for future applications of an environmentally friendly material for photocatalysis.

Finally, in Chapter 8 different synthetic routes were followed to achieve crystalline TiO_2 nanoparticles with different properties as size and charge.
Titanium oxide is used in different areas as paint, catalyst and as scaffold in solar cells (dye solar cells and in the last couple of years in perovskite solar cells).
In our case, we used it as the mesoporous layer in perovskite solar cells, and the different properties lead to differences in the solar to energy conversion efficiency, more accentuated in the open-circuit voltage value, demonstrating that the efficiency not only depends on the photoactive material, but also in the nature of the titanium oxide nanoparticle.

Perspective

When I started this thesis 4 years ago, it seemed that the possible use of QDs and UCNP outside the lab would be unthinkable for at least more than a decade, but time flies and it does in ways we cannot imagine.

This year, in a big electronics conference, Samsung announced the commercialization of a new TV using QDs-LEDs, also, in my last two years, the group developed and patented a system able to detect cystic fibrosis and work is done to use a similar system for the detection of other diseases.

All of this encourages me and future generations to continue the work with QDs and UCNP for different applications.

It is true that we started different projects that due to different reasons (lack of interest of third parties, lack of time…) we did not finish but were really interesting and the preliminary results obtained were encouraging.

One of them is to use the hybrid system of QDs@SiO_2-Au and then attach antibodies also to the surface, this way we will be able to follow the target of the antibody, and if it is a cancerous cell, gold can be used for heat therapy. This can be also possible using UCNP instead of QDs, uniting heat therapy with photodynamic therapy.

Regarding UCNP a future investigation line could be the direct injection of the UCNP@hydrotalcite in cells and see the mechanism of recycling of the nanoparticles inside a biocompatible material as well as continue the study of the direct incubation of UCNP with cells.

We incubated UCNP with neutrophils and observed the apparition of filament-like arms in the cells that could possibly be NETs.

NETs were first described in 2004, as neutrophils extracellular traps formed by the extrusion of intracellular material to concentrate the invading microorganisms.

The nature of these NETs depends on the intracellular material released, and this is directly associated with the time after the contact of the microorganism and the cell

The material released can be a) Nuclear DNA after the degradation of the nuclear envelope and formation of vesicles in the membrane (30-60 min), b) Nuclear DNA after the degradation of the nucleus and the plasma membrane (3-4 h), c) Mitochondrial DNA.

After these NETs are formed, the cells will slowly dye, so a possibility is to take advantage of this NET formation to attack selectively cancer cells.

Another possibility is to take advantage of the fluorescence and absorbance overlap between UCNP and some QDs for FRET and use the mixture in solar cells, this way, the photoactive layer will be able to absorb a bigger section of the solar spectrum.

Finally, we also synthesized kesterite for its application in solar cells. Perovskite solar cells are the hot topic right now, but there are many groups that are looking for alternatives that use more earth abundant materials, being kesterite one of them. We were able to synthesize pure kesterite, but the manufacture of the cells was fruitless, as the kesterite layer was too thin and the cells were short-circuited. We could not continue with this work but if the layer thickness could be increased, this new cell structure could open new pathways to increase the efficiency.

Taking all of this into consideration, I feel free to say that the field of semiconductor materials has a promising future, continuing with the promising past.

UNIVERSITAT ROVIRA I VIRGILI
SEMICONDUCTOR NANOPARTICLES AS PLATFORM FOR BIO-APPLICATIONS AND ENERGY RELATED SYSTEMS.
Alba María Matas Adams
Dipòsit Legal: T 55-2016

UNIVERSITAT ROVIRA I VIRGILI
SEMICONDUCTOR NANOPARTICLES AS PLATFORM FOR BIO-APPLICATIONS AND ENERGY RELATED SYSTEMS.
Alba María Matas Adams
Dipòsit Legal: T 55-2016